The Josephson mixer : a swiss army knife for microwave quantum optics

Emmanuel Flurin

▶ **To cite this version:**

Emmanuel Flurin. The Josephson mixer : a swiss army knife for microwave quantum optics. Quantum Physics [quant-ph]. Ecole normale supérieure - ENS PARIS, 2014. English. NNT : 2014ENSU0024 . tel-01241123v2

HAL Id: tel-01241123

https://theses.hal.science/tel-01241123v2

Submitted on 14 Feb 2019

HAL is a multi-disciplinary open access archive for the deposit and dissemination of scientific research documents, whether they are published or not. The documents may come from teaching and research institutions in France or abroad, or from public or private research centers.

L'archive ouverte pluridisciplinaire **HAL**, est destinée au dépôt et à la diffusion de documents scientifiques de niveau recherche, publiés ou non, émanant des établissements d'enseignement et de recherche français ou étrangers, des laboratoires publics ou privés.

Département de Physique
École Normale Supérieure

Laboratoire Pierre Aigrain

THÈSE de DOCTORAT

Spécialité : Physique Quantique

The Josephson mixer

A Swiss army knife for microwave quantum optics

---

présentée par

Emmanuel Flurin

pour obtenir le grade de docteur de l'École Normale supérieure

sous la direction de Benjamin Huard et de Michel Devoret

Soutenue le 10 Decembre 2014

Devant le jury composé de :

Yasunobu	**Nakamura**	Rapporteur
Göran	**Johansson**	Rapporteur
Fabien	**Portier**	Examinateur
Philippe	**Grangier**	Examinateur
Michel	**Brune**	Président
Benjamin	**Huard**	Directeur de thèse

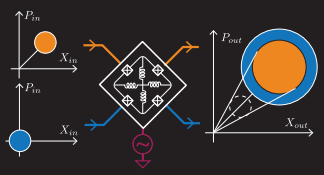

This thesis work explores unique features offered by the Josephson mixer in the upcoming field of microwave quantum optics. We have demonstrated three major roles the Josephson mixer could play in emerging quantum information architectures.

First, we have designed and fabricated a state-of-the-art practical quantum limited amplifier with the best quantum efficiency achieved to date. This tool is crucial for probing mesoscopic systems with microwaves, and in particular superconducting circuits. Hence, it has enabled us to realize successfully the stabilization of quantum trajectories of a superconducting qubit by measurement-based feedback.

Second, we have shown how this circuit can generate and distribute entangled microwave radiations on separated transmission lines at different frequencies. Using two Josephson mixers, we have provided the first demonstration of entanglement between spatially separated propagating fields in the microwave domain, the so-called Einstein-Podolsky-Rosen states.

Finally, we have used the Josephson mixer as a frequency converter. Acting as a switch, it is able to dynamically turn on and off the coupling to a low loss cavity. This feature allowed us to realize a quantum memory for microwaves. In combination with the ability to generate entanglement, we have measured the time-controlled generation, storage and on-demand release of an entangled state, which is a prerequisite for nodes of a quantum network.

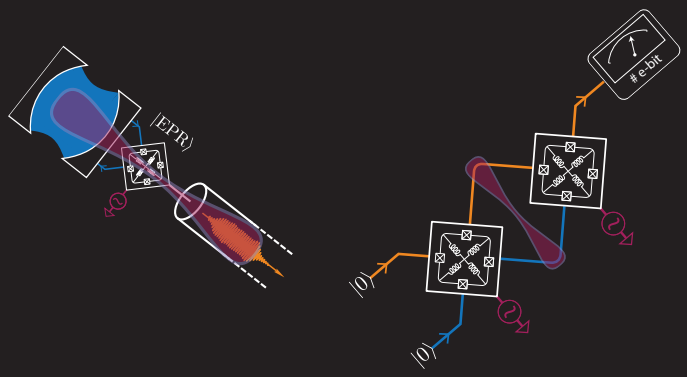

2014 | The Josephson Mixer, a Swiss army knife for microwave quantum optics | Emmanuel Flurin

The Josephson Mixer, a Swiss army knife for microwave quantum optics

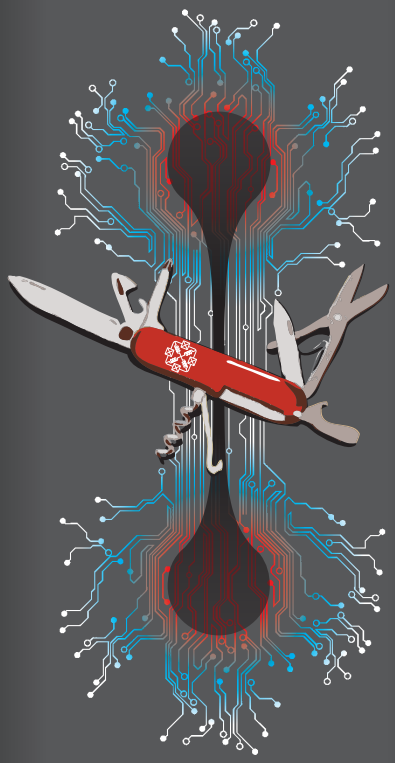

Emmanuel Flurin
Quantum electronics group
LPA - École Normale Supérieure

Nous comprenons la Nature en lui résistant.

Gaston Bachelard

Le mauvais génie d'un roi, Giorgio de Chirico, 1914-15, l'harmonie cachée ou allégorie de quatre années de thèse de physique

ACKNOWLEDGMENTS

Je tiens d'abord à exprimer ma gratitude envers les membres du jury qui ont accepté de consacrer de leur temps à mon travail de thèse :Yasunobu Nakamura, Göran Johansson, Fabien Portier, Philippe Grangier, et Michel Brune.

Ces quatre années passées avec le groupe Qelec ont été incroyables, je suis toujours entré dans cette salle de manip perdue au bout du grand hall de l'ENS avec le coeur joyeux à l'ouvrage, en dépit du cliquetis assourdissant des cryostats. Ce groupe est synonyme pour moi d'un cocktail de bonne humeur, de détermination, de soutien, d'entraide et d'amitié. Tout d'abord un grand merci à Benjamin Huard de m'avoir fait confiance pour mener quelques-unes des toutes premières expériences du jeune groupe. Merci pour ton dynamisme, ta patience et ta quête de l'excellence ; tu représentes pour moi un véritable modèle de chercheur tant sur le plan humain que scientfique.

Merci Michel Devoret pour ton soutien scientifique si précieux au début de ma thèse, pour ces discussions passionnantes et ces aphorismes que je ruminerai encore des années. Merci Philippe Campagne-Ibarcq pour ton allégresse et ton entrain indéstructibles pendant ces belles années, mon jumeau scientifique et mon meilleur acolyte pour les virées parisiennes.

Merci Nicolas Roch, Jean-Damien Pillet, Landry Bretheau, Vladimir Manucharyan et François Mallet, une belle brochette de jeunes chercheurs au caractère déjanté, les uns après les autres vous avez insufflé à l'équipe un parfait équilibre entre camaraderie et excellence scientifique. Les andouillettes à la Montagne et les joutes scientifiques sur le tableau blanc resteront gravés dans ma mémoire. J'espère avoir l'occasion de refaire équipe avec vous dans le futur. Merci Igor Ferrier-Barbut, fils caché du groupe Qelec, pour ton amitié solide comme un roc et ta complicité sans faille. Merci à Danijela Markovic pour ta bonne humeur et ta persévérance lors de cette trop courte année de collaboration scientifique.

Merci également à Mazyar Mirrahimi et Pierre Rouchon pour toutes ces discussions enrichissantes et ce profond souffle mathématique. Merci à toute l'équipe des Takis Boys, Jérémie Viennot, Takis Kontos, Mathieu Dartaille, Matthieu Desjardin, Matthieu Delbecq, Matthieu Baillergeau, Laure Bruhat, Quentin Wilmart... pour ces innombrables pauses cafés passées à refaire le monde de la physique méso et merci Takis pour tes imitations inoubliables. Merci à Erwann Boquillon, Jean-Marc Berroir, Kris Van Houcke, Abhay Shukla et Gabriel Hétet pour ces semestres de fructueuse collaboration pour l'enseignement de la matière condensée à l'ENS.

Je tiens aussi à exprimer ma gratitude à tous les gens du département qui ont rendu ce travail possible. Merci à Michael Rosticher et José Palomo pour votre aide et votre patience en salle blanche. Merci à Anne Matignon, Fabienne Renia pour votre efficacité et votre assistance dans le labyrinthe administratif. Merci à Jack Olejnik, Pascal Morfin, Jules Silembo et tous les membres de l'atelier mécanique pour la réalisation des pièces indispensables aux succès des expériences. Merci à David Darson et Yann Colin pour votre expértise informatique.

Merci à Imran Mahboob pour m'avoir communiqué sa curiosité scientifique au Japon et de m'avoir guidé vers les circuits supraconducteurs. Merci à Nicolas Bergeal et Jérôme Lesueur, mes professeurs de physique quantique à l'ESPCI pour m'avoir introduit à ce champ de la physique fascinant.

Merci à Rémi, Gaby, Myrtille, Yoann pour votre amitié indéfectible. Merci à mes parents, mes frères et soeurs, mes cousins, mes grand-parents pour votre soutien sans faille et pour l'intérêt que vous avez porté à mon travail. Pour finir, merci Hélène d'avoir accepté de partager ta vie avec un physicien.

À mon frère

Le groupe Qelec 2011-2014

CONTENTS

1 INTRODUCTION 1
1.1 The Josephson Ring Modulator 3
1.2 Phase-preserving amplifier at the quantum limit 4
1.3 Generating and witnessing entanglement 6
1.4 Time-controlled generation, storage and on-demand release of an entangled state. 7
1.5 Perspective 10

I JOSEPHSON MIXER 13

2 JOSEPHSON RING MODULATOR 15
2.1 Classical double-balanced mixer 15
2.2 The original Josephson Ring Modulator 16
2.2.1 Three-wave mixing 18
2.2.2 Tunability 18
2.2.3 Stability 19
2.2.4 Phase-slip 20
2.3 The shunted Josephson Ring Modulator 22
2.3.1 Symmetric configuration 22
2.3.2 Third order expansion 24
2.3.3 Stability 24
2.3.4 Broken symmetry configuration 25

3 JOSEPHSON MIXER 29
3.1 Dynamics of a Josephson mixer 29
3.1.1 Normal mode decomposition 29
3.1.2 Participation ratio 31
3.1.3 Quadratic Hamiltonian 31
3.1.4 Three-wave mixing Hamiltonian 32
3.1.5 Parametric interaction term for a pumped Josephson mixer 32
3.1.6 Beyond third-order expansion: Kerr effect 34
3.2 Design of the Josephson Ring Modulator 35
3.3 Design of the resonators 36
3.3.1 Distributed resonators 36
3.3.2 Lumped-element version 38
3.3.3 Coupling to the transmission lines 39
3.3.4 Mapping between distributed and lumped resonators 39
3.4 Experimental characterization of the Josephson mixer 42
3.4.1 Case of the original Josephson Ring Modulator 42
3.4.2 Case of the shunted Josephson Ring Modulator 44
3.4.3 Asymmetric shunted Josephson ring 47
3.5 Conclusion 49

II PARAMETRIC AMPLIFIERS 51
4 AMPLIFICATION OF QUANTUM MICROWAVE SIGNALS 53
4.1 Quantum-limited amplifier 53
4.2 Phase-preserving amplifier 54
4.3 Phase-sensitive amplifier 54
4.4 Heralded noiseless amplifier 55
4.5 Quantum limited measurement and back-action 56
4.6 Degenerate parametric amplifiers 57
4.6.1 Phase-sensitive amplification 57
4.6.2 Phase-preserving amplification 58
4.6.3 Flux-driven amplification 58
4.6.4 Travelling-wave parametric amplifier 59
5 JOSEPHSON MIXER AS AN AMPLIFIER 63
5.1 Non-degenerate parametric amplifier 63
5.1.1 Quantum Langevin equation 64
5.1.2 Self-oscillation regime 67
5.2 Practical parametric amplifier requirements 67
5.3 Gain and Bandwidth 67
5.3.1 Design constraints 68
5.3.2 Measured gain and bandwidth 69
5.4 Frequency tunability 69
5.5 Dynamical range 70
5.5.1 Exhausted Josephson non-linearity 70
5.5.2 Pump depletion 72
5.5.3 Measured dynamical range 73
5.6 Measuring the quantum efficiency 73
5.6.1 Tunnel junction calibration 73
5.6.2 Calibration using a thermal source 76
5.6.3 Calibration using a superconducting qubit as a spectrometer 76
5.7 Low-impedance Josephson Mixer 79
5.7.1 Design 79
5.7.2 Experimental realization 80
5.7.3 Gain and bandwidth performances 80
5.7.4 Quantum efficiency and dynamic range 81
5.8 Performance summary 83
5.9 Conclusion 85

III ENTANGLEMENT GENERATION AND WITNESS 87
6 ENTANGLEMENT WITH CONTINUOUS VARIABLES 89
6.1 Entanglement, a purely quantum resource 89
6.2 Purification principle 90
6.3 Quantum information with continuous-variable 90
6.4 EPR state 91
6.4.1 Two-mode squeezing 91
6.4.2 EPR state as a maximally entangled state 92

6.4.3 EPR state as a Gaussian state 93
6.4.4 Representation of the EPR quantum correlations 94
6.4.5 Marginal distribution of the EPR state 95
6.4.6 Link with the original EPR state 96
6.5 Measures and witness of continuous-variable entanglement 97
6.5.1 Entanglement witness 97
6.6 Josephson mixer as an entanglement witness 99
6.6.1 Coherent recombination of modes 100
6.6.2 Field amplitude interferences 100
6.6.3 Interference of fluctuations as an entanglement witness 101
6.6.4 Link with the EPR non-locality paradox 103
6.6.5 Quantifying Gaussian entanglement with a circuit 104
7 GENERATING ENTANGLED MICROWAVE RADIATIONS WITH A JOSEPHSON MIXER 107
7.1 State of the art of EPR state generation 107
7.1.1 In quantum optics 107
7.1.2 In quantum microwaves 107
7.1.3 Non-classical interferometry experiment 109
7.2 Experimental setup 111
7.3 Field amplitude characterization 112
7.4 Experimental demonstration of entanglement generation 115
7.4.1 Noise measurement 115
7.4.2 Entanglement characterization 117
7.4.3 Effect of the decoherence and reconstructed Wigner distribution 118
7.5 Noise calibration 119
7.5.1 Calibration setup 120
7.5.2 Pump leakage compensation circuit 120
7.5.3 Modeling the imperfections of the circuit 122
7.5.4 Calibration principle 123
7.5.5 Experimental calibration of gain and imperfection 124
7.5.6 Noise measurement procedure 126
7.5.7 Experimental calibration of the vacuum fluctuation level 127
7.6 Conclusion 129
IV ENTANGLEMENT STORAGE 131
8 QUANTUM MEMORY FOR MICROWAVE LIGHT 135
8.1 Spin ensemble 136
8.2 Mechanical resonator 137
8.3 Microwave cavities 138
8.3.1 Parametric conversion as a tunable coupling 139
8.3.2 Microwave storage in a microstrip resonator 140
8.3.3 Microwave storage in a 3D superconducting cavity 140
8.4 Dynamics of the Josephson mixer as a memory 141
8.4.1 Quantum Langevin equation 141

8.4.2 Amplitude scattering coefficient 143
8.5 Dynamical coupling rates 144
8.5.1 Limits on the coupling rates 145
8.5.2 Effect of the antennas 145
8.6 Determination of the coupling to the antennas 146
8.7 Condition for reaching the strong coupling regime 147
9 IMPLEMENTATION OF A SUPERCONDUCTING QUANTUM MEMORY 149
9.1 Design of the memory 149
9.1.1 Required specifications 149
9.1.2 Impact of the 3D geometry on the Josephson mixer design 150
9.2 Experimental characterization of the 3D memory device 152
9.2.1 Tunability and participation ratios 152
9.2.2 Stability of the device in flux 153
9.2.3 Reflection measurements 154
9.2.4 Kerr effect 158
9.2.5 Estimation of the memory lifetime 159
9.2.6 Estimation of the coupling rate 160
9.3 Demonstration of the catch and release of a microwave pulse 161
9.3.1 Time-controlled storage and retrieval 161
9.3.2 Catch and release of coherent pulses 164
9.3.3 Efficiency 166
9.3.4 Lifetime 167
9.3.5 Number of operations within a lifetime 169
10 ENTANGLEMENT OF THE MEMORY WITH A PROPAGATING FIELD 171
10.1 Experimental demonstration of entanglement distribution 172
10.1.1 Field Programmable Gate Array (FPGA) 172
10.1.2 Measured quadrature histograms 173
10.1.3 Inferring memory mode properties from the measurement 175
10.2 Calibration of the measured amplitudes 176
10.2.1 Measurement of the amplitude gain 177
10.2.2 Determination of the gain of the detection setup 178
10.3 Characterization of the entangled state 179
10.3.1 Reconstruction of the covariance matrix 179
10.3.2 Measured covariance matrix 180
10.3.3 Reconstruction of the Wigner distribution 181
10.3.4 Evidence of entanglement 181
10.3.5 Lifetime of the entangled state 182
10.4 Conclusion 184
10.5 Perspectives 185

V APPENDIX 189
A QUANTUM CIRCUITS 191
A.1 Circuit quantization 191
A.2 Dissipation and input/ouptut formalism 192
A.2.1 The transmission line 193

A.2.2 Impedance of a semi-infinite transmission line 193
A.2.3 Propagating modes in the transmission line 194
A.3 Propagating mode quantization 195
A.4 Defining the quantum field operator in the time domain 197
A.5 Wavelet basis and flying oscillators 199
A.6 Quantum Langevin equation 200
B POSITIVE PARTIAL TRANSPOSE CRITERION AND NEGATIVITY 205
B.1 Positive Partial Transpose criterion and Negativity 205
B.1.1 Covariance matrices and Symplectic transformations 206
B.1.2 PPT criterion from the covariance matrix 207
B.1.3 Measure of entanglement for a bipartite gaussian state 207
B.1.4 PPT criterion for a general two-mode squeezed vacuum state 209
C EXPERIMENTAL TECHNIQUES 211
C.1 Low noise measurment 211
C.2 Sample holder 215
C.3 Translation between the notations of this work and previous ones 217
C.4 Nanofabrication processes for Josephson mixer 217
C.4.1 Substrate cleaning 217
C.4.2 Spin coating 217
C.4.3 Aluminum deposition on sapphire chip for e-beam writing 218
C.4.4 e-beam lithography 218
C.4.5 Development 218
C.4.6 Aluminum deposition 219
C.4.7 Lift-off 219
C.5 Grids in the microstrip resonators 219
C.6 Room temperature resistance of Josephson junctions 220
C.7 Amplifying chain 221

VI BIBLIOGRAPHY 223

BIBLIOGRAPHY 225

1 INTRODUCTION

Electromagnetic modes are involved in almost all experiments probing the quantum world. In the optical domain, they are good quantum systems at room temperature owing to the large energy of their photons compared to $k_B T$, which prevents thermal excitations to develop. Similarly, pure states can be reached for their low energy microwave counterparts as long as they are cooled down below 100 mK, which is easily reached in dilution refrigerators. Few facts currently enable delicate physics experiments with quantum microwave modes. First, the telecommunication industry has developed equipments with an unprecedented level of control and measurement resolution of classical microwave signals up to tens of GHz. Second, their energy quanta are smaller than the gap of many usual superconductors. Therefore, superconducting materials can host microwave modes with so little decoherence that the quality factors reach few 10^{10}. Third, they couple to a variety of mesoscopic systems, like Rydberg atoms, superconducting circuits, defects in diamond, mechanical resonators or quantum dots [1, 2, 3, 4].

Using Rydberg atoms or superconducting circuits, whose coupling can overcome decoherence, it was recently demonstrated that a wide variety of non-classical states of microwave modes can be prepare [5, 6, 7, 8, 9, 10, 11]. Given the success of these experiments, the importance of preparing, manipulating and detecting microwave modes in the quantum regime becomes critical. In this context, the group of Michel Devoret at Yale University designed and realized in 2010 a quantum device called the Josephson Ring Modulator (JRM) [12, 13], which implements the three-wave mixing of microwave radiations. This mixing results from the coupling of three separated modes described by annihilation operators $\hat{a}$, $\hat{b}$ and $\hat{c}$ with an interaction term of the form

$$H = \hbar\chi(\hat{a} + \hat{a}^\dagger)(\hat{b} + \hat{b}^\dagger)(\hat{c} + \hat{c}^\dagger). \tag{1}$$

Importantly, these three modes can be addressed separately both in space and frequency. In practice, one of the modes, say $\hat{c}$, acts as a classical signal called the pump so that the interaction term effectively couples the $\hat{a}$ and $\hat{b}$ modes with a dynamically tunable strength $\chi\langle\hat{c}\rangle$, whose effects depend on pump amplitude, phase and frequency. This behavior offers versatility and extensive temporal control of the interaction through the pump "knob".

Although widely used in the optical domain, such a three-wave mixer was a missing component in the quantum microwave toolbox. **This thesis explores unique features offered by this powerful device in the rising field of microwave quantum optics. We have identified and demonstrated three major roles the Josephson mixer could play in emerging quantum information architectures.**

First, it is a crucial tool in the measurement setups of superconducting circuits. We have designed and fabricated a state-of-the-art **practical quantum limited am-**

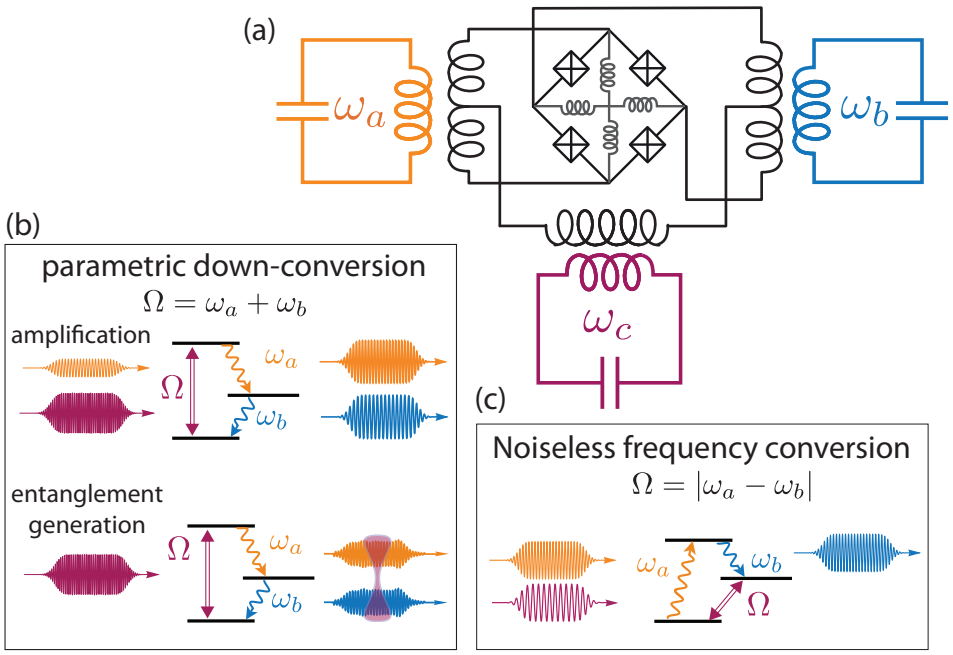

Figure 1: (a) Electronic scheme of a shunted Josephson Ring Modulator (JRM) inductively coupled to three modes $\hat{a}$, $\hat{b}$ and $\hat{c}$. (b) When the pump is operated at the sum frequency $\Omega = \omega_a + \omega_b$, the JRM performs a parametric down-conversion. It can then be used for amplification and entanglement generation. (c) When the pump is operated at the difference frequency $\Omega = |\omega_a - \omega_b|$, the JRM performs a noiseless frequency conversion.

plifier with the best quantum efficiency demonstrated to date. In particular, it has enabled us to realize successfully the stabilization of quantum trajectories of a superconducting qubit by measurement based feedback.

Second, entanglement being instrumental in quantum machines, we have shown how this circuit can generate and distribute **entangled microwave radiations** on separated transmission lines and different frequencies by spontaneous parametric down-conversion. Using two Josephson mixers, we have provided the first demonstration of entanglement between spatially separated propagating fields in the microwave domain. Therefore, a new variety of entangled states, the so-called EPR states (after Einstein, Podolsky and Rosen [14]), which are encoded on continuous variables, is now available in this frequency range.

Finally, we have shown that it could constitute the central component of a potential quantum network based on continuous-variable entanglement. The device essentially acts as a regular mixer performing frequency conversion but without adding extra noise. Used as a switch, it is able to open and close the coupling to a high-quality factor cavity in time-controlled way. We have demonstrated how this feature leads to a new kind of **quantum memory**. Coupled to its ability to generate entanglement, we have demonstrated the **time-controlled generation, storage and on-demand**

release of an entangled state, which is the prerequisite for the node of a quantum network.

Following this path, this thesis describes my theoretical work and three experiments I have performed during my PhD work.

1.1 THE JOSEPHSON RING MODULATOR

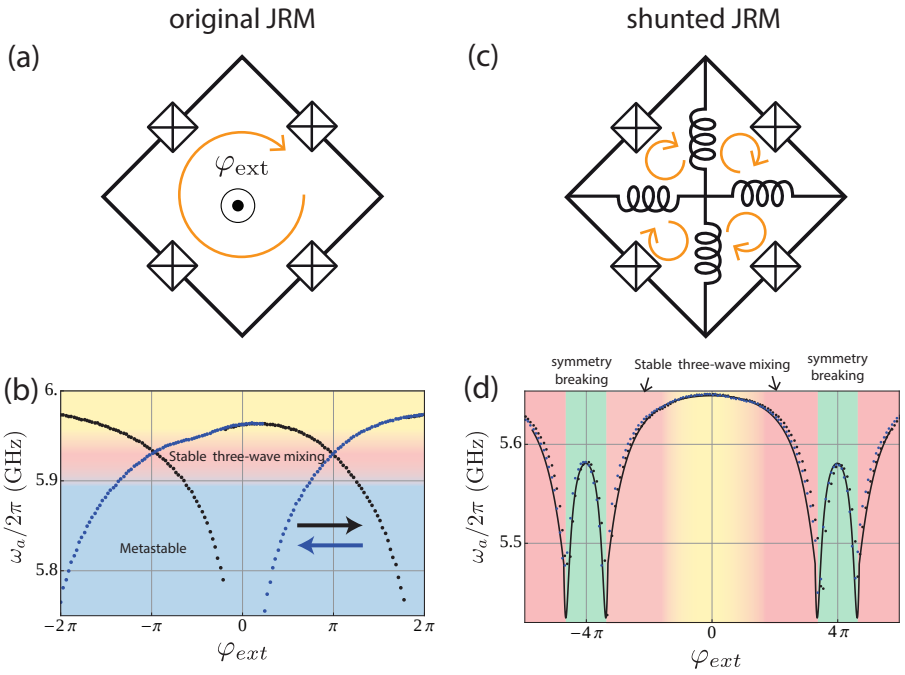

Figure 2: (a) Electronic scheme of the original JRM [13]. (b) Measured resonance frequency of a mode of the Josephson mixer as a function of the reduced magnetic flux threading the loop. (one flux quantum corresponds to 2π). Blue (black) dots indicate a sweep with decreasing (increasing) flux bias. The useful frequency range for amplification is colored in red. (c) Electronic scheme of the shunted JRM. (d) Dots: Measured resonance frequency of a mode of the Josephson mixer as a function of the reduced magnetic flux threading the loop. Blue (black) dots indicate a sweep with decreasing (increasing) flux bias. Line: theoretical expectation for the same. The useful flux range is colored in red, the flux range corresponding to the symmetry breaking is colored in green.

The Josephson mixer and its active component, the so-called Josephson ring modulator (JRM), are introduced in chap. 2. It consists in a ring of four identical Josephson junctions (Fig. 2a). This circuit was invented at Yale in 2010 [12, 13] with the initial purpose of being operated as a phase preserving quantum limited amplifier. This original circuit was successfully demonstrated to operate as an efficient amplifier but suffered from an intrinsic instability when the magnetic flux threading the loop exceeds half a flux quantum. This instability limits the frequency tunability of the device, which consists a serious drawback.

During the beginning of my PhD work, we have proposed a way to solve this issue. First, the source of this instability has been identified. Indeed, when a magnetic flux is threading the loop, an average supercurrent develops in the ring across each of the junctions (Fig. 2a). Such a current bias costs energy. Therefore, beyond half a flux quantum, it is favorable for the system to rearrange its supercurrents by absorbing a flux-quantum. Then, the JRM undergoes a spontaneous phase-slip and reaches a lower energy state. This instability leads to a hysteretic behavior of the resonance frequency when the flux is swept (Fig. 2b).

To solve this issue, we have proposed to divide the original loop in four sub-loops with shunting linear inductors as shown in Fig. 2c. This slight modification adds constraints on the possible repartition of supercurrents in the ring. In particular, the spontaneous phase-slip is inhibited. Furthermore, this modification has the great advantage not to corrupt the pure three-wave mixing character of the original JRM, as long as the symmetries of the circuit are preserved.

Interestingly, for a range of values of the inductors, we have discovered that for magnetic flux biases around two flux quanta threading the whole loop ($\varphi_{ext} = 4\pi$), this shunted JRM breaks the initial left-right symmetry of its supercurrents in the loop. It becomes more favorable to decrease the super current flowing in two opposite junctions at the expense of the two other junctions. This unexpected and beautiful phenomenon can be perfectly modeled, understood and demonstrated.

In the end, the range of stability of the JRM has been highly extended despite this symmetry breaking. Note that the latter is perfectly reversible as opposed to spontaneous phase-slips and its flux threshold can be engineered by design of the shunting inductors.

The physics of the shunted JRM and its symmetry breaking has also been probed experimentally in chapter 3 (Fig. 2d). Indeed, the measurement of the dependence of the resonance frequencies with the applied magnetic flux has enabled us to characterize the JRMs and extract the values of their physical parameters.

1.2 PHASE-PRESERVING AMPLIFIER AT THE QUANTUM LIMIT

With the advent of circuit QED architectures, a strong renewed interest in quantum limited amplifiers rose in the last decade. Buidling on the seminal work of Yurke and coworkers in the 1980's [15, 16, 17], several new implementations of superconducting amplifiers were developed. Among the family of linear amplifiers, all implementations [18, 19, 20, 21, 8, 22, 23, 24, 25] used single modes until the Yale group introduced the Josephson Ring Modulator [12, 13].

In the Josephson mixer, parametric amplification takes place when a continuous wave, the pump, is sent to mode $\hat{c}$ at the frequency Ω chosen to be at the sum of the frequencies of the fields $\hat{a}$ and $\hat{b}$, $\Omega = \omega_a + \omega_b$. In the rotating frame, the fast rotating terms in Eq. (1) average down to zero and the effective Hamiltonian reduces to the so-called parametric down-conversion Hamiltonian

$$H = \hbar\chi(\hat{a}^\dagger\hat{b}^\dagger\hat{c} + \hat{a}\hat{b}\hat{c}^\dagger) \tag{2}$$

The elementary process associated with this Hamiltonian corresponds to splitting a pump photon into a photon on $\hat{a}$ and $\hat{b}$ modes as sketched in Fig. 1b.

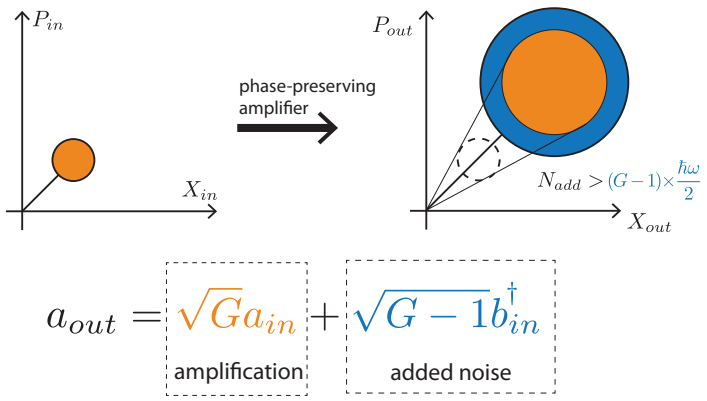

Figure 3: Contour of the Wigner function of a coherent state at the input of a quantum limited phase preserving amplifier. After amplification, the amplitude of the state has been multiplied by the amplitude gain $\sqrt{G}$. However, the signal to noise ratio has been degraded by at least the minimum amount allowed by quantum mechanics. It corresponds to an added noise of half a photon referred to the input (blue). This added noise is provided by the vacuum fluctuations of another mode $\hat{b}$, whose presence is essential for phase preserving amplification.

Crucially, there is no restriction on the spatial and temporal extent of the three modes involved in the three-wave mixing, except that they should be independent. In particular, they can be both spatially and spectrally non-degenerate. It means that their input channels can be distant and their resonance frequencies can be non-commensurate. This reveals a big advantage to prevent the large pump power to affect the dynamics of the system producing a signal worth amplifying. A practical consequence is that the device acts as a phase-preserving amplifier since the three modes $\hat{a}$, $\hat{b}$ and $\hat{c}$ are never temporally matched.

In this case, the amplitude of the field at the input of mode $\hat{a}$ is linearly amplified by $\sqrt{G}$ whatever its phase as shown in Fig. 3. Due to the no-cloning theorem however, it is in fact impossible to perform a phase preserving amplification without adding to the signal at least half a photon of noise referred to the input (Fig. 3), which is known as the quantum limit [26]. In the case of the Josephson mixer, the physical origin of these extra-fluctuations is clear, they are provided by the vacuum fluctuations at the input of the mode $\hat{b}$. The Josephson mixer is thus a good candidate for implementing a quantum limited phase preserving amplifier.

The stabilization of the JRM with the shunting inductors enabled us to realize a practical quantum limited amplifier (Fig. 4a,b). By practical we mean an amplifier whose frequency range can be conveniently matched to the system of interest despite fabrication uncertainties. With this first realization, the working frequency can be tuned over 400 MHz. Moreover, its gain ($G > 20$ dB) is large enough to overcome the noise added by the following amplifier in the detection setup. At this gain, it has a sufficiently wide bandwidth (3 MHz) compared to the dynamics of probed systems. Finally, it can sustain few photons per bandwidth at its input (-116 dBm).

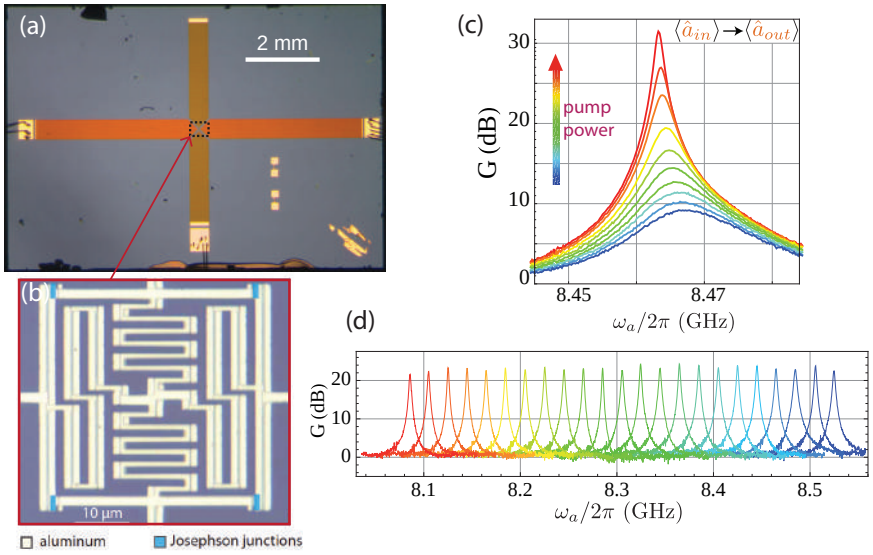

Figure 4: (a) Optical microscope image of the Josephson mixer (b) The shunted JRM is located at the crossing of two superconducting *lambda/2* microstrip resonators hosting the modes $\hat{a}$, $\hat{b}$ and $\hat{c}$. (c) Amplification gain as a function of frequency for an increasing pump power. (d) As a widely tunable amplifier, the Josephson mixer can reach 20 dB of amplification gain over a frequency span of 400 MHz.

We have also characterized the noise performances of three different Josephson mixers using three independent types of calibration. The noise performance can be quantified by the quantum efficiency which quantifies how large is the total signal to noise ratio compared to the quantum limit. Two experiments are based on intrinsically calibrated noise source, the noise emitted by a temperature controlled load gives an efficiency $\eta = 72\%$ and the noise emitted by a voltage biased tunnel junction indicates $\eta > 50\%$. The third experiment uses a superconducting qubit as a spectrometer to calibrate the input signal and gives $\eta = 82\%$. These figures corresponds to the best demonstrated quantum efficiencies achieved to date in the microwave domain.

1.3 Generating and witnessing entanglement

The possibility to couple various mesoscopic systems to microwave signals and the availability of high performance microwave instruments make microwave quantum optics a cornerstone for future quantum machines. In this perspective, continuous variable entanglement between microwave modes becomes highly desirable. Before our work, first efforts in the microwave domain included the demonstration of entanglement between sidebands of a single mode in 2011 by the Zurich group [8] and strong correlations were observed between modes of a single transmission line in the same year by the Chalmers group [22]. Strong correlations were also observed at the output of a Josephson mixer in 2010 by the Yale group [27], but without demonstrating entanglement. Finally, after our work, a collaboration between Munich, Tokyo and Bilbao lead to the demonstration of entanglement between separated transmission lines [28] using path

entanglement. I will now present how non local entangled microwave radiation can be produced, manipulated and measured by the Josephson mixer.

As a quantum limited amplifier, the Josephson mixer leaves a non-classical imprint on its environment that persists long enough to be observed experimentally. In parametric amplification regime, the circuit induces correlations between propagating modes that cannot be explain classically. In particular when the input of $\hat{a}$ and $\hat{b}$ modes start in their vacuum state, entangled microwave radiations arise spontaneously from parametric-down conversion (Fig. 1), as with optical parametric oscillators in the optical domain.

This process generates a so-called Einstein-Podolsky-Rosen (EPR) state, or spatially separated two-mode squeezed vacuum state. The entanglement between the output of $\hat{a}$ and $\hat{b}$ modes can be revealed in the cross correlations between well chosen quadratures of the two fields which fall below the level of vacuum noise.

The experiment realizes the generation of continuous-variable entanglement and its witnessing using a quantum circuit. Actually, this circuit is made of two parts as shown in Fig. 5a. A first Josephson mixer generates an EPR state on two microwave transmission lines. Each part of the EPR pair propagates along distinct transmission line, at a distinct frequency and across a few microwave components. Then, a second Josephson mixer, called the witness, collects the propagating radiations at its inputs and recombines them. The measured fluctuations at one output of the second device are presented in Fig. 5c as a function of the phase ϕ of the pump of the witness. As the ϕ varies, the noise at the output of the witness exhibits interference fringes which go under the level of amplified vacuum noise (solid grey line). Remarkably, such a drop in the output noise level can only be observed if the input modes are entangled. The entanglement is thus witnessed by the noise level on its outputs.

Furthermore, the contour of the Wigner function of the state at the input of the witness can be inferred from this measurement (Fig. 5b). As expected from entangled modes, when the modes are considered separately, each seems occupied by a thermal state. But when considered together, strong correlations beyond the quantum uncertainty develop.

All in all, we describe a non-classical interference experiment, which is by the way the first implementation of an SU(1,1) interferometer, demonstrating that Josephson mixers can entangle and disentangle usable EPR states of microwave light. The present experiment realizes the first demonstration at microwave frequencies of the entanglement between propagating fields on spatially separated transmission lines.

1.4 Time-controlled generation, storage and on-demand release of an entangled state.

Going one step further in the manipulation of entangled quantum microwaves, we have demonstrated the efficient distribution and the time-controlled storage of an EPR state of light. Replacing one of the two transmission lines above by a superconducting $3D$ cavity, and working with pulsed signals, we have realized a quantum memory for microwave signals.

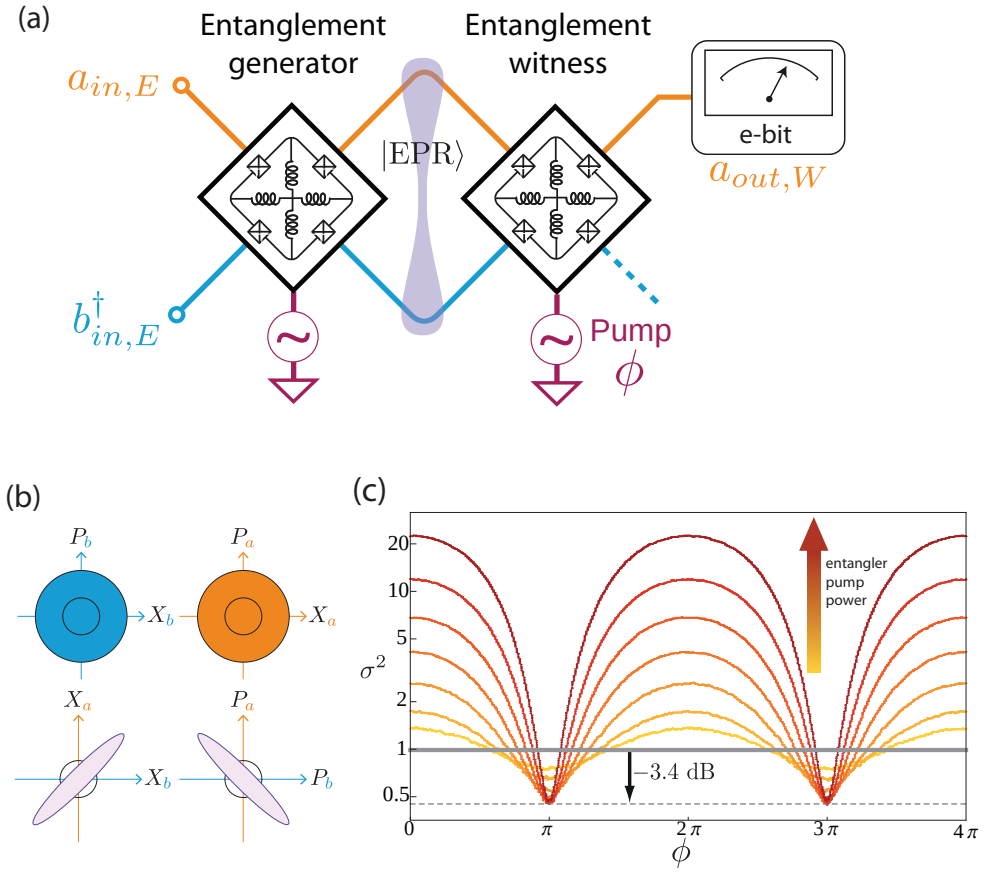

Figure 5: (a) Scheme of the experiment. Two Josephson mixers are placed in series. The first one generates the entangled state under study over two transmission lines. The second Josephson mixer acts as a witness of entanglement at its inputs. (b) Contours of the marginal distributions of the Wigner function of the state incoming on the two ports of the witnessing mixer. Cross-correlations between a and b input modes appear as tilted ellipses in the phase space with quadratures of different modes. (c) The noise at the output of the witness probes directly the cross-correlations between modes. The solid grey line corresponds to vacuum fluctuation amplified by the witnessing device. A drop of the fluctuations below this limit can only be explained by non-classical correlations.

Several implementations of quantum memories for microwave radiation have been realized in the past few years. In order to store the state of microwave signals, some use spin ensembles [29, 30, 31], or mechanical oscillators [32], while others use superconducting cavities with tunable input coupling [33, 34]. Our own implementation is sketched in Fig. 6b, where the JRM allows an on-demand access to the long lived cavity based on noiseless frequency conversion. Its main advantage consists in the ability to generate entanglement between the memory and the output port.

Noiseless frequency conversion is another regime of the Josephson mixer. The frequency of the pump tone is now chosen to be at the difference between the frequencies

of the modes $\hat{a}$ and $\hat{b}$, $\Omega = |\omega_a - \omega_b|$. In the rotating frame, the effective Hamiltonian reduces to a beam-splitter Hamiltonian with an implicit frequency conversion.

$$H = \hbar\chi(\hat{a}^\dagger\hat{b}\hat{c} + \hat{a}\hat{b}^\dagger\hat{c}^\dagger) \tag{3}$$

The elementary process corresponds to the conversion of photons between the mode $\hat{a}$ and $\hat{b}$ mediated by the pump at a rate $\chi|\langle c\rangle|$ as sketched in Fig. 1c. Therefore, the noiseless frequency conversion generates a coupling between the long lived cavity mode b and the propagating modes at the input of mode a. This pump field can then be varied in time to switch on and off the coupling.

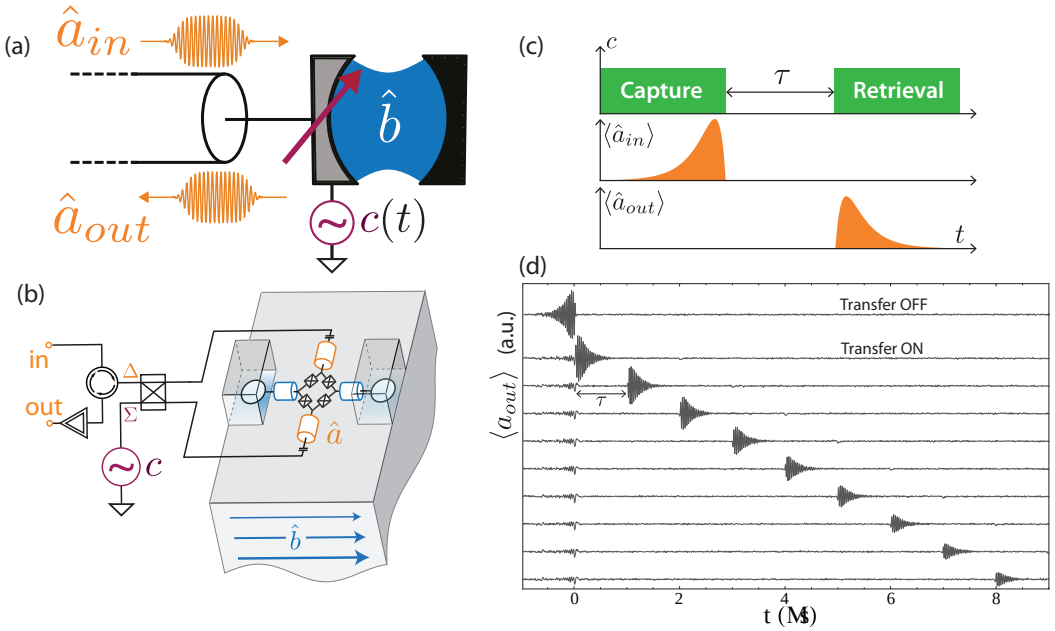

Figure 6: (a) Simplified schematics of the quantum memory. When the pump is driven at $\Omega = |\omega_a - \omega_b|$, the JRM behaves as a beam splitter with an implicit frequency conversion whose transparency depends on the pump amplitude. (b) Schematics of the device. The core of the device is similar to the usual design (Fig. 4) excepted that one of the two transmission lines is replaced by a superconducting $3D$ cavity that defines the memory mode. (c) Protocol of the capture, storage and release of a incoming microwave pulse. (d) Measured output amplitude as a function of time. In the first trace, the pump is always turned off and the measured amplitude corresponds to the reflected incoming pulse. In the following traces, the pump is turned on and varied in time as indicated in (c). The storage time is varied from 0 μs to 8 μs.

A first measurement consists in the capture, storage and retrieval of a microwave pulse. The protocol is quite simple, we turn the pump tone on when the incoming pulse reaches the memory input. The signal pulse has been designed such that it is optimally absorbed by the memory. The pump tone is turned off after the absorption and turned back on at a later time τ to retrieve the pulse in the transmission line. The measured output amplitude in time shown in Fig. 6d demonstrate that this protocol can be performed with a great efficiency for a few microseconds.

However, the unique ability of this device lies the possibility to combine this storage operation with the entanglement generation demonstrated previously. A second measurement consists in the generation, storage and characterization of an EPR state distributed between the memory and the transmission line. The protocol is sketched in Fig. 7b. The pump is first applied at $\Omega = \omega_a + \omega_b$ to generate an EPR state shared between the memory and the propagating mode. The propagating mode complex amplitude is measured and at a later time, the pump is turned on again at $\Omega = |\omega_a - \omega_b|$ to activate the noiseless conversion. The memory mode is then retrieved in the transmission line and its complex amplitude is measured. By analyzing the cross-correlations between these two measurements, we have been able to show that the memory preserves the entanglement of the EPR state. Furthermore, the contours of the EPR state Wigner function have been inferred from this correlation measurement (Fig. 7c) and the entanglement quantified.

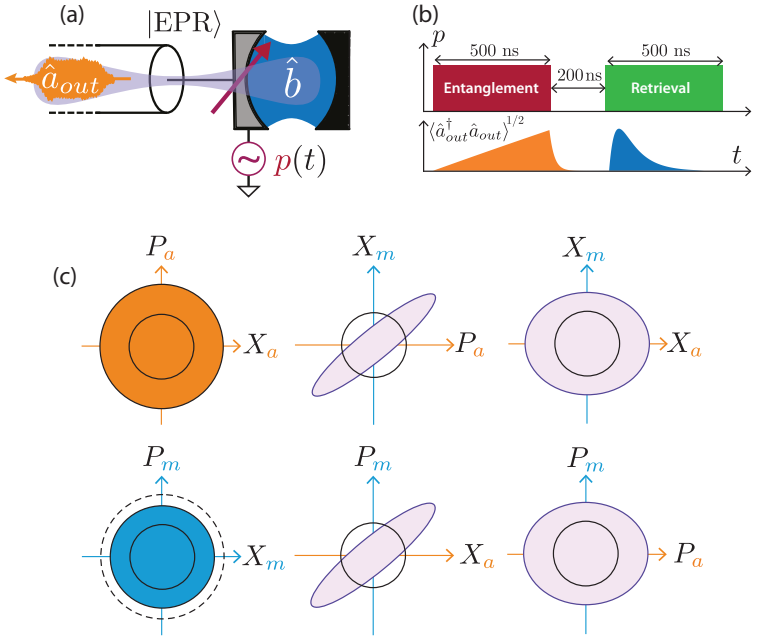

Figure 7: (a) When the pump is shined at $\Omega = \omega_a + \omega_b$, an EPR state is distributed between the transmission line and the memory. (b) Protocol for the entanglement distribution, storage and retrieval. (c) Contour of the marginal Wigner distributions reconstructed from the correlation measurements corresponding to the protocol (b).

1.5 PERSPECTIVE

The experiments performed during this thesis show that the Josephson mixer can be used as a quantum limited amplifier, an entanglement generator and witness and a quantum memory. All these capabilities can be combined in a single device which makes it particularly useful for quantum information processing. The results open various perspectives, which could be reached by tackling a few experimental challenges.

One first needs to extend the lifetime of the quantum memory. With a proper $3D$ microwave design, one should improve the few microseconds lifetime by one or two orders of magnitude. Moreover, the quantum efficiencies achieved in this work could be improved by replacing the commercial microwave components by optimized on-chip designs or fully $3D$ designs based on superconducting waveguides.

Then, by combining the quantum memory with a superconducting qubit, one could perform non-Gaussian operations. This paves the way to the realization of exotic quantum information protocols, such as remote preparation of arbitrary Fock states and quantum teleportation of Schrödinger cat states [35]. One can also consider the implementation of error correction protocols such as quantum distillation [36] in order to overcome the inevitable decoherence. Furthermore, a new paradigm has recently been introduced [37] for mapping the quantum state of a qubit onto two Schrödinger cat states in a microwave cavity. Quantum error correction protocols seem to enable protecting this qubit from decoherence, while avoiding the hardware complexity of usual error correction based on large qubit registers. There, a slightly modified version of the memory could play a key role in the two-qubit gates and in the stabilization of such qubits.

Part I

JOSEPHSON MIXER

2

JOSEPHSON RING MODULATOR

Mixers are instrumental components for microwave engineering, but they are dissipative. In this section, we introduce a superconducting circuit realizing lossless three wave mixing.

2.1 CLASSICAL DOUBLE-BALANCED MIXER

The double balanced mixer is a standard electronics component. It is a passive mixer in which the local oscillator input (LO) and radio-frequency input (RF) are balanced. The main non-linear element is the diode ring modulator, which consists in four diodes placed in Wheatstone bridge configuration as shown in Fig. 8(a). The high symmetry of the mixer leads to suppress all the odd harmonics from frequency modulation.

The first diode ring modulators are based on vacuum tube and were fabricated during the First World War by the US Army Signal Corps. They are still widely used for radio-transmissions; an example of radio-receiver is shown in Fig. 8(d). Surprisingly, diode ring modulators are also valuable for vintage music effect [38], as shown in Fig. 8(e).

The diode ring modulator is today a central component for passive mixer in the microwave range like the GaAs diode ring modulator shown in Fig. 8(a) or the familiar Marki doubly-balanced mixers that we use everyday in the lab.

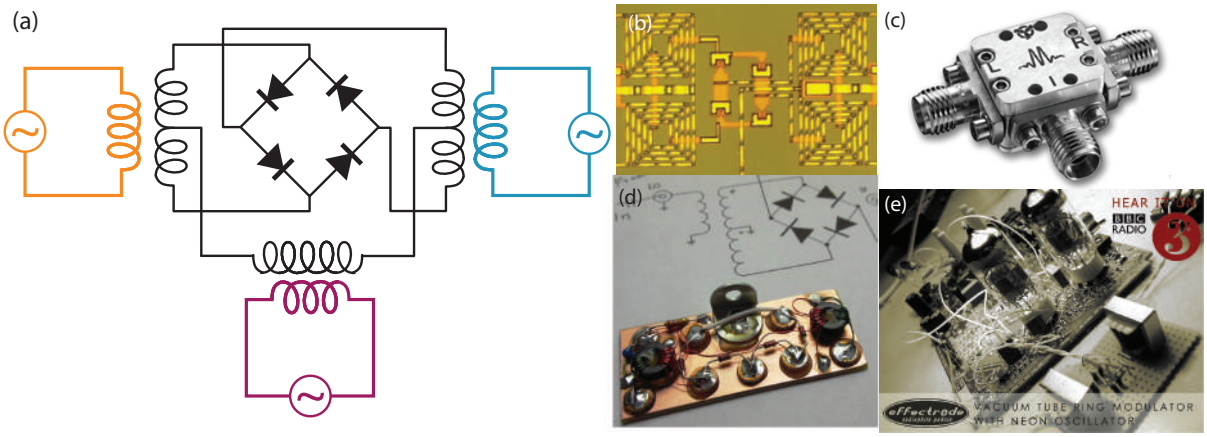

Figure 8: (a) Electronic scheme of a passive doubly-balanced mixer based on diode ring modulator. (b) Microscope image of a GaAs diode ring modulator chip for a $16-22$ GHz mixer from Thomasnet (c) Package for microwave doubly balanced mixer from Marki. (d) Picture of ring modulator as a radio-recever mixer. (e) Vacuum tube ring modulator for vintage guitar effect.

However, these devices made of dissipative elements are far from being quantum limited. Instead of diodes, one can use superconducting tunnel junctions called Josephson junctions. Crucially, such devices are the only non-linear dissipation-less elements avail-

able in the microwave domain. Embedded in superconducting circuits, they represent a key element for the implementation of such a mixer in the quantum regime.

2.2 THE ORIGINAL JOSEPHSON RING MODULATOR

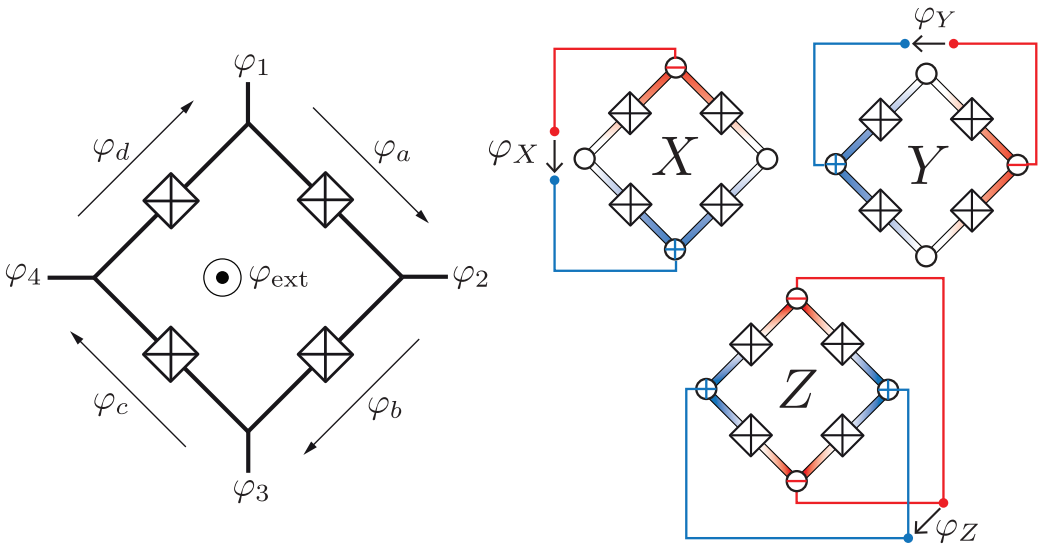

Figure 9: (a) The original Josephson Ring Modulator (JRM) from the work of the Yale group [13, 12] consists in a ring of four Josephson junctions. (b) Schematic of the normal modes of the ring X,Y and Z.

The Josephson Ring Modulator is constituted of four identical Josephson junctions labeled a, b, c and d forming a close-loop thread by a magnetic flux Φ_{ext}. The magnetic flux provides a phase bias to the junctions which induces a super-current flowing in the ring such that the screened magnetic flux threading the loop can only be an integer number of flux quanta.

The phase difference between the order parameters of the superconductor on each side of the junction is linked to the voltage across the junction by the first Josephson relation, $V_i = \varphi_0 \partial_t \varphi_i$ where $\varphi_0 = \hbar/2e$ is the reduced flux quantum and $i = a, b, c, d$. Besides, when operated with a bias current lower than their critical current I_0, Josephson junctions behave as pure nonlinear inductors with inductance $\boxed{L_J(\varphi_i) = \varphi_0/(I_0 \cos\varphi_i)}$. They are the only known nonlinear and non-dissipative circuit elements working at microwave frequencies.

The flux biasing of the junctions in the loop are related by

$$\varphi_a + \varphi_b + \varphi_c + \varphi_d = \varphi_{ext} + 2n\pi \tag{4}$$

where $\varphi_{ext} = \Phi_{ext}/\varphi_0$ is the reduced magnetic flux and n the integer number of flux quanta threading the loop.

The ring can be addressed by external circuits through the nodes 1,2,3 and 4 such that weak oscillating currents can be applied. Given the symmetry of the ring, the

magnetic flux is equally shared between the junctions. Hence, the phase difference across them can be expressed as a function of the reduced fluxes at the nodes

$$\begin{cases} \varphi_a &= \varphi_2 - \varphi_1 + \dfrac{\varphi_{ext}}{4} + n\dfrac{\pi}{2} \\ \varphi_b &= \varphi_3 - \varphi_2 + \dfrac{\varphi_{ext}}{4} + n\dfrac{\pi}{2} \\ \varphi_c &= \varphi_4 - \varphi_3 + \dfrac{\varphi_{ext}}{4} + n\dfrac{\pi}{2} \\ \varphi_d &= \varphi_1 - \varphi_4 + \dfrac{\varphi_{ext}}{4} + n\dfrac{\pi}{2}. \end{cases} \tag{5}$$

Let us introduce the notation $\tilde{\varphi}_{ext} = \varphi_{ext} + 2n\pi$.

The Hamiltonian of the system is simply given by the sum of the four junction Hamiltonians

$$H_{\text{ring}} = -E_J \left[\cos\varphi_a + \cos\varphi_b + \cos\varphi_c + \cos\varphi_d\right] \tag{6}$$

where $E_J = \varphi_0 I_0$ is the Josephson energy and I_0 is the critical current of the junctions.

The normal modes of the circuit can be found by expanding the Hamiltonian up to the second order in $\varphi_{1,2,3,4}$. Then, it can be expressed as a function of the inductance matrix $\mathcal{L}$ and the flux vector $\boldsymbol{\varphi} = \varphi_0 \left(\varphi_1 \ \varphi_2 \ \varphi_3 \ \varphi_4\right)$

$$H_{\text{ring}} = \boldsymbol{\varphi}\frac{\mathcal{L}^{-1}}{2}\boldsymbol{\varphi}^T + o(|\boldsymbol{\varphi}|^2) \tag{7}$$

where

$$\mathcal{L}^{-1} = \frac{I_0}{\varphi_0}\cos\left(\frac{\tilde{\varphi}_{ext}}{4}\right)\begin{pmatrix} 2 & -1 & 0 & -1 \\ -1 & 2 & -1 & 0 \\ 0 & -1 & 2 & -1 \\ -1 & 0 & -1 & 2 \end{pmatrix}. \tag{8}$$

The normal modes of the Josephson ring are directly given by the eigenmodes of the inductance matrix. They can be expressed as a combination of node fluxes[1]

$$\begin{cases} \varphi_X &= \varphi_3 - \varphi_1 \\ \varphi_Y &= \varphi_4 - \varphi_2 \\ \varphi_Z &= \frac{1}{2}(\varphi_2 + \varphi_4 - \varphi_3 - \varphi_1) \\ (\varphi_W &= \frac{1}{2}(\varphi_2 + \varphi_4 + \varphi_3 + \varphi_1)) \end{cases} \iff \begin{cases} \varphi_2 - \varphi_1 &= \frac{1}{2}(\ \ \varphi_X & -\varphi_Y & +2\varphi_Z) \\ \varphi_3 - \varphi_2 &= \frac{1}{2}(\ \ \varphi_X & +\varphi_Y & -2\varphi_Z) \\ \varphi_4 - \varphi_3 &= \frac{1}{2}(-\varphi_X & +\varphi_Y & +2\varphi_Z) \\ \varphi_1 - \varphi_4 &= \frac{1}{2}(-\varphi_X & -\varphi_Y & -2\varphi_Z). \end{cases} \tag{9}$$

Note that the W mode is not coupled to the ring since its eigenvalue is zero. Therefore, the ring is coupled to three orthogonal microwave modes: X and Y are differential modes and Z is a common mode as represented on Fig 9.

1 The choice of normal modes prefactors is important. It is given by the terminal combination across which the mode impedances is defined as shown in Fig. 9. Note that there is a mistake in the choice of the Z mode prefactor in our published work [39] leading to a missing factor 4 on the Z impedance.

Remarkably, the full ring Hamiltonian can be put under a very compact form when expressed in terms of its normal modes thanks to its high symmetry.

$$\boxed{H_{\text{ring}} = -4E_J \cos\frac{\varphi_X}{2}\cos\frac{\varphi_Y}{2}\cos\varphi_Z\cos\frac{\tilde{\varphi}_{ext}}{4} - 4E_J \sin\frac{\varphi_X}{2}\sin\frac{\varphi_Y}{2}\sin\varphi_Z\sin\frac{\tilde{\varphi}_{ext}}{4}.} \tag{10}$$

2.2.1 *Three-wave mixing*

At rest, no current is applied to the nodes $\varphi_{X,Y,Z} = 0$. Then, small current modulations around this equilibrium point can be considered. The third order expansion of the Hamiltonian in $\varphi_{X,Y,Z}$ exhibits a very pure three-wave mixing term in the sense that it is the only third order term.

$$\boxed{\begin{aligned} H_{\text{ring}} \;=\; & -4E_J\cos\left(\frac{\tilde{\varphi}_{ext}}{4}\right) && \text{energy at rest} \\ & +\tfrac{1}{2}E_J\cos\left(\frac{\tilde{\varphi}_{ext}}{4}\right)(\varphi_X^2+\varphi_Y^2+4\varphi_Z^2) && \text{inductance} \\ & -E_J\sin\left(\frac{\tilde{\varphi}_{ext}}{4}\right)\varphi_X\varphi_Y\varphi_Z && \text{three wave mixing} \\ & +O(|\varphi|^4). \end{aligned}} \tag{11}$$

This powerful result shows that the Josephson Ring Modulator can carry out the operation of mixing three orthogonal modes while producing a minimal number of spurious nonlinear effects. The Wheatstone-bridge type of symmetry eliminates most of the unwanted terms in the Hamiltonian which would induce unwanted types of mixing.

Therefore, by coupling the normal modes of the ring to resonant quantum fields with the corresponding symmetries, differential for X and Y and common for Z, a dissipationless circuit based on the Josephson ring implements a pure quantum mixer.

However, the strength of the mixing term depends on the magnetic flux applied. It is optimum for $\varphi_{ext} = 2\pi$, however this particular bias point is highly unstable. I will demonstrate in section 2.2.3 that the best trade-off between stability and mixing strength is in a short range around $\varphi_{ext} = \pi$.

2.2.2 *Tunability*

Importantly, the Josephson ring embedded in a superconducting resonator contributes to the total inductance of the circuit as can be seen from second order terms in 11. Moreover, the inductance of the ring is modulated by the magnetic flux bias and is given by

$$L_{X,Y} = \frac{\varphi_0}{I_0\cos\left(\frac{\tilde{\varphi}_{ext}}{4}\right)} \qquad \text{and} \qquad L_Z = \frac{\varphi_0}{4I_0\cos\left(\frac{\tilde{\varphi}_{ext}}{4}\right)}. \tag{12}$$

Hence, by tuning the flux bias, one can tune the resonance frequency of the superconducting resonator embedding the ring. The potential frequency tunability is an

essential requirement for practical devices. In particular, in amplification mode, the mixer must match the frequency of the system under investigation within its limited bandwidth.

However, the stability range of the device isn't sufficient to offer an efficient three-wave mixing on a wide frequency range as we will see in the following section.

2.2.3 *Stability*

In this section, we are investigating the unstability of the original Josephson ring and eventually present a way for solving this issue.

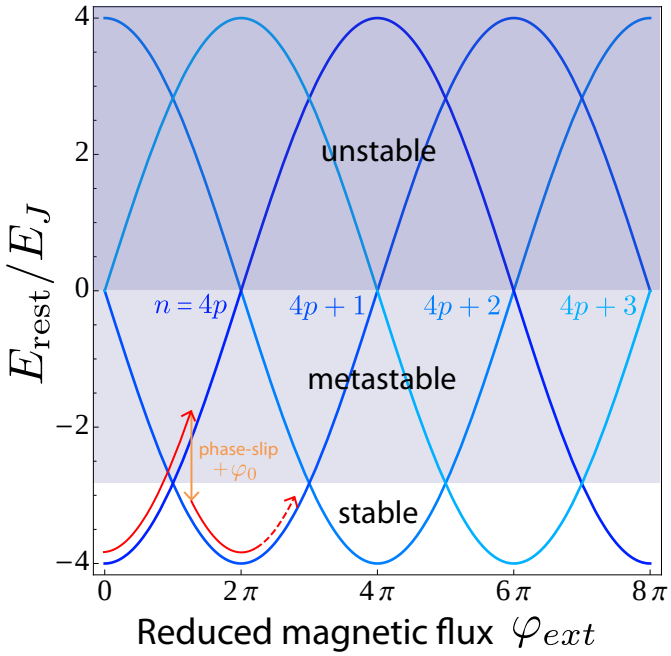

Figure 10: Energy state of the ring at rest, for the four configurations of the phases across the junctions satisfying $\varphi_a + \varphi_b + \varphi_c + \varphi_d = \varphi_{ext} + 2n\pi$. Each configuration is 8π-periodic (four flux quanta) but the overall periodicity remains 2π (single flux quanta). When the system enters the metastable zone, it can undergo a phase-slip (orange arrow) to return in the lower energy state. It corresponds to the entrance of a flux quantum in the ring through a junction. A phase-slip necessarily occurs before reaching the unstable zone. Thus, the system behaves hysteretically when the magnetic flux bias is swept.

Importantly, four distinct configurations of the flux across the ring coexist depending on the number of flux quanta threading the loop. However, their energy at rest and stability vary with the magnetic flux bias. The energy as a function of the number of flux-quanta in the ring and of magnetic flux is given by

$$E_{\text{rest}} = -4E_J \cos\left(\frac{\varphi_{ext}}{4} + n\frac{\pi}{2}\right). \tag{13}$$

The four distinct configurations correspond to quantum-flux number $n = 4p$, $n = 4p+1$, $n = 4p+2$ and $n = 4p+3$.

Moreover, the flux configurations are unstable when at least one potential curvature $\partial^2 H/\partial\varphi^2_{X,Y,Z}$ is negative which is equivalent to say that the inductance of at least one of the normal modes is negative, $L_{X,Y,Z} < 0$. Therefore, only two configurations are stable simultaneously as shown on Fig. 10. These configurations are separated by a single flux-quantum only.

2.2.4 *Phase-slip*

Two stable configurations can coexists. However when the magnetic flux is ramped up so that the system transits from a global minimum to a local minimum of the potential, the occupied configuration becomes metastable. The system can then tunnel through the potential barrier to reach the global minimum. Such an event is called **phase-slip**. It corresponds to the entrance of a flux-quantum in the loop through one of the junctions of the ring, which are the weakest links.

We would like to understand the dynamics of the phase-slip and find the height of the potential barrier. When a phase slip occurs, a flux-quantum enters in the ring, an extra $\pi/2$-phase is incremented across each of the Josephson junction. However, the junction across which the flux-quantum has slipped through, evolves in the opposite way. It actually acquires a $-3\pi/2$ phase such that the overall phase across the ring is kept constant during the process, according to Eq. (4). In the end, it leads to a $\pi/2$ phase and an extra-flux quantum.

For instance, let us say that the flux-quantum slips across the junction a then

$$\begin{cases} \varphi_a & \rightarrow & \varphi_a - \frac{3\pi}{2} & \overset{[+2\pi]}{\equiv} & \varphi_a + \frac{\pi}{2} \\ \varphi_b & \rightarrow & \varphi_b + \frac{\pi}{2} & & \\ \varphi_c & \rightarrow & \varphi_c + \frac{\pi}{2} & & \\ \varphi_d & \rightarrow & \varphi_d + \frac{\pi}{2}. & & \end{cases} \tag{14}$$

Therefore the phase-slip corresponds to crossing the potential landscape along the line $-3\varphi_a = \varphi_b = \varphi_c = \varphi_d$ corresponding also to $\varphi_X = \varphi_Y = 2\varphi_Z$. One can prove that it is, indeed, the lowest potential barrier to cross in order to reach the global minimum. The cut of the ring potential is represented on Fig. 11

Fig. 11(b) shows the ring potential when the system is initialized in the lower energy configuration for magnetic flux bias at $\varphi_{ext} = 0$. The bias is slowly swept up to $\varphi_{ext} = 2\pi$. On can show that the potential barrier maximum is for $-3\varphi_a = \varphi_b = \varphi_c = \varphi_d = \pi/2 - \dfrac{\varphi_{ext}}{4}$. Therefore, the height of the barrier to pass during a phase slip is given by

$$\Delta E_{barrier} = 4E_J \cos\frac{\varphi_{ext}}{4}\left(1 - \sin\frac{\varphi_{ext}}{4}\right). \tag{15}$$

For mode frequencies around 9 GHz and critical current of 3 μA, at zero temperature, one can show that the system undergoes a spontaneous phase-slip by tunneling across the barrier when the magnetic flux bias reaches $\varphi^{PS}_{ext} \sim 1.7\pi$.

Note that in parametric amplification mode, phase-slips can be induced by the strong pump tone. Thus, the Josephson ring is actually unpractical for even smaller magnetic flux biases.

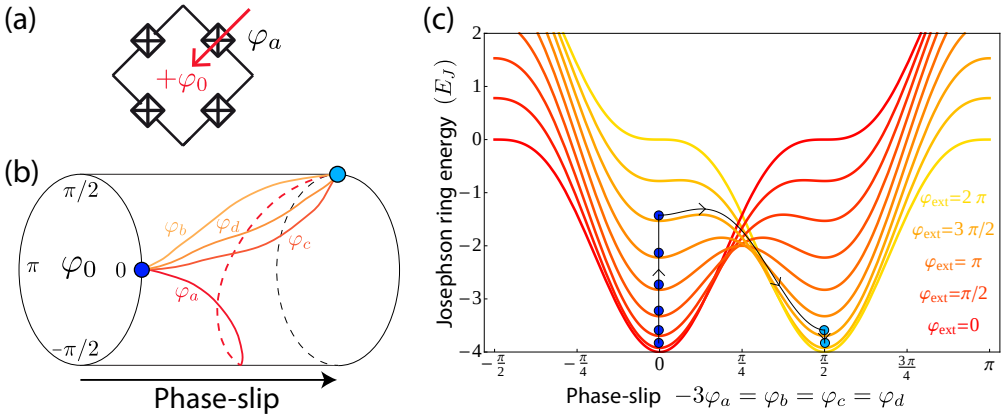

Figure 11: (a) A flux-quantum enters the ring through the junction a. (b) Schematics of the phase trajectories during the phase-slip. (c) Cut of the Josephson ring potential along the phase-slip path for different magnetic fluxes. Note that the two minima coexists but are separated by a potential barrier.

A way to extend the stability range of the Josephson Ring modulator is to add constraints to the phases across the ring to prevent the entrance of flux-quanta by phase slip. The strategy we have implemented consists in shunting the ring with inductors as shown on Fig. 9(b). Four identical linear inductors link the four nodes together, hence defining four sub-loops, one per junction. The ring dynamics then recovers a periodicity of one flux quantum. Note that the circuit keeps the symmetry of the original ring which is essential to preserve a pure three-wave-mixing Hamiltonian.

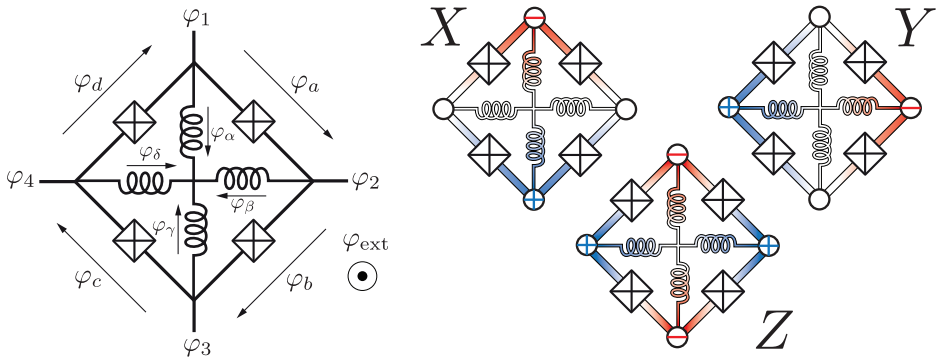

Figure 12: (a) The shunted Josephson Ring Modulator (JRM) consists in a ring of four identical Josephson junctions shunted by four linear inductors. (b) Schematic of the normal modes of the ring X,Y and Z

The circuit Hamiltonian reads

$$\begin{aligned} H_{\text{ring}} &= -E_J \quad [\cos\varphi_a + \cos\varphi_b + \cos\varphi_c + \cos\varphi_d] \\ &\quad +\tfrac{1}{2}E_L \quad [\varphi_\alpha^2 + \varphi_\beta^2 + \varphi_\gamma^2 + \varphi_\delta^2] \end{aligned} \tag{16}$$

where $E_L = \dfrac{\varphi_0^2}{L}$ is the shunting inductance energy and $\varphi_{\alpha,\beta,\gamma,\delta}$ the flux across each of them.

The current across the inductances is $\varphi_0\varphi/L$, hence the charge conservation leads to

$$\frac{\varphi_0}{L}(\varphi_\alpha + \varphi_\beta + \varphi_\gamma + \varphi_\delta) = 0 \tag{17}$$

and the flux bias gives for each sub-loop, according to the faraday law,

$$\begin{cases} \varphi_a + \varphi_\alpha - \varphi_\delta &= \frac{\varphi_{ext}}{4} + 2n_a\pi \\ \varphi_b + \varphi_\beta - \varphi_\alpha &= \frac{\varphi_{ext}}{4} + 2n_b\pi \\ \varphi_c + \varphi_\gamma - \varphi_\beta &= \frac{\varphi_{ext}}{4} + 2n_c\pi \\ \varphi_d + \varphi_\delta - \varphi_\gamma &= \frac{\varphi_{ext}}{4} + 2n_d\pi. \end{cases} \tag{18}$$

2.3.1 *Symmetric configuration*

Given the symmetry of the ring, it is natural to consider a symmetric configuration for which the super-current is equal in each loop at rest. Therefore, the super-current

flowing in two neighboring loops cancels in each shunting inductance (Fig. 13(a)). Thus, using Eq. (17), we get that

$$\varphi_\alpha = \varphi_\beta = \varphi_\gamma = \varphi_\delta = 0. \tag{19}$$

Therefore, the bias of the junction at rest is given by $\varphi_a = \varphi_b = \varphi_c = \varphi_d \equiv \varphi_{ext}/4\ [2\pi]$, the magnetic flux is distributed equally between the four junctions as in the original configuration. The shunting inductances do not contribute to the junctions flux bias.

Out of equilibrium, the symmetric configuration leads to

$$\begin{cases} \varphi_a &= \varphi_2 - \varphi_1 + \dfrac{\varphi_{ext}}{4} + 2n_a\pi \\ \varphi_b &= \varphi_3 - \varphi_2 + \dfrac{\varphi_{ext}}{4} + 2n_b\pi \\ \varphi_c &= \varphi_4 - \varphi_3 + \dfrac{\varphi_{ext}}{4} + 2n_c\pi \\ \varphi_d &= \varphi_1 - \varphi_4 + \dfrac{\varphi_{ext}}{4} + 2n_d\pi. \end{cases} \tag{20}$$

Therefore, the flux biases of junctions are identical to the unshunted ring case Eq. (5). However, the flux bias is now 2π-periodic on each junction, instead of $\pi/2$-periodic. Thus, the coexistence of several symmetric configurations has disappeared.

Crucially, the normal modes of the shunted ring are identical to the unshunted ring since the symmetry of the circuit is preserved. The out of equilibrium bias of the shunting inductance is given by

$$\begin{cases} 4\varphi_\alpha &= -3\varphi_1 + \varphi_2 + \varphi_3 + \varphi_4 &= 2\varphi_Z + 2\varphi_X \\ 4\varphi_\beta &= \varphi_1 - 3\varphi_2 + \varphi_3 + \varphi_4 &= -2\varphi_Z + 2\varphi_Y \\ 4\varphi_\gamma &= \varphi_1 + \varphi_2 - 3\varphi_3 + \varphi_4 &= 2\varphi_Z - 2\varphi_X \\ 4\varphi_\delta &= \varphi_1 + \varphi_2 + \varphi_3 - 3\varphi_4 &= -2\varphi_Z - 2\varphi_Y. \end{cases} \tag{21}$$

The shunted ring Hamiltonian of Eq. (16) becomes

$$\boxed{\begin{aligned} H_{\text{ring}} &= -4E_J \cos\frac{\varphi_X}{2}\cos\frac{\varphi_Y}{2}\cos\varphi_Z\cos\frac{\varphi_{ext}}{4} - 4E_J \sin\frac{\varphi_X}{2}\sin\frac{\varphi_Y}{2}\sin\varphi_Z\sin\frac{\varphi_{ext}}{4} \\ &\quad + \frac{1}{4}E_L\left(\varphi_X^2 + \varphi_Y^2 + 2\varphi_Z^2\right). \end{aligned}} \tag{22}$$

The new Hamiltonian is identical to the original one (10) but for the two following points. First, the magnetic flux is here defined in a unique way, only one symmetric configuration exists[2]. Second, new quadratic terms appear to describe the contribution of the shunting inductor into the overall ring inductance. Note that the inductive contribution to the modes X, Y and to the mode Z is different by a factor 2.

2 Note that the unshunted behavior can be recovered by considering that the symmetric configuration becomes unstable and breaks down as soon as $\varphi_{ext} > 2\pi$ in the limit of $L \to \infty$.

2.3.2 *Third order expansion*

One can expand the Hamiltonian up to the third order leading to[3]

$$\boxed{\begin{aligned} H_{\text{ring}} &= -4E_J \cos\left(\frac{\varphi_{ext}}{4}\right) \\ &\quad +\tfrac{1}{2}\left(\frac{E_L}{2} + E_J \cos\frac{\varphi_{ext}}{4}\right)(\varphi_X^2 + \varphi_Y^2) \\ &\quad +\tfrac{1}{2}\left(E_L + 4E_J \cos\frac{\varphi_{ext}}{4}\right)\varphi_Z^2 \\ &\quad -E_J \sin\left(\frac{\varphi_{ext}}{4}\right)\varphi_X\varphi_Y\varphi_Z \\ &\quad +O(|\varphi|^4). \end{aligned}} \tag{23}$$

The three-wave-mixing term is unchanged as expected from the symmetry of shunting inductors and remains the only third order term in the Hamiltonian.

2.3.3 *Stability*

We claimed earlier that this new design improves the stability of the ring. In fact, the symmetric configuration is stable as long as all the partial derivatives with respect to the eigen-modes are positive, $\partial^2 H_{\text{ring}}/\partial\varphi_{X,Y,Z}^2 > 0$ (potential minimum). In other words, the ring inductances associated to the normal modes must all remain positive

$$\begin{cases} L_{X,Y} &= \dfrac{\varphi_0^2}{\dfrac{E_L}{2} + E_J \cos\dfrac{\varphi_{ext}}{4}} = 2L||L_J(\varphi_{ext}) > 0 \\ L_Z &= \dfrac{\varphi_0^2}{E_L + 4E_J \cos\dfrac{\varphi_{ext}}{4}} = L||\dfrac{1}{4}L_J(\varphi_{ext}) > 0. \end{cases} \tag{24}$$

One can show that the Z mode inductance always becomes negative before X and Y modes: $\text{sign}(L_Z) < \text{sign}(L_{X,Y})$.

Therefore, it is the Z mode that sets the stability of the ring. The symmetric configuration is stable as long as

$$\boxed{4E_J \cos\frac{\varphi_{ext}}{4} > -E_L} \Leftrightarrow \boxed{\frac{1}{L_J(\varphi_{ext})} > -\frac{1}{4L}}. \tag{25}$$

In particular, the symmetric configuration is always stable if $E_L > 4E_J$.

Finally, the maximum ring inductance that can be reached by the modes X and Y before the mode Z breaks down is given by

$$L_{X,Y}^{\max} = \frac{\varphi_0^2}{\dfrac{E_L}{2} - \dfrac{E_L}{4}} = 4L. \tag{26}$$

Therefore, the ring inductance excursion range for the X and Y modes in the symmetric configuration is essentially determined by the value of the shunting inductance

3 Note that this differs from the Hamiltonian of our paper [39] because of another definition for φ_Z

L. The subsequent frequency tunability of the device is set by the shunting inductance.

$$\boxed{\frac{2L}{1+\frac{2L}{L_J^0}} < L_{X,Y}(\varphi_{ext}) < 4L} \tag{27}$$

.

2.3.4 *Broken symmetry configuration*

An interesting case develops at fluxes where $4E_J \cos\frac{\varphi_{ext}}{4} < -E_L$. The Josephson ring phase bias arrangement undergoes a symmetry breaking. In this case, the phase of the common mode is not anymore a potential minimum and two minima at $\pm\langle\varphi_Z\rangle \neq 0$ develop on each side of a saddle point (Fig. 13(b)). Therefore, the phase of the mode Z acquires a non-zero average value. One can define $\delta = |\langle\varphi_Z\rangle|$ as the order parameter for the symmetry breaking.

The broken symmetry consists in a rearrangement of the super-currents in the shunted ring. Indeed, at some point it becomes more favorable to phase-bias the shunting inductances at the expense of the Josephson junctions and of the symmetry.

Hence, two energetically equivalent broken-symmetry configurations coexist as the two minima appear. The new equilibrium points of the Z-mode are solutions of the following equation

$$\frac{\partial H}{\partial\langle\varphi_Z\rangle} = 0 \Leftrightarrow \langle\varphi_Z\rangle = -4\frac{E_J}{E_L}\cos\frac{\varphi_{ext}}{4}\sin\langle\varphi_Z\rangle. \tag{28}$$

It can be solved in the limit of small order parameters $\delta \ll 1$ by expanding the equation to the third order leading to

$$\delta = |\langle\varphi_Z\rangle| \approx \sqrt{6}\sqrt{1+\frac{E_L}{4E_J\cos\frac{\varphi_{ext}}{4}}} = \sqrt{6}\sqrt{1+\frac{L_J(\varphi_{ext})}{4L}}. \tag{29}$$

Hence, the Hamiltonian is given by

$$\boxed{\begin{aligned} H_{\text{ring}} \;=\; & -4E_J\cos\frac{\varphi_X}{2}\cos\frac{\varphi_Y}{2}\cos\left(\varphi_Z \pm \delta\right)\cos\frac{\varphi_{ext}}{4} \\ & -4E_J\sin\frac{\varphi_X}{2}\sin\frac{\varphi_Y}{2}\sin\left(\varphi_Z \pm \delta\right)\sin\frac{\varphi_{ext}}{4} \\ & +\frac{1}{4}E_L\left(\varphi_X^2+\varphi_Y^2+2(\varphi_Z\pm\delta)^2\right). \end{aligned}} \tag{30}$$

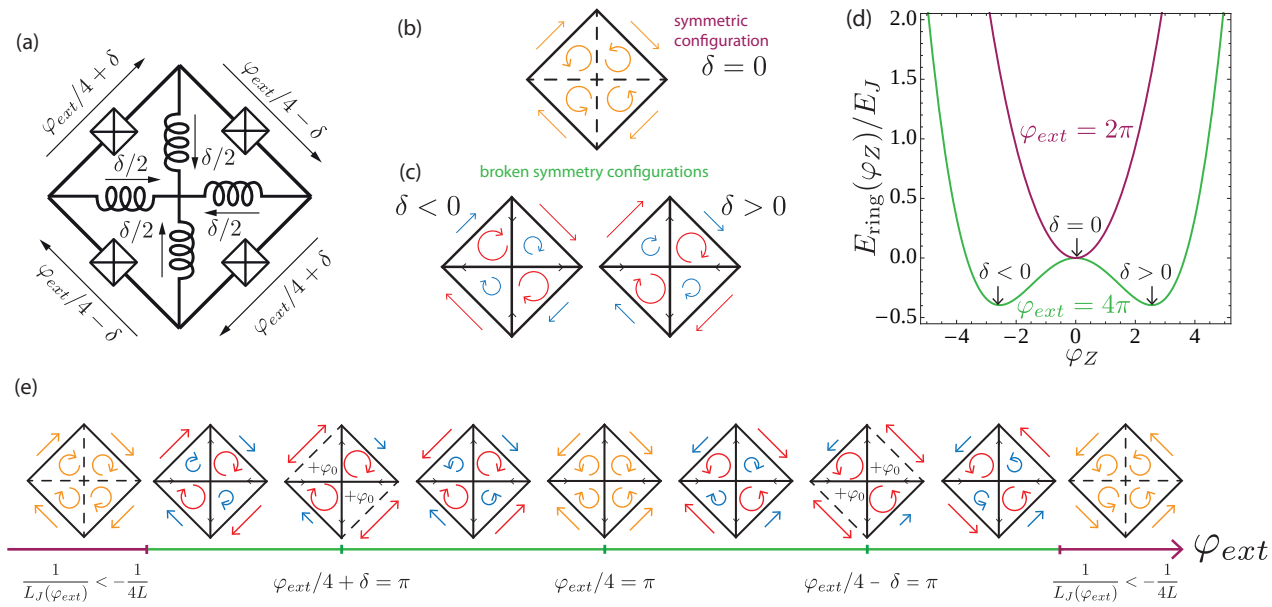

Figure 13: (a) Phase differences in the shunted JRM. The symmetric configuration is not always the most energetically favorable and a finite phase offset δ may develop as shown in the figure. (b) Symmetric configuration of supercurrents ($\delta = 0$). Average phase differences are represented as straight arrows while average currents are represented as circular arrows. Red (blue) color indicate larger (smaller) phase or intensity. There are no average current in the central shunting inductors in this configuration (dashed lines). (c) For magnetic flux bias around $\varphi_{ext} = 4\pi$, where δ can be nonzero, average currents develop in the central inductors. The system undergoes a symmetry breaking as two degenerate phase configurations coexist. (d) Cut of Josephson ring potential along φ_Z, for $\varphi_{ext} = 2\pi$ and $\varphi_{ext} = 4\pi$, while $\varphi_X = \varphi_Y = 0$. (e) Evolution of phase differences and supercurrents as a function of magnetic flux. For fluxes far enough from $\varphi_{ext} = 4\pi$ so that $L_J(\varphi_{ext})^{-1} + 1/4L > 0$, the symmetric configuration holds and $\delta = 0$. When the flux is closer to $\varphi_{ext} = 4\pi$, a symmetry breaking occurs. Here, we have represented the case where $\delta > 0$, but the opposite case is equally possible. The dependence of δ on flux can be obtained from Eq. (29). There are two interesting flux biases for which $\varphi_{ext}/4 \pm \delta = \pi$ where the phase difference across two opposite junctions slips from $\pm\pi$ to $\mp\pi$ as the average current cancels out. This is when flux quanta may enter the ring without compromising the stability of the current phase configuration. Note that the current directions invert around these flux points. At $\varphi_{ext} = 4\pi$, a symmetric configuration is reached but with a different symmetry than the one at $\delta = 0$.

The Hamiltonian can be expanded up to third order to highlight the properties of the broken-symmetry configurations

$$\begin{aligned} H_{\rm ring} \;=\; & -4E_J\cos\delta\cos\frac{\varphi_{ext}}{4}+\frac{E_L}{4}\delta^2 \\ & +\tfrac{1}{2}\left(\frac{E_L}{2}+E_J\cos\delta\cos\frac{\varphi_{ext}}{4}\right)(\varphi_X^2+\varphi_Y^2) \\ & +\tfrac{1}{2}\left(E_L+4E_J\cos\delta\cos\frac{\varphi_{ext}}{4}\right)\varphi_Z^2 \\ & \mp E_J\cos\delta\sin\frac{\varphi_{ext}}{4}\varphi_X\varphi_Y\varphi_Z \\ & \pm E_J\sin\delta\cos\frac{\varphi_{ext}}{4}\left(\varphi_X^2\varphi_Z+\varphi_Y^2\varphi_Z\right) \\ & +O(|\varphi|^4). \end{aligned} \tag{31}$$

A few remarks can be done about this new Hamiltonian. The effective inductances of the differential modes X and Y are modified, in particular, one can show that the inductance decreases when the magnetic flux is ramped up to π. The slope of the resonator frequency changes abruptly when the symmetry breaks at $\cos\frac{\varphi_{ext}}{4} = \frac{E_L}{4E_J}$.

There is still a three wave mixing term but its rate is degraded by a factor depending on the order parameter. Moreover, other third order mixing terms have appeared. As expected the three-wave mixing term has lost in purity after the symmetry breaking.

3

JOSEPHSON MIXER

Now that the dynamics and stability of the Josephson Ring Modulator is well captured, we will focus on the Josephson mixer, which is a device comprising a JRM connected to three spatially separated modes. This device is the core of all the experiments discussed in this thesis.

3.1 DYNAMICS OF A JOSEPHSON MIXER

Here, we introduce the minimal circuit describing the three resonant modes coupled to the JRM. The Josephson ring embedded in microwave resonators forms a circuit that we called the Josephson mixer.

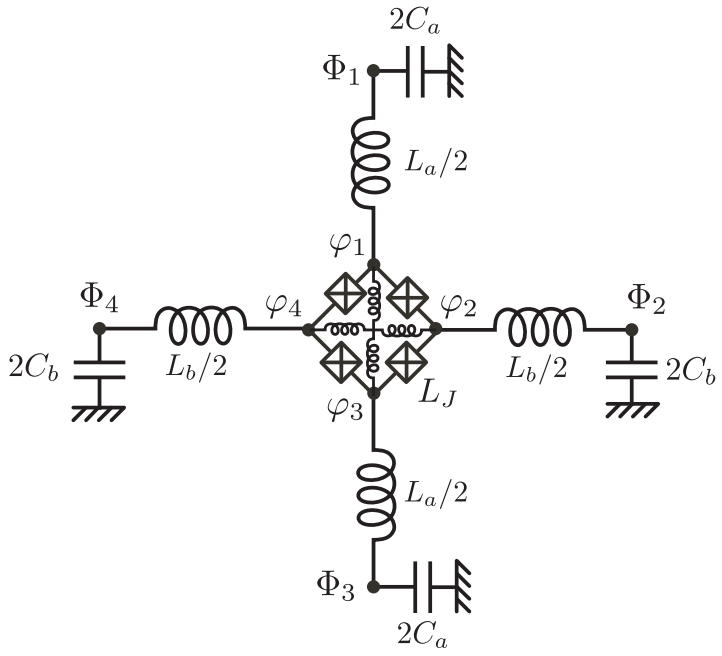

Figure 14: Schematics of the equivalent circuit used in the model.

The three first resonant modes of the circuit can be modeled with the lumped-element circuit represented in Fig. 14.

3.1.1 *Normal mode decomposition*

The four nodes of the ring are fed by three resonant modes of the superconducting circuit. The circuit has the same symmetry as the ring, the normal modes can be decomposed on the same basis. The differential modes (Φ_a, Q_a) and (Φ_b, Q_b) and the

common mode (Φ_c, Q_c) can be expressed as a combination of fluxes $\Phi_{1,2,3,4}$ and charges $Q_{1,2,3,4}$ (see Fig. 14).

$$\begin{aligned} \Phi_a &= \Phi_1 - \Phi_3 \\ \Phi_b &= \Phi_2 - \Phi_4 \\ \Phi_c &= \frac{\Phi_1 + \Phi_3 - \Phi_2 - \Phi_4}{2} \end{aligned} \tag{32}$$

where $\Phi_{1,2,3,4}$ are the fluxes at the nodes of the circuit through which the circuit is capacitively coupled to the propagating modes.

$$\begin{aligned} Q_a &= \frac{Q_1 - Q_3}{2} \\ Q_b &= \frac{Q_2 - Q_4}{2} \\ Q_c &= \frac{Q_1 + Q_3 - Q_2 - Q_4}{2} \end{aligned} \tag{33}$$

where $Q_{1,2,3,4}$ are the charges at the nodes of the circuit. Note that the modes are defined such that $[\Phi_\mu, Q_\mu] = i\hbar$.

Let us relabel the normal modes of the Josephson ring for simplicity

$$\begin{aligned} \varphi_a &= \varphi_1 - \varphi_3 && (= \varphi_X) \\ \varphi_b &= \varphi_2 - \varphi_4 && (= \varphi_Y) \\ \varphi_c &= \frac{\varphi_1 + \varphi_3 - \varphi_2 - \varphi_4}{2} && (= \varphi_Z). \end{aligned} \tag{34}$$

The normal modes of the whole circuit and their impedance can easily be obtained graphically. Indeed, under the system symmetries, some flux nodes are equivalent. Thus few circuit elements do not contribute to the impedance of the mode which enables us to simplify dramatically the effective circuit. The normal mode decomposition of the circuit is shown in Fig 15.

For instance, the differential mode Φ_a benefits from the left/right symmetry and the up/down anti-symmetry leading to the simplification $\varphi_2 = \varphi_4 = 0$ and $\Phi_2 = \Phi_4 = 0$. Hence, the inductors $L_b/2$ and the horizontal central inductors do not contribute to the impedance of the mode, leading to the simplification shown in Fig. 15(a). The decomposition of the mode Φ_b is very similar.

The decomposition of the common mode Φ_c benefits from the left/right symmetry and the up/down symmetry, leading to the simplifications $\Phi_2 = \Phi_4$, $\Phi_1 = \Phi_3$, $\varphi_1 = \varphi_3$ and $\varphi_2 = \varphi_4$.

From these effective circuits, we can easily extract the inductance for each normal mode.

$$\begin{aligned} L_a^{tot}(\varphi_{ext}) &= L_a + (L_J(\varphi_{ext}) || 2L) &&= L_a + L_a^{JRM}(\varphi_{ext}) \\ L_b^{tot}(\varphi_{ext}) &= L_b + (L_J(\varphi_{ext}) || 2L) &&= L_b + L_b^{JRM}(\varphi_{ext}) \\ L_c^{tot}(\varphi_{ext}) &= \frac{L_a + L_b}{4} + \left(\frac{L_J(\varphi_{ext})}{4} || L\right) &&= \frac{L_a + L_b}{4} + L_c^{JRM}(\varphi_{ext}) \end{aligned} \tag{35}$$

where $L_{a,b,c}^{JRM}(\varphi_{ext})$ are the inductances of the JRM, that were similarly defined in Eq. (24).

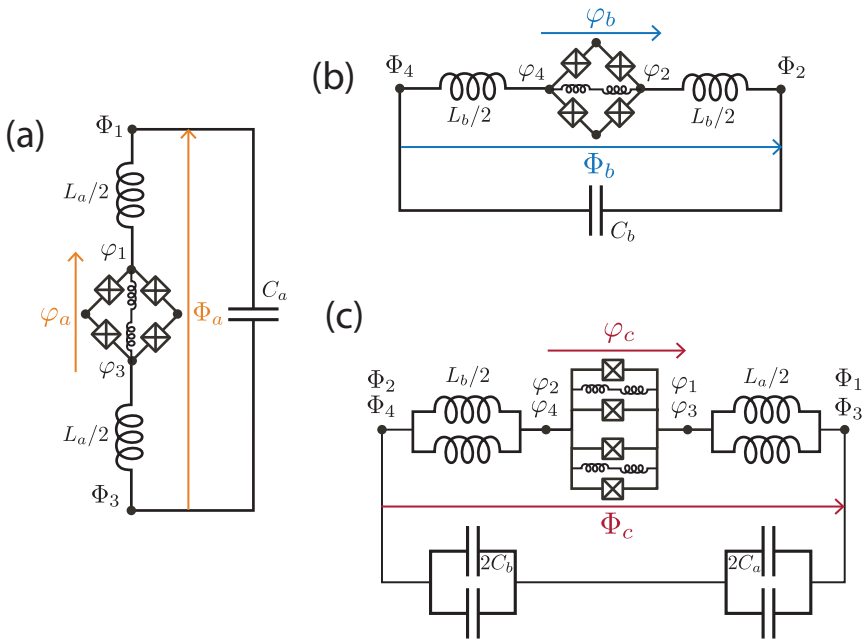

Figure 15: Equivalent circuit for the normal modes a, b and c, (a) differential mode a (b) differential mode b (c) common mode c

3.1.2 *Participation ratio*

The relation between the ring phase biases $\varphi_{a,b,c}$ and the circuit ones $\mathbf{\Phi}_{a,b,c}$ can be extracted from the equivalent circuits. This relation defines the **participation ratio** of the ring in the mode $\xi_{a,b,c}$. It represents the fraction of the respective mode energy contained in the Josephson Ring Modulator. Many constraints on devices using JRMs can be expressed as a function of participation ratios as will be discussed in sections 5.2 and 9.1

$$\begin{aligned}
\xi_a(\varphi_{ext}) &\equiv \frac{\varphi_0\varphi_a}{\mathbf{\Phi}_a} = \frac{L_a^{JRM}(\varphi_{ext})}{L_a + L_a^{JRM}(\varphi_{ext})} \\
\xi_b(\varphi_{ext}) &\equiv \frac{\varphi_0\varphi_b}{\mathbf{\Phi}_b} = \frac{L_b^{JRM}(\varphi_{ext})}{L_b + L_b^{JRM}(\varphi_{ext})} \\
\xi_c(\varphi_{ext}) &\equiv \frac{\varphi_0\varphi_c}{\mathbf{\Phi}_c} = \frac{L_c^{JRM}(\varphi_{ext})}{\frac{1}{4}(L_a + L_b) + L_c^{JRM}(\varphi_{ext})}.
\end{aligned} \tag{36}$$

3.1.3 *Quadratic Hamiltonian*

When the ring inductance is expanded to the second order (see Eq. (23)), one can show that the quadratic part of the full circuit Hamiltonian is simply given by

$$H_{(2)} = \frac{\mathbf{\Phi}_a^2}{2L_a^{tot}(\varphi_{ext})} + \frac{Q_a^2}{2C_a} + \frac{\mathbf{\Phi}_b^2}{2L_b^{tot}(\varphi_{ext})} + \frac{Q_b^2}{2C_b} + \frac{\mathbf{\Phi}_c^2}{2L_c^{tot}(\varphi_{ext})} + \frac{Q_c^2}{2C_c} \tag{37}$$

with $C_c = \dfrac{4C_aC_b}{C_a + C_b}$.

As a consequence, the resonance frequency of each mode can be tuned by varying the magnetic flux threading the ring. For small participation ratios, it can be expressed as a function of the bare frequency $\omega_\mu^0 = 1/\sqrt{L_\mu C_\mu}$ with $\mu = a, b, c$,

$$\boxed{\omega_\mu(\varphi_{ext}) = \frac{1}{\sqrt{L_\mu^{tot}(\varphi_{ext})C_\mu}} \approx \omega_\mu^0(1 - \frac{1}{2}\xi_\mu(\varphi_{ext}))}. \tag{38}$$

3.1.4 *Three-wave mixing Hamiltonian*

The three-wave mixing Hamiltonian of the whole circuit can be expressed as a function of the mode fluxes.

$$\begin{aligned} H_{3\mathrm{WM}} &= \frac{\varphi_0^2}{L_J^0}\sin\frac{\varphi_{ext}}{4}\varphi_a\varphi_b\varphi_c \\ &= \frac{1}{\varphi_0 L_J^0}\xi_a(\varphi_{ext})\xi_b(\varphi_{ext})\xi_c(\varphi_{ext})\sin\frac{\varphi_{ext}}{4}\Phi_a\Phi_b\Phi_c. \end{aligned} \tag{39}$$

We can now quantize the fields by introducing the creation and anihilitions operators of the modes a, b and c.

$$\begin{aligned} \Phi_a &= \sqrt{\hbar Z_a/2}(a + a^\dagger) \\ \Phi_b &= \sqrt{\hbar Z_b/2}(b + b^\dagger) \\ \Phi_c &= \sqrt{\hbar Z_c/2}(c + c^\dagger), \end{aligned} \tag{40}$$

with the characteristic impedances of the modes $Z_\mu = \sqrt{L_\mu^{tot}(\varphi_{ext})/C_\mu} = L_\mu^{tot}(\varphi_{ext})\omega_\mu$.

As a result, we obtain the so-called three-wave-mixing Hamiltonian in its quantum form

$$\boxed{H = \hbar\omega_a a^\dagger a + \hbar\omega_b b^\dagger b + \hbar\omega_c c^\dagger c + \hbar\chi(a + a^\dagger)(b + b^\dagger)(c + c^\dagger)}. \tag{41}$$

The coupling term between the three quantum field amplitudes is given by

$$\chi = \frac{\sqrt{\hbar}}{2\sqrt{2}\varphi_0 L_J^0}\xi_a\xi_b\xi_c\sqrt{Z_a Z_b Z_c}\sin\frac{\varphi_{ext}}{4}. \tag{42}$$

It can be reexpressed under the form

$$\boxed{\chi = \frac{1}{2}\sqrt{\frac{\xi_a\xi_b\xi_c\omega_a\omega_b\omega_c}{2E_{JRM}/\hbar}}\sin\frac{\varphi_{ext}}{4}}. \tag{43}$$

with $E_{JRM} = \varphi_0^2\frac{(L_J^0)^2}{L_a^{JRM}L_b^{JRM}L_c^{JRM}}$, a term of the order of magnitude of the characteristic Josephson ring energy.

3.1.5 *Parametric interaction term for a pumped Josephson mixer*

The Josephson mixer is mostly used as a parametric mixer. A parametric interaction between the quantum fields a and b is induced by a pump field p. The pump signal is

sent on the common mode c but far off-resonance. The pump mode is strongly driven to overcome this large frequency detuning. Thus, it can be considered as a classical pump field p, leading to the following Hamiltonian

$$H = \hbar\omega_a a^\dagger a + \hbar\omega_b b^\dagger b + \hbar\chi(p+p^*)(a+a^\dagger)(b+b^\dagger). \tag{44}$$

We would like to be able to evaluate the total parametric interaction term $\chi|p+p^*|$.

From equation (39), we get that

$$\begin{aligned} \chi|p+p^*| &= \frac{|\varphi_p|}{2L_J^0}\sin\frac{\varphi_{ext}}{4}\xi_a\xi_b\sqrt{Z_a Z_b} \\ &= \frac{|\varphi_p|}{2L_J(\varphi_{ext})}\tan\frac{\varphi_{ext}}{4}\xi_a\xi_b\sqrt{L_a^{tot}L_b^{tot}\omega_a\omega_b} \\ &= \frac{|\varphi_p|}{2}\tan\frac{\varphi_{ext}}{4}\sqrt{\xi_a\xi_b\omega_a\omega_b}\frac{L^{JRM}(\varphi_{ext})}{L_J(\varphi_{ext})}, \end{aligned} \tag{45}$$

where $L^{JRM}(\varphi_{ext}) = 2L||L_J(\varphi_{ext})$.

Besides, we have

$$\begin{aligned} \left|\frac{1}{\omega_a}\frac{\partial\omega_a}{\partial\varphi_{ext}/4}\right| &= \frac{1}{2}\left|\frac{1}{L_a^{tot}}\frac{\partial L^{JR}(\varphi_{ext})}{\partial\varphi_{ext}/4}\right| \\ &= \frac{1}{2}\frac{1}{L_a^{tot}}\xi_a\frac{L^{JRM}(\varphi_{ext})}{L_J(\varphi_{ext})}\tan\frac{\varphi_{ext}}{4}. \end{aligned} \tag{46}$$

As a consequence, the parametric interaction can be determined experimentally from the frequency-flux bias relation,

$$\boxed{\chi|p+p^*| = |\varphi_p|\sqrt{\frac{\partial\omega_a}{\partial\varphi_{ext}/4}\frac{\partial\omega_b}{\partial\varphi_{ext}/4}}}. \tag{47}$$

Note that this expression highlights the parametric character of the interaction between the modes. The resonance frequencies of the modes are parameters which are frequency modulated. The strength of the parametric interaction results from the susceptibility of these resonance frequencies to the flux delivered by the pump across the junctions.

Finally, the strength of parametric interaction can also be estimated using physical parameters of the circuit.

- For the **unshunted Josephson ring**, the expression simplifies to

$$\chi|p+p^*| = \frac{|\varphi_p|}{2}\tan\frac{\varphi_{ext}}{4}\sqrt{\xi_a\xi_b\omega_a\omega_b}. \tag{48}$$

  It can be evaluated at the magnetic flux bias $\varphi_{ext} = \pi$,

$$\chi|p+p^*| \sim \frac{|\varphi_p|}{2}\sqrt{\xi_a\xi_b\omega_a\omega_b}. \tag{49}$$

- For the **shunted Josephson ring**, we get

$$\chi|p+p^*| = \frac{|\varphi_p|}{2}\sin\frac{\varphi_{ext}}{4}\frac{L^{JRM}(\varphi_{ext})}{L_J^0}\sqrt{\xi_a\xi_b\omega_a\omega_b}. \tag{50}$$

This expression can be expressed for $\varphi_{ext} = 2\pi$ which corresponds to the typical magnetic flux bias for which the non-linearity starts being effective,

$$\chi|p+p^*| \sim \frac{|\varphi_p|}{2}\frac{2L}{L_J^0}\sqrt{\xi_a\xi_b\omega_a\omega_b}. \tag{51}$$

In principle, the amplitude of the pump mode can be varied in the range $0 < |\varphi_p| < 2\pi$ as a nob to vary the strength of the interaction. However, for the Taylor expansion of the Hamiltonian not to break down, it is required to keep the pump flux such that $|\varphi_p| \ll \pi$. Therefore, the maximum parametric interaction strength can be estimated to $|\varphi_p^{\max}| \sim \frac{1}{2}$ leading to rather simple and intelligible expression

$$\boxed{\chi|p_{\max}+p^*_{\max}| \sim \frac{1}{4}\sqrt{\xi_a\xi_b\omega_a\omega_b}\left|\begin{array}{ll}\times\dfrac{2L}{L_J^0} & \text{shunted ring}\\ \times 1 & \text{unshunted ring}\end{array}\right.}. \tag{52}$$

Note that these expressions of the coupling term will be extensively used in this work.

3.1.6 *Beyond third-order expansion: Kerr effect*

Higher order non-linearities bring spurious effects.

In particular, the Kerr effect results from the fourth order non-linear term provided by the Josephson Ring Modulator. Remarkably, it doesn't vanishes in the rotating wave approximation (RWA) since only mode populations comes into play. The corresponding Hamiltonian is of the form

$$H_{Kerr} = \hbar K_{aa}(a^\dagger a)^2 + \hbar K_{bb}(b^\dagger b)^2 + \hbar K_{ab}a^\dagger a b^\dagger b + \hbar K_{ap}|p|^2 a^\dagger a + \hbar K_{bp}|p|^2 b^\dagger b. \tag{53}$$

Two type of terms appear, self-Kerr terms that involve only one mode to the fourth power and cross-Kerr terms that couple the populations of two modes. The self-Kerr effect induces anharmonicity in the modes whereas the cross-Kerr effect induces a linear shift of the resonance frequency of one mode depending on the population of the other mode.

The Kerr terms can be easily derived from the Josephson Hamitonian involving fourth order of field operators. Hence starting from the ring Hamiltonian, we get

$$\begin{aligned} H_K &= -\frac{E_J}{16}\cos\frac{\varphi}{4}\left[\varphi_a^2\varphi_b^2 + \varphi_a^2\varphi_p^2 + \varphi_b^2\varphi_p^2 + \frac{\varphi_a^4}{24} + \frac{\varphi_b^4}{24}\right] \\ &= -\frac{\cos\varphi/4}{16L_J^0}\left[\hbar^2 Z_a Z_b \xi_a^2\xi_b^2 a^\dagger a b^\dagger b + \hbar Z_a\xi_a^2\varphi_p^2 a^\dagger a + \hbar Z_b\xi_b^2\varphi_p^2 b^\dagger b\right. \\ &\quad \left. + \frac{\hbar^2}{16}Z_a^2\xi_a^4(a^\dagger a)^2 + \frac{\hbar^2}{16}Z_b^2\xi_b^4(b^\dagger b)^2\right]. \end{aligned} \tag{54}$$

The frequency shifts due to the pump tone read

$$\begin{aligned} K_{ap}|p|^2 &= -\frac{1}{16}\omega_a\xi_a|\varphi_p|^2\frac{L_{JRM}(\varphi_{ext})}{L_J(\varphi_{ext})} \\ K_{bp}|p|^2 &= -\frac{1}{16}\omega_b\xi_b|\varphi_p|^2\frac{L_{JRM}(\varphi_{ext})}{L_J(\varphi_{ext})}. \end{aligned} \tag{55}$$

In a way, these terms are harmless if the pump amplitude is kept constant. Indeed, it corresponds to a renormalization of the resonance frequency.

The Kerr terms for a and b read

$$\begin{aligned} K_{ab} &= -\frac{1}{16}\sqrt{\xi_a^5\omega_a\frac{Z_a}{Z_Q}}\sqrt{\xi_b^5\omega_b\frac{Z_b}{Z_Q}}\frac{L_{JRM}(\varphi_{ext})}{L_J(\varphi_{ext})} \\ K_{aa} &= -\frac{1}{256}\xi_a^5\omega_a\frac{Z_a}{Z_Q}\frac{L_{JRM}(\varphi_{ext})}{L_J(\varphi_{ext})} \\ K_{bb} &= -\frac{1}{256}\xi_b^5\omega_b\frac{Z_b}{Z_Q}\frac{L_{JRM}(\varphi_{ext})}{L_J(\varphi_{ext})}. \end{aligned} \tag{56}$$

Note that the self-Kerr terms are much weaker than the cross-Kerr terms.

3.2 DESIGN OF THE JOSEPHSON RING MODULATOR

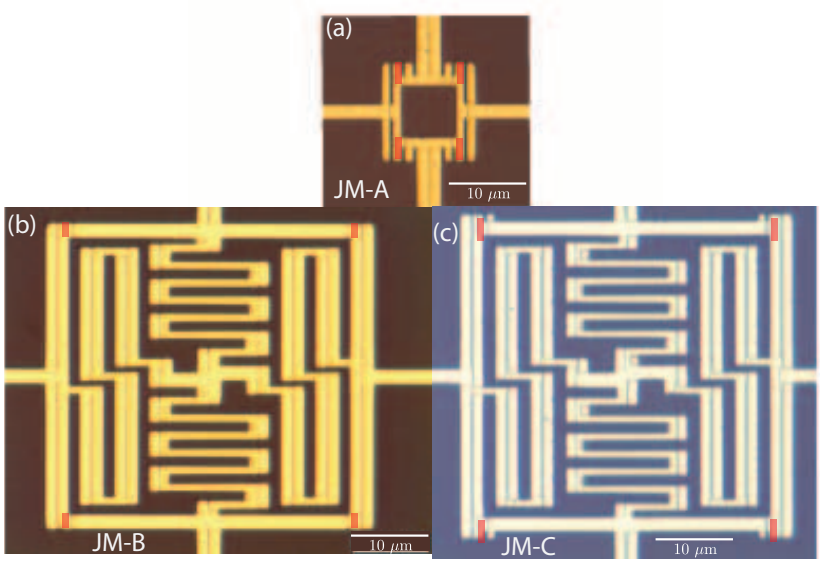

Figure 16: Optical microscope image of the Josephson rings where Josephson junctions are colored in red. (a) The original Josephson Ring Modulator without shunting inductances (JM-A). Shunted Josephson Ring Modulators are shown (b) (JM-B) and (c) (JM-C). The meanders in the center of the ring implement the four shunting inductances. Note that the stripes on the meanders are due to the fabrication process based on shadow evaporation.

The Josephson rings presented in Fig. 16 are realized in a single e-beam lithography step and a single aluminum evaporation step. The Josephson junctions are fabricated using a standard shadow evaporation technic [40] at each corner of the rings. They are highlighted in Fig. 16 by areas colored in red. The critical current of the $Al/Al_2O_3/Al$ Josephson junctions is proportional to the area of the tunnel barrier colored in red, it is designed to be in the μA range.

The shunting inductors shown on Fig. 16(b) and (c) are made of simple aluminum meanders cross-linking the ring. The meanders are closely packed in a 40 μm $\times$ 40 μm area in order to maximize their geometric inductance proportional to their length of

4×100 μm while minimizing the spurious geometric inductors in series with the junctions.

Note that the Yale group have implemented their own version of the shunted Josephson ring for their parametric amplifiers following this work. A smart trick from Yale was to replace the four central linear inductors by four large Josephson junctions, the eight junction Josephson ring is shown in Fig. 17. Remarkably, the physics is excepted to be exactly the same as long as shunting junctions are larger than the ring junction. Indeed in the symmetric configuration the central junctions are not flux biased so that they behave just as linear inductors. One big advantage of the shunting junctions over the shunting inductors is that the inductance provided by a junction is much more compact. Thus, the spurious geometric inductance in series with the junctions is lowered. Furthermore, the value of the shunting inductance is much better controlled through the junction area; thus it is easily adjustable. Note that to create large enough shunting junctions, it is convenient to use a 100 keV e-beam writer which is not accessible in Paris.

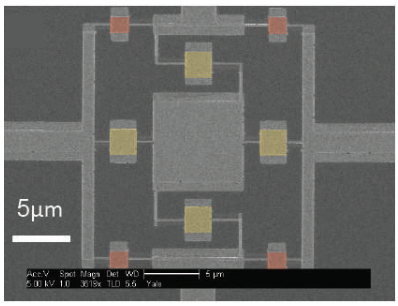

Figure 17: SEM picture of the eight-junctions shunted Josephson ring from the Yale group [41], in red the ring junctions and in yellow the shunting junctions

3.3 DESIGN OF THE RESONATORS

The superconducting resonators coupled to the ring can be realized in various ways. Their loss rate should be low enough compared to their bandwidth to reach a descent quantum efficiency. Hence, the chosen resonator technology must be adapted to this purpose.

3.3.1 *Distributed resonators*

Our microwave cavities consist in two $\lambda/2$ superconducting microstrip resonators crossing at their center, where the Josephson ring is inserted. They are made of a strip of aluminum evaporated at the same time as the JRM. The ground plane consists of evaporated gold at the back of the high resistivity silicon substrates. The 500 μm-wide strip and the ground plane are separated by 600 μm so that the characteristic impedance is 50 Ω. The resonance frequencies are simply given by the inverse of the length times the

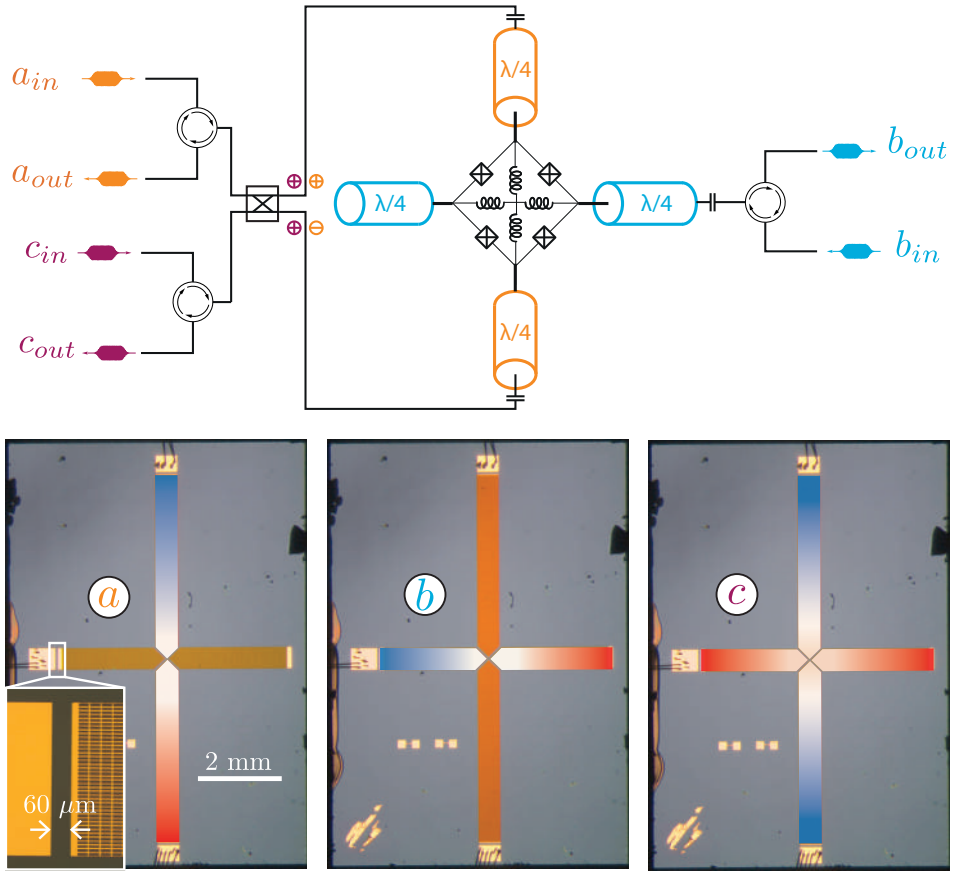

Figure 18: Optical microscope image of the Josephson rings where Josephson junctions are colored in red. (a) The original Josephson ring without shunting inductances. (b) and (c) Shunted Josephson rings, the meanders in the center of the ring implement the four shunting inductances. Note that the stripes on the meanders are due to the fabrication process based on shadow evaporation.

effective wave velocity. This microstrip technology for Josephson mixers has originally been implemented at Yale [42]. This technique makes it possible to fabricate resonators and Josephson junctions in a single e-beam lithography step and a single evaporation step. The main advantage is the ease of fabrication. There are no crossing lines on the chip, the ground plane is well defined everywhere underneath the aluminum strips and the gap capacitors provides reasonably large coupling thanks to the large width of strips.

The first three modes of the microstrip structure are shown in Fig. 18. The fundamental differential modes a and b are two $\lambda/2$ modes that cross at their voltage node. The Josephson ring benefits from their current anti-node in order to maximize the inductive coupling. Their resonance frequencies are chosen to be around $\omega_a/2\pi = 9$ GHz and $\omega_b/2\pi = 6$ GHz. The common mode c is shared between the two orthogonal strips. Its resonance frequency is in between ω_a and ω_b, it is given by

$$\omega_c = \frac{4c}{\sqrt{\epsilon_r}(\lambda_a + \lambda_b)} = \frac{2\omega_a\omega_b}{\omega_a + \omega_b} = 2\pi \times 7.2 \text{ GHz}. \tag{57}$$

Note that slight deviations to the expression are observed due to the cross shape.

As a remark, the very first implementation of the Josephson mixer at Yale [12] is shown in Fig. 19(a). The two microwave cavities were made of dual-strip line $\lambda/4$ resonators that ended on the Josephson ring. Several drawbacks appeared, such as the necessary crossing of the strip line near the ring and the need for large plate capacitor for the coupling to the feedline. As a consequence, several fabrication steps were required and this technological choice has been abandoned for the microstrip.

However, a drawback of the microstrip resonator as opposed to coplanar waveguide resonator, strip-line or $3D$ cavity for instance is the rather large radiation loss-rate. Indeed, the large electric dipole induced between the strip and the ground is radiating at the extremity of the resonator where the transverse electric mode get altered. On the contrary, for coplanar wave-guide, this dipole moment vanishes due to the surrounding ground plane on both sides and the remaining quadrupole moment is very weak thanks to the small section of the structure.

As a consequence, highly optimized coplanar waveguide resonator can reach quality factors up to a million [43] whereas we have never reached in practice more than a few 10^4 for the quality factor of microstrip resonators. However, this is more than enough for amplifiers for which large bandwidth is desired (see part ii), but it is a limitation for quantum memories we have implemented (see part iv).

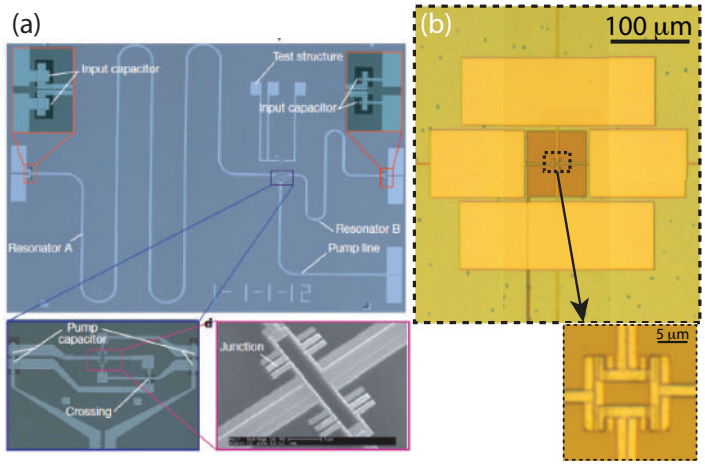

Figure 19: Other implementation of the resonators (a) Optical picture of the very first implementation of the Josephson mixer by the Yale group [12]. It consists of $\lambda/4$ strip-line resonators. (b) Our lumped-element implementation of the Josephson mixer [44]. The capacitors are large plate capacitors made of Aluminum/Silicon Nitride/Aluminum, most of the inductance is ensured by the Josephson ring.

3.3.2 *Lumped-element version*

We have also worked on a lumped-element implementation of the Josephson mixer [44] shown in Fig. 19(b). The goal was to increase the participation ratio of the Josephson

ring in the host resonator and to lower the impedance of the modes in order to be able to increase the bandwidth of the parametric amplifier, as discussed in the following part in section 5.7. To do so, we got rid of the resonator inductance so that most of the mode inductance comes from the Josephson ring. The issue is then to fabricate large enough capacitors to be in the right frequency range. The capacitors consist in large plate capacitors (large rectangles in Fig. 19(b)). The top and ground plates are made of aluminum and are separated by 200 nm of amorphous dielectric silicon-nitride leading to capacitor in the $3-6$ pF range.

3.3.3 *Coupling to the transmission lines*

The modes are coupled to feed lines through capacitors. For microstrip, the coupling capacitors are simply formed by small gaps (few tenths of μm) between the microstrip feed lines and the microstrip resonator as shown in Fig. 18(lower).

Crucially, the mode being spatially non-degenerate, they can be addressed specifically using the right combination of input ports. 180^o-hybrid couplers enable to distribute the signal on the port with the proper symmetry, differential or common, as shown in Fig. 18(upper). Hence, the differential mode a is excited through the differential port (Δ) of a 180^o-hybrid coupler, which distributes the signal with opposite phases across the $\lambda/2$ resonator. On the other hand, the common mode c is addressed by the common port (Σ) of the 180^o-hybrid coupler which distributes the signal with identical phases across the resonator.

On the contrary, the differential mode b is excited through a single port as shown in Fig. 18(a), as a consequence both the differential and common spatial modes b and c are coupled through this port. The reason why we do not use (necessarily) a second hybrid coupler on both sides of the resonator is to avoid extra insertion-losses, which would degrade the quantum efficiency of the device.

As a drawback, the $\lambda/2$ mode is slightly asymmetrized by the single-port capacitive coupling. The voltage node appears to be slightly shifted out of the center of the resonator leading to a small cross-talk between the differential mode b and common mode c. This minor issue is solved by increasing the length of the uncoupled microstrip arm (right arm on Fig. 18(b)) by about twenty micrometers, the exact length is determined using a microwave circuit simulation.

3.3.4 *Mapping between distributed and lumped resonators*

A single resonant mode of a distributed circuit is characterized by three main parameters: its resonance frequency ω_0, its characteristic impedance Z_0 and its quality factor Q. These quantities can be mapped onto the R, L and C elements of a lumped RLC oscillator with identical properties in the vicinity[1] of the resonance frequency. Importantly, this mapping depends on the specific type of distributed mode, for instance $\lambda/4$ or $\lambda/2$, and on the specific termination of the mode, open-circuit or short-circuit, that defines the boundary conditions. Moreover, it also depends on the type of RLC

1 This is valid as long as the considered frequencies are far from other resonant modes

oscillator, parallel or series. Therefore, the three $\lambda/2$ modes in open-circuit microstrip line can be individually[2] mapped on the parallel RLC model presented in Fig. 20.

The correspondence between both representations is determined by deriving the input impedance of the circuits in the vicinity of the resonance frequency [45]. It is given by

$$Z_{in}^{\lambda/2}[\omega] \approx \frac{Z_0}{\frac{\pi}{2}\frac{1}{Q} + i\pi\frac{\omega-\omega_0}{\omega_0}} \Leftrightarrow Z_{in}^{RLC}[\omega] = \left(\frac{1}{R} + \frac{1}{i\omega L} + i\omega C\right)^{-1}, \tag{58}$$

leading to

$$\boxed{\begin{array}{lllllll} \omega_0 & = & \dfrac{1}{\sqrt{LC}} & & L & = & \dfrac{2}{\pi}\dfrac{Z_0}{\omega_0} \\ Z_0 & = & \dfrac{\pi}{2}\sqrt{\dfrac{L}{C}} & \Leftrightarrow & C & = & \dfrac{\pi}{2}\dfrac{1}{\omega_0 Z_0} \\ Q & = & R\sqrt{\dfrac{C}{L}} & & R & = & \dfrac{2}{\pi}QZ_0 \end{array}}. \tag{59}$$

The capacitive coupling of an RLC oscillator to a transmission line of characteristic impedance Z_c in the limit of small coupling $(\omega_0 C_c)^{-1} \gg Z_c$ can be viewed from the oscillator point of view as an apparent increase of the characterisic impedance of the transmission line. This limit corresponds to the high-Q limit which is always achieved in our experiment.

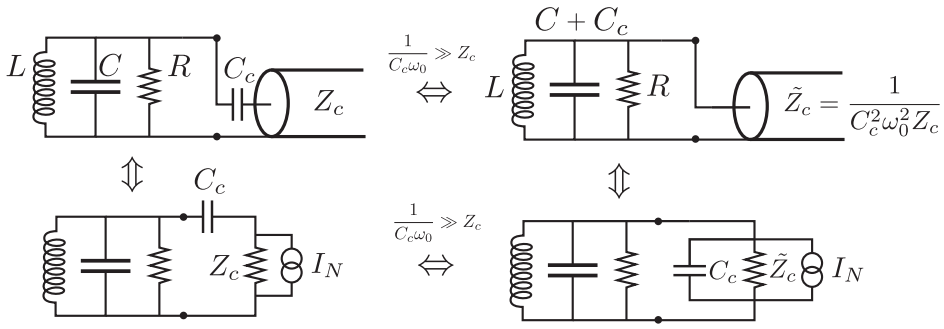

Figure 20: In the limit of small capacitive coupling between an RLC oscillator and a transmission line, the equivalent characteristic impedance of the line viewed from the oscillator is enhanced to $\tilde{Z}_c = (C_c^2\omega_0^2 Z_c)^{-1} \gg Z_c$.

2 Note that the mapping of the distributed c mode on the lumped element circuit differs from that of a and b modes

Indeed, in the vicinity of the resonance frequency, the impedance of the coupling capacitor C_c in series with the transmission line reads

$$\begin{aligned} Z_{load} &= \frac{1}{jC_c\omega} + Z_c \\ &\overset{\omega\sim\omega_0}{\approx} \frac{1}{jC_c\omega}(1 + jC_c\omega_0 Z_c) \\ &\overset{(\omega_0 C_c)^{-1}\gg Z_c}{\approx} \frac{1}{jC_c\omega}\frac{1}{1 - jC_c\omega_0 Z_c} \\ &\approx \frac{1}{jC_c\omega + C_c^2\omega_0^2 Z_c} \\ &\approx \frac{1}{jC_c\omega}||\frac{1}{C_c^2\omega_0^2 Z_c}. \end{aligned} \tag{60}$$

Thus, in the limit of small coupling, the equivalent circuit is a capacitor C_c in parallel with a load resistance $\tilde{Z}_c = (C_c^2\omega_0^2 Z_c)^{-1}$ as illustrated in Fig. 20. Hence, from the point of view of the oscillator, its capacity slightly increases from C to $C + C_c$ and the effective characteristic impedance of the transmission line considerably rises

$$\boxed{\tilde{Z}_c = \frac{1}{C_c^2\omega_0^2 Z_c} \gg Z_c}. \tag{61}$$

According to Eq. (311), the external capacitive coupling rate to the transmission line reads

$$\kappa_{ext} = \omega_0 \tilde{Z}_c \sqrt{\frac{C + C_c}{L}} \approx \frac{1}{C_c^2\omega_0 Z_c}\sqrt{\frac{C}{L}} = \frac{\pi}{2C_c^2\omega_0 Z_c Z_0}. \tag{62}$$

Then, the external[3] quality factor of the equivalent $\lambda/2$ resonator is given by

$$Q_{ext} = \frac{\pi}{2C_c^2\omega_0^2 Z_c Z_0}. \tag{63}$$

3 We differentiate two contributions to the quality factor. The external one is due the coupling to transmission lines. The internal one is due to other losses.

In this section, I will present the characterization of four different Josephson rings embedded in identical $\lambda/2$ distributed resonators.

The normal modes of the Josephson mixers can be easily probed with reflection measurement at cryogenic temperature. The reflection coefficient is measured with a vector network analyzer. This apparatus measures the amplitude and phase of the reflected signal as a function of frequency, and compares it to the injected signal. The experimental setup is shown in Fig. 21. The signal generated at room temperature is strongly attenuated and thermalized to the base temperature of a dilution refrigerator before reaching the microwave circuit in its sample holder. The reflected signal is then separated from the incoming one by circulators. At last, it is strongly amplified with a low-noise cryogenic amplifying chain and sent back to the network analyzer.

The measured complex reflection coefficient $r[\omega]$ probes the mismatch between the resonant mode input impedance $Z_{in}[\omega]$ and the feed line characteristic impedance Z_c as a function of the frequency. It can also be expressed as a function of the coupling rate κ_{ext}, the loss rate κ_{loss} and the resonance frequency ω_0.

$$r[\omega] = \frac{Z_{in}[\omega] - Z_c}{Z_{in}[\omega] + Z_c} = \frac{\kappa_{ext} - \kappa_{loss} + 2i(\omega - \omega_0)}{\kappa_{ext} + \kappa_{loss} - 2i(\omega - \omega_0)}. \tag{64}$$

When the external coupling is larger than the internal losses $\kappa_{ext} > \kappa_{loss}$, the phase of the reflected signal picks up a 2π phase shift as the frequency varies across the resonance frequency (Fig. 21(c)). The width of the phase-shift is given by $\kappa_{ext} + \kappa_{loss}$. It is then possible to track the resonance frequencies of the probed modes as a function of the applied magnetic flux threading the superconducting loop as shown in Fig. 22. The behavior of the resonance frequency enables us to determine *in situ* the main characteristics of the Josephson ring embedded in resonators such as the stability and participation ratios. The critical current of the Josephson junction and the values of the various inductances can be inferred from the theoretical model.

3.4.1 *Case of the original Josephson Ring Modulator*

The first sample (JM-A) we have fabricated and measured during my PhD work was an unshunted version of the Josephson ring shown in Fig. 16(a). The critical current of the junctions is about 3 μA.

The resonance frequency of the a and b modes as a function of the magnetic flux threading the loop is shown in Fig. 22. Strikingly, a strong hysteresis behavior appears depending on the sweeping direction of the magnetic flux. This hysteresis is associated to the metastability of the unshunted JRM described in section 2.2.3 due to the coexistence of two stable states. The frequency jump corresponds to the change of stable state by the entrance of a flux quantum in the superconducting loop.

The typical working point of the device is around $\varphi_{ext} = \pi$, highlighted by a red colored area in Fig. 22. Indeed, this bias point is the best trade off between stability and mixing efficiency. The stability is degraded for higher fluxes (blue area) especially when the mixer is pumped. Reciprocally, the efficiency of the three-wave mixing vanishes at

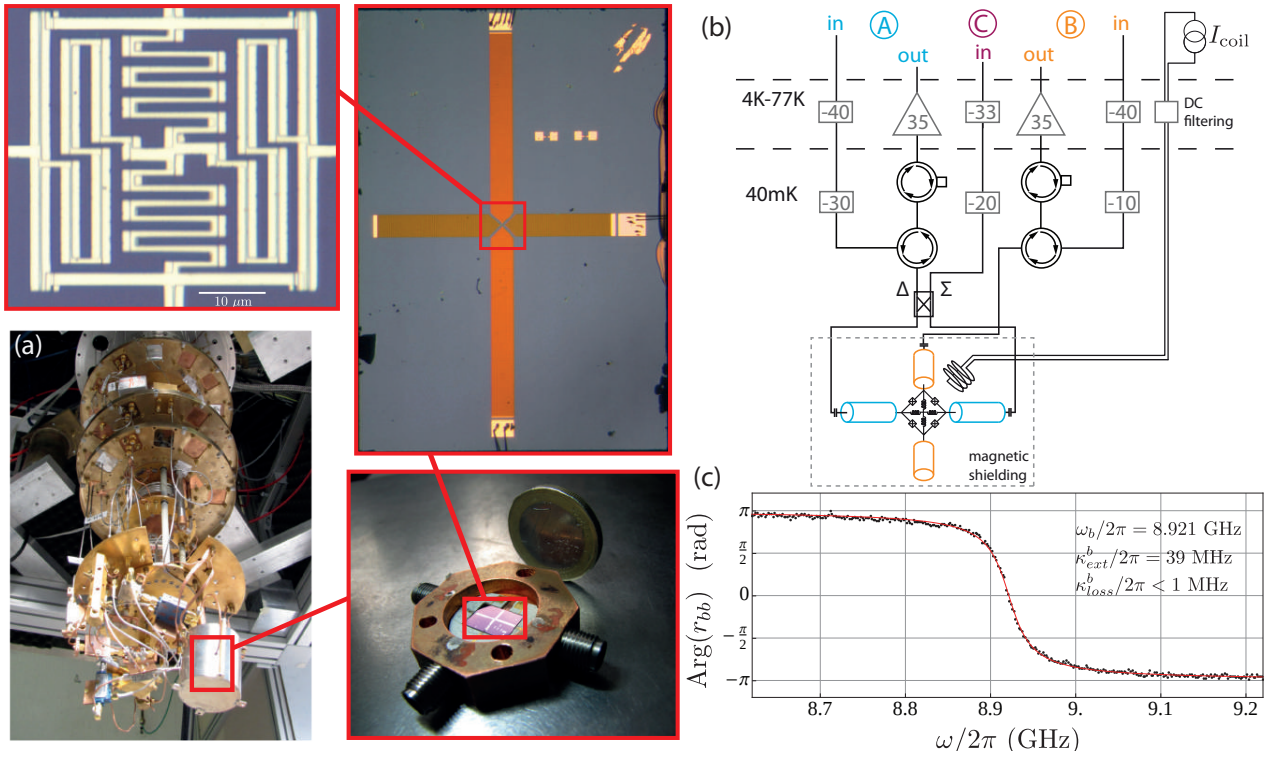

Figure 21: (a) The sample is placed in its sample holder and fixed at the bottom of a dilution refrigerator at about 40 mK. (b) Simplified schematic of the setup used to characterize the Josephson mixers. (c) Phase of the reflection coefficient $\mathrm{Arg}(r_{bb})$ as a function of frequency, measured at $\varphi_{ext} = 0$. This measurement enables to determine the resonance frequency of the Josephson mixer $\omega_b/2\pi$ and its external coupling rate $\kappa^b_{ext}/2\pi$.

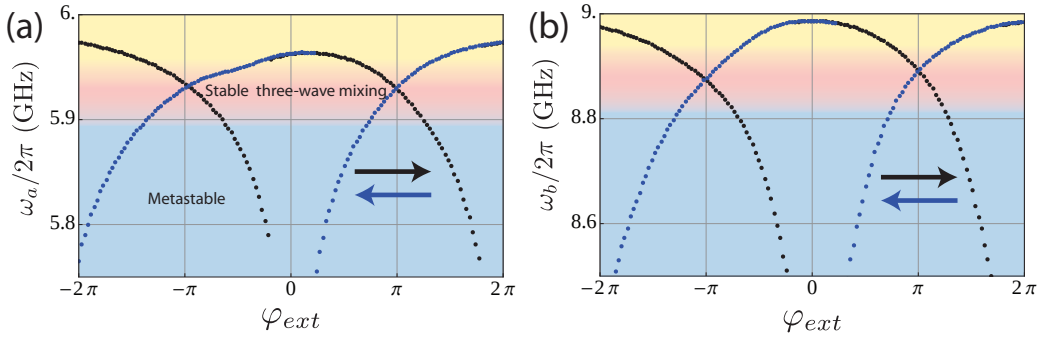

Figure 22: Tunability of the resonance frequency of mode a and b as a function of the reduced magnetic flux φ_{ext} threading the loop for the unshunted Josephson ring presented in Fig. 16(a). The flux is swept either increasingly (black dots) or decreasingly (blue dots). The yellow areas represent frequencies for which the three-wave mixing amplitude is too weak for being exploited. The red areas display the effective tunability range for which the three-wave mixing is stable and efficient. The blue area represent frequencies for which the configuration is highly metastable.

lower fluxes (yellow area). As a consequence, the useful tunability of the device is restricted to less than hundred MHz for both a and b modes.

3.4.2 *Case of the shunted Josephson Ring Modulator*

Here, I present the frequency behavior of two very similar shunted Josephson rings, JM-B shown in Fig. 16(b) and JM-C shown in Fig. 16(c). Both samples differ only by the value of the critical current of their junctions, their resonators are identical as well as the shunting inductances and the overall ring shape.

The measured resonance frequencies ω_a and ω_b as a function of the flux bias φ_{ext} are presented in Fig. 23(a,b) for JM-B and (c,d,e) for JM-C.

As a first remark, the original hysteric behavior has totally disappeared. This is one of the main consequences of the shunting inductances (see section2.3). Moreover, the 8π-periodicity is recovered as shown in Fig. 16(e) on several period.

As a second remark, the flux-frequency behavior is qualitatively different between both samples, small arches develop around $\varphi_{ext} = 4\pi$ for JM-C. These small arches correspond to the symmetry breaking of the flux configuration in the ring described in section 2.3.4. The configuration change is triggered by the instability of the Z mode of the ring. Hence, a lower-energy configuration of supercurrents is reached by the ring by breaking the Z symmetry. As a consequence, the value of the Josephson inductances has been modified which leads to an observable change in the a and b mode frequencies.

3.4.2.1 *Frequency dependence*

Despite qualitative differences in the behavior of the two samples, one can model the flux modulation of the resonance frequencies using Eq. (38) and Eq. (24). The corresponding theory is shown as solid lines in Fig. 23 and is in excellent agreement with the measurements. Note that the model has been slightly improved on top of Eq. (24) to take into account stray inductances in series with the junctions.

The fitting parameters being inductance ratios, we can start from the distributed $\lambda/2$ inductances given by $L_a^{\lambda/2} = 2Z_0/\pi\omega_a = 980$ pH and $L_b^{\lambda/2} = 2Z_0/\pi\omega_b = 560$ pH (see Eq. (59)). As a result, for both samples, we find that the four shunting inductances are in the range $L = 26 \pm 2$ pH, the four spurious series inductors are in the range $L_{series} = 30 \pm 2$ pH. For the sample JM-B, the critical current of junctions is $I_0 = 1 \pm 0.05$ μA corresponding to a Josephson inductance of $L_J^0 = 330$ pH. For the sample JM-C, the critical current of junctions is $I_0 = 3.1 \pm 0.1$ μA corresponding to a Josephson inductance of $L_J^0 = 105$ pH.

Therefore, the fitting parameters are consistent between the two samples. They are all in the same range, except the critical currents of the junctions, which are consistent with the expectation of their area and resistance measured at room temperature (see section C.6). However the fitted values of the shunting inductances are much smaller than expected from the linear geometric inductance model $\mu_0 l = 100$ pH. It is not so surprising given that the meanders are highly packed into the ring. Large mutual inductances develops between the meanders which reduce the overall value.

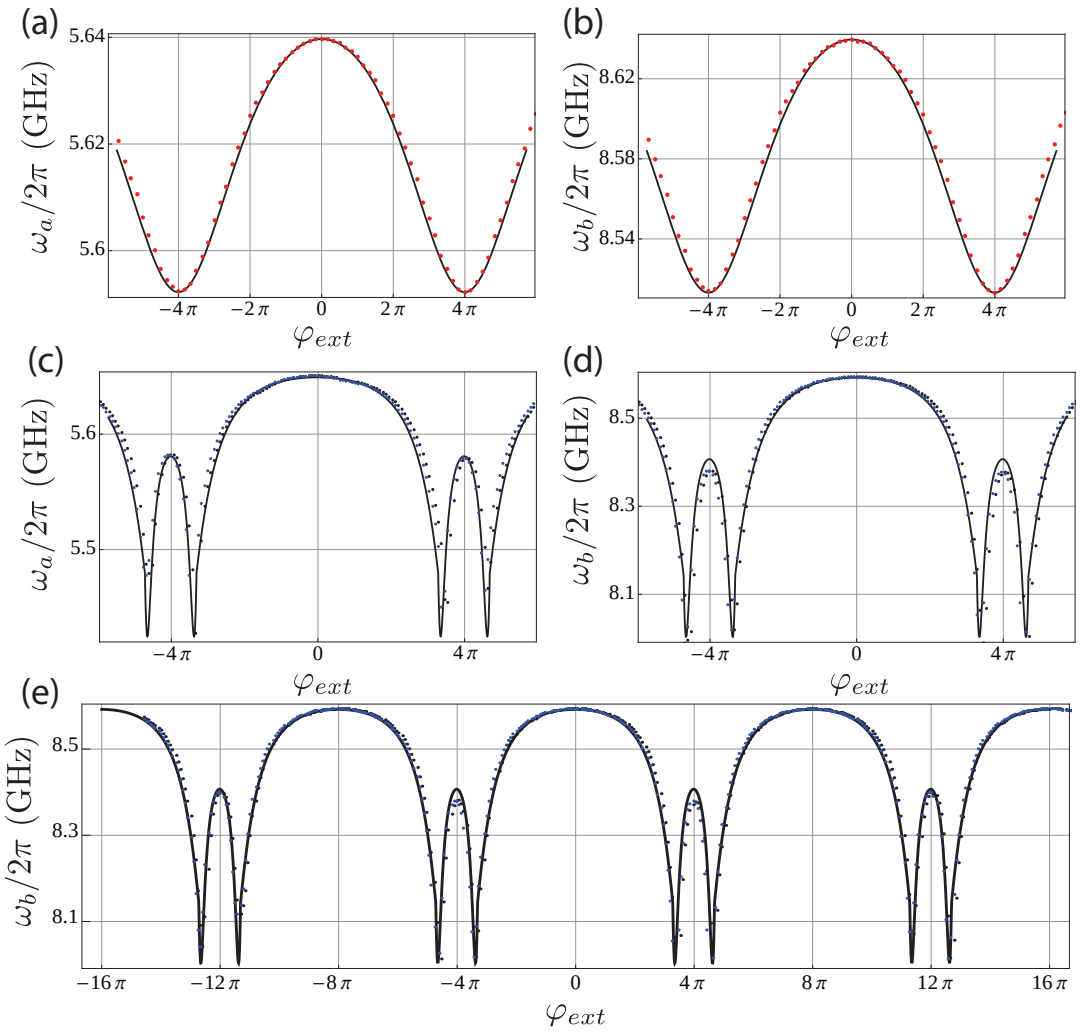

Figure 23: Measured resonance frequencies of the resonance frequencies of modes a and b as a function of the reduced magnetic flux φ_{ext} threading the loop. (a) and (b) corresponds to the shunted Josephson ring JM-B presented in Fig. 16(b). Traces (c), (d) and (e) correspond to the shunted Josephson ring JM-C presented in Fig. 16(c). Black (blue) dots were measured for increasing (decreasing) flux. The lines are obtained using Eq. (38) as explained in the text.

Using Eq. (25) and by taking into account the series inductors, the symmetry breaking condition reads

$$\frac{1}{L_c^{JRM}(\varphi_{ext})} = \frac{4}{L_{series} + L_J(\tilde{\varphi}_{ext})} + \frac{1}{L} < 0. \tag{65}$$

Here, $\tilde{\varphi}_{ext}$ is the flux bias across junctions slightly modified by the presence of the series inductors. Indeed, a small amount of flux is consumed by the phase biasing of theses linear inductors. In the limit of small series inductances, we have

$$\tilde{\varphi}_{ext} - \varphi_{ext} = -4\frac{L_{series}}{L}\sin\frac{\tilde{\varphi}_{ext}}{4} \approx -4\frac{L_{series}}{L}\sin\frac{\varphi_{ext}}{4}. \tag{66}$$

The minimum inverse inductance corresponds to a junction bias of $\tilde{\varphi}_{ext} = \varphi_{ext} = 4\pi$. It reads

$$\frac{4}{L_{series} - L_J^0} + \frac{1}{L} = \begin{cases} (40\text{ pH})^{-1} > 0 & \text{for JM-B} \\ (-67\text{ pH})^{-1} < 0 & \text{for JM-C.} \end{cases} \tag{67}$$

Therefore, JM-B never undergoes the symmetry breaking since its ring inductance mode always stays positive. Actually, the Josephson inductances in JM-B are so large that they are mostly short-circuited by the shunting inductances and the whole tunability is rather limited. On the contrary for JM-C, the Josephson inductances $L_J^0 = 105$ pH and the shunting inductances $4L = 104$ pH are more balanced, therefore the ring does not stay in the symmetric configuration for all fluxes but it explores a broader range of frequencies.

3.4.2.2 *Ring inductance*

From the fitting procedure, the Josephson ring inductance of a and b can be extracted for each sample. Note that, for both samples, the ring inductance seen by the two modes a and b is similar up to the uncertainties of fitting parameters. It is given by

$$L_{a,b}^{JRM} = \frac{1}{\dfrac{1}{L_{series} + L_J(\tilde{\varphi}_{ext})} + \dfrac{1}{2L}}. \tag{68}$$

The inductance value taken by the ring is shown in Fig. 24(a) for each sample. It can be understood quite well at various bias point

- At zero flux bias $\varphi_{ext} = 0$, the ring inductance of JM-B is larger than for JM-C, $L_{a,b}^{JRM,B} > L_{a,b}^{JRM,C}$. It is obvious since its zero-flux Josephson inductance L_J^0 is larger.

- At flux bias around $\varphi_{ext} = 2\pi$, the ring inductance values are crossing and are equal to the shunting inductances, $L_{a,b}^{JRM,B} = L_{a,b}^{JRM,C} = 2L$. This flux bias corresponds to the case where the Josephson inductance $L_J(\varphi_{ext}) = L_J^0/\cos(\varphi_{ext}/4)$ goes to infinity. Note that the actual crossing value is slightly shifted due to the presence of series inductances as mentioned in Eq. (66).

- For flux bias in the range $2\pi < \varphi_{ext} < 6\pi$, the Josephson inductance goes negative $L_J(\varphi_{ext}) < 0$. As a consequence, in the symmetric configuration, the smaller the zero-flux Josephson inductance the higher the ring inductance. JM-B stays in the symmetric configuration while JM-C undergoes the symmetry breaking.

Given the above discussion, the three wave mixing operates for flux biases between 2π and the symmetry breaking point $\tilde{\varphi}_{ext}^{SB}$. The useful tunability range of the ring inductance can thus easily be estimated. Indeed, the maximum inductance of the symmetric configuration is reached at $\tilde{\varphi}_{ext}^{SB}$. There, the inductance of the c mode diverges so that $L_{series} + L_J(\tilde{\varphi}_{ext}^{SB}) = -4L$ (see Eq. (65). Therefore, the ring inductance at this peculiar bias point does not depend neither on the Josephson inductance nor on the series inductance, and the maximum ring inductance reads

$$L_{a,b}^{JRM,\max} = 4L. \tag{69}$$

Moreover, at $\tilde{\varphi}_{ext} \sim 2\pi$, the ring inductance depends only on the shunting inductance and

$$L^{JRM}(\tilde{\varphi}_{ext} = 2\pi)_{a,b} = 2L. \tag{70}$$

Therefore, the useful inductance tunability is simply determined by the value of the shunting inductance, $\Delta L^{JRM}_{a,b} \sim 2L$. Remarkably, one can easily estimate the useful frequency tunability of the Josephson mixer which reads

$$\Delta\omega_{a,b} \sim \frac{2L}{L_{a,b}}\omega_{a,b} = \frac{\pi L}{Z_0}\omega^2_{a,b}. \tag{71}$$

Leading to $\Delta\omega_a/2\pi \sim 170$ MHz and $\Delta\omega_b/2\pi \sim 400$ MHz.

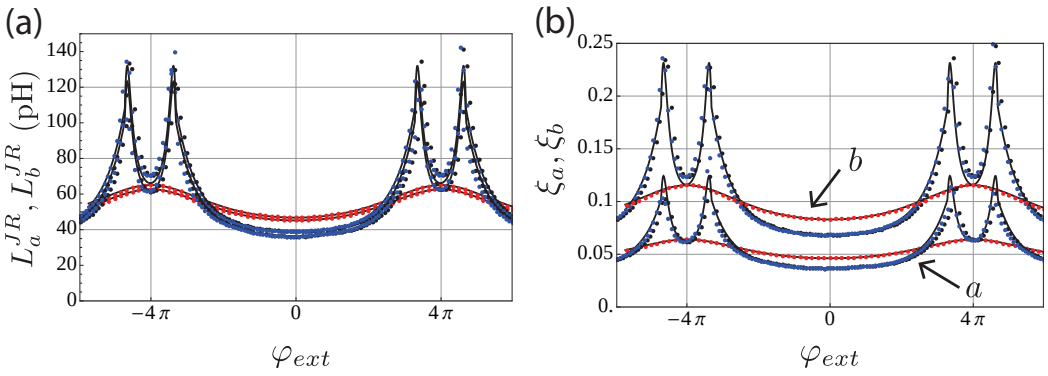

Figure 24: Inferred Josephson ring inductances (a) and participation ratios (b) as a function of the magnetic flux bias, for sample JM-B (red dots) and JM-C (blue dots).

3.4.2.3 *Participation ratio*

The participation ratio defined in Eq. (36) gives the ratio of inductive energy stored in the ring to the total inductive energy of the mode. It is a crucial figure for the efficiency of three-wave mixing by being directly related to the non-linear coupling rate χ as indicated in Eq. (43) and Eq. (52). The participation ratio can easily be estimated from the fitting procedure of the resonance frequency as a function of flux. It is shown in Fig. 24(b). Note that the participation ratio is proportional to the frequency of the mode, hence a difference between a and b curves.

3.4.3 *Asymmetric shunted Josephson ring*

In order to explore further the physics of the symmetry breaking of the supercurrent configuration, I have fabricated a sample JM-D very similar to JM-C, but whose junctions critical currents are slightly asymmetric with respect to the Z mode as shown in Fig. 25(b).

The Josephson ring fabricated for the experiment is shown in Fig. 25(a). The sample is identical to JM-C but the area of the Josephson junctions have been increased by 15% for the top-left and bottom-right junctions and decreased by 15% for the top-right

and bottom-left junctions, so that the symmetry is broken with respect to the c (or Z) mode. Thus, the expected critical current are $I_0^+ = 3.6\ \mu$A and $I_0^- = 2.6\ \mu$A.

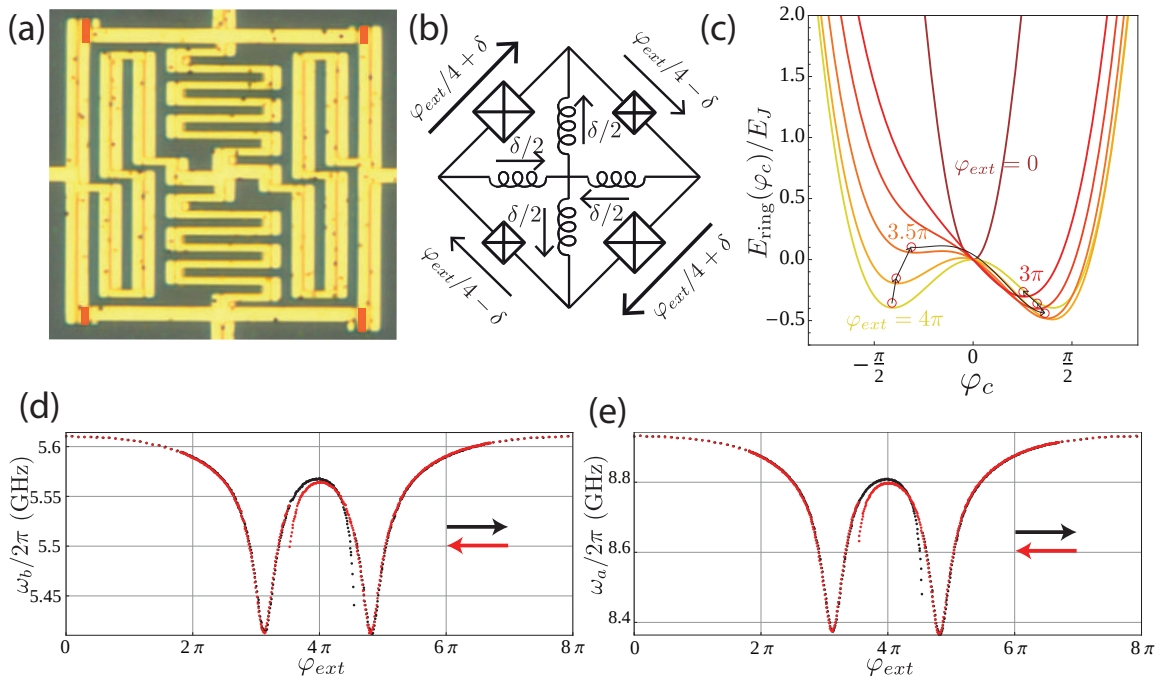

Figure 25: Asymmetric shunted Josephson ring. (a) Microscope image of sample JM-D. The Josephson junctions are colored in red. (b) Schematic of the asymmetric Josephson ring. (c) Josephson ring potential as a function of the common mode phase φ_c for different flux biases. (d) Frequency of the mode a as a function of the flux biases. (e) Frequency of the mode b as a function of the flux bias.

For a symmetric ring, when the symmetry is broken, two energetically degenerate super current configurations appears corresponding to Fig. 25(b). One for $\delta > 0$ and one for $\delta < 0$. In the asymmetric case, one of the two configurations is preferred by the system compared to the other, so that we can evidence the existence of both configurations.

For instance, when $2\pi < \varphi_{ext} < 4\pi$, the Josephson energy is increasing with flux bias. Then it is energetically more favorable to increase the flux-bias on the small junction and decrease it on the large one. Thus, the configuration $\delta > 0$ is chosen by the system as soon as the biasing of the shunting inductance costs less energy than readjusting the flux bias on the junction. On the contrary, when $4\pi < \varphi_{ext} < 6\pi$, the Josephson energy is now decreasing with flux bias. Then the opposite configuration $\delta < 0$ is more favorable energetically. It corresponds to an increase of the flux bias on the large junction and a decrease on the small junctions. Note that, the two configurations are energetically equivalent for $\varphi_{ext} = 4\pi$. Indeed the only difference between the configurations is the direction of the flowing super current.

The two configurations $\delta > 0$ and $\delta < 0$ are separated by a potential barrier in the $\varphi_a, \varphi_b, \varphi_c$ phase space and they are metastable. A hysteretic behavior in the Josephson ring potential is shown in Fig. 25(c). The flux bias is first slowly decreased from 6π to

4π in order to prepare the system in the configuration $\delta < 0$. At $\varphi_{ext} = 4\pi$ the two configurations are equivalent (yellow curve). As the flux bias is decreased, the trapping configuration becomes less favorable energetically than $\delta > 0$ (orange curve). Then, the potential barrier separating the two minima vanishes and the system falls abruptly into the potential well. Finally, the $\delta > 0$ configuration comes back to the symmetric configuration at $\varphi_{ext} = 0$ (purple curve).

The curvature of the two minima being different with respect to the a and b modes, the ring inductance is abruptly modified during the configuration change. Thus, the hysteresis behavior can be tracked by monitoring the resonance frequency while the flux is swept in both directions as presented in Fig. 25(d) and (e). Indeed, the abrupt change of resonance frequency depending of the sweeping direction is measured in the small arches.

One can notice that the two sweeping directions are not exactly equivalent. This is certainly due to slight deviation in the critical current of the junctions. Moreover, despite the change in critical currents, the system behavior is not dramatically modified outside of the small arch compare to the symmetric sample JM-C. This indicates that the Josephson ring is quite resilient against fabrication imperfections. Here, the system does not undergo a proper symmetry breaking since the initial symmetry is broken by construction. As a consequence, the transition between the large arches and the small arch is much more smooth than for the previous devices measured in Fig. 23.

3.5 CONCLUSION

These experiments illustrate one of the strengths of superconducting circuits. Their Hamiltonian can be engineered with versatility and their signals can be measured with great precision so that they enable the investigation of many subtle physical phenomena. As a perspective, one could build a quantum two-level system based on the two broken configurations discussed here. This system could be tuned using an external magnetic field similarly to flux quits. Further studies and calculations are needed to determine if such a device could bring some advantage compared to other superconducting qubits with respect to noise properties or the three mode coupling. All in all, this new circuit brings a new interesting species in the vast zoology of superconducting circuits.

The main unpublished results of this part are the following, while the rest of the results can be found in Ref. [39]

- Dynamics of phase slips in the JRM.
- Determination of a symmetry breaking in the phase and supercurrent configuration in the ring (Fig. 13)
- Practical expression of the maximal strength of parametric amplification as a function of geometrical parameters in Eq. (52)
- Practical expression of the Kerr terms in the JRM in Eq. (55)
- Demonstration of three kinds of behavior of the resonance frequencies of the Josephson mixer as a function of flux, with good theoretical agreement (Figs. 22 and 23)
- Measurement of the resonance frequencies for a ring of four Josephson junctions with unequal critical currents, and demonstration of two possible configurations during the symmetry breaking Fig. 25

Part II

PARAMETRIC AMPLIFIERS

4

AMPLIFICATION OF QUANTUM MICROWAVE SIGNALS

The decoherence of a quantum system can be interpreted as unread measurements by its environment [46].

In order to observe measurement back action, where the evolution of the system depends on the observed measurement outcome, the observer must extract more information than the rest of the environment. In particular, when such a control on the system is reached, it becomes possible to track the trajectory of a quantum system and potentially correct it from residual error arising from the decoherence.

Many quantum systems couple well to microwave signals [4, 47, 3], and can therefore be measured using microwave modes. In order to extract more information out of these microwave modes than the environment, one needs to measure them with a precision of the order of zero point fluctuations. Quantum limited amplifiers are designed for this purpose. Such devices are able to linearly amplify an input signal while adding to it the minimum amount of noise allowed by quantum mechanics.

In the last decade, the community of superconducting circuits has provided a strong push towards improving the efficiency of microwave amplifiers, so that most of the information extracted from these quantum systems can now be recorded.

The first part of my PhD work consisted in the implementation of a practical amplifier with a near-unity quantum efficiency. By practical I mean a device that is reliable and easy to fabricate. Its frequency must be tunable so that it can be matched with the device under study. Its gain must be large enough over a sufficiently wide bandwidth to overcome noise added by the following amplifier in the detection setup. Finally, it must sustain at least a few photons at its input.

The implementation of such devices has paved the way to several experiments in the group such as the active feedback of the quantum trajectory of a single quantum system [48].

In this chapter, I will first present the limitations imposed by quantum mechanics on the efficiency of linear amplifiers. Second, I will present our implementation of Josephson mixers as practical quantum limited amplifiers. I will then show how we managed to reach up to 80% efficiency with concrete circuits. Finally, I will present the design of an optimized Josephson mixer based on low impedance lumped element resonators.

4.1 QUANTUM-LIMITED AMPLIFIER

A linear amplifier is a device that transforms an input field $\langle a_{in} \rangle$ into an output field $\langle a_{out} \rangle$ with an amplitude gain $\sqrt{G}$. Importantly, both input and output fields must be well defined quantum fields and in particular, they must respect commutation relations,

$$\left[a_{in}, a_{in}^{\dagger}\right] = \left[a_{out}, a_{out}^{\dagger}\right] = 1. \tag{72}$$

As a consequence, if we try to build a noiseless linear amplifier with a gain $\sqrt{G}$, one can immediately see than its input/output scattering relation $a_{out} = \sqrt{G}a_{in}$ leads to ill-defined input/output operators since they cannot simultaneously respect both commutation relations (72).

This fact has been noticed by Caves in 1982 [26], clarifying the earlier work by Haus and Mullen [49] and leading the so-called Caves theorem, which states that a phase-preserving linear amplifier must necessarily add a finite amount of noise. It is also a direct consequence of the no-cloning theorem [50] stating that an arbitrary quantum state cannot be duplicated with unit fidelity.

4.2 PHASE-PRESERVING AMPLIFIER

One can give up on the noiseless character of the amplifier and accept that the signal is degraded by the minimum amount of noise. Then, the amplifier has to involve an extra-operator $\mathcal{N}$ which commutes with a_{in} and provides a source of uncontrolled fluctuations in the scattering relation

$$a_{out} = \sqrt{G}a_{in} + \mathcal{N}. \tag{73}$$

In order to satisfy the commutation relations (72), we need $[\mathcal{N}, \mathcal{N}^\dagger] = -(G-1)$, leading to an added noise given by

$$\langle \delta\mathcal{N}^2 \rangle = \frac{1}{2}\langle \left\{\mathcal{N}, \mathcal{N}^\dagger\right\} \rangle \geq \frac{1}{2}|\langle \left[\mathcal{N}, \mathcal{N}^\dagger\right] \rangle| = \frac{G-1}{2}. \tag{74}$$

The minimum added noise associated with the quantum limit corresponds to half a quantum of the noise referred to the input.

As a consequence, the quantum limit is reached when the amplifier involves, as an extra-operator, a so-called 'idler' mode b_{in}, left in the vacuum state and amplified by a linear gain $\sqrt{G-1}$ such that

$$\boxed{a_{out} = \sqrt{G}a_{in} + \sqrt{G-1}b_{in}^\dagger}. \tag{75}$$

One can check that all the commutation relations are respected, $\left[a_{in}, a_{in}^\dagger\right] = \left[a_{out}, a_{out}^\dagger\right] = \left[b_{in}, b_{in}^\dagger\right] = 1$.

For a quantum limited amplifier, the added noise comes from the amplified vacuum fluctuations of the extra-mode b_{in} involved in the process.

4.3 PHASE-SENSITIVE AMPLIFIER

Another solution consists in giving up on the phase-insensitivity of the amplifier and preserving its noiseless character. In this case, the observer would be allowed to amplify only one of the two quadratures of the field at a time. Note that this is not surprising if one considers that the added noise is a consequence of Heisenberg uncertainty principle, implying that there is a price to pay for measuring simultaneously two non-commuting quantities, which are here the two quadrature of the field. Hence, one can evade the quantum limit by looking only at one quadrature.

Interestingly, the phase-sensitive quantum limited amplifier is a special case of the phase preserving one for which the idler mode is the input field itself (up to an extra phase), $b_{in} = e^{i\phi} a_{in}$, leading to a scattering relation

$$\boxed{a_{out} = \sqrt{G} a_{in} + e^{i\phi} \sqrt{G-1} a_{in}^{\dagger}} \tag{76}$$

for which the commutation relations still hold.

When expressed as a function of the quadratures of the field X_{in} and P_{in}, defined from $a_{in} = X_{in} + iP_{in}$ and $a_{out} = X_{out} + iP_{out}$, in the limit of large gain $G \gg 1$ and for $\phi = 0$, the scattering relation reads

$$\boxed{\begin{array}{rcl} X_{out} & = & 2\sqrt{G} X_{in} \\ P_{out} & = & \dfrac{1}{2\sqrt{G}} P_{in} \end{array}}. \tag{77}$$

The phase-sensitive quantum limited amplifier then amplifies a single quadrature at the expense of the other. Note that the phase sensitive character of the amplifier is quite unusual among the standard available devices in microwave technologies.

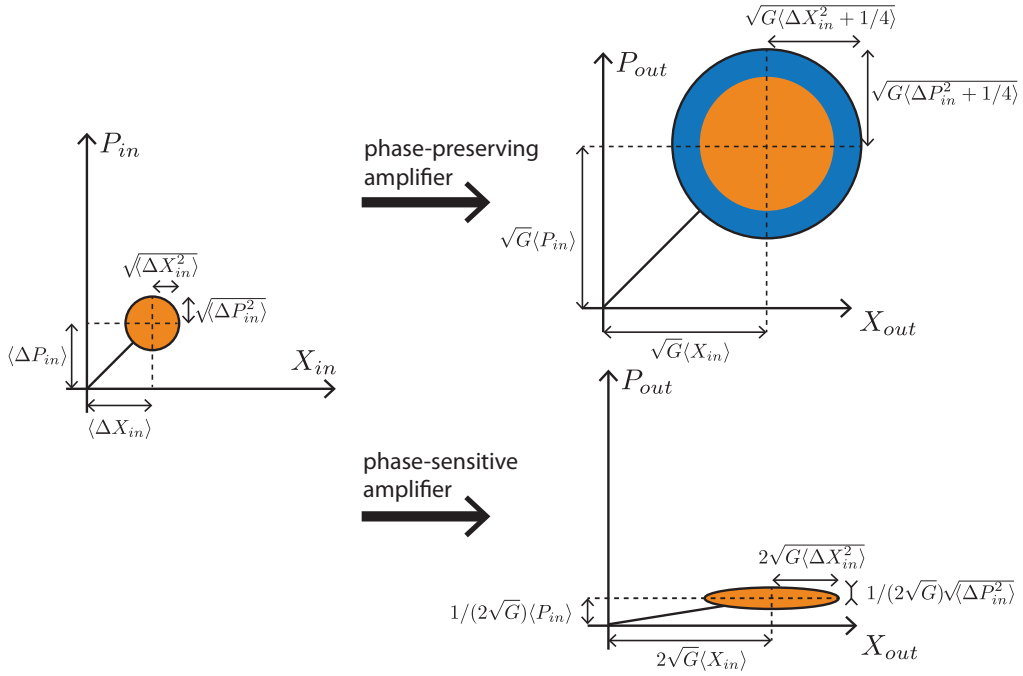

Figure 26: On the left, the contour of the Wigner distribution of an input state is represented in phase space. A phase preserving amplifiers necessarily degrade the signal to noise ratio due to uncertainty principle, the extra noise is represented in blue. A phase-sensitive amplifier, amplifies one quadrature at the expense of the other one, in this case, one can evade the added noise.

4.4 HERALDED NOISELESS AMPLIFIER

As a remark, recent advances in quantum optics have unveiled a new class of quantum limited amplifiers where both the noiseless character and its phase-insensitivity are

preserved. The price to pay is that it becomes a non-deterministic process. Indeed, by heralding the successful amplification events, one can evade the no-cloning theorem. The heralded noiseless amplifier has been experimentally demonstrated in the optical range by the Brisbane group in [51].

4.5 Quantum limited measurement and back-action

Measurement of a quantum system is randomly perturbing its state. The strength and nature of this back-action depends on the detector. In a partial measurement performed by an ideal quantum limited apparatus, the system remains in a pure state whose evolution can be tracked down perfectly, knowing the measurement record. The two types of quantum limited amplifiers are suited for two different types of measurement, leading to a different back-action.

- A phase-preserving amplifier is suited for **heterodyne measurements**, consisting in the measurement of both quadratures of the field simultaneously.

  In this case, the half quantum of noise added by the phase-preserving amplifiers does not reveal a limitation on the knowledge acquired about the system, but the fact that two incompatible (non-commuting) quantities are measured simultaneously. Indeed, the extra-noise is a manifestation of the extra back-action of the amplifier on the system under measurement. Remarkably, when the measurement outcomes of both quadratures are fully taken into account, it is possible to keep the system in a pure (non-mixed) quantum state. The quantum back-action of a phase-preserving amplifier on a superconducting qubit has been demonstrated by the Yale group in 2013 [52].

- A phase-sensitive amplifier is suited for **homodyne measurements**, consisting in the measurement of a single-quadrature of the field at a time.

  In this case, this half quantum of extra-noise is absent, meaning that only compatible (commuting) quantities are measured. There will still be as much quantum back-action on the system as in the previous case but its nature can be different. In particular, the tracking of a superconducting qubit trajectory with a phase-preserving amplifier and its back-action have been demonstrated by the Berkeley group in 2013 [53].

To conclude, both kinds of amplifiers can be non-information degrading when all the recorded information is reinvested. Ideal implementation of these quantum limited amplifiers makes it possible to track perfectly the trajectory of the system. Hence in the ideal implementation case, both types of amplifiers can reach a 100% quantum efficiency, despite the fact that the phase-preserving one adds an apparent noise while the phase-sensitive one does not.

Degenerate parametric amplifiers are spatially and temporally degenerate. All dynamics takes place within a single spatial mode of a resonator and within its temporal bandwidth.

The majority of degenerate parametric amplifiers exploit a weakly nonlinear oscillator called a Duffing oscillator. These degenerate amplifiers have in common a fourth order term in the field operator c in their Hamiltonian

$$H_{\text{Duff}} = \hbar\omega_c c^\dagger c + \hbar\chi c^\dagger c^\dagger cc. \tag{78}$$

Such oscillators have been successfully implemented with superconducting circuits. Elaborating Yurke's pioneering work from 1980's [15], the Josephson Bifurcation Amplifier (JBA), which was developed at Yale in 2004 [18], consists of a large Josephson junction embedded in a microwave resonator. It was first used as a bifurcation amplifier, meaning that a macroscopic bifurcation of the resonator was triggered by the tiny signal and that it goes beyond a threshold. However, it can also be used in a linear mode as a degenerate parametric amplifier when pumped at two frequencies situated symmetrically with respect to the frequency of the signal to amplify. It is the so-called doubly pumped JBA [54]. Other degenerate parametric amplifiers have been implemented in Boulder using an array of SQUIDs embedded in a coplanar wave-guide (CPW) superconducting resonator [55] or a SQUID embedded in a lumped element resonator as in Berkeley [23, 24] or in a coplanar waveguide as in Zurich [8]. Note that they are all referred to as Josephson Parametric Amplifier (JPA).

4.6.1 *Phase-sensitive amplification*

The JPA or JBA are strongly pumped at the resonator frequency ω_c (Fig. 27(a)). In order to highlight the amplification term, one must split the field mode in two contributions $c = p_0 + \delta c$, where p_0 is a scalar number standing for the classical pump tone and δc a small quantum field such that $[\delta c, \delta c^\dagger] = 1$ and $p_0 \gg \sqrt{\langle \delta c^2 \rangle}$. Therefore, the Hamiltonian can be expressed in the rotating wave approximation as

$$H_{\text{Duff}} \approx (\hbar\omega_c + 2\hbar\chi|p_0|^2)\delta c^\dagger \delta c + \underbrace{\hbar\chi(p_0^2 \delta c^{\dagger 2} + p_0^{*2}\delta c^2)}_{\text{squeezing Hamiltonian}}. \tag{79}$$

A squeezing term appears in the Hamiltonian. The evolution operator associated with this Hamiltonian term is the so-called single-mode squeezing operator.

$$S(r) = e^{r\delta c^2 - r^*\delta c^{\dagger 2}}, \tag{80}$$

where r is the squeezing parameter which can be expressed as a function of the pump p_0.

The evolution of the input field mode by the squeezing operator enables us to establish the scattering relation of the phase-sensitive amplifier as mentioned in Eq. (76)

$$\delta c_{out}[\omega_c] = S^\dagger \delta c_{in}[\omega_c] S = \sqrt{G}\delta c_{in}[\omega_c] + e^{i\phi}\sqrt{G-1}\delta c_{in}^\dagger[\omega_c], \tag{81}$$

where $\sqrt{G} = \cosh|r|$ and $\phi = \mathrm{Arg}(r)$.

4.6.2 *Phase-preserving amplification*

Note that a degenerate amplifier can be used as a phase-preserving amplifier, as demonstrated by the Zurich group [8]. Indeed, if the signal to amplify has a smaller bandwidth than half that of the amplifier, one can detune the signal by $\delta\omega$ from the pump frequency ω_c (Fig. 27(b)) without loosing too much gain. Then, due to the energy conservation, a new idler mode develops at $2\omega_c - (\omega_c + \delta\omega) = \omega_c - \delta\omega$. Hence, signal mode $\delta c[\omega_c + \delta\omega]$ and idler mode $\delta c[\omega_c - \delta\omega]$ are well separated from pump mode $c[\omega_c]$. Note that the signal and idler modes are defined within the bandwidth of the same resonator.

Hence the phase preserving amplifier scattering relation is satisfied and

$$\delta c_{out}[\omega_c + \delta\omega] = \sqrt{G}\underbrace{\delta c_{in}[\omega_c + \delta\omega]}_{\text{signal}} + \sqrt{G-1}\underbrace{\delta c_{in}^{\dagger}[\omega_c - \delta\omega]}_{\text{idler}}. \tag{82}$$

4.6.3 *Flux-driven amplification*

Degenerate amplifiers can also be flux driven if they contain a SQUID. Actually, by modulating the flux threading the SQUID, the effective inductance of the resonator is modulated as well as the resonance frequency of the resonator, leading to a parametric amplification. Here, the parametric character of the amplification appears directly as a parameter of the system (its frequency) modulated in time.

In this case, the active Hamiltonian term is a third order term. Thus, we obtain a degenerate three-wave mixing squeezing Hamiltonian of the form

$$H_{D3WM} = \hbar\omega_c c^{\dagger}c + \hbar\chi(pc^{\dagger 2} + p^{\dagger}c^2), \tag{83}$$

where p is the flux-driven pump mode (Fig. 27(c)).

Importantly, the flux modulation must take place at twice the resonator frequency $2\omega_c$ in order to get a non-vanishing squeezing term. The flux-driven mode has several advantages. Indeed, the flux-pumping at $2\omega_c$ enables us to efficiently filter out the strong pump tone that could otherwise saturate the following amplifier in the chain. Moreover, in general, there is no resonance at $2\omega_c$. As a consequence, the flux-driven pump is 'stiff' in a sense that the energy of the pump regenerates faster than it is taped out during the amplification process, which leads to a better energy dynamic range.

Such flux driven amplifiers have first been implemented by the NEC group in Tokyo [20] but also at Chalmers [22] for the observation of the dynamical Casimir effect using parametric amplification. Lumped-element versions have also recently been implemented at Berkeley and Santa Barbara based on a plate capacitor and a single SQUID [24] and at Saclay based on interdigitated capacitor and a SQUID array [56].

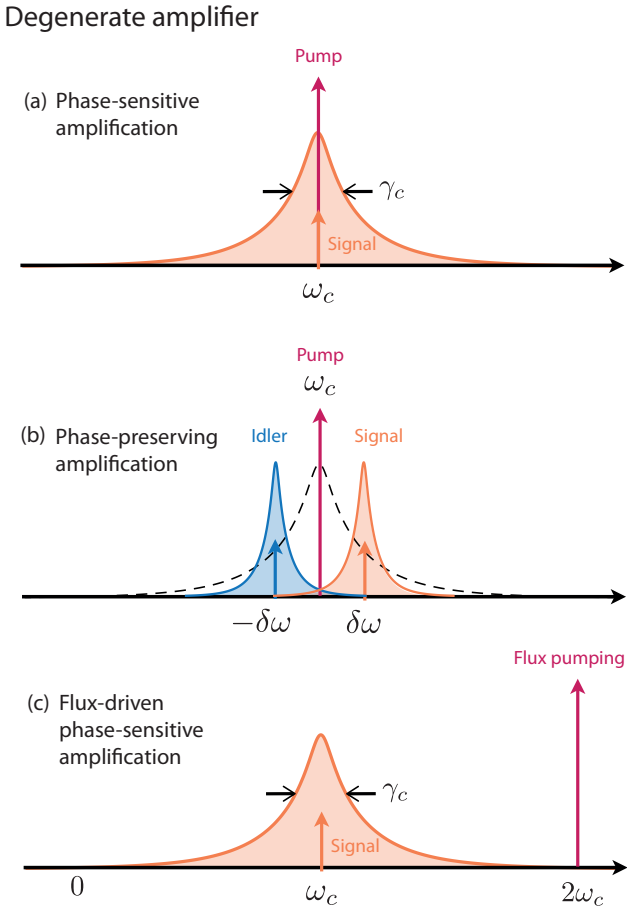

Figure 27: Spatially and temporally degenerate parametric amplifiers can be run in various modes (a) Phase-sensitive mode: the signal frequency is locked to the pump frequency. The whole bandwidth of the amplifier can be used. (b) Phase-preserving mode: the signal frequency is detuned by $\delta\omega$ from the pump frequency. The effective signal bandwidth (orange) must not overlap with the effective idler bandwidth (blue). (c) SQUID amplifiers can be flux-driven at twice the signal frequency and operated in phase-sensitive mode as shown on the schematic or in phase-preserving mode.

4.6.4 *Travelling-wave parametric amplifier*

Dynamical bandwidth of parametric amplifiers is limited by the resonant mode that hosts a non-linearity. One can evade this constraint by replacing the resonant mode by a propagating mode. However, the non-linearity then gets diluted and the overall gain vanishes to zero.

A promising way to solve this issue is to distribute non-linearities all along the transmission line that carries the propagating modes similarly to fiber amplifiers in optics. When a pump tone and the signal to amplify are sent side by side in the non-linear transmission line, the four wave mixing non-linearity mixes them together leading to a traveling wave parametric amplification. Note that a non-trivial requirement is that the pump and signal must be phase matched all along the line, meaning that the

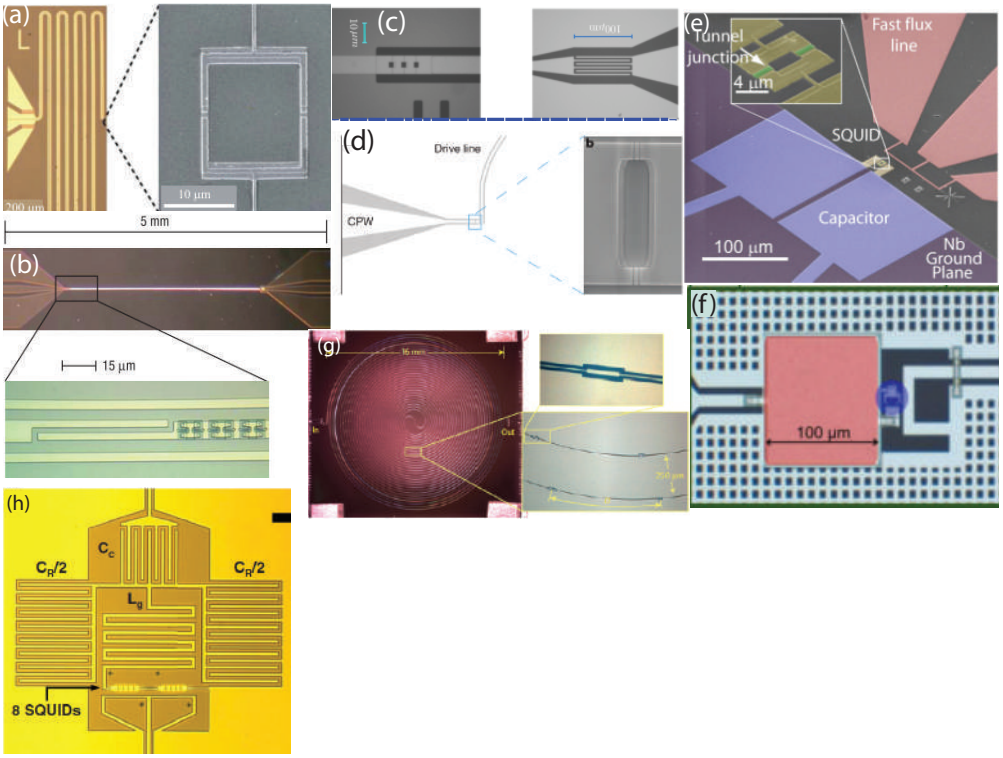

Figure 28: A non-exhaustive list of degenerate amplifier implementations, (a) Josephson Bifurcation Amplifier by the Yale group [21], (b) Josephson Parametric Amplifier (Josephson metamaterial) by the Boulder group [19], (c) Josephson Parametric Amplifier by the Zurich group [8], (d) Flux-driven Josephson Parametric Amplifier by the Chalmers group [22], (e) Lumped element Josephson Parametric amplifier by the Berkeley group [23] (f) Lumped element single-ended Josephson Parametric Amplifier by the Santa Barbara group [24]. (g) Travelling wave parametric amplifier from Caltech [25]. (h) Lumped element flux-driven parametric amplifier from Saclay [56].

dispersion relation must stay linear. This effect constitutes the current limitation on the bandwidth for traveling wave amplifiers.

The first implementation (Fig. 28) of such an amplifier has been realized at Caltech [25]. It is based on thin disordered superconducting wires made of NbTiN which provides a non-linear kinetic inductance. These kinetic inductances are distributed along the central conductor of coplanar-wave guide transmission line. In order to increase the performance of the distributed amplifier, 1 m-long coplanar wave-guide is arranged in a double spiral of 16 mm-diameter shown in Fig. 28(g). In the end, the amplifier with a 10 GHz-bandwidth centered around 12 GHz is obtained. However, the gain is of about 10 dB, which is not large enough to beat the noise temperature of the following High Electrion Mobility Transistor (HEMT) amplifier. Noise performances are close to standard superconducting parametric amplifiers.

Another implementation has recently been performed by the Berkeley group [57]. The device consists of a lumped-element transmission line whose elementary pattern is composed of a Josephson junction connected to a grounded plate capacitor. The

pattern is repeated few thousand times along a centimeter-scale line forming a non-linear meta-material. The bandwidth reaches 2 GHz for a 15 dB gain [58].

5

JOSEPHSON MIXER AS AN AMPLIFIER

5.1 NON-DEGENERATE PARAMETRIC AMPLIFIER

The Josephson Mixer is the only spatially non-degenerate parametric amplifier based on superconducting circuits. It was first proposed and realized by Bergeal and coworkers in the Yale group in 2010 [13, 12].

It is both spatially and temporally non-degenerate. Indeed, the signal, idler and pump modes are three separated spatial modes of the device. We will denote the signal mode as a, the idler mode as b and the pump mode as p. In general the pump mode is chosen to be non-resonant to ensure the 'stiff' pump conditions. Resonant frequencies and bandwidths of the two resonant modes a and b are chosen independently, therefore they are fully temporally non-degenerated. They avoid any overlap in space and/or frequency (Fig. 29).

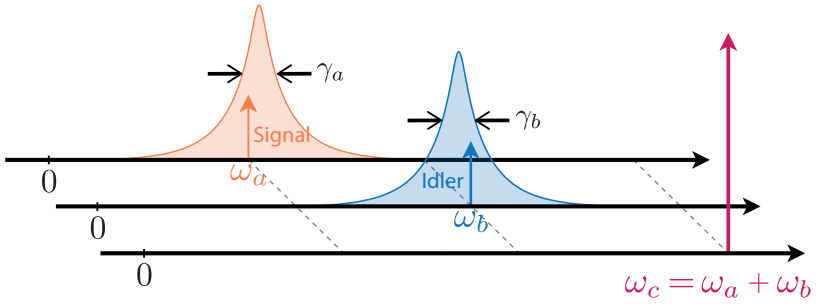

Figure 29: Spatially and temporally non-degenerate parametric amplifiers where the signal, idler and pump mode are three spatially and temporally separated modes

A practical consequence is that the circuit is only operable as a phase-preserving amplifier, since signal and idler modes are never temporally matched.

Note that hybrid mechanical/superconducting architectures can also implement non-degenerate parametric amplifiers [59, 32]. In that case, the amplification process is shared between a mechanical mode and a superconducting resonator mode.

The unique character of the Josephson mixer is its non-linear active element based on the Josephson Ring Modulator (see Part i). This four-Josephson junction ring is bridging the three modes a, b and p symmetrically so that it provides a pure **non-degenerate three-wave-mixing** Hamiltonian as demonstrated in section 2.3.

$$H_{JM} = \hbar\omega_a^{res} a^\dagger a + \hbar\omega_b^{res} b^\dagger b + \hbar\chi(a^\dagger + a)(b^\dagger + b)(p^\dagger + p). \tag{84}$$

In the amplification mode, the pump is driven at the sum of the idler and signal frequencies, $\omega_p = \omega_a + \omega_b$. In the rotating wave approximation, only the terms that

respect energy conservation are kept. Therefore the three-wave mixing Hamiltonian reduces to

$$H_{JM} = \hbar\omega_a^{res} a^\dagger a + \hbar\omega_b^{res} b^\dagger b + \underbrace{\hbar\chi(pa^\dagger b^\dagger + p^\dagger ab)}_{\text{non-degenerate amplifiaction}} \quad . \tag{85}$$

In order to extract rigorously the figure of merit of the Josephson mixer as an amplifier from this Hamilonian, one must use the Quantum Langevin equation formalism.

5.1.1 *Quantum Langevin equation*

Quantum Langevin equation gives the evolution of electromagnetic modes a and b coupled to propagating modes $a_{in/out}$ and $b_{in/out}$. The two Langevin equations for signal and idler read

$$\begin{cases} \dfrac{\partial a}{\partial t} &= \dfrac{i}{\hbar}[H_{JM}, a] - \dfrac{\kappa_a}{2}a + \sqrt{\kappa_a}a_{in} \\ \dfrac{\partial b}{\partial t} &= \dfrac{i}{\hbar}[H_{JM}, b] - \dfrac{\kappa_b}{2}b + \sqrt{\kappa_b}b_{in}. \end{cases} \tag{86}$$

The amplification Hamiltonian couples linearly the two Langevin equations

$$\begin{cases} \dfrac{\partial a}{\partial t} &= -i\omega_a^{\text{res}} a - i\chi p b^\dagger - \dfrac{\kappa_a}{2}a + \sqrt{\kappa_a}a_{in} \\ \dfrac{\partial b}{\partial t} &= -i\omega_b^{\text{res}} b - i\chi p a^\dagger - \dfrac{\kappa_b}{2}b + \sqrt{\kappa_b}b_{in}. \end{cases} \tag{87}$$

5.1.1.1 *Stiff pump hypothesis*

The stiff pump approximation consists in considering the pump as a classical drive that is unaffected by the amplification process. It stands on two requirements. First, the pump has to be non-resonant and its effective bandwidth κ_p much larger than the idler and signal bandwidths, $\kappa_p \gg \kappa_a, \kappa_b$. Therefore its time dynamics can be considered as instantaneous. Second, it should be strongly driven, $|\langle p_{in}\rangle| \gg 1$, so that quantum fluctuations are negligible.

Schematically, when its energy is consumed in the amplification process, it is immediately refilled by the strong drive. The pump mode behaves as if it had a classical energy reservoir that is not easily depleted. The approximation holds as long as the pump power is significantly larger than the total output power of all amplified signals.

In quantum Langevin equations, we can then replace the pump annihilation operator p by its average value in the coherent state

$$p \to |\langle p\rangle| e^{i\omega_p t + \varphi} = p_0 e^{i\omega_p t}. \tag{88}$$

For the sake of simplicity, we only consider the case where $\omega_p = \omega_a^{\text{res}} + \omega_b^{\text{res}}$. Therefore, we will also define the detuning $\Delta = \omega_a - \omega_a^{res} = -(\omega_b - \omega_b^{res})$.

5.1.1.2 *Scattering relation in the frequency domain*

In the frequency domain, the quantum Langevin equations form a simple linear system and read

$$\left\{\begin{array}{rcl} 0 &=& i(\omega_a-\omega_a^{\rm res})a[\omega_a]-i\chi p_0 b^\dagger[\omega_b]-\frac{\kappa_a}{2}a[\omega_a]+\sqrt{\kappa_a}a_{in}[\omega_a] \\ 0 &=& i(\omega_b-\omega_b^{\rm res})b[\omega_b]-i\chi p_0 a^\dagger[\omega_a]-\frac{\kappa_b}{2}b[\omega_b]+\sqrt{\kappa_b}b_{in}[\omega_b]. \end{array}\right. \tag{89}$$

By inserting the input/ouput relations, one can eliminate the field operators a and b from the linear system

$$\left\{\begin{array}{rcl} \sqrt{\kappa_a}a[\omega_a] &=& a_{out}[\omega_a]+a_{in}[\omega_a] \\ \sqrt{\kappa_b}b[\omega_b] &=& b_{out}[\omega_b]+b_{in}[\omega_b]. \end{array}\right. \tag{90}$$

Therefore, the system can easily be transformed into scattering relations

$$\left\{\begin{array}{rcl} a_{out}[\omega_a] &=& r_{aa}a_{in}[\omega_a]+s_{ab}b_{in}^\dagger[\omega_b] \\ b_{out}^\dagger[\omega_b] &=& s_{ba}a_{in}[\omega_a]+r_{bb}b_{in}^\dagger[\omega_b]. \end{array}\right. \tag{91}$$

This defines the scattering matrix

$$\begin{pmatrix} a_{out}[\omega_a] \\ b_{out}^\dagger[\omega_b] \end{pmatrix} = \begin{pmatrix} r_{aa} & s_{ab} \\ s_{ba} & r_{bb} \end{pmatrix} \begin{pmatrix} a_{in}[\omega_a] \\ b_{in}^\dagger[\omega_b] \end{pmatrix}, \tag{92}$$

where the scattering coefficients read

$$\begin{array}{rcl} r_{aa} &=& \dfrac{(1-i\delta_b)(1-i\delta_a)+|\rho|^2}{(1-i\delta_b)(1+i\delta_a)-|\rho|^2}, \\ r_{bb} &=& \dfrac{(1+i\delta_b)(1+i\delta_a)+|\rho|^2}{(1-i\delta_b)(1+i\delta_a)-|\rho|^2}, \\ s_{ab} &=& \dfrac{2i\rho}{(1-i\delta_b)(1+i\delta_a)-|\rho|^2}, \\ s_{ba} &=& \dfrac{-2i\rho^*}{(1-i\delta_b)(1+i\delta_a)-|\rho|^2}, \end{array} \tag{93}$$

with dimensionless variables such as cooperativity

$$\mathcal{C}=|\rho|^2=\left|\frac{2\chi p_0}{\sqrt{\kappa_a\kappa_b}}\right|^2 \tag{94}$$

and the reduced detunings

$$\delta_a=\frac{\Delta}{\kappa_a/2} \quad \text{and} \quad \delta_b=-\frac{\Delta}{\kappa_b/2}. \tag{95}$$

A remarkable property of the scattering relation is its symplectic character implying that

$$\boxed{\begin{array}{rcl} |r_{aa}|^2-|s_{ab}|^2 &=& 1 \\ |r_{bb}|^2-|s_{ba}|^2 &=& 1 \end{array}}. \tag{96}$$

This property is necessary for the field operator to be well-defined along the scattering process i.e. output operators preserve their canonical commutation relations.

We define the spectral gain as $\sqrt{G} = |r_{aa}| = |r_{bb}|$ and the spectral cross-gain as $\sqrt{G-1} = |s_{ba}| = |s_{ab}|$. The scattering relation of the amplifier can now be expressed as a function of the gain and pump phase ϕ

$$\begin{pmatrix} a_{out}[\omega_a] \\ b^\dagger_{out}[\omega_b] \end{pmatrix} = e^{i\alpha} \begin{pmatrix} e^{i\beta}\sqrt{G} & ie^{i\phi}\sqrt{G-1} \\ ie^{-i\phi}\sqrt{G-1} & e^{-i\beta}\sqrt{G} \end{pmatrix} \begin{pmatrix} a_{in}[\omega_a] \\ b^\dagger_{in}[\omega_b] \end{pmatrix} \tag{97}$$

with the phases $\alpha = -\mathrm{Arg}\left[(1-i\delta_a)(1+i\delta_b) - \mathcal{C}\right]$ and $\beta = \mathrm{Arg}\left[(1-i\delta_a)(1-i\delta_b) - \mathcal{C}\right]$.

Note that these phases are either gobal phases as α or phases that can be absorbed by a redefinition of the pump phase as β. Hence up to a redefinition of the phase reference of the pump at each frequency, the scattering relations read

$$\boxed{\begin{pmatrix} a_{out}[\omega_a] \\ b^\dagger_{out}[\omega_b] \end{pmatrix} = \begin{pmatrix} \sqrt{G} & e^{i\varphi}\sqrt{G-1} \\ e^{-i\varphi}\sqrt{G-1} & \sqrt{G} \end{pmatrix} \begin{pmatrix} a_{in}[\omega_a] \\ b^\dagger_{in}[\omega_b] \end{pmatrix}}. \tag{98}$$

Note that when the amplifier is probed at resonance $\delta_a = \delta_b = 0$, the gain is simply given by

$$\boxed{\sqrt{G_0} = \frac{1+\mathcal{C}}{1-\mathcal{C}} \underset{\mathcal{C}\to 1^-}{\longrightarrow} +\infty}. \tag{99}$$

It diverges when the cooperativity reaches unity. It corresponds to a threshold where the parametric down-conversion exactly compensates the losses of the resonator $\chi|p| \to \sqrt{\kappa_a\kappa_b}/2$.

In the limit of a large gain, there is a useful expression for the gain as a function of frequency for a small detuning

$$\boxed{G[\Delta\omega] \approx \frac{G_0}{1 + G_0\left(\frac{1}{\kappa_a} + \frac{1}{\kappa_b}\right)^2 \Delta\omega^2}}. \tag{100}$$

Thus, the spectral shape of the direct gain is a Lorentzian whose maximum is G_0 and dynamical bandwidth γ is given by

$$\boxed{\gamma = \frac{2}{\sqrt{G_0}\left(\frac{1}{\kappa_a} + \frac{1}{\kappa_b}\right)}}. \tag{101}$$

The dynamical bandwidth decreases as the gain peaks and the product of the maximal amplitude gain and the bandwidth is thus constant, as generally expected for parametric amplifiers

$$\sqrt{G_0} \times \gamma = \frac{2}{\left(\frac{1}{\kappa_a} + \frac{1}{\kappa_b}\right)} = \text{const.} \tag{102}$$

5.1.2 *Self-oscillation regime*

When the pump is driven above threshold $\mathcal{C} \geq 1$, the system enters in the self-oscillation regime. Indeed, when the parametric gain overcomes the damping rate, exponentially increasing oscillations spontaneously develop, triggered by vacuum fluctuations. However, in an actual physical system, the development of oscillations is limited for two reasons. First, higher order non-linear terms start to rapidly dominate the physical evolution leading to saturation of the parametric gain. Second, the stiff pump approximation breaks down and the pump drive gets depleted. Note that this regime is analogous to the lasing regime in optics.

5.2 PRACTICAL PARAMETRIC AMPLIFIER REQUIREMENTS

The goal of my work on the microwave amplifier was to build a practical and reliable parametric amplifier that would be operated in real physics experiments. Hence, far from being a proof-of-principle device, strict specifications were required to guarantee the success of the feedback experiment lead in the group in parallel with my work. In order to perform a quantum non-destructive single-shot read out of a superconducting qubit in a circuit QED architecture, one needs

- A large power gain G of the order of 20 dB, in order to neglect the 20-40 photons of noise added by the following amplification stage made with state-of-the-art high electron mobility transistors (Caltech HEMT amplifiers). This figure contains the typical attenuation between the Josephson Mixer and the HEMT.
- A quantum efficiency η close to 1 to minimally degrade the signal-to-noise ratio at the single photon level, when operated in the phase preserving mode.
- A wide dynamical bandwidth $\gamma/2\pi$ of the order of 10 MHz, which corresponds to a signal processing time of a few tenths of a nanosecond that is shorter than typical timescale for controlling circuit QED architecture dynamics.
- The 1dB-compression point P_{1dB} quantifies the amount of input power beyond which the power gain decreases by 1 dB. The amplifier must be able to sustain a few photons per dynamical bandwidth at its input.
- A tunable resonant frequency on a range larger than 100 MHz so that the center frequency of the amplifier can match the transition frequency of the system despite the fabrication uncertainties.

5.3 GAIN AND BANDWIDTH

The gain $\sqrt{G_0}$ and dynamical bandwidth γ are inversely proportional, see Eq.(101).

Indeed, a parametric amplifier can be seen as a device which extends the temporal envelop of the incoming signal rather than directly multiply its amplitude. The amplifier transforms a dirac pulse in time into a decaying exponential envelope at a rate γ^{-1} with the original amplitude as illustrated on Fig. 30. The parametric amplifier offers

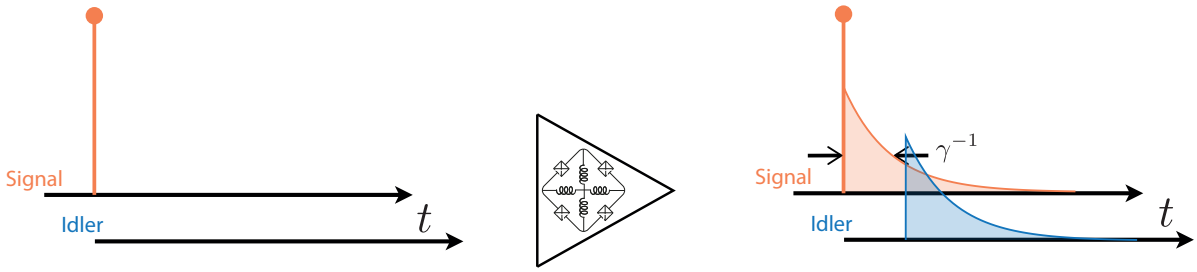

Figure 30: Pulsed response of the parametric amplifier, it offers a temporal persistence over γ^{-1} that provides an overall energy gain.

a temporal persistence over γ^{-1} that provides an overall energy gain. On the contrary, for signal much longer than this timescale, the accumulation of the persistence effect provides a proper amplitude gain $\sqrt{G}$.

5.3.1 *Design constraints*

The gain of Josephson mixers is controlled by the pump power at the sum frequency. We have previously seen that we could in principle reach an infinite gain by increasing the pump power up to reach a unit cooperativity $\mathcal{C} \to 1$. However, the fraction of the pump current flowing in the junctions must remain well below their critical current for the three-wave-mixing approximation to hold. As a consequence, the maximum cooperativity that can be achieved is bounded, as shown in section 3.1.5. Thus the bound must be sufficient to access the high-gain amplification regime. The cooperativity bound for shunting JRM reads

$$\boxed{\mathcal{C}_{max} = \left|\frac{2\chi p_{max}}{\sqrt{\kappa_a \kappa_b}}\right|^2 \sim \frac{1}{16}\xi_a \xi_b Q_a Q_b \left(\frac{2L}{L_J^0}\right)^2 > 1}. \tag{103}$$

Let us evaluate the high gain condition for two different samples JM-B and JM-C, first characterized in section 3.4.2. Importantly, the only difference these between samples is the critical current of their junctions.

Thus the coupling rates of both samples are $\kappa_a/2\pi = 29$ MHz and $\kappa_b/2\pi = 39$ MHz, their frequencies are $\omega_a/2\pi \sim 5.6$ GHz and $\omega_b/2\pi \sim 8.5$ GHz leading to quality factors $Q_a \sim 190$ and $Q_b \sim 220$. In order to evaluate the participation ratios ξ_a and ξ_b, which depend on the flux φ_{ext}, we can assume $\varphi_{ext} = 2\pi$ since it maximizes the three wave mixing term used in the amplification. We find $\xi_a = 2L/L_a^{tot} \sim 0.06$ and $\xi_b = 2L/L_b^{tot} \sim 0.1$ (see Fig. 23(e)).

The only difference is their critical current leading to Josephson inductances of $L_J^{0,B} \sim 300$ nH and $L_J^{0,C} \sim 100$ nH.

As a result we get that

$$\frac{1}{8}\xi_a \xi_b Q_a Q_b \left(\frac{2L}{L_J^0}\right)^2 \sim \begin{cases} 0.4 & \leq 1 \quad \text{for JM-B} \\ 3.5 & > 1 \quad \text{for JM-C.} \end{cases} \tag{104}$$

Remarkably, it has been experimentally verified that JM-B has not reached the high-limit gain but not by far, since the maximum power gain obtained with this sample was 12 dB. On the contrary, JM-C has comfortably reached this limit, as we have even been able to observe the self-oscillation regime.

5.3.2 *Measured gain and bandwidth*

We present here the measurement of the sample JM-C.

Reflection gain as a function of frequency is shown in Fig. 31 for Signal (a) and Idler (b) at various pump powers. The magnetic flux bias is set to $\varphi_{ext} = 2.5\ \pi$ and the pump tone is shined at $\omega_p = 14.071$ GHz. The Lorentzian shape of the reflection gain is well reproduced by the theory up to 35 dB corresponding to plain traces. Higher pump powers correspond to dashed traces for which the self-oscillation threshold seems to be exceeded. Saturation of the gain is observed as well as a strong Kerr-effect.

The maximum gain as a function of cooperativity is shown in Fig. 31(c). The behavior is as expected up to 20 dB. Then the gain slightly saturates. Note that the measurement has probably been performed with too much input power for such a high gain, hence the saturation may be due to the saturation of a dynamic range.

Finally, the dynamical bandwidth fitted at half gain is plotted as a function of the linear power gain on a log-log scale for the signal mode. The relation $\sqrt{G_0} \propto \gamma^{-1}$ is well verified on a wide range of gain from 5 dB to 30 dB.

Note that Josephson mixer JM-C has a dynamical bandwidth of 3 MHz for a 20 dB gain, which is below the specification that requires 10 MHz. Nonetheless, we have later fabricated a Josephson mixer with a bare bandwidth of 100 MHz leading to practical amplifiers with about 10 MHz dynamical bandwidth [48], which could be used to readout a qubit dispersively.

5.4 FREQUENCY TUNABILITY

The maximum bandwidth that can be achieved with parametric amplifiers based on high-quality factor cavities, represents a fraction of percent of the resonance frequency. Hence, an essential requirement for such a practical amplifier is to be frequency tunable in order to match the bandwidth of the system under study despite irreproducibilities originating from fabrication uncertainties. Indeed, frequency tunability is an essential requirement for a reliable and practical amplifier.

The tunability of the device has been improved a lot by shunting the Josephson ring with linear inductors. It has stabilized working points of the device and enabled us to explore a much larger range of frequencies. Importantly, the whole flux tunability shown in Fig. 32(a) is largely related to the value of the shunting inductances L as demonstrated in section 3.4.2.2.

$$\Delta\omega_{a,b} \sim \frac{L}{L_{a,b}}\omega_{a,b} = \pi\frac{L}{Z_0}\omega_{a,b}^2 \sim \begin{cases} 2\pi \times 400 \text{ MHz} & \text{signal} \\ 2\pi \times 170 \text{ MHz} & \text{idler.} \end{cases} \tag{105}$$

The estimated tunability range is in good agreement with the experimental results shown in Fig. 32(b). We obtain a 20 dB-gain over a frequency range larger than

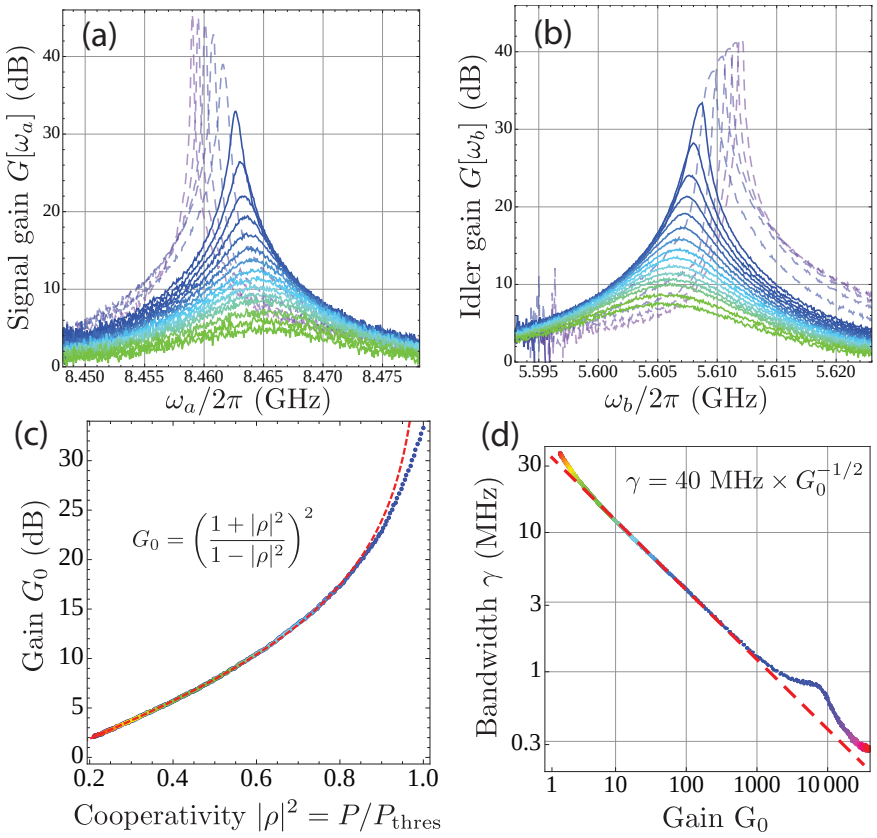

Figure 31: Magnitude of the reflection coefficient for signal (a) and idler (b) represented as a function of the input frequency for increasing pump power (measured at the level of the generator, with about $60-70$ dB of power attenuation). The pump frequency is $\omega_p/2\pi = 14.071$ GHz. (c) Maximum as a function of the pump power (d) Bandwidth of the amplifier as a function of gain. Colors of the dots encode the pump power in every plot.

400 MHz. Each curve corresponds to one value of the flux bias indicated by color lines in the frequency-flux plot. For each flux bias, the pump parameters are adjusted for the gain to reach 20dB.

5.5 DYNAMICAL RANGE

The maximal input power is limited by two main physical issues, which will be detailed in the following.

5.5.1 *Exhausted Josephson non-linearity*

Josephson non-linearity can be exhausted. The energy stored in signal and idler modes exhausts the non-linearity of the Josephson junction by exciting higher non-linear terms in the expansion of Eq. (22). However, note that thanks to its very symmetric

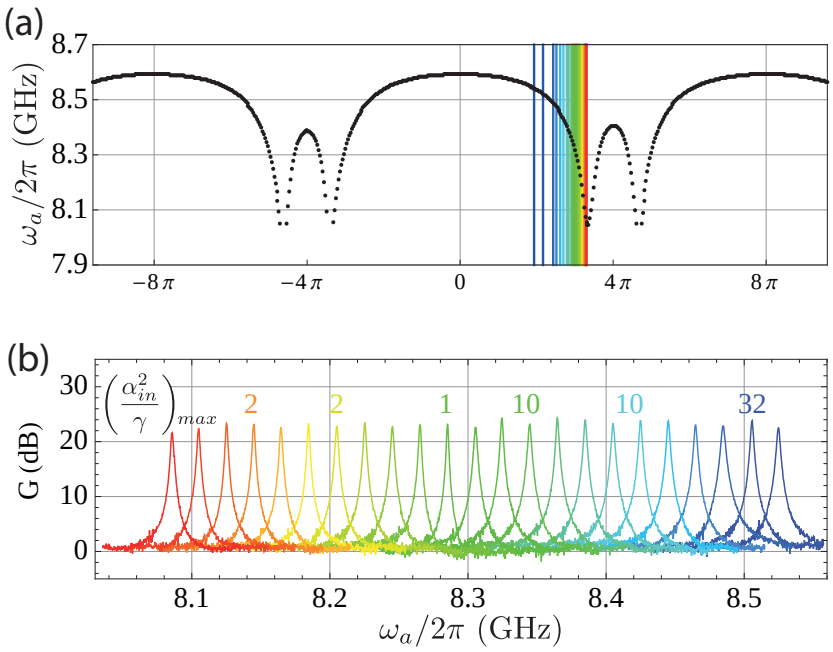

Figure 32: (a) Dots: Measured resonance frequency ω_a^{res} of signal mode as a function of flux applied φ_{ext} to the ring modulator without pump. (b). Reflection gain measured on the signal port as a function of frequency for various values of the flux indicated by the color lines in (a). Pump parameters are optimized for each curve. The numbers on top represent the 1dB-compression point (maximum input power) expressed in input photon rate per dynamical bandwidth for six different working frequencies coded by color.

Hamiltonian eliminating several higher order terms, the Josephson mixer is quite robust at high powers.

The flux across a single junction in the ring due to the amplified modes a and b is typically given by (Eq. (9))

$$\frac{\varphi_a}{2} + \frac{\varphi_b}{2} = \xi_a \sqrt{\frac{Z_a}{2Z_Q}}(a + a^\dagger) + \xi_b \sqrt{\frac{Z_b}{2Z_Q}}(b + b^\dagger), \tag{106}$$

where $Z_Q = \varphi_0^2/\hbar = \hbar/(2e)^2 \sim 1\ \mathrm{k}\Omega$ is superconducting resistance quantum.

The fraction of the amplified current flowing through the junctions must remain well below their critical current for the three-wave-mixing approximation to hold. This translates in an upper bond on the phase difference across the junctions

$$\langle \left(\frac{\varphi_a}{2} + \frac{\varphi_b}{2}\right)^2 \rangle \sim \frac{1}{4} \ll \pi^2. \tag{107}$$

Considering for simplicity equal impedances $Z_a = Z_b = Z_0$, equal coupling rates $\kappa_a = \kappa_b = \gamma\sqrt{G}$ and a large gain limit, $\langle a^\dagger a \rangle = \langle b^\dagger b \rangle = \langle a^\dagger b^\dagger \rangle = G\alpha_{in}^2/\kappa_a$, the upper bound on the mean input photon number per dynamical bandwidth reads

$$\boxed{\left(\frac{\alpha_{in}^2}{\gamma}\right)_{max} = \frac{1}{4\sqrt{G}} \frac{Z_Q}{Z_0} \frac{1}{(\xi_a^2 + \xi_a\xi_b + \xi_b^2)}}. \tag{108}$$

For a magnetic flux bias $\varphi_{ext} = 2\pi$, the dynamical range upper bound can be estimated to 30 photons per dynamical bandwidth for a 20 dB power gain. An important trend is that the dynamical range is inversely proportional to the square of the participation ratio. We have shown that the participation ratios rise rapidly with magnetic flux bias, leading to a dynamical range upper bound reduced to 5 photons near the symmetry breaking point for JM-C.

Note that this upper-bond is quite optimistic. Actually, non-linear effects such as the cross-Kerr effect might disturb the Lorentzian line-shape of the gain well below this bound. As a consequence, the measured 1dB-compression point might lie below this range.

5.5.2 *Pump depletion*

The other mechanism is the depletion of the pump energy. Indeed if the amplified signal power represents a non-negligeable fraction of the pump power, the stiff pump approximation beaks down. The dynamics of the pump cannot be neglected, then signal, idler, and pump modes must be treated on the same footing.

The stiff pump approximation holds as long as the output photon flow $|\alpha_{out}|^2 \approx |\beta_{out}|^2$ is much smaller than the input pump photon flow $|p_{in}|^2$,

$$|\alpha_{out}|^2 \approx |\beta_{out}|^2 = G|\alpha_{in}|^2 \ll |p_{in}|^2 = \frac{1}{2}\kappa_c|p|^2 \sim \frac{\kappa_a\kappa_b\kappa_c}{8\chi^2}. \tag{109}$$

Using the expression of the coupling rate χ in Eq. (43) and by gathering the participation ratio dependencies, the input photon per dynamical bandwidth is bounded by

$$\boxed{\frac{|\alpha_{in}|^2}{\gamma} \ll \frac{1}{\sqrt{G}}\frac{1}{(\xi_a\xi_b\xi_c)^2}\frac{1}{Q_c\sqrt{Q_aQ_b}}\frac{Z_Q}{Z_0}\frac{(L_J^0)^2}{L_c\sqrt{L_aL_b}}}. \tag{110}$$

Importantly, this upper-bond is highly dependent on the participation ratios. As expected, the more the participation ratios are low, the less the pump can be depleted.

The upper bond can be evaluated to $\sim$ 3000 photons per bandwidth for a non-resonant pump tone $Q_c \sim 1$ and a 20 dB-gain at flux bias $\varphi_{ext} = 2\pi$ leading to a pump mode participation ratio of $\xi_c \sim 0.07$. As a consequence, the pump depletion should not be the dominant limitation for this flux bias.

However, close to the symmetry breaking point, the inductance of the pump mode diverges leading to a participation ratio close to one, $\xi_c \sim 1$. In other words, a very weak pump tone is needed to reach a 20 dB-gain. Hence, at this flux bias the upper bound decreases to $\sim$ 2 photons per bandwidth. In this case, the pump depletion is the dominant limitation on dynamical range. Besides, it limits the maximum gain that can be achieved since amplified vacuum fluctuations are important enough to saturate the pump power.

5.5.3 *Measured dynamical range*

The measured dynamical ranges are presented in Fig. 32(b). Numbers on top represent the 1dB-compression point (maximum input power) expressed in input photon rate per dynamical bandwidth for six different working frequencies coded by color.

A trend shows that the 1dB-compression point decreases rapidly when the flux-bias gets closer to the symmetry breaking point as expected from the two saturation mechanisms.

5.6 MEASURING THE QUANTUM EFFICIENCY

The main challenge in the measurement of the efficiency of an amplifier consists in determining the absolute amplitude of the signals at its input. We have performed various kinds of calibration of this amplitude and determined lower bounds on the efficiency of the Josephson mixer used as an amplifier.

Two calibrations have consisted in generating noise at the input of the amplifier using a self-calibrated noise source. For one calibration, we used a voltage biased tunnel junction emitting electron shot noise eV and for the other one, a temperature controlled load emitting Johnson-Nyquist noise k_BT. The other way used a superconducting qubit as a spectrometer. The dephasing induced by the field to which the qubit is coupled allows us to estimate the amplitude of that field. We have performed these three types of calibration on Josephson mixers during three independent experiments.

5.6.1 *Tunnel junction calibration*

The noise properties and the quantum efficiency of the JM-C sample have been calibrated using the electron shot-noise across a voltage-biased NIN tunnel junction placed at the input (Fig. 33a). This noise, which is well-understood and therefore of predictable amplitude, plays the role of an *in situ* calibrated signal. For small electronic temperatures ($k_BT_e \ll \hbar\omega$), the noise from the tunnel junction presents two regimes as a function of voltage. For $eV < \hbar\omega$, zero-point fluctuations across the junction dominate with a power spectral density $S_p(\omega) = \frac{\hbar\omega}{2}$, while for $eV > \hbar\omega$, electrons in the junction produce non-equilibrium shot noise and $S_p(\omega) = \frac{eV}{2}$. The electronic temperature T_e in the electrodes of the junction sets the sharpness of the crossover between these two regimes [60] as $S_p = S_p^+ + S_p^-$ with

$$S_p^{\pm}[\omega] = \frac{1}{4}(eV \pm \hbar\omega)\coth\frac{eV \pm \hbar\omega}{2k_BT_e}. \tag{111}$$

We used as a tunnel junction an aluminum Josephson junction shown in Fig. 33(b) kept in its normal state by neodymium permanent magnets close-by. We measured *in situ* a normal resistance of 43.9 Ω for the tunnel junction. The output spectral density was recorded with a spectrum analyzer and averaged over a 2 MHz bandwidth around the center frequency of the amplifier (see Fig. 33(c)). Its dependence with bias voltage was obtained (Fig. 33(d)) for an amplifier gain of 23 dB with the same settings as in

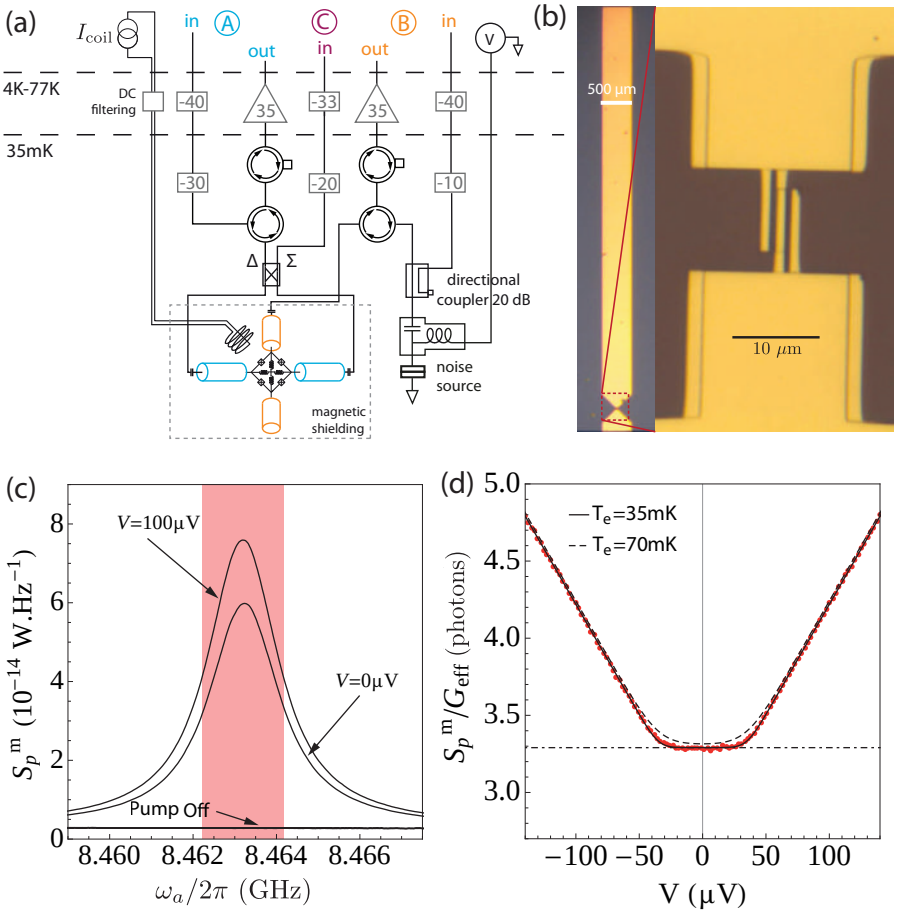

Figure 33: (a) Simplified schematic of the setup used for the calibration of the Josephson mixers. The tunnel junction is voltages biased through a bias tee, it is placed at the input of b mode. Optical microscope picture of the tunnel junction placed at the end of a 50 Ω microstrip transmission line. (c) Power spectral density as a function of frequency measured at the output of signal out for three settings: pump off and $V = 0\mu$V, pump on and $V = 0\mu$V,or $V = 100\mu$V. The colored area represents the averaging range used in the right panel. (c) Average power spectral density over a 2 MHz bandwidth around the center frequency of the amplifier as a function of bias voltage V. The solid line shows what is expected by using Eq. (113) and fitting an overall gain $G_{eff} = 94.6$ dB and an extra noise N_{add} of 2.8 quanta coming from both the unavoidable quantum noise of the idler port (0.5 quanta) and the unwanted losses between the tunnel junction and the amplifier (2.3 photons). The gain G_{eff} allows us to express this power spectral density in units of photon number or quantum.

Fig. 31. The measured power spectral density can be described by an expression of the form

$$S_p{}^m[\omega_a] = G_{eff}(S_p + N_{add}\,\hbar\omega_a). \tag{112}$$

where N_{add} is the noise added by the amplifying chain referred at its input.

In the shot noise regime, it is possible to calibrate the effective system gain $G_{eff} = \mathrm{d}S_p{}^m/\mathrm{d}(eV/2) = 94.6$ dB from the NIN tunnel element to the spectrum analyzer including a possible attenuation from the element to the input port of the amplifier.

Without any additional calibration, we extracted the apparent system added noise $N_{add} = 2.8$ at the plateau (Fig. 33(b)). Remarkably, an electronic temperature T_e equal to the refrigerator mixing chamber temperature of 35 mK describes perfectly the crossover. It is worth emphasizing that the noise power of the total measurement setup is presented in Fig. 33 without any background subtraction and is therefore the absolute system noise. It is straightforward to compare the noise measurement with and without our device. Turning off the pump tone, the same noise measurement using only the state-of-the-art HEMT amplifier at 4 K yielded an apparent added noise 20 times larger than with the pump on. Indeed, Josephson mixer acting as a pre-amplifier leads to a rise of the signal-to-noise ratio of the whole amplifying chain by a factor 20.

The notion of added noise is quite an artificial characterization. It describes the reduction of the signal to noise ratio (SNR) by the addition of spurious noise. However, for a phase preserving amplifier operating near the quantum limit, it is fair to consider that the reduction of the SNR is essentially due to a decrease of the signal coming from unavoidable insertion losses rather than from the addition of spurious noise. A more consistent model consists in considering that the active part of the device acts as a perfect phase preserving amplifier but that unavoidable losses at the input decrease the quantum efficiency of the whole setup. Importantly, the insertion losses must be modeled as beam splitters with a transparency η which adds unavoidable vacuum fluctuations $(1-\eta)\hbar\omega/2$ leading to an increase of the apparent noise.

Crucially, the phase preserving character implies that the measurement is necessary blurred by half-a-photon resulting from the Heisenberg uncertainty saying that it is impossible to measure perfectly both quadratures simultaneously.

Hence, the measured power spectral density is fairly described by an expression of the form

$$S_p{}^m[\omega] = G_{chain}\left(\underbrace{\eta}_{\substack{\text{insertion}\\ \text{losses}}} S_p[\omega] + \underbrace{(1-\eta)\frac{\hbar\omega}{2}}_{\substack{\text{vaccum noise}\\ \text{from losses}}} + \underbrace{\frac{\hbar\omega}{2}}_{\substack{\text{quantum}\\ \text{limit}}}\right), \tag{113}$$

η is the quantum efficiency of the phase-preserving amplifying chain, equal to the one for an ideal setup. The noise temperature of the following HEMT amplifier is negligible for such a Josephson mixer gain as shown in Fig. 33(a). Thus it has not been taken into account here except through a slight apparent decrease of the quantum efficiency.

The quantum efficiency and the gain of the total amplifying setup can be extracted from the previous parameters

$$\begin{aligned} \eta &= \frac{2}{2N_{add}+1} = 0.3 \\ G_{chain} &= \eta^{-1}G_{eff} = 99.8 \text{ dB}. \end{aligned} \tag{114}$$

The main source of inefficiency is well understood. Indeed, a large fraction of the inefficiency is due to the unwanted insertion loss between the noise source and the Josephson mixer inherent to our type of low temperature measurement setup. The insertion losses are mainly due to the various connectors (~ -1dB) and the circulator (~ -1dB), leading to an estimated inefficiency of ~ 0.6.

Also, the impedance of the tunnel junction itself is imperfectly matched at microwave frequencies [61]. Indeed, given the size of the junction ($\simeq 10\ \mu\text{m}^2$) and previous experiments on similar junctions, we estimated its capacitance to be in the $0.7\ \text{pF} - 1\ \text{pF}$ range. Using the resistance of the junction and the characteristic impedance of the amplifier, we calculated that the inefficiency due to the RC filtering of the junction noise represents $\sim 0.55 - 0.60$. Taking this noise source impedance mismatch into account, the actual efficiency of the Josephson mixer can be inferred to be $\eta_{\text{infered}} = 0.5 - 0.55$.

5.6.2 *Calibration using a thermal source*

The Josephson mixer efficiency has been calibrated for the experiment dealing with the generation of entangled radiation. Here, I present identical experimental data with slightly modified notation in order to emphasise the quantum efficiency calibration.

In this experiment, the calibration is performed using a temperature-controlled $50\ \Omega$ load emitting Johnson-Nyquist noise. The procedure is detailed in section 7.5.

The noise emitted by an impedance-matched load reads

$$S_p[\omega, T] = \frac{\hbar\omega}{2} \coth\left(\frac{\hbar\omega}{2kT}\right). \tag{115}$$

Hence, one can determine the efficiency of the amplifier by measuring the power spectral density at room temperature as a function of the noise source temperature and the dilution refrigerator base temperature to check the consistency of the measurement. Indeed, losses being modeled as beam splitters as shown in Fig. 34(a), the dilution refrigerator temperature modifies the noise density at the other input of the beam splitter.

The normalized power spectral density can be expressed as a function of the quantum efficiency η and the noise emitted by the impedance-matched load at the noise-source temperature T_{ns} and for a dilution refrigerator temperature T_{dil} (Fig. 34a).

$$\frac{S_a - S_{\text{off}}}{(G-1)G_{\text{LNA}}} = \eta S[T_{\text{ns}}, \omega_a] + (1-\eta) S[T_{\text{dil}}, \omega_a] + \frac{\omega_a}{\omega_b} S[T_{\text{dil}}, \omega_b]. \tag{116}$$

Note that the ratio ω_a/ω_b is due to the frequency conversion of the noise from b to a during the amplification process. Importantly, in this experiment, the gain of the parametric amplifier was kept below 10 dB which is not enough to overcome the noise added by the following HEMT amplifier. Then, the power spectral density background has been carefully removed as detailed in section 7.5.5. As a consequence, the measured efficiency corresponds to the effective quantum efficiency of the Josephson mixer only.

The spectral noise density measured as a function of the noise source temperature and of the dilution refrigerator base temperature shown in Fig. 34(b) is in excellent agreement with the theory for the quantum efficiency of the Josephson mixer of $\boxed{\eta = 72\ \%}$.

5.6.3 *Calibration using a superconducting qubit as a spectrometer*

The quantum efficiency of a Josephson mixer has also been estimated during the experiment performed by Philippe Campagne-Ibarcq in our group [48] that has demon-

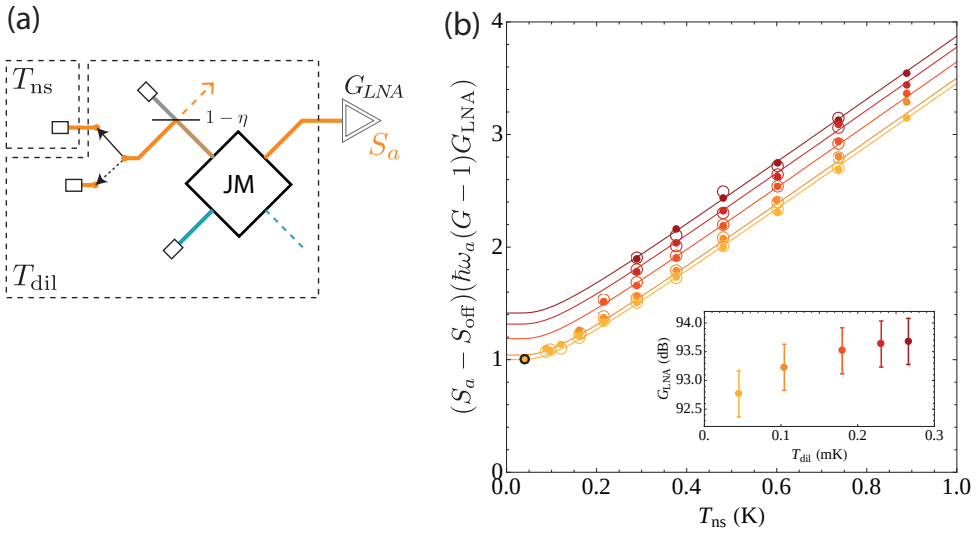

Figure 34: (a) Equivalent setup, all losses and inefficiencies are modeled by beam-splitters coupling the propagating modes of interest to a bath at dilution refrigerator temperature T_{dil}. (b) Dots: The measured power spectral density normalized following Eq. (116) as a function of noise source temperature $T_{\rm ns}$ for various values of the dilution refrigerator temperature $T_{\rm dil} = 45$ mK, 100 mK, 180 mK, 230 mK and 260 mK (represented by colors from yellow to red). Circles: same data for decreasing temperatures $T_{\rm ns}$ from one point to the next. Lines: theory using Eq. (116).

strated the stroboscopic feedback of a superconducting qubit enabling the stabilization of quantum trajectories. The Josephson mixer used in this experiment is centered on 7.748 GHz with 22dB of gain over 6 MHz dynamical bandwidth. Note that the bandwidth of the modes has been doubled for this experiment compared to $JM-C$.

The amplifier sits at the output of a superconducting 3D cavity, which is coupled to a superconducting qubit in the dispersive regime. It is possible to calibrate the occupation of the 3D cavity by measuring how much the field induces dephasing on the qubit. Indeed, in the dispersive regime, the resonance frequency of the cavity depends on the qubit state $\omega_{cav} = \omega^0_{cav} \pm \chi/2$. Here, the bandwidth κ of the cavity is larger than the dispersive shift χ. When a coherent pulse is sent through the cavity at ω^0_{cav}, the average field amplitudes corresponding to the two qubit states differ only by a phase shift (Fig. 35b). In that case, the pulse extracts information on the qubit at a rate given by $\kappa D^2/2$, where D is the distance between the two possible field amplitudes in the Fresnel space [62].

Since D^2 is simply related and proportional to the average photon number in the cavity, measuring the extra dephasing $\Gamma^{extra}_{\varphi} = \kappa D^2/2$ of the qubit as a function of field amplitude leads to a proper calibration of the number of photons in the cavity. Using this calibration, it was possible to infer the total amplification of the measurement setup from the 3D cavity. Then, by measuring the variance of the fluctuations for a coherent state in the cavity, it was possible to calculate the fraction of added noise on top of the original zero point fluctuations in the cavity. This allowed us to estimate a total efficiency of $\eta_{tot} = 0.67$. A large part of the inefficiency are attributed to losses

through the input port of the cavity, which were perfectly determined and unrelated to the Josephson mixer efficiency. In the end, the efficiency of the full detection setup from the output of the 3D cavity to the measurement apparatus was estimated to be $\eta = 0.82$. To my knowledge, this is the best quantum efficiency achieved to date on a circuit QED experiment with a parametric amplifier.

The distribution of a million measured amplitudes of the output field, when the qubit is prepared in state $|g\rangle$ or $|e\rangle$ with equal probability is shown in Fig. 35(c) and (d). In Fig. 35(c) the Josephson mixer is turned off. The measurement fidelity of the qubit state is low, its state cannot be discriminated in a single shot. In Fig. 35(d), the Josephson mixer is turned on, as a result a great enhancement of the measurement fidelity is observed. The qubit state can be discriminated in a single shot for a read-out amplitude of 1.6 photons integrated on 11 cavity bandwidths. Note that this qubit readout is both single-shot and QND (quantum non demolition).

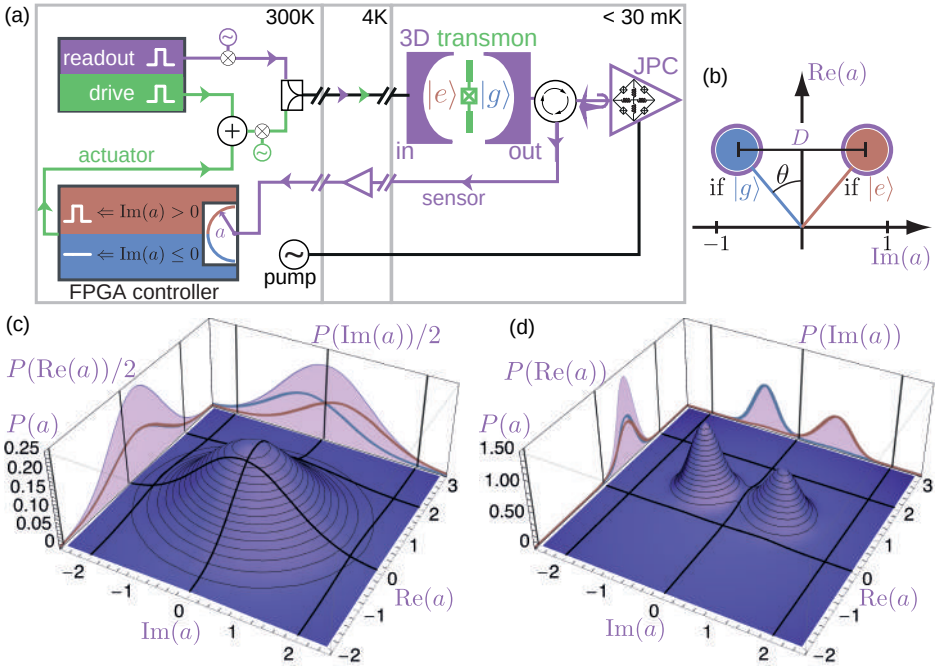

Figure 35: (a) Simplified setup of the feedback experiment detailed in [48] . (b) Phase acquired by the measurement pulse after its dispersive interaction with the qubit. (c),(d) Probability density with the Josephson mixer (c) off and (d) on, extracted from 10^6 measurement outcomes when the qubit is prepared in state $|g\rangle$ or $|e\rangle$ with equal probability. The axes are expressed in units of square root of photon numbers in the 3D cavity in the steady state. The halved probability density that corresponds to the preparation of $|g\rangle$ (respectively, $|e\rangle$) only is plotted in blue (orange), together with the projections along the real and imaginary axes. Turning the pump of the amplifier on as in (d) results in a great enhancement of the measurement fidelity, compared to the case without (c).

Using the gain-bandwith-power relations we have just established, I will show that it is possible to design a Josephson mixer with a dynamical bandwidth of 100 MHz for a 20dB-gain and 5 photons dynamic range per bandwidth with a central frequency around 7 GHz. Note that these performances seem to be the optimal performance achievable with the Josephson mixer technology [44].

In the following I will show that we have been able to implement a device close to such an optimal point.

5.7.1 *Design*

For simplicity, the optimal parameters have been derived in the case of an unshunted Josephson ring.

- **Quality factors**. If the gain is kept fixed, the dynamical bandwidth can be increased by decreasing both quality factors according to

$$\sqrt{G} \times \gamma = \frac{2}{\frac{1}{\kappa_a} + \frac{1}{\kappa_b}}. \tag{117}$$

  In order to reach 100 MHz at 20 dB-gain, we must fix $\kappa_a \sim \kappa_b \sim 2\pi \times 1$ GHz leading to quality factors $Q_a \sim Q_b \sim 7$.

- **Participation ratios**. The participation ratios can be increased to reach the high gains limit

$$\frac{1}{16}\xi_a \xi_b Q_a Q_b > 1. \tag{118}$$

  As a consequence, it constrains $\xi_a \sim \xi_b > 0.6$. In the standard implementation of the resonator, one would need to decrease the critical current of the junction to be able to reach the range $\xi_a \sim \xi_b \sim 0.6$. However, it would greatly affect the dynamical range of the amplifier.

- **Impedance**. In order to guarantee 5 photons dynamic range per bandwidth, the device must satisfy the following relation

$$\left(\frac{\alpha_{in}^2}{\gamma}\right)_{max} = \frac{1}{4\sqrt{G}} \frac{Z_Q}{Z_0} \frac{1}{(\xi_a^2 + \xi_a \xi_b + \xi_b^2)} = \frac{1}{43} \frac{Z_Q}{Z_0} \sim 5 \Rightarrow Z_0 \sim 5\ \Omega. \tag{119}$$

  Thus, in order to keep a good dynamic range, the characteristic impedance of the resonator must be greatly decreased. Or in other words, in order to keep junctions with a fairly high critical current, the resonator inductance must be decreased.

  Moreover, the pump depletion criterion for the unshunted Jospehson ring is fairly satisfied for this impedance.

$$\frac{|\alpha_{in}|^2}{\gamma} \sim 5 \ll \frac{1}{\sqrt{G}} \frac{1}{(\xi_a \xi_b)^{3/2} \xi_c} \frac{1}{Q_c \sqrt{Q_a Q_b}} \frac{Z_Q}{Z_0} \sim 80. \tag{120}$$

Importantly, such a low impedance is difficult to implement with conventional transmission line resonators. Lumped-element resonators are much more suited for this task. On one hand, the mode inductance is mostly ensured by the unshunted Josephson ring guarantying high participation ratios. It requires $L_a \sim L_b \sim Z_0/\omega_0 \sim 100$ nH leading to $I_0 \sim 4$ μA. On the other hand, the mode capacitance can be made of a large plate capacitor in the range $C_a \sim C_b \sim (Z_0\omega_0)^{-1} \sim 5$ pF.

- **Implementation of the coupling**. Given the impedance mismatch between a $Z_c = 50$ Ω transmission line and the $Z_0 = 5$ Ω impedance of the mode, there is no need for coupling capacitance. Indeed, the quality factor for galvanic coupling is directly given by $Q_a \sim Q_b \sim \dfrac{Z_c}{Z_0} \sim 10$ which is consistent with the architecture.

5.7.2 *Experimental realization*

We have fabricated a low-impedance lumped-element device targeting the above stated criterions. Schematics of the device is shown in Fig. 36(a). The modes of the Josephson mixer consist in the unshunted Josephson ring inductance in parallel with plate capacitors connected together on one ground plate.

A picture of the device is shown in Fig. 36(b). Its *in situ* characterization has enabled us to extract its main characteristics. The ring inductance is $L_{JR}(\varphi_{ext}) = 90 \text{ nH}/\cos(\varphi_{ext})$, corresponding to a critical current $I_c = 3.6$ μA. The wires connecting the ring to the capacitors provide a spurious geometric inductance of the order of 50 nH in series with the ring. The capacitors consists of large plate capacitors (large rectangles in Fig. 36(b)), the top and ground plates are made of aluminum and are separated by 200 nm of amorphous silicon-nitride dielectric leading to a capacitor of 3 pF for the a mode and 6 pF for the b mode.

5.7.3 *Gain and bandwidth performances*

The resonance frequency as a function of the magnetic flux is shown in Fig. 37(a) as expected from an unshunted Josephson ring, the dependence is 2π-periodic and hysteretical. The measured quality factors, shown in inset, going from 10 to 25 are larger than expected by the design, but consistent with the measured inductance and capacitance of the device. Therefore, the impedance of the mode is going from 5 to 2 Ω.

The gain as a function of frequency and pump power is presented in Fig. 37(b). In spite of quality factors being larger then expected, the dynamical bandwidth still reaches up to $\boxed{50 \text{ MHz}}$ for a 20 dB gain. Remarkably, the frequency tunability of the amplifier for a 20dB gain is as high as $\boxed{900 \text{ MHz}}$ thanks to the high participation ratios of the ring. Note that the larger flux biases are not necessarily stable due to the hysterical behavior.

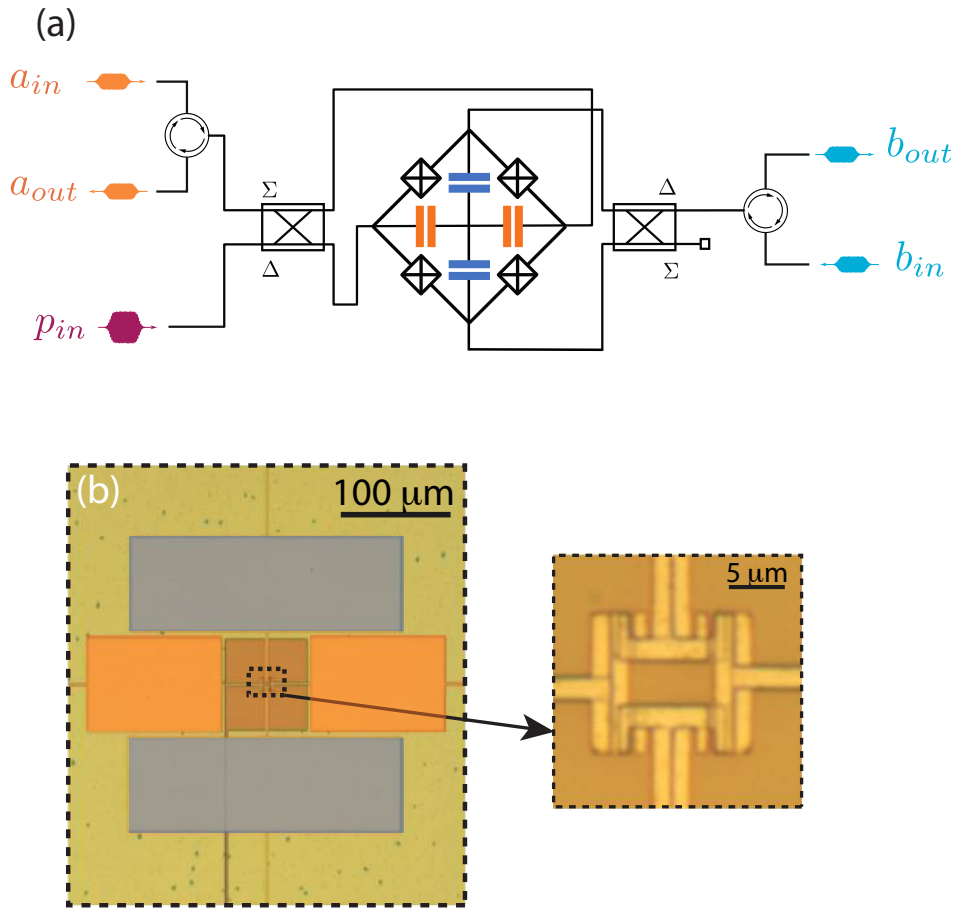

Figure 36: (a) Schematic of the experimental setup at base temperature ($T_{dil} = 50$ mK). The modes of the Josephson mixer consist in the unshunted Josephson ring inductance in parallel with plate capacitors connected to the ground. Modes a and b are addressed in reflection through the Δ ports of two hybrid couplers, the pump mode being fed through the Σ port. (b) Optical picture of the device showing the capacitors (left) and the Josephson junction ring (right).

5.7.4 *Quantum efficiency and dynamic range*

The calibration of the quantum efficiency of the lumped-element Josephson mixer is performed using a temperature-controlled load connected to the input of the amplifier similarly to the description in section 5.6.2. The noise measurement gives an absolute calibration of the gain of the low noise amplifying chain $G_{LNA} = 62.3$ dB. Moreover, the quantum efficiency can be extracted from the measurement shown in Fig. 38(a), leading to a quantum efficiency of $\boxed{\eta \sim 0.62}$. Note that the cross-over between quantum noise and thermal noise is not quantitatively reproduced by the noise data. Therefore, this measured quantum efficiency must be taken carefully.

The measurement of the 1 dB-compression is shown in Fig. 38(b). For $G = 21.4$ dB, we observe that the amplifier behaves linearly at low powers until it reaches the 1dB-compression point at an absolute power of $\boxed{P_{\mathrm{1dB}} = -112 \text{ dBm}}$ reaching the JRM. At 6.76 GHz and for a dynamical bandwidth of 50 MHz, this power corresponds to 4.5

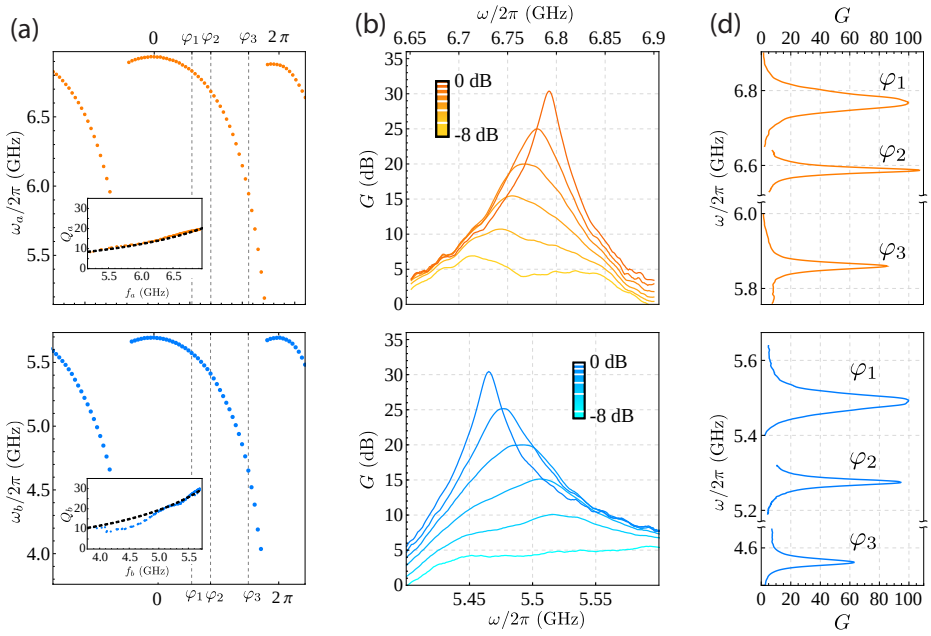

Figure 37: (a) Flux tunability of the resonant frequencies of resonators a and b (pump off). The dependence is 2π-periodic and hysteretical. The insets show the measured quality factors as a function of frequency. Dashed lines are the expected quality factors. (b) Gain in reflection at the flux φ_1 for a and b modes. The color bar indicates the pump power referred to the parametric self-oscillation threshold. The pump frequency is 12.26 GHz (c) Gain in reflection for a and b modes measured at the different fluxes labelled.

photons per dynamical bandwidth. Note that the dynamical range is remarkably high in absolute power compared to the transmission line resonator amplifiers ranging from -130 to -115 dBm. Such a high sustained power is consistent with the very low mode impedance ranging from 2 to 5 Ω.

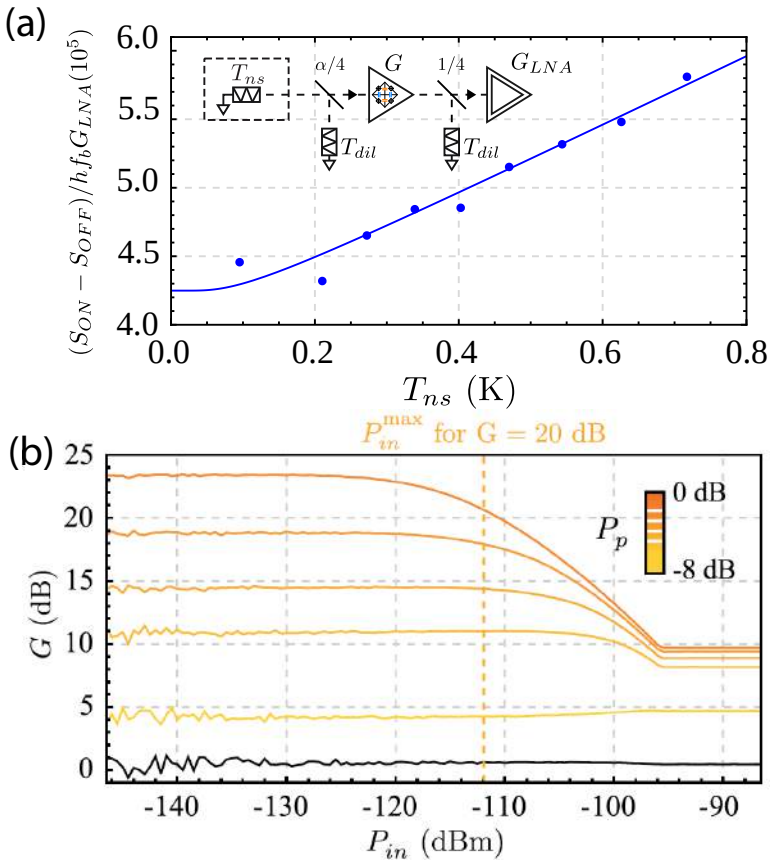

Figure 38: Difference between measured spectral densities out of resonator b, its input being connected to the noise source, as a function of T_{ns} when the pump is turned on (S_{ON}) and when the pump is turned off (S_{OFF}). The data are normalized by the energy of a quantum in resonator b and the gain G of the Josephson amplifier set to be approximately 32 dB. The inset shows a schematic of the measurement setup (note that we plugged -6 dB attenuators on the Δ ports of the hybrid couplers in order to suppress interferences occurring in the wiring which disturbed the effective impedance of the incoming line). (b) Output power P_{out} of the amplifier as a function of input power P_{out} measured at 5.47 GHz for different pump power (blue color scale), gain varying from 0 to 32 dB.

5.8 PERFORMANCE SUMMARY

	Need for cQED	Unshunted JRM	Shunted JRM	Low-impedance mixer
reference	[63]	[42] Yale	[39, 48] Paris	in prep. Paris
Resonator impedance		$\lambda/2$ Microstrip $\sim 50\ \Omega$	$\lambda/2$ Microstrip $\sim 50\ \Omega$	Lumped 2 to 5 Ω
Frequency	$5-12$ GHz	$6-8$ GHz	$6-9$ GHz	$4-7$ GHz
Gain	≥ 20 dB	≥ 20 dB	≥ 20 dB	≥ 20 dB
Q Efficiency η	~ 1	> 0.3 Th. L	0.3 TJ 0.72 Th. L 0.8 qubit	~ 0.62 Th. L
Bandwidth @20 dB	~ 10 MHz	11 MHz	~ 3 MHz ~ 10 MHz not shown	50 MHz
Dynamical range per DBW@20 dB	> 1 ph. per DBW	1 to 10 ph. per DBW	1 to 40 ph. per DBW	20 ph. per DBW
Dynamical range @20 dB	> -125 dBm	-130 to -115 dBm	-130 to -115 dBm	-112 dBm
Tunability @20 dB	> 100 MHz	60 MHz	400 MHz	900 MHz

Table 1: Summary of the characteristics of amplifiers based on Josephson mixers. The abbreviations 'Th. L' stands for Temperature controlled load, 'qubit' stands for measurement induced dephasing of a qubit in a cavity and 'TJ' stands for Voltage bias tunnel junction.

5.9 CONCLUSION

This work on parametric amplification gave birth to two new generations of nearly quantum limited phase preserving amplifiers. We have realized a practical widely tunable amplifier which can be fabricated in a single lithography and evaporation step. Its specifications overcome the requirements of circuit-QED experiments as summed up in the following table. Moreover, the amplifiers that I have designed and fabricated, have enabled us to perform various experiments of circuit QED in which I had the pleasure to take part. We performed the stabilization of superconducting qubit trajectories [48], observation of past and future interference in the fluorescence of qubit [64] or direct Wigner tomography of a non-classical field generated by quantum-Zeno dynamics (submitted).

On the other hand, the dynamics of three-wave mixing and parametric amplification sets various constraints on the physical parameters, which we have discussed here. By pushing these constraints to their limits, we have designed and fabricated a nearly optimal Josephson mixer. Indeed, taking advantage of the low impedance that can be achieved in lumped element circuits, we have succeeded in creating a phase-preserving amplifier that is close to the quantum limit, wide-band, has a high dynamical range and is widely tunable. However, the fabrication process of the device is more complex than the microstrip version, mainly due to the fabrication of large plate capacitors. The fabrication process can still be optimized and made simpler and more reliable. Importantly, the low-impedance amplifier could be used as a quantum limited preamplifier in other systems given that its specifications make it suitable for a wide range of experiments in the microwave domain and in mesoscopic physics.

The main results of this part are the following

- Successful realization of a practical state-of-the-art non-degenerate amplifier.
- Almost quantum limited as shown by three distinct noise calibration experiments in section 5.6

The main unpublished results of this part are the following

- An overview of the various kinds of amplifiers with their pictures in Fig. 28
- A list of crucial specifications to consider for circuit QED experiments in section 5.2
- Useful expressions leading to the dynamical range of the amplifier in Eqs. (108) and (110)
- Design, realization and measurement of an optimal Josephson mixer as a wide-band amplifier with large dynamical range in section 5.7

Part III

ENTANGLEMENT GENERATION AND WITNESS

6

ENTANGLEMENT WITH CONTINUOUS VARIABLES

As a quantum limited amplifier, the Josephson mixer leaves a non-classical imprint on its environment that persists far enough to be observed and tested experimentally. In parametric amplification mode, the circuit actually induces correlations between propagating modes that cannot be explained classically. Highly entangled microwave radiation arises spontaneously from parametric-down conversion.

In this part, I will demonstrate that our circuit generates Einstein-Podolsky-Rosen entangled radiation starting from vacuum. The state is distributed over two separated transmission lines and experiences a non-local path. The witness of the entanglement is performed with a second Josephson mixer. This second circuit recombines the propagating state and enables us to probe the quantumness of correlations at its inputs. Remarkably, the combination of two mixers forms unique quantum circuit, performing non-classical interferometry.

6.1 ENTANGLEMENT, A PURELY QUANTUM RESOURCE

Entanglement is "the characteristic trait of quantum mechanics", as Schrödinger phrased it in the early days of quantum theory in 1935 [65]. Indeed, entanglement is a purely quantum information resource. The concept of entanglement refers to the fact that in a composite system, ignorance about the part is always compatible with the maximal knowledge about the whole [66, 67].

To illustrate this general principle, let's consider the simplest composite system which consists of two qubits. The system can be prepared in a maximally entangled state $(|00\rangle + |11\rangle)/\sqrt{2}$. In principle, such a Bell state can be prepared from the vacuum with a unitary evolution, a deterministic and reversible operation. This implies that the Bell state is a pure state, we get the maximal knowledge about the whole state, in other word the system entropy is zero.

One can shared the Bell state between Alice and Bob. From their subjective point of view, Alice and Bob's states seems to be random. Indeed, by discarding Bob, Alice gets a maximally mixed state, $\rho_a = \mathrm{Tr}_b(\rho_{ab}) = (|0\rangle\langle 0| + |1\rangle\langle 1|)/2$ with an entropy corresponding to one bit.

In a sense, the quantum information about the state is hidden in the non-local correlations between the sub-parts. A measure of this entanglement consists in quantifying the mutual information $E(\rho_{ab}) = \frac{1}{2}\left[S(\rho_a) + S(\rho_b) - S(\rho_{ab})\right]$ of Alice and Bob where $S(\rho) = -\mathrm{Tr}\left[\rho \log_2(\rho)\right]$ is the Von Neumann entropy. It compares the entropy of the whole to the entropy about the individual parts. It measures the information hidden in the entanglement which is expressed in term of entangled-bits[1]. In this case, Alice and Bob share one entangled bit.

1 By definition, one entangled-bit is the amount of entanglement of a Bell state, hence the factor $1/2$ in the mutual information $(1e - bit = 2sharedbits)$

6.2 PURIFICATION PRINCIPLE

The fact that ignorance about the part is always compatible with the maximal knowledge about the whole has been highlighted as the purification principle in the informational derivation of quantum theory by Chiribella and coworkers in [67]. It states that "every mixed state arises in an essentially unique way by discarding one component of a compound system in a pure state." [68]

In such a framework, quantum theory appears to be the only information theory where truncated knowledge about our local environment (in a highly mixed state) is still compatible with a global picture where all processes are pure and reversible. In particular, the increase of entropy during a thermal equilibration required by the second principle can be translated in term of the increase of entanglement among parts of a system that remains itself pure [69].

Note that in this derivation, the quantum theory differs from a classical theory of information by the purification principle only. It is equivalent to a law of conservation of information according to which information can never be destroyed but can only be discarded.

6.3 QUANTUM INFORMATION WITH CONTINUOUS-VARIABLE

Instead of using qubit registers to encode entangled states such as Bell states, it is possible to use continuous variables. Quantum information can be encoded in variables whose spectrum is continuous such as position and momentum of a particle in a trap, quadratures of an electromagnetic mode (propagating or not) or the polarization of a bright light beam and other implementations of the harmonic oscillator. It is important to note that all quantum information protocols based on qubits have their counterparts with continuous variables [70, 71, 72, 73, 74, 75, 36, 76, 77].

The quadratures of electromagnetic modes described as Shannon wavelet in section A.5 are analogue to position and momentum of particles up to a scaling factor. Let us define the quadrature of the field as

$$\begin{aligned} X_k &= \mathrm{Re}(a_k) = \frac{a_k + a_k^\dagger}{2}, \\ P_k &= \mathrm{Im}(a_k) = \frac{a_k - a_k^\dagger}{2i}. \end{aligned} \tag{121}$$

These physical systems are then equivalent from the quantum information viewpoint since the quadratures X_k and P_k are dimensionless hermitian observables, which verify the canonical commutation relation similarly to the position and momentum of a particle.

$$[X_k, P_{k'}] = \frac{i}{2}\delta_{k,k'}. \tag{122}$$

The Hamiltonian of propagating modes then reads

$$H = \sum_k \hbar\omega_k (a_k^\dagger a_k + 1/2) = \sum_k \hbar\omega_k (X_k^2 + P_k^2). \tag{123}$$

Thus, the stationary states of the Hamiltonian are Fock states $\{|n\rangle_k\}$ such that $a_k|n\rangle_k = \sqrt{n}|n-1\rangle_k$

6.4.1 *Two-mode squeezing*

The Josephson mixer is a remarkably versatile tool for information processing with continuous variables. In particular, it can act as an entanglement source for microwave fields.

Indeed, the interaction Hamiltonian realized by the Josephson mixer when the pump is applied at the sum frequency $\omega_a + \omega_b$ comes down to the so-called Parametric-Down conversion Hamiltonian. This Hamiltonian corresponds to the coherent creation and annihilation of twin-photons in two spatially separated modes a and b when the pump mode p is driven with a coherent state,

$$H_{int} = \hbar\chi(pa^\dagger b^\dagger + p^* ab). \tag{124}$$

In chapter 5.1.1, using the quantum Langevin equation, we have derived the scattering relation between input and outputs associated with this interaction Hamiltonian. Here, we will describe the transformation of incoming wavelets $a_{in,k}$ and $b_{in,k}$ into outgoing wavelets $a_{out,k}$ and $b_{out,k}$ using a unitary operator (Fig. 39). This is the two mode squeezing operator defined as

$$\begin{aligned} a_{out,k} &= S(r,\phi)^\dagger a_{in,k} S(r,\phi), \\ b^\dagger_{out,k} &= S(r,\phi)^\dagger b^\dagger_{in,k} S(r,\phi). \end{aligned} \tag{125}$$

Following the form of the interaction Hamiltonian, it reads

$$\boxed{S(r,\phi) = e^{re^{i\phi}a^\dagger_{in,k}b^\dagger_{in,k} - re^{-i\phi}a_{in,k}b_{in,k}}}. \tag{126}$$

with $re^{i\phi}$ the squeezing parameter. Note that for sake of simplicity, we will drop the k subscript labeling the propagating mode.

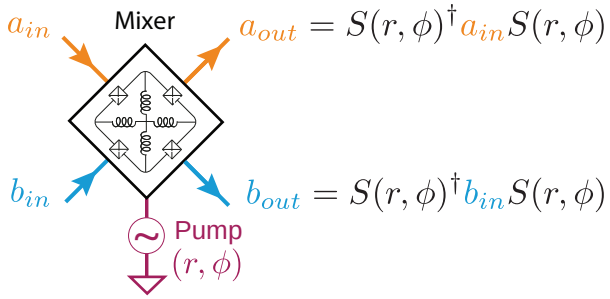

Figure 39: The Josephson mixer is described in term of input/ouput related by the two mode squeezing operator

The squeezing operator can be factorized in the normal order[2] using the disentangling theorem [78],

$$S(r,\phi) = e^{e^{i\phi}\tanh(r)a^\dagger_{in}b^\dagger_{in}} e^{-\log(\cosh(r))(a^\dagger_{in}a_{in} + b^\dagger_{in}b_{in} + 1)} e^{-e^{-i\phi}\tanh(r)a_{in}b_{in}}. \tag{127}$$

2 The normal order is such that all creation operators are put to the left of all annihilation operators in a product using commutation relation.

The normally ordered form enables us to compute analytically the evolution of propagating operators as well as state evolution.

It leads to a linear scattering relation between propagating modes

$$\boxed{\begin{array}{rclcrcl} a_{out} & = & S(r,\phi)^\dagger a_{in} S(r,\phi) & = & \cosh(r) a_{in} & + & e^{i\phi}\sinh(r) b_{in}^\dagger \\ b_{out}^\dagger & = & S(r,\phi)^\dagger b_{in}^\dagger S(r,\phi) & = & e^{-i\phi}\sinh(r) a_{in} & + & \cosh(r) b_{in}^\dagger \end{array}} \tag{128}$$

The scattering relation is identical to the one obtained with the quantum Langevin equation in the previous part in Eq. (98). Therefore, the squeezing parameter r and the phase ϕ can be identified to the amplitude gain $\sqrt{G}$ of the parametric amplifier and to the pump phase through

$$\begin{array}{rcl} \cosh(r) & = & \sqrt{G} = \dfrac{\kappa_a\kappa_b + 4\chi^2|p|^2}{\kappa_a\kappa_b - 4\chi^2|p|^2}, \\ \phi & = & \mathrm{Arg}(p). \end{array} \tag{129}$$

Moreover, the two-mode squeezed vacuum state generated by the mixer can be determined by applying the squeezing operator to the vacuum.

$$\boxed{|\mathrm{Sq}(r,\phi)\rangle = S(r,\phi)|0\rangle_{a_{in}}|0\rangle_{b_{in}} = \cosh(r)^{-1}\sum_{n=0}^{\infty} e^{in\phi}\tanh(r)^n |n\rangle_{a_{out}}|n\rangle_{b_{out}}}. \tag{130}$$

The excitations in modes a and b are generated coherently from vacuum, then the resulting state consists of a superposition of twin Fock states which is highly entangled.

Note that for a squeezing parameter going to infinity, the squeezed state corresponds to a balanced superposition of all twin Fock states. This is the direct extension of Bell states for continuous variables. However, such a state is not physical since its energy goes to infinity as well. Indeed, the average photon number in each mode is related to the squeezing parameter by

$$\bar{n} = \langle \mathrm{Sq}(r)|a_{out}^\dagger a_{out}|\mathrm{Sq}(r)\rangle = \sinh(r)^2 = \langle \mathrm{Sq}(r)|b_{out}^\dagger b_{out}|\mathrm{Sq}(r)\rangle. \tag{131}$$

To get a better physical hint, we can rewrite the squeezed state as a function of the average photon number

$$|\mathrm{Sq}(\bar{n},\phi)\rangle = \frac{1}{\sqrt{\bar{n}+1}}\sum_{k=0}^{\infty} e^{ik\phi}\left(1+\frac{1}{\bar{n}}\right)^{-\frac{k}{2}} |k\rangle_{a_{out}}|k\rangle_{b_{out}} \equiv |EPR\rangle. \tag{132}$$

Note that when a two-mode squeezed vacuum state is generated on spatially separated modes then it is the physical realization of the so-called EPR state named after the Einstein-Podolsky-Rosen though experiment that will be briefly described in section 6.4.6.

6.4.2 *EPR state as a maximally entangled state*

Electromagnetic modes live on an equally spaced ladder of energy levels, their Hilbert space is much larger than in the case of two level systems. Therefore they can host

significantly more quantum information and in particular more entanglement. Remarkably, for a given amount of energy, the two-mode squeezed state is actually maximally entangled.

It is possible to quantify the strength of the entanglement between Alice and Bob similarly to the Bell state. As long as the state is pure, the whole system is perfectly known and its entropy is zero. How much ignorance is there about the parts when measured individually? If Alice discards the information about Bob, the resulting state is

$$\rho_a = \mathrm{Tr}_b(|\mathrm{Sq}(\bar{n})\rangle\langle\mathrm{Sq}(\bar{n})|) = \frac{1}{\cosh(r)^2}\sum_{n=0}^{\infty}\tanh(r)^{2n}|n\rangle_a\langle n|_a. \tag{133}$$

It corresponds to a thermal state as it follows the Boltzmann distribution of the energy with an average photon number $\bar{n}$. It can be written under the more explicit form

$$\rho_a = \frac{1}{Z}\sum_{n=0}^{\infty} e^{-n\frac{\hbar\omega}{kT}}|n\rangle_a\langle n|_a, \tag{134}$$

where the effective temperature of individual modes is given by $\frac{kT}{\hbar\omega} = \frac{1}{\log(1+\frac{1}{\bar{n}})} \approx \bar{n}$ for $\bar{n} \gg 1$. Crucially, the thermal state is the maximally mixed state for a given energy, so that the two-mode squeezed vacuum state is maximally entangled.

A measure of entanglement for a pure state is directly given by the mutual information $E(\rho_a) = \frac{1}{2}(S(\rho_a) + S(\rho_b) - S(\rho_{ab}))$. Note that for continuous variable, the Von Neumann entropy is defined with the natural logarithmic as opposed to the qubit case where the logarithm in base 2 is used [70]. Therefore, entanglement strength reads

$$\begin{aligned} E(\rho_a) &= \frac{1}{2}\left[-\mathrm{Tr}(\rho_a\log\rho_a) - \mathrm{Tr}(\rho_b\log\rho_b) + 0\right] \\ &= \cosh(r)^2\log\cosh(r)^2 - \sinh(r)^2\log\sinh(r)^2 \\ &\underset{e^r\gg 1}{\rightarrow} 2r = \log(\bar{n}). \end{aligned} \tag{135}$$

Interestingly, the amount of entanglement encoded in an EPR state can be in principle very large. However, the decoherence due to photon loss rises linearly with the average photon number whereas the entanglement increase in a logarithmic way. Hence a trade off between the sensitivity to decoherence and amount of entanglement must be found.

6.4.3 *EPR state as a Gaussian state*

A quantum state can be equivalently described by its quasi probability distribution in phase-space as the Wigner distribution [1]. The Gaussian states are states whose Wigner representation is a Gaussian distribution. Hence, their general form reads

$$W(\boldsymbol{\xi}) = \frac{4}{\pi^2\sqrt{det\boldsymbol{V}}}\exp\left[-2\boldsymbol{\xi}\boldsymbol{V}^{-1}\boldsymbol{\xi}^T\right], \tag{136}$$

where $\boldsymbol{\xi} = (X_a, P_a, X_b, P_b)$ for a two-mode state. For the sake of simplicity, all states are displaced such that their mean is set to zero $\langle\xi\rangle = 0$.

The covariance matrix $\boldsymbol{V}$ is a 4×4 matrix, which encodes the second moment of the Wigner function corresponding to the second moment of the symmetrized operators

$$V_{i,j} = 4 \int \xi_i \xi_j W(\boldsymbol{\xi}) \mathrm{d}^4 \boldsymbol{\xi} = 2\langle \xi_i \xi_j + \xi_j \xi_i \rangle. \tag{137}$$

Remarkably, Gaussian states are completely determined by their covariance matrix (and their mean value sets to zero here). Note that the definition is chosen such that vacuum state corresponds to a unity covariance matrix.
A key feature is that the set of Gaussian state is invariant under Gaussian operations which are any unitary operation arising from a Hamiltonian that is bilinear in the mode operators. For instance, the Hamiltonian of one-mode squeezing ($a^\dagger a^\dagger + aa$), two mode squeezing ($a^\dagger b^\dagger + ab$), beam-splitting ($a^\dagger b + ab^\dagger$), phase shift ($a^\dagger a$) or displacement ($a + a^\dagger$) result in Gaussian operations. Therefore, **an EPR state is Gaussian** since it corresponds to the Gaussian transformation of vacuum which is Gaussian. Note that an important consequence of the bilinear character of Gaussian operation is that scattering relations between the input and output operators are always linear.

6.4.4 *Representation of the EPR quantum correlations*

EPR states are maximally entangled states for continuous variable. How can we characterize such an entanglement? In which measurement basis?

Obviously, the state is perfectly correlated on the photon number basis. However, a more natural way to characterize Gaussian states is to explore correlations in the quadratures phase space (X_a, P_a, X_b, P_b) through their covariance matrices. These correlations are accessible with Gaussian measurements whose outcome are linear in the field operators, such as homodyne detection that measures one quadrature at a time or heterodyne detection that measures both quadratures at a time (see section 4.5). Note that these Gaussian measurements are naturally performed with phase-sensitive or phase-preserving quantum limited amplifiers (see section 4.5).

In order to reveal the quantum correlations in phase space, one can link the variance of the output state to the variance of the vacuum state at the input by rewriting the scattering relation as

$$\begin{aligned} a_{out} + e^{i\phi} b^\dagger_{out} &= e^r (a_{in} + e^{i\phi} b^\dagger_{in}), \\ a_{out} - e^{i\phi} b^\dagger_{out} &= e^{-r} (a_{in} - e^{i\phi} b^\dagger_{in}). \end{aligned} \tag{138}$$

The scattering relation can be expressed as a function of the quadrature of the a and b modes assuming that $\phi = 0$ for clarity

$$\begin{aligned} X_a^{out} \pm X_b^{out} &= e^{\pm r} (X_a^{in} \pm X_b^{in}), \\ P_a^{out} \mp P_b^{out} &= e^{\pm r} (P_a^{in} \mp P_b^{in}). \end{aligned} \tag{139}$$

Starting from vacuum, the covariance of the EPR state is thus given by

$$\begin{aligned} \langle (X_a^{out} \pm X_b^{out})^2 \rangle &= \tfrac{1}{2} e^{\pm 2r}, \\ \langle (P_a^{out} \mp P_b^{out})^2 \rangle &= \tfrac{1}{2} e^{\pm 2r}. \end{aligned} \tag{140}$$

The squeezed nature of the state appears clearly. The two outgoing modes a and b are indeed highly correlated in position and anti-correlated in momentum.

Therefore, the Wigner representation of Gaussian EPR states can be entirely described by

$$W(x_a, p_a, x_b, p_b) = \frac{4}{\pi^2} \exp\left\{-e^{-2r}\left[(x_a + x_b)^2 + (p_a - p_b)^2\right]\right\} \times \exp\left\{-e^{2r}\left[(x_a - x_b)^2 + (p_a + p_b)^2\right]\right\} \quad (141)$$

and the covariance matrix of EPR states in the basis $\boldsymbol{\xi} = (X_a, P_a, X_b, P_b)$ reads

$$\boldsymbol{V} = \begin{pmatrix} \cosh(2r) & 0 & \sinh(2r) & 0 \\ 0 & \cosh(2r) & 0 & -\sinh(2r) \\ \sinh(2r) & 0 & \cosh(2r) & 0 \\ 0 & -\sinh(2r) & 0 & \cosh(2r) \end{pmatrix}. \quad (142)$$

6.4.5 *Marginal distribution of the EPR state*

The Wigner representation of the EPR state is four dimensional. Yet, it's possible to get a grasp on its structure by looking at its marginal distribution in various subspaces.

The marginal distributions of the Wigner function in position (x_a, x_b) and momentum (p_a, p_b) are Gaussian

$$W_{xx}(x_a, x_b) = \int\int \mathrm{d}p_a \mathrm{d}p_b W(x_a, p_a, x_b, p_b) = \frac{2}{\pi} \exp[-e^{-2r}(x_a + x_b)^2 - e^{2r}(x_a - x_b)^2)] \quad (143)$$

and

$$W_{pp}(p_a, p_b) = \int\int \mathrm{d}x_a \mathrm{d}x_b W(x_a, p_a, x_b, p_b) = \frac{2}{\pi} \exp[-e^{-2r}(p_a - p_b)^2 - e^{2r}(p_a + p_b)^2)]. \quad (144)$$

As presented on Fig. 40, their contours are ellipses revealing the squeezing of the two-mode correlations beyond vacuum fluctuations.

In contrast, there is no evidence of squeezing if one looks at a single mode marginal distribution in phase space (x_a, p_a) or (x_b, p_b). As expected from Eq. (134), it corresponds to a thermal state containing $\bar{n} = \sinh(r)^2$ photons in each mode on average.

With our choice of phase for the squeezing parameter, there is no correlation between x_a and p_b nor between x_b and p_a. The marginal distribution of the Wigner function is then identical in all sub-spaces $\{(x_a, p_a), (x_b, p_b), (x_a, p_b), (x_b, p_a)\}$

$$W_{xp}(u, v) = \frac{1}{\pi(\bar{n} + 1/2)} \exp\left(-\frac{u^2 + v^2}{\bar{n} + 1/2}\right). \quad (145)$$

Crucially, high intermode correlations of position and momentum are obtained at the expense of an increased uncertainty on the position and momentum of single modes, as revealed by these apparent thermal fluctuations.

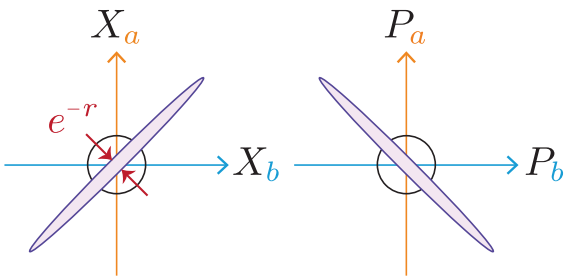

Figure 40: Contour of the marginal distribution of the Wigner representation of the gaussian EPR state for an average photon number of $\bar{n} = \sinh(r)^2 = 4$. The quadratures (x_a, x_b) are correlated beyond zero-point fluctuations represented with a black circle. The quadrature (p_a, p_b) are anti-correlated beyond zero-point fluctuations. Those quadrature pairs are squeezed by a factor e^r.

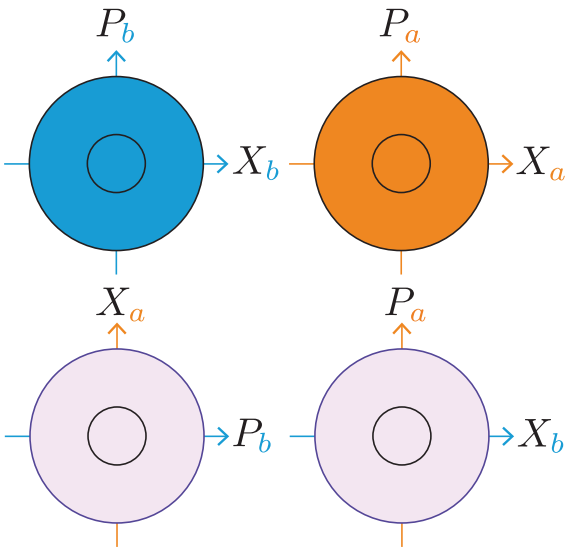

Figure 41: Contour of the marginal distribution of the Wigner representation of the gaussian EPR state for an average photon number of $\bar{n} = \sinh(r)^2 = 4$. When the modes are taken individually, their quadratures (x_a, p_a) and (x_b, p_b) exhibit uncorrelated thermal fluctuations above the zero-point fluctuations represented with a black circle. The quadrature pairs (x_a, p_b) and (x_b, p_a) present identical uncorrelated thermal fluctuations.

Actually, the fundamental reason for such a trade-off originates from Liouville's theorem which states that the volume of the quantum state in phase space must be preserved under a unitary transformation. Thus a squeezing of the fluctuations in subspaces (x_a, x_b) and (p_a, p_b) implies an increase of the fluctuation in other subspaces.

6.4.6 *Link with the original EPR state*

The counterintuitive consequences of entanglement have been highlighted for the first time by Einstein, Podolsky and Rosen (EPR) in 1935 in the form of a thought experi-

ment describing two distant particles perfectly correlated with respect of their positions and momenta [14].

The original EPR Wigner function of the perfectly correlated state can be written as

$$W(x_a, p_a, x_b, p_b) \propto \delta(x_a - x_b)\delta(p_a + p_b). \tag{146}$$

Although this state is unphysical since its energy is infinite, it can be approached by the two-mode squeezed state for large squeezing parameter $r \gg 1$ leading to strongly squeezed quantum correlation between position and momentum as previously mentioned. The most important property of the original EPR states sits in its non-local character. Therefore, a two-mode squeezed vacuum state can be assimilated as an EPR state when its modes are spatially separated.

6.5 MEASURES AND WITNESS OF CONTINUOUS-VARIABLE ENTANGLEMENT

As shown in the previous section, a Josephson mixer is expected to produce an EPR state on two spatially separated modes. However, these quantum states are very fragile and suffer from decoherence mainly due to energy loss during their propagation or possibly from pure dephasing due to pump phase noise for instance.

The decoherence is modeled by the interaction of the mode a or b with their environment. Indeed, the state under study gets entangled with an unmonitored degree of freedom that is finally traced out which leads to an information leak, decoherence. Note that even if one succeed to monitor the extra-mode, the left bipartite entanglement shared between a and b is necessarily degraded, this property is know as monogamy of entanglement [79].

We would like to decide whether or not a state is entangled even in presence of decoherence.

6.5.1 *Entanglement witness*

For a pure state, the measure of entanglement encoded in a bipartite system E(AB) is essentially unique. It coincides with the mutual information through $I(AB) = S(A) + S(B) - S(AB) = 2E(AB)$. For mixed states, the measure of entanglement is not unique anymore and it does not coincide anymore with the mutual information $E(AB) \neq \frac{1}{2}I(AB)$. It is non-trivial to determine whether or not a mixed state is entangled even knowing its density matrix.

Indeed, it exists in classical physics two equivalent definitions of the mutual information, $I(AB) = S(A) + S(B) - S(AB)$ and $J(A|B) = S(A) - S(A|B)$. $S(A|B)$ defines the conditional entropy that quantifies the maximal information one can get on A by performing an optimum set of measurement on B [80]. Following Bayes' rule, these measures of mutual information coincide by definition for a classical state.

On the contrary, they don't coincide for non-classical states. The difference between these quantities is defined as the discord $D(A|B) = I(AB) - J(A|B)$ and is always zero for classical states. Hence, discord is the actual measure of non-classical correlation. In particular, an entangled state has always a non-zero discord but it is not a sufficient condition.

Indeed, a bipartite non-entangled state ρ_{ab} at the input can be described by a statistical mixture of separable pure states $\rho_{a,i} \otimes \rho_{b,i}$ such as

$$\rho_{ab} = \sum_i p_i \rho_{a,i} \otimes \rho_{b,i}. \tag{147}$$

Remarkably, for a mixed state, the separability of a quantum state doesn't imply that its discord is zero. As a consequence, it exists a class of separable mixed state that are neither classical nor entangled. Amazingly, discordant correlation has only been discovered in 2001 by Ollivier and Zurek [80] and simultaneously by Henderson and Vedral [81].

Therefore, the nature of correlations of mixed states can be decomposed in three contributions: Classical correlations and Discordant correlations and Entanglement. We illustrate these quantities on a pair of qubits.

- No correlation

  A state without correlation can be described as

  $$\rho_{ab} = \frac{1}{4}\left(|00\rangle\langle 00| + |11\rangle\langle 11| + |10\rangle\langle 10| + |01\rangle\langle 01|\right) \tag{148}$$

  therefore the mutual information expressed in bits vanishes $I(AB) = 1 + 1 - 2 = 0$.

- Classical correlations

  A state encoding classical information only has a positive mutual information but a zero discord. Two classically correlated bits shared between Alice and Bob can be represented as

  $$\rho_{ab} = \frac{1}{2}\left(|00\rangle\langle 00| + |11\rangle\langle 11|\right) \tag{149}$$

  for which the measurement of 0 and 1 are perfectly correlated between Alice and Bob in this basis only. This state got $I(AB) = 1 + 1 - 1 = 1$ bit of mutual information which is classical since its discord is zero $D(A|B) = D(B|A) = 0$.

- Discordant correlations

  Discord highlights subtle quantum correlations which are neither classical correlation nor entanglement but arise from the probabilistic structure of the statistical mixture. Discord can appear in a separable mixed state such as [82]

  $$\rho_{ab} = \frac{1}{4}\left(|00\rangle\langle 00| + |11\rangle\langle 11| + |+0\rangle\langle +0| + |+1\rangle\langle +1|\right) \tag{150}$$

  where $|+\rangle = 1/\sqrt{2}(|0\rangle + |1\rangle)$.

Such a state is separable i.e. not entangled. However, it is not classical either since its discord is non-zero $D(B|A) = 0.20$ [82]. Note that the measure of discord isn't symmetric with respect to Alice and Bob. In this case, we have $D(A|B) = 0$.

Remarkably, this very peculiar quantity can be used as a resource for quantum information processing such as quantum illumination [83]. Note that contrary to entanglement, which is difficult to generate and preserve, discord is non-zero for almost every mixed state [84] and contradicts the idea that quantum effects are fragile.

- Entanglement

  An entangled state is always described with a non-separable density matrix. When pure, its mutual information is a unique measure of entanglement, in particular it coincides with the discord $E(AB) = \frac{1}{2}I(AB) = D(A|B) = D(B|A)$.

  For instance, the Bell state is a pure maximally entangled state.

$$\begin{aligned} \rho_{ab} &= \tfrac{1}{2}\left(|00\rangle + |11\rangle\right)\left(\langle 00| + \langle 11|\right) \\ &= \tfrac{1}{2}\left(|00\rangle\langle 00| + |11\rangle\langle 11| + |11\rangle\langle 00| + |00\rangle\langle 11|\right) \\ &= \tfrac{1}{2}\left(|{+}{+}\rangle\langle{+}{+}| + |{-}{-}\rangle\langle{-}{-}| + |{+}{+}\rangle\langle{-}{-}| + |{-}{-}\rangle\langle{+}{+}|\right) \end{aligned} \tag{151}$$

  where $|\pm\rangle = 1/\sqrt{2}(|0\rangle \pm |1\rangle)$. As a pure state, the entanglement measure gives $E(AB) = \frac{1}{2}I(AB) = \frac{1}{2} + \frac{1}{2} - 0$ ebits. Note that perfect correlations between a and b don't depend on the choice of basis.

The fact that separable mixed states can exhibit quantum correlations makes it difficult to define a measure of entanglement. It is however possible to identify entanglement through two criteria, violation of local realism using a Bell-like inequality or demonstration of the inseparable character of a mixed state.

Measures of entanglement for mixed states are based on such criteria such as the negativity, which quantifies the non-separable character of states with the positive partial transpose (PPT) criterion. Note that the PPT criterion and negativity are derived for Gaussian state in term of the covariance matrix in appendix B.1. However, all measures are not equivalent. In particular, they don't witness all types of entanglement. Therefore, one must use the right witness of entanglement depending on the state under study.

6.6 JOSEPHSON MIXER AS AN ENTANGLEMENT WITNESS

An entanglement witness uses measurement outcomes to demonstrate whether a quantum state belonging to a certain class is entangled. In this section, I will show that this task can be implemented coherently by the Josephson Mixer used as a witnessing quantum circuit.

6.6.1 *Coherent recombination of modes*

The Josephson mixer performs a linear coherent combination of the two modes at its inputs. Contrarily to passive component such as beam splitters, the frequency conversion performed by the Josephson mixer leaves an imprint of the pump phase ϕ as an extra phase offset in the recombination, which will be an essential parameter of the witness. In order to benefit from the sensitivity increase of quantum limited amplification, it is operated in amplification mode ($\omega_p = \omega_a + \omega_b$). Thus the coherent interferences resulting from the mode combination are amplified by an amplitude gain $\sqrt{G} = \cosh(r)$.

The output mode is expressed as a function of the input modes using the scattering relation described previously in Eq.(128)

$$a_{out} = S(r,\phi)^\dagger a_{in} S(r,\phi) = \cosh(r) a_{in} + e^{i\phi} \sinh(r) b_{in}^\dagger. \tag{152}$$

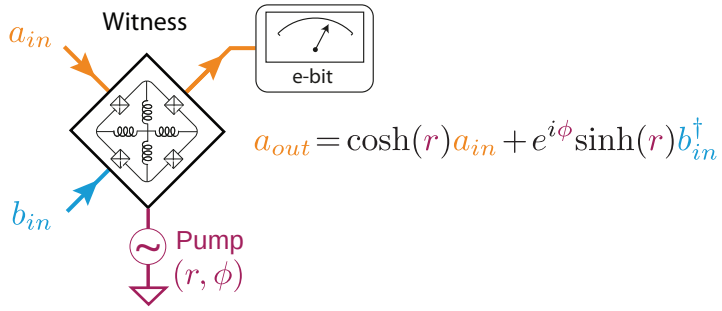

Figure 42: The witness of entanglement consists in a quantum circuit recombining coherently the modes a_{in} and b_{in} into the output mode a_{out}. This circuit is implemented by the Josephson mixer in amplification mode.

6.6.2 *Field amplitude interferences*

First, we only consider the average value of the field amplitudes. In this case, the scattering relation reads

$$\langle a_{out} \rangle = \cosh(r) \langle a_{in} \rangle + e^{i\phi} \sinh(r) \langle b_{in} \rangle^*. \tag{153}$$

Therefore, when properly choosing the fields incoming on the a and b ports such that $\langle a_{in} \rangle = \tanh(r) \langle b_{in} \rangle^* \approx \langle b_{in} \rangle^*$, destructive interferences between incoming fields cancel the output field on a for a given phase ϕ. This effect was advertised in Ref. [85] as an anti-laser in the optical domain.

Experimental measurement of this interference effect are shown in Fig. 44. A Josephson mixer set at a gain $\cosh(r)^2 = 10$ dB recombines two equal amplitude signals[3]. As expected from the interference term in Eq. (153), the output signal amplitude nearly

3 In practice, the condition on the amplitude was ensured by using a second Josephson mixer at the input.

cancels for a pump phase $\phi = \pi$. Recently, Schackert and coworkers have investigated the energy conservation involved in this signal cancellation by measuring the extra energy found in the output of the pump mode [86].

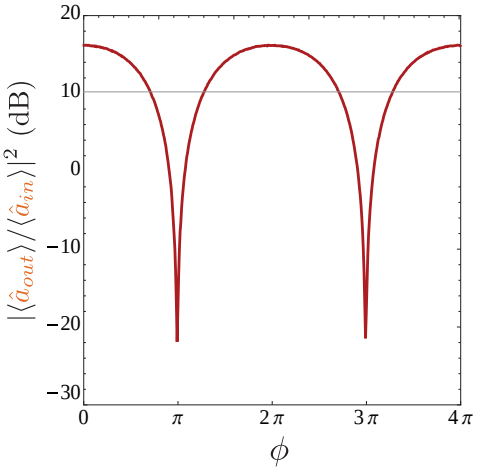

Figure 43: Measured amplitude $|\langle a_{out} \rangle|^2$ (normalized by $|\langle a_{in} \rangle|^2$) while the input fields are set to $\langle a_{in} \rangle = \tanh(r)\langle b_{in} \rangle \approx \langle b_{in} \rangle$ as a function of pump phase ϕ for a Josephson Mixer gain $\cosh(r)^2 = 10$ dB. The solid grey line corresponds to the case where $\langle b_{in} \rangle = 0$.

Crucially, the destructive interferences only concern the mean value of the fields but not their fluctuations. In fact, when two non-entangled fields destructively interfere with the Josephson mixer, their average values cancel but their fluctuations are on the contrary amplified by the gain of the mixer since their fluctuations are not correlated. Our entanglement witness uses the reciprocal argument by measuring the interferences of quantum fluctuations.

6.6.3 *Interference of fluctuations as an entanglement witness*

What is the magnitude of the fluctuations resulting from the coherent recombination of a and b modes? For sake of simplicity and without loss of generality, the average value of the fields can always be set to zero with a local displacement, hence we consider the case where $\langle a_{in} \rangle = \langle b_{in} \rangle = 0$ leading to $\langle a_{out} \rangle = \langle b_{out} \rangle = 0$.

The variance of the output field as a function of the input field is then given by

$$\begin{aligned} \mathrm{Var}(a_{out}) &= \tfrac{1}{2}\langle (a_{out}^\dagger a_{out} + a_{out} a_{out}^\dagger) \rangle \\ &= \tfrac{1}{2}\langle \{\cosh(r) a_{in} + e^{i\phi}\sinh(r) b_{in}^\dagger, \cosh(r) a_{in}^\dagger + e^{-i\phi}\sinh(r) b_{in}\} \rangle \\ &= \cosh(r)^2 \langle a_{in}^\dagger a_{in} \rangle + \sinh(r)^2 \langle b_{in}^\dagger b_{in} \rangle \\ &\quad + 2\sinh(r)\cosh(r)\mathrm{Re}(e^{-i\phi}\langle a_{in} b_{in} \rangle) + \tfrac{1}{2}\cosh(2r). \end{aligned} \tag{154}$$

In particular for two coherent states at the inputs whose average field amplitudes destructively interfere as mentioned previously, it is easy to show that $\mathrm{Var}(a_{out}) = \frac{1}{2}\cosh(2r) = \bar{n} + \frac{1}{2}$. It corresponds to thermal fluctuations resulting from amplification of quantum fluctuations that haven't been canceled out unlike their average

components.

Moreover, for a separable state distributed between the input a and b, one can show that the output fluctuations are always larger than thermal fluctuations corresponding to these amplified vacuum fluctuations. As mentioned previously, a bipartite non-entangled state ρ_{ab} at the input can be described by a statistical mixture of separable pure states $\rho_{a,i} \otimes \rho_{b,i}$

$$\rho_{ab} = \sum_i p_i \rho_{a,i} \otimes \rho_{b,i}. \tag{155}$$

Therefore, for a separable state, the following inequalities are satisfied

$$\begin{aligned} \langle a_{in}^\dagger a_{in} \rangle_{\rho_{ab}} &\geq \sum p_i |\langle a_{in} \rangle_{\rho_{ai}}|^2, \\ \langle b_{in}^\dagger b_{in} \rangle_{\rho_{ab}} &\geq \sum p_i |\langle b_{in} \rangle_{\rho_{bi}}|^2, \\ \langle a_{in} b_{in} \rangle_{\rho_{ab}} &= \sum p_i \langle a_{in} \rangle_{\rho_{ai}} \langle b_{in} \rangle_{\rho_{bi}}. \end{aligned} \tag{156}$$

Hence,

$$\begin{aligned} \mathrm{Var}(a_{out}) &\geq \sum p_i |\cosh(r) \langle a_{in} \rangle_{\rho_{ai}} + e^{i\phi} \sinh(r) \langle b_{in}^\dagger \rangle_{\rho_{bi}}|^2 + \tfrac{1}{2}\cosh(2r) \\ &\geq \tfrac{1}{2}\cosh(2r). \end{aligned} \tag{157}$$

As a consequence, we have the following statement

$$\boxed{(a_{in}, b_{in}) \text{ separable} \Rightarrow \frac{\mathrm{Var}(a_{out})}{\frac{1}{2}\cosh(2r)} \geq 1}. \tag{158}$$

The equality is realized for vacuum at inputs which sets a lower bound to the fluctuations produced by a separable state.

Finally, the witnessing of the entanglement is given by the contraposition of statement Eq.(158),

$$\boxed{\sigma^2 \equiv \frac{\mathrm{Var}(a_{out})}{\frac{1}{2}\cosh(2r)} < 1 \Rightarrow (a_{in}, b_{in}) \text{ entangled}}. \tag{159}$$

The witness realized by the Josephson mixer consists in comparing the measured fluctuations generated by recombining the input state to the fluctuations produced by vacuum state.

The physical picture for this witness is that in case of an entangled state, quantum fluctuations are correlated in a non-local way. Hence, quantum fluctuations at the inputs a_{in} and b_{in} can interfere destructively generating a measurable drop of noise power at the output a_{out} compared to amplified vacuum fluctuations. The entanglement witness is in principle general and not limited to Gaussian states.

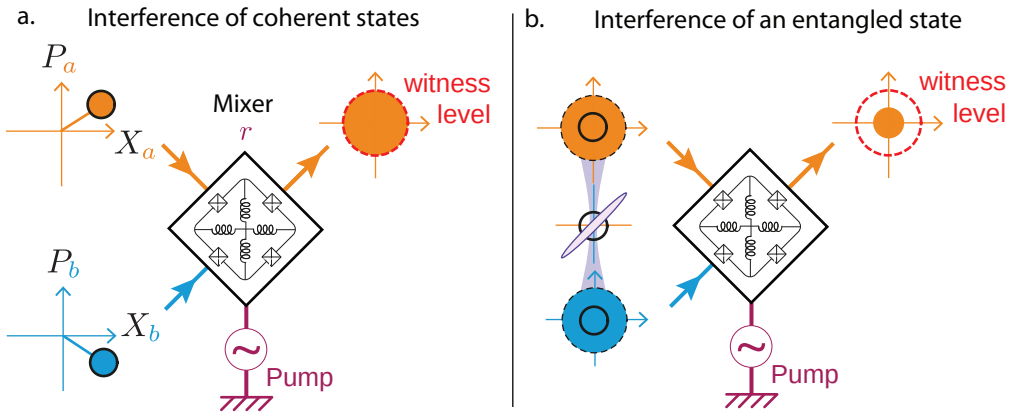

Figure 44: Schematic representing the level of fluctuations as a Wigner contour in the phase space at the input and the output of the mixer. (a) When two coherent states are recombined, the average field amplitude can interfere destructively resulting in a zero amplitude state. However, the field fluctuations being uncorrelated cannot interfere leading to amplified quantum fluctuation defining the witness boundary. (b) In the case of a state whose fluctuations are quantum correlated between a and b, the fluctuations can interfere destructively for a given pump phase and lead to a drop of the output fluctuations below the entanglement witness boundary. Such a drop of fluctuations constitute a proof of entanglement of the input state.

6.6.4 *Link with the EPR non-locality paradox*

When the witness inequality Eq.(159) is expressed as a function of input quadratures (X_a, P_a, X_b, P_b), one can show that it is analoguous to the EPR non-locality paradox [87]. Indeed

$$\begin{aligned}\mathrm{Var}(a_{out}) &= \cosh(r)^2(\langle X_a^2\rangle + \langle P_a^2\rangle) + \sinh(r)^2(\langle X_b^2\rangle + \langle P_b^2\rangle) \\ &+ 2\sinh(r)\cosh(r)\left[\cos(\phi)(\langle X_a X_b\rangle - \langle P_a P_b\rangle) + \sin(\phi)(\langle X_a P_b\rangle + \langle P_a X_b\rangle)\right].\end{aligned} \tag{160}$$

For simplicity, we choose the pump phase $\phi = \pi$ and we assume that the amplitude gain $\cosh(r) \gg 1$, such that $\cosh(r) \approx \sinh(r)$,

$$\begin{aligned} & \sigma^2 < 1 \\ \Leftrightarrow\quad & \mathrm{Var}(a_{out}) < \frac{1}{2}\cosh(2r) \\ \Leftrightarrow\quad & \langle(\cosh(r)X_a - \sinh(r)X_b)^2\rangle + \langle(\cosh(r)P_a + \sinh(r)P_b)^2\rangle < \frac{1}{2}\cosh(2r) \\ \Leftrightarrow\quad & \langle(X_a - X_b)^2\rangle + \langle(P_a + P_b)^2\rangle < 1. \end{aligned} \tag{161}$$

For conjugated variables, the Heisenberg uncertainty principle gives $\langle X^2\rangle + \langle P^2\rangle \geq |[X, P]| = 1$. However the inequality Eq.(161) above isn't in contradiction with the Heinseinberg principle since $[X_1 - X_2, P_1 + P_2] = 0$. But EPR highlighted in their paper that by measuring X_a and P_b of an EPR state, one could infer the conjugated variable X_a and P_a with a better accuracy than the Heisenberg uncertainty principle.

There are two ways of resolving the paradox, first the conjugated variable are predetermined by a hidden variable, the Heiseinberg principle arises only from the measurement processes on one object. Or the measurement of one particle projects the state of the other particle at a distance, leading to the EPR non-locality paradox.

John Bell [88, 89] in 1964 has shown that this paradox could be decided experimentally. In 1982, Alain Aspect and coworkers demonstrated in a famous experiments [90, 91] the violation of Bell's inequality. Since then, various experiments [92, 93, 94, 95, 96] have tried to close the loopholes of the original one. As far as this thesis is concerned, we assume that entanglement is valid and we use it as a quantum resource paving the way to elaborate information processing. Therefore, this inequality is a witness for non-local quantum correlation, hence entanglement.

6.6.5 *Quantifying Gaussian entanglement with a circuit*

For symmetric Gaussian states, the witness realized by the Josephson mixer can be related to a measure of entanglement. Symmetric Gaussian states correspond to the case where the fluctuation level on mode a and b is balanced, $\mathrm{Var}(a_{out}) = \mathrm{Var}(b_{out})$. In this case, the drop of fluctuation below the witness bound (Eq. 159) can be easily interpreted. It corresponds to a squeezing of the correlations between the input mode below the vacuum fluctuation as shown in Fig. 45.

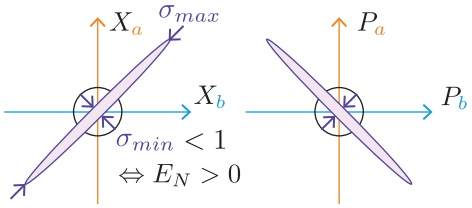

Figure 45: Contour of the marginal Wigner distribution. The squeezing rate of the correlations beyond the vacuum fluctuation $\sigma_{min} < 1$ implies that the a and b modes are entangled.

Therefore, the witness discriminates optimally the symmetric EPR states and in this case its value is directly related to a measure of the strength of the entanglement. Indeed, for a large witness gain $\cosh(r)^2 \gg 1$, the minimum of the fluctuation variance on a_{out} for symmetric EPR states is directly related to the logarithmic negativity E_N that is a measure of entanglement as detailed in appendix B.1.4.

$$E_N = -\log(\sigma_{min}^2) = \log\left[\frac{1}{2}\cosh(2r)\right] - \log\left[\mathrm{Var}(a_{out})^{\min}\right]. \tag{162}$$

Note that the logarithmic negativity gives an upper-bond on the number of entangled bits that one can extract from the state with a distillation protocol.

The purity of a state defines the degree of mixedness of the state. For symmetric squeezed states, the purity can be directly related to the measure of the witness and in particular to its minimum and maximum σ^2_{max} and σ^2_{min} through

$$\text{Purity} = \text{Tr}(\rho^2_{AB}) = \frac{1}{\sigma^2_{max}\sigma^2_{min}}. \tag{163}$$

7

GENERATING ENTANGLED MICROWAVE RADIATIONS WITH A JOSEPHSON MIXER

7.1 STATE OF THE ART OF EPR STATE GENERATION

7.1.1 *In quantum optics*

Nowadays, EPR states are routinely generated in quantum optics. Several experimental methods exist in order to produce such an EPR state. The first demonstration in 1992 by Ou *et al.* [97] was based on a non-degenerate optical parametric oscillator (NOPO) whose two-mode squeezed state was degenerate in frequency but non-degenerate in polarization, which enabled to spatially separate the beams with a polarized beam splitter (PBS) at the output.

Another route consists in combining two out-of-phase single-squeezed states on a 50/50 beam spitter, resulting into a spatially-separated two mode squeezed state or EPR state. The single-mode squeezed state can be prepared with a degenerate OPO [71] or exploiting the $\chi^{(3)}$ Kerr non-linearity of a pumped fiber loop [98]. Moreover EPR-based quantum communication protocols have been implemented, such as the unconditional quantum teleportation [71, 99, 100] as well as quantum dense coding [101]. Finally, this quadrature entanglement was also transformed into continuous-variable polarization entanglement exhibiting correlations in the Stokes operators describing the polarization of two beams [102].

7.1.2 *In quantum microwaves*

Earlier attempts by Yurke and coworkers in 1988 [16] showed how to generate single mode squeezed states in the microwave domain using superconducting circuits. They reported the first observation of squeezing of microwave thermal fluctuation below the vacuum noise [17]. Their parametric device was a DC-biased Josephson parametric amplifier (JPA).

After two decades of hibernation, the field of quantum microwaves finally woke up after the dawn of circuit QED [103] and nano-mechanical devices [104] which both need efficient measurement based on quantum limited amplifier.

Meanwhile, strong advances in microwave engineering and nanofabrication occurred driven by telecommunication network and silicon based technologies. These technological breakthroughs have enabled a much more accurate control of the microwave signal in term of sensitivity, time control or phase stability, a better control of the circuit nano-fabrication using electron lithography as well as the commercialization of cryogen-free dilution refrigerator whose wide room is well suited for these experiments. Furthermore, superconducting qubit experiments have shown the way to improve the coherence of quantum circuits by a careful control of the electromagnetic environment.

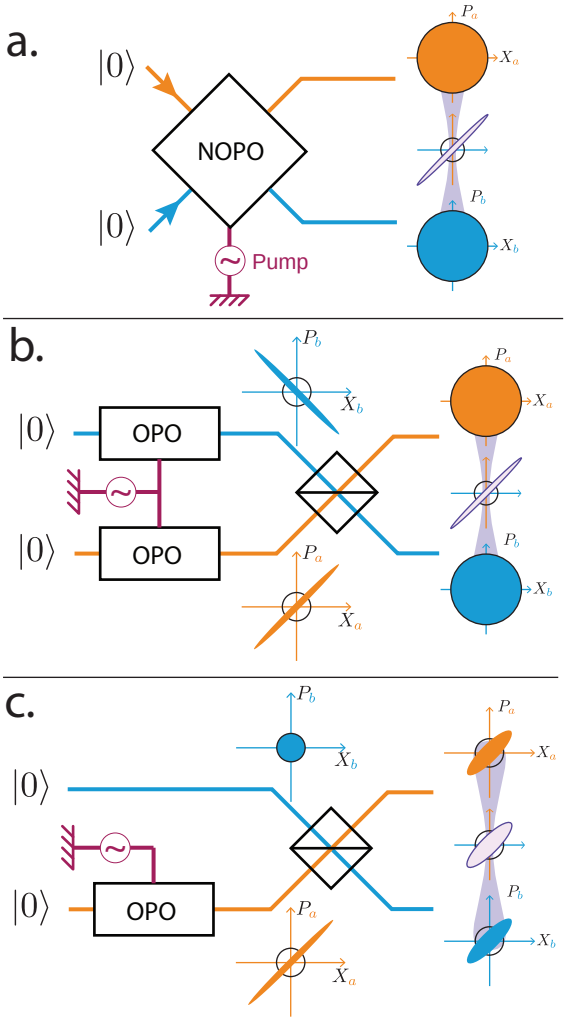

Figure 46: Schematic representing different methods to produce continuous-variable entanglement. **a** The most direct method to generate an EPR state is to pump an NOPO (non-degenerate optical parametric oscillator). The modes must be non-degenerate in polarization [97], in frequency or spatially like in the case of the Josephson mixer. **b** Another method consists in generating two identical single-mode squeezed state with two separated OPO driven with the same local oscillator and then recombine them on a 50/50 beam splitter. The method is used extensively in optics [71, 98]. In the microwave domain the Boulder group is exploring this path. **c** Finally, one can mix a single-mode squeezed vacuum state with the vacuum onto a 50/50 beam splitter to generate a continuous-variable entangled state where single-mode squeezing persists at the expense of the correlation squeezing. This method has been explored by the Munich group [28].

In 2008, the Boulder group presented a degenerate amplifier [19] able to produce single mode squeezed states less than 10 dB below vacuum fluctuations [7]. Using two sidebands of a mode in degenerate parametric amplifiers, one can then produce spatially degenerate two-mode squeezed states [8, 22].

In order to produce an EPR pair, delocalized on two transmission lines, one needs to go a step further. Our experiment [105] exploits directly the frequency and spatial non-

degeneracy of the Josephson mixer, leading to a pure EPR state. Shortly afterwards, the Munich group [28] followed another route which consists in splitting a single-mode squeezed vacuum state on a 50/50 splitter resulting into a spatially degenerate path-entangled state. Note that one could recover a proper two-mode squeezed state by performing a local unsqueezing on both modes leading to local thermal uncorrelated states. Then, the squeezing parameter is half of the initial single mode squeezed state [36].

7.1.3 *Non-classical interferometry experiment*

In conventional interferometers such as the Mach-Zehnder, Fabry-Perot and Michelson interferometers, the interference arises from splitting and recombining light beams via beam splitters (Fig. 47a). A coherent state is injected in the interferometer then split into two coherent states that probe a phase-shift Φ on one path. After recombination, fringes appear in the average value of the resulting field as a function of Φ. The phase resolution is related to the average photon number $\bar{n}$ that probed the phase shift [106, 107] through $\Delta\Phi = \bar{n}^{-1/2}$. Note that the sensitivity is ultimately limited by the photon "shot-noise", quantum fluctuations associated with the coherent state. This limit is defined as the standard quantum limit in interferometry. It is actually a classical limit since it can be overcome using quantum resources.

The experimental setup we are considering, is a very peculiar interferometer known as SU(1,1) interferometer as depicted by Yurke in 1986 [106]. Its schematic is represented on Fig. 47b. SU(1,1) stands for the symplectic symmetry group associated with the two-mode squeezing operator as opposed to the standard SU(2) interferometers where SU(2) is the rotation symmetry associated to beam splitters.

Here, we replace the beam splitters by active parametric devices such as the Josephson mixer obeying the symplectic symmetry SU(1,1). The first mixer, here called the "entangler", generates an EPR state across the arms from the input vacuum and a pump tone which defines the phase reference. The EPR state propagates in the arms of the interferometer. Remarkably, the average value of the fields in the interferometer is zero. Probing fields are the quantum correlated fluctuations between the arms: the quantum correlated "shot-noise" is probing the interferometer.

The EPR state is recombined on the second mixer, here called the "witness". This recombination results in interference fringes in the output fluctuations level as mentioned in the previous part. The interference pattern depends on the relative phase of the witness pump and the entangler pump but also on the phase-shift Φ accumulated on each path by the entangled state. The resulting phase sensitivity depends on the entanglement strength or equivalently on the average photon number $\bar{n}$ of the correlated fluctuations that probed the phase shift in absence of decoherence. Indeed, the sensitivity [106, 107] reaches $\Delta\Phi = \bar{n}^{-1}$. Our experiment represents the first realization of SU(1,1) interferometer. Shorlty after, a similar device has been implemented in the optical domain by Ou [108].

This interferometer exploits the entanglement as a quantum resource in order to beat the standard quantum limit in classical Mach-Zehnder interferometer. Note that a recent analysis [109] of these general classes of Gaussian interferometers suggests

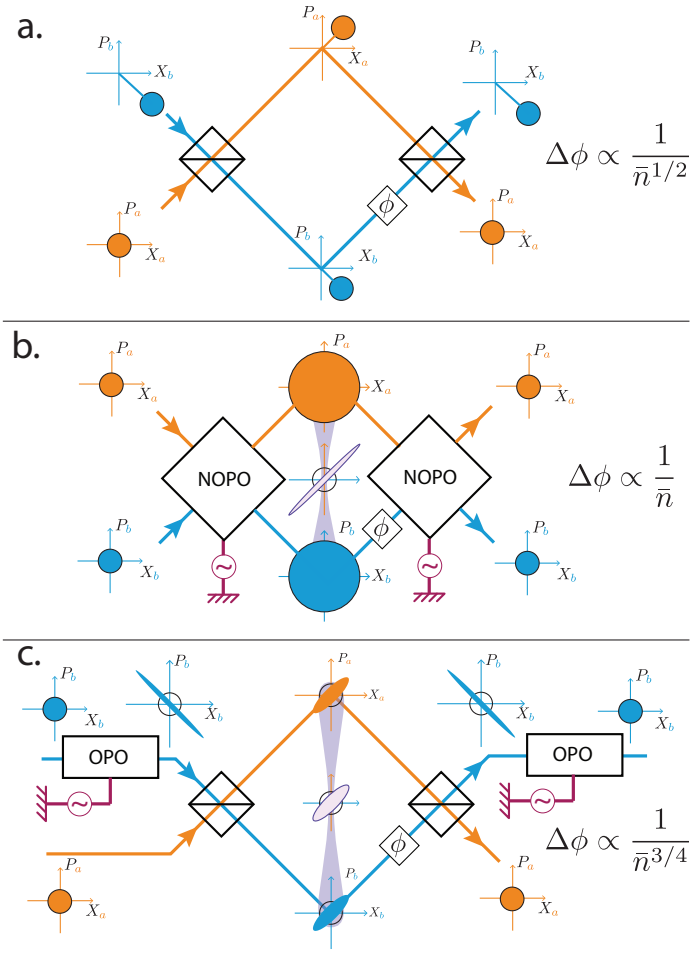

Figure 47: **a.** Standard Mach-Zhender interferometer probed with coherent state. An unknown phase shift Φ can be determined with a precision $\Delta\Phi = n^{-1/2}$. This interferometer is based on the average value of coherent states with an SU(2) symmetry associated to beamsplitters. **b.** The beam splitter can be replaced by non-degenerate parametric oscillator (NOPO) or Josephson mixer associated with the symmetry SU(1,1). Such a SU(1,1) interferometer exploits the quantum correlated fluctuation to probe the phase shift. Indeed, an EPR state is generated, one part probes the phase-shift Φ, then the state is recombined, disentangled and collected. In the ideal case, a precision $\Delta\Phi = n^{-1}$ can be reached thanks to the non-classic resources. **c.** When a standard Mach-Zhender interferometer is probed with a squeezed state generated by an OPO, a precision of $\Delta\Phi = n^{-3/4}$ can be reached thanks to the path-entanglement created when the squeezed state is split.

that thermal fluctuations added on top of the EPR state could surprisingly help to determine Φ by exploiting discord correlations.

Yet, another strategy to beat this standard quantum limit consists in injecting a single-mode squeezed vacuum state in a standard Mach-Zehnder interferometer as shown on Fig. 47c. As mentionned earlier, the splitting of the squeezed state on the beam-splitter generates a "path-entangled" state shared between arms of the interferometer [110], the state is then recombined on the other beam-splitter resulting in a reduction of output noise. In the ideal case, phase sensitivity [107] can reach

$\Delta\Phi = \bar{n}^{-3/4}$ beating the SQL using quantum resources. The ultimate sensitivity is however smaller than in the SU(1,1) case since the amount of entanglement shared is smaller. Note that this strategy has been implemented recently by the Laser Interferometer Gravitational-Wave Observatory (LIGO) [111] which consists in a Michelson interferometer with 4 km-long arms.

Finally, the use of EPR state in interferometry has been recently proposed in order to probe the existence of correlated fluctuations between two overlapping Michelson interferometers [112]. Such fluctuations could originate from an expected quantum gravity effect named holographic noise [113]. Such an experiment named 'holometer' is under construction at the Fermilab, it represents one of the most promising test toward quantum gravity.

7.2 EXPERIMENTAL SETUP

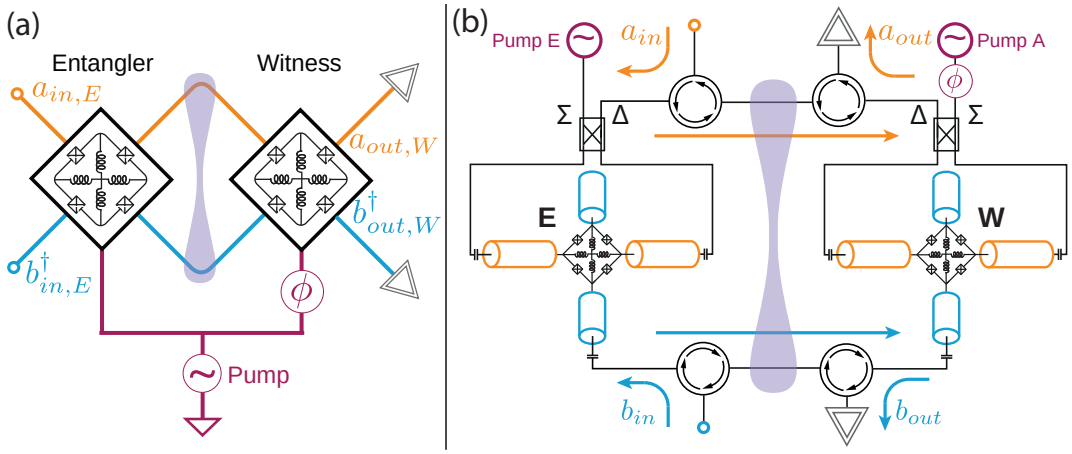

Figure 48: **a.** Schematics of experiment, two Josephson mixers realize an interferometer where the "entangler" is feeding the "witness" with an EPR state via two separate transmission lines. The output modes of the witness are amplified and measured separately at room temperature. **b** Schematics of the experimental setup at base temperature of a dilution refrigerator. Each Josephson mixer consists in a JRM coupling two $\lambda/2$ superconducting resonators addressed via a 180°-hybrid coupler or a single ended port. Both mixers are designed with the same geometry as $JM-C$ of part i and ii. Their resonance frequencies are matched at $\omega_a/2\pi = 5.578$ GHz and $\omega_b/2\pi = 8.812$ GHz using two independent flux biases. The pump frequencies are set to $\Omega/2\pi = 14.390$ GHz. Microwave circulators separate the input and output of the Josephson mixers. Input ports are represented as open circles, and at each output port the double triangle symbolizes the low-noise amplifying measurement setup with total gain G_{LNA}.

The experimental setup is a quantum circuit able to first generate an EPR state and second to witness its entanglement in a coherent way. As represented in Fig. 48, the circuit consists in two Josephson mixers set "back-to-back" .

A first mixer, called the "entangler", is driven by a pump tone at the frequency $\Omega/2\pi = 14.390$ GHz while its two input ports a_{in} and b_{in} are terminated by cold loads

ensuring that only vacuum quantum noise enters the device. The entangler generates an EPR state that propagates on two spatially separated transmission lines across several microwave elements. The modes are at two distinct frequencies $\omega_a/2\pi = 5.578$ GHz and $\omega_b/2\pi = 8.812$ GHz such as $\omega_a + \omega_b = \Omega$. These frequencies are tunable with separate flux bias set on each mixer. These frequencies have been chosen in order to match the mode frequencies of the mixers.

The entangled state is then recombined by the second mixer called the "witness". This mixer is driven at the exact same frequency Ω but with an extra phase ϕ compared to the entangler phase reference. In order to witness gaussian entangled state, the output mode a_{out} is amplified with a low-noise amplifying setup. Finally, the measurement of the noise spectral density $S_a[\omega_a]$ is performed at room temperature using a commercial spectrum analyzer.

Importantly, our circuit is able to guarantee the entanglement of a propagating state in a coherent manner (unlike inferred tomography see section 10. We demonstrate that an entangled state can be generated but also we show the ability to exploit this quantum resource to perform other tasks. In particular, the implementation of a witness protocol. This experiment paves the way to new resources for quantum microwaves with continuous variables for the realization of complex protocols such as quantum teleportation, dense coding as well as new quantum architecture such as a local quantum network.

7.3 FIELD AMPLITUDE CHARACTERIZATION

Before using the setup as an interferometer based on field fluctuations, it can be characterized using the average field amplitude only.

Reflection and transmission coefficients between input and output ports were measured with a vector network analyzer. From these measurements, we are first able to extract precisely the squeezing parameters of each mixer r_E and r_W by switching them on one at a time. Morever, when both mixers are switched on simultaneously, we can determine reflection and transmission as a function of pumps dephasing ϕ. Transmission coefficient exhibits an interference pattern as can be seen on Fig. 49. Indeed, when pumps are out-of-phase ($\phi = \pi$), the first mixer performs two-mode squeezing of a coherent state while the second mixer performs the inverse operation resulting in two-mode "unsqueezing", which leads to destructive interference. Indeed, we observe experimentally a reflection gain of 1 and the extinction of fringes when the gain of the mixers are equal. On the contrary, when the pump are in-phase, the coherent state is squeezed twice in the same direction of phase space. From the contrast of these interference fringes from $a_{in,E}$ to $a_{out,W}$ and $b_{in,E}$ to $a_{out,W}$, we were able to extract how losses affect the interference and deduce the loss unbalance between the arms of the interferometer.

From the scattering relation Eq. (128) for each mixer, we get the transmission and reflection coefficients as a function of the squeezing parameters r_W and r_E. Losses are modeled as beam splitters of transparency α and β (see Fig.(49)). Transmission and

reflection coefficients are then given by the sum of amplitudes on each path with a dephasing ϕ.

$$r_{a\to a} = \frac{\langle a_{out}\rangle}{\langle a_{in}\rangle} = \sqrt{1-\alpha}\cosh r_E \cosh r_W + e^{i\phi}\sqrt{1-\beta}\sinh r_E \sinh r_W. \tag{164}$$

Similarly, the total transmission with frequency conversion from b to a reads

$$t_{b\to a} = \frac{\langle a_{out}\rangle}{\langle b_{in}^{\dagger}\rangle} = \sqrt{1-\alpha}\sinh r_E \cosh r_W + e^{i\phi}\sqrt{1-\beta}\cosh r_E \sinh r_W. \tag{165}$$

These measurements are not calibrated all the way to the vector network analyzer. Reflection coefficient is normalized with respect to the case where the mixers are both switched off, leading to $r_{a\to a}/\sqrt{1-\alpha}$. The transmission is normalized with respect to the maximum gain leading also to $t_{b\to a}/\sqrt{1-\alpha}$. Thus, the only parameter about losses that can be extracted from the measurement is the unbalance between the losses $(1-\beta)/(1-\alpha)$.

The measurement results are presented in figure 49. The gain of the witness is kept fixed to $G_W = \cosh^2 r_W = 10$ dB. The solid grey line corresponds to the case when the entangler is turned off. As expected, the measured transmission does not depend on the pump phase difference. When the entangler is turned on, interference fringes around the grey line appear and strongly develop as the entangler gain is increased from $\cosh^2 r_E = 0.2$ dB to 9.8 dB. The interference fringes are in close agreement with the theoretical expectation displayed in dashed lines using a single fit parameter which is the loss imbalance $(1-\beta)/(1-\alpha) = 0.945$. Thus, this measurement in combination with the noise calibration (chapter 7.5) enables us to extract $\alpha = 0.37$ and $\beta = 0.40$.

This measurement represents the first realization of the SU(1,1) interferometer where a coherent state is amplified, propagated on separated transmission lines and recombined coherently with another mixer as described in Yurke's work [106].

It is interesting to note that in the case of destructive interference $\phi = \pi$ the energy of the entangler pump is first transformed through parametric down-conversion from ω_p to ω_a and ω_b. It propagates under the form of an inseparable state and the witness then gives the energy back to the pump at ω_p as highlighted by Shackert et al. [86].

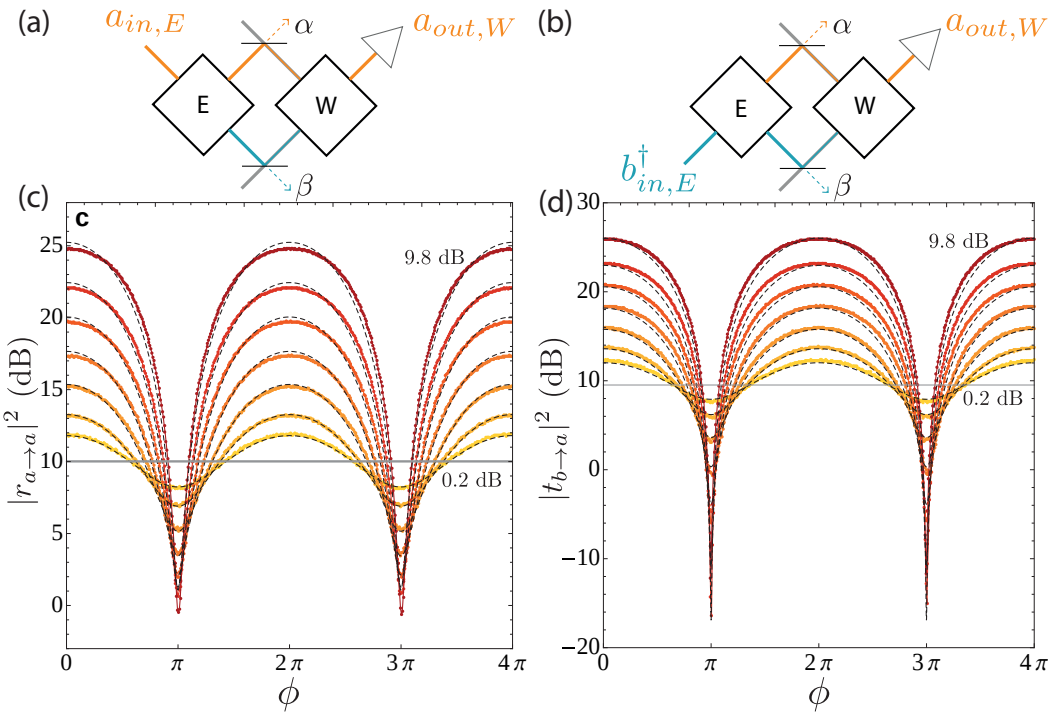

Figure 49: **a.**, **b.** Scheme of the scattering coefficient measurements by a vector network analyzer connected between the $a_{in,E}$ or $b_{in,E}$ input port and the $a_{out,W}$ output port. The setup is calibrated by turning on and off each Josephson mixer separately. Losses are modeled as beam splitters of transparency α and β coupling a cold load to the signals. **c.** Color traces: Transmission measurements of $|t_{a\to a}|^2$ as a function of phase difference ϕ between both pump signals. The gain of the witness is set to $G_W = \cosh^2 r_W = 10$ dB (solid gray line). Each trace and color corresponds to a different gain for the entangler $G_E = \cosh^2 r_E = 0.2, 0.8, 1.8, 3.2, 5, 7.2, 9.8$ dB. Dashed lines: fits to the data using equation (164), where the single fit parameter is the loss imbalance $(1-\beta)/(1-\alpha) = 0.945$. **d.** Same measurement as in panel 3c, but between input mode b_{in} and output mode a_{out} (frequency conversion measurement).

7.4.1 *Noise measurement*

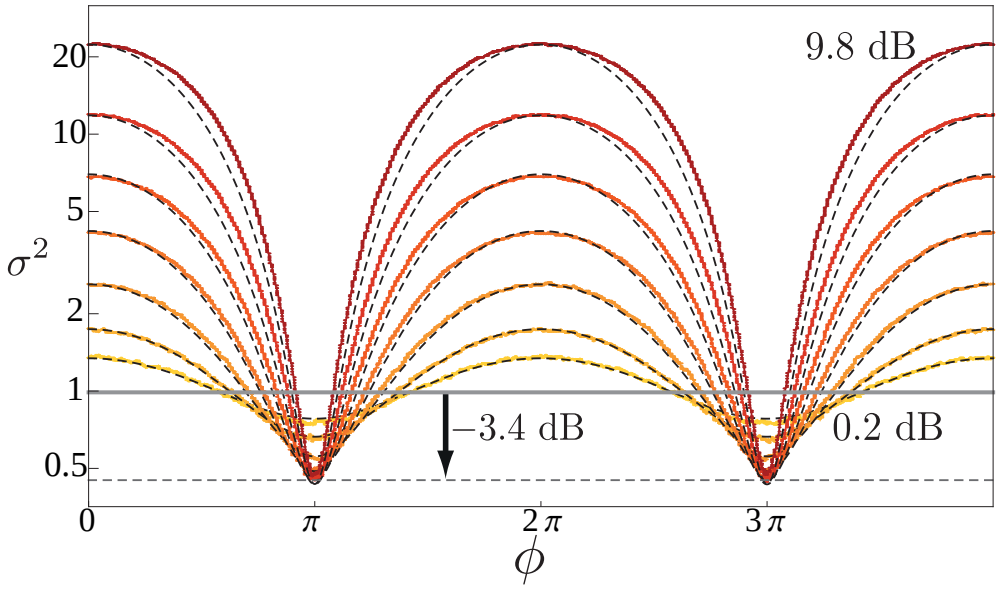

Figure 50: Color traces: variance of the output mode $\mathrm{Var}(a_{out,W})$ normalized to the case of vacuum input on the witness (divided by $\cosh(2r_W)/2$), as a function of phase difference ϕ. The variance is determined by measuring the spectral density of the noise at the witness $a_{out,W}$ output when only quantum noise enters the entangler $a_{in,E}$,$b_{in,E}$ inputs. An absolute calibration allows exact conversion between both quantities with an error of at most ±2.5%. Each color corresponds to the gains of the entangler $G_E = \cosh^2 r_E = 0.2, 0.8, 1.8, 3.2, 5, 7.2, 9.8$ dB with a fixed gain on the witness $G_W = \cosh^2 r_W = 10$. The horizontal line at $\sigma^2 = 1$ is the measured noise for amplified vacuum at the output of the witness ($r_E = 0$). For ϕ close to π, the measured noise goes below this level, demonstrating entanglement. Dashed lines: predicted variance using Eq. (168) using $\alpha = 0.37$ and $\beta = 0.40$.

Importantly, this interferometry experiment can be performed with vacuum fluctuations only at the input. In this case, the output fluctuations also exhibit fringes as function of the phase ϕ between the pump signals. As depicted above, for given values of pump phase ϕ, the output fluctuations are demonstrated to be quieter than the vacuum fluctuation amplified by the witness.

The measurement presented in Fig. 50 is the measure of the witness σ^2 which consists in the calibrated variance $\mathrm{Var}(a_{out,W})$ normalized by the amplified vacuum fluctuations $\frac{1}{2}\cosh 2r_W$. The output variance of the witness is measured from spectral noise density for the mixers switch on $S_{\mathrm{on}}[\omega_a]$ and then off $S_{\mathrm{off}}[\omega_a]$ with a spectrum analyzer at room temperature. The witness reads

$$\sigma^2 = \frac{\mathrm{Var}(a_{out,W})}{\frac{1}{2}\cosh 2r_W} = \frac{1}{\frac{1}{2}\cosh 2r_W}\left(\frac{S_{\mathrm{on}}[\omega_a] - S_{\mathrm{off}}[\omega_a]}{G_{\mathrm{LNA}}\hbar\omega_a} + \frac{1}{2}\right) \tag{166}$$

where G_{LNA} is the calibrated gain of the low-noise amplifying setup. The calibration procedure is detailed in section7.5.

When only the entangler is turned off $\cosh^2 r_E = 0$ dB, the measured spectral noise density at the output of the witness as a function of phase ϕ corresponds to the grey line on figure 50 for a witness gain $\cosh^2 r_W = 10$ dB. It coincides with the witness threshold $\sigma^2 = 1$. In this case, the fluctuation at the output of the witness does not depend on pump phase as expected.

When the entangler gain is turned on with a gain $\cosh^2 r_E = 0.2, 0.8, 1.8, 3.2, 5, 7.2, 9.8$ dB, fringes appears in the spectral noise density. Importantly, we observe a drop of the fluctuations compared to the case where the entangler is turned off. Remarkably, the drop of the witness below one, $\sigma^2 < 1$, directly indicates correlations between the input beams that are stronger than classically allowed. This demonstrates that the witness input modes are entangled.

Hence, an entangled state has been generated by the entangler from the vacuum, it has propagated in this very peculiar interferometer before being recombined and partially disentangled by the witness when the pump are out of phase $\phi = \pi$.

The relation between the input and output fields is given by

$$a_{out,W} = r_{a\to a} a_{in,E} + t_{b\to a} b^\dagger_{in,E} + \sqrt{\alpha}\cosh r_W a_{th} + e^{i\phi}\sqrt{\beta}\sinh r_W b^\dagger_{th} \tag{167}$$

where a_{th} and b_{th} are the input modes of the beam splitters modeling the losses, $r_{a\to a}$ and $t_{b\to a}$ are amplitude reflection and transmission coefficient described in Eq.(164).

All the input modes are supposed to be in the vacuum state as indicated by the noise calibration (section7.5), leading to $(\Delta a_{in,E})^2 = (\Delta b_{in,E})^2 = (\Delta a_{th})^2 = (\Delta b_{th})^2 = 1/2$.

Hence, the variance of the output fluctuations reads

$$\begin{aligned} \mathrm{Var}(a_{out,W}) &= \tfrac{1}{2}\langle\{a_{out,W}, a^\dagger_{out,W}\}\rangle_{\rho_{out}} \\ &= \tfrac{1}{2}\left(\cosh 2r_E - 1\right)\left(\bar{\alpha}\cosh^2 r_W + \bar{\beta}\sinh^2 r_W\right) \\ &\quad + \tfrac{1}{2}\cos\phi\sqrt{\bar{\alpha}\bar{\beta}}\sinh 2r_E \sinh 2r_W \\ &\quad + \tfrac{1}{2}\cosh 2r_W \end{aligned} \tag{168}$$

with $\bar{\alpha} = 1 - \alpha = 0.63$ and $\bar{\beta} = 1 - \beta = 0.60$.

The corresponding theory is shown as dashed lines in Fig. 50. It is in excellent agreement with the measurements. Note that there is no fitting parameter since they have all been characterized independently from the noise calibration or from the coherent amplitude characterization.

Finally, when the gains of the mixers are nearly equal ($G_E = 9.8$ dB, $G_W = 10$ dB) and their pumps are out of phase, it is interesting to note that the absolute level of fluctuations at the input of the witness $\mathrm{Var}(a_{in}, W) = \bar{\alpha}/2\cosh 2r_E$ is larger than the level of fluctuations at its output $\mathrm{Var}(a_{out}, W) < \mathrm{Var}(a_{in}, W)$. It is also true for the b mode, $\mathrm{Var}(b_{out}, W) < \mathrm{Var}(b_{in}, W)$. Remarkably, a noisy state can be transformed into a quieter state in a unitary way. This observation is a striking feature of the entanglement, for which subpart of a state are less known than the whole state. The noise is quantum correlated between a and b, hence their recombination can lead to a quieter state through a unitary transform.

7.4.2 *Entanglement characterization*

The contrast of the fringes grows as the entangler gain increases. Whereas the constructive interference continuously increases, the minimum of the witness σ_{min} rapidly saturates to -3.4 dB shown in Fig. 51(a), unlike the measurement of the coherent amplitude where a full extinction of the fringes is observed. As discussed in section 6.6.5, the strength of entanglement is related to the drop of fluctuations, in case of symmetric gaussian state. Indeed, the strength of the entanglement can be quantified by the logarithmic negativity[1]

$$E_N = -\log \sigma^2_{\text{min}}. \tag{169}$$

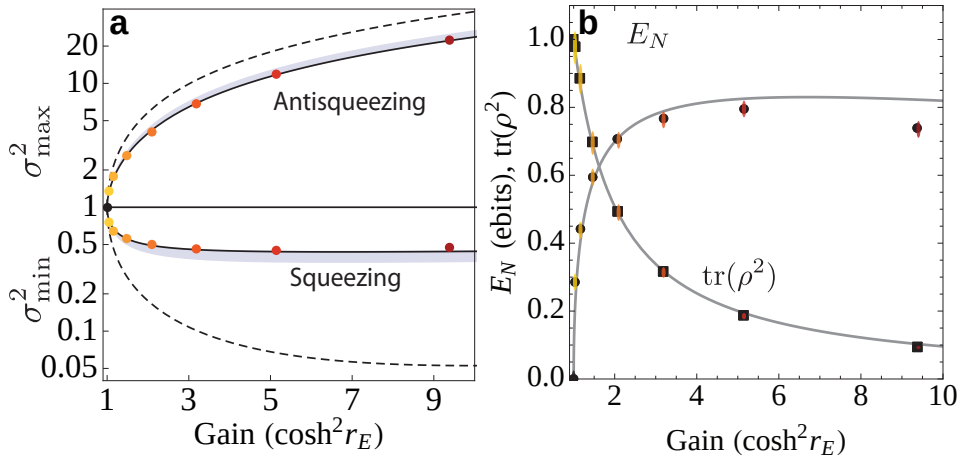

Figure 51: **a.** Dots: Noise level measured at $\phi = 0$ (anti-squeezing) and $\phi = \pi$ (squeezing) as a function of gain G_E, with $G_W = 10$. The size of the dots is larger than the error bar. Solid lines: prediction using Eq. (168) with $\alpha = 0.37$ and $\beta = 0.4$. Colored area: consistent values of the noise using the uncertainty in the calibration of the losses α and β. Dashed lines: same prediction but without losses, $\alpha = \beta = 0$. **b.** Solid dots: logarithmic negativity measure of entanglement, with errors bars. Solid squares: entanglement purity. Lines: theoretical predictions based on Eqs. (168), (337) and (170).

The logarithmic negativity extracted from the noise fringes is plotted on Fig. 51b. The saturation of entanglement strength is related to the decoherence of the entangled state during its propagation between the mixers. The decoherence can be entirely modeled through the energy losses due to beam splitter coupling to the bath as can be seen from agreement between theory and experiment in Fig. 51

1 In our article published in PRL [105] associated with this experiment, the logarithmic negativity is expressed with $\log_2$ instead of a $\log_e$. The convention $\log_e$ is the correct one for Gaussian state [70]. This is the reason why the numerical values used here are different from the published values by a factor $\log(2)$.

7.4.3 *Effect of the decoherence and reconstructed Wigner distribution*

The decoherence of the entangled state can also be characterized by its purity $\mathrm{Tr}(\rho_{ab}^2)$ where ρ_{ab} is the density matrix of the EPR state. The EPR state, when coupled to the bath, is getting more and more mixed. The purity of a symmetric gaussian state is directly related to the asymmetry between the constructive and destructive interferences. It is quantified by

$$\mathrm{Tr}(\rho_{ab}^2) = \frac{1}{\sigma_{\mathrm{max}}^2 \sigma_{\mathrm{min}}^2}. \tag{170}$$

The experimental estimation of the purity is plotted with the logarithmic negativity on Fig. 51b.

Interestingly, the more an EPR state contains photons ($\bar{n} = \sinh^2 r_E$), the more it is sensitive to decoherence. In other words, the more the state is close to the vacuum state, the less it is sensitive to photon losses along the path. In the experiment, when the gain of the entangler increases, the purity of the state undergoes a quick decrease and the logarithmic negativity saturates. Therefore, there is a trade off between entanglement strength and purity of the state.

The logarithmic negativity reaches a maximum value $E_N = 0.80 \pm 0.03$ ebits but the purity of the state is as low as $\mathrm{tr}(\rho^2) = 19\% \pm 1\%$ for a gain of $\cosh^2 r_E = 7.2$ dB corresponding to an average photon number $\bar{n} = 2.16$. Given that the entangler dynamical bandwidth $\gamma = 2\pi \times 12$ MHz sets the characteristic temporal extent of the mode to 80 ns, the usable entanglement is generated at a rate of 10 Mebits/s.

However, a better trade-off appears at smaller gain. Indeed for $\bar{n} = 0.51$ corresponding to a gain $\cosh^2 r_E = 1.8$ dB, the logarimthic negativity reaches $E_N = 0.60 \pm 0.05$ ebits for a purity of $\mathrm{tr}(\rho^2) = 70\% \pm 3\%$. The dynamical bandwidth is given by $\gamma = 2\pi \times 23$ MHz leading to a temporal extent of the mode of 44 ns. The usable entanglement is then generated at a rate of 14 Mebits/s.

Note that the entanglement rate seems to decrease when the entangler gain increases. Indeed, even without decoherence, there is a trade off for the entanglement rate. The entanglement strength being $E_N \sim 2r_E$ yet the bandwidth of the parametric amplifier is $\Delta\omega_0 / \cosh r_E$, thus the entanglement rate in absence of losses reads

$$\Gamma_E = \frac{\Delta\omega_0}{2\pi} \frac{r_E}{\cosh r_E}. \tag{171}$$

The entanglement rate reaches its maximum for a squeezing parameter $r_E \sim 1.2$ corresponding to a gain of $\cosh^2 r_E \approx 5$ dB. This trade-off sets a limit on the rate at which a parametric amplifier generates entanglement.

The Wigner distributions at the input of the witness are reconstructed in Fig. 52 for the two previous cases. For a gaussian symmetric state, the axes of the squeezed cross-correlations are given by σ_{min} and σ_{max}.

Realization of quantum protocols such a teleportation requires a finite amount of entanglement but a high purity. In order to increase the purity of the entangled state, one can perform a distillation protocol [70] in order to purify and concentrate entanglement. The quantum distillation is a non-deterministic error detection protocols. It consists in post-selection of states which have been less likely to decohere. Note that for a proper

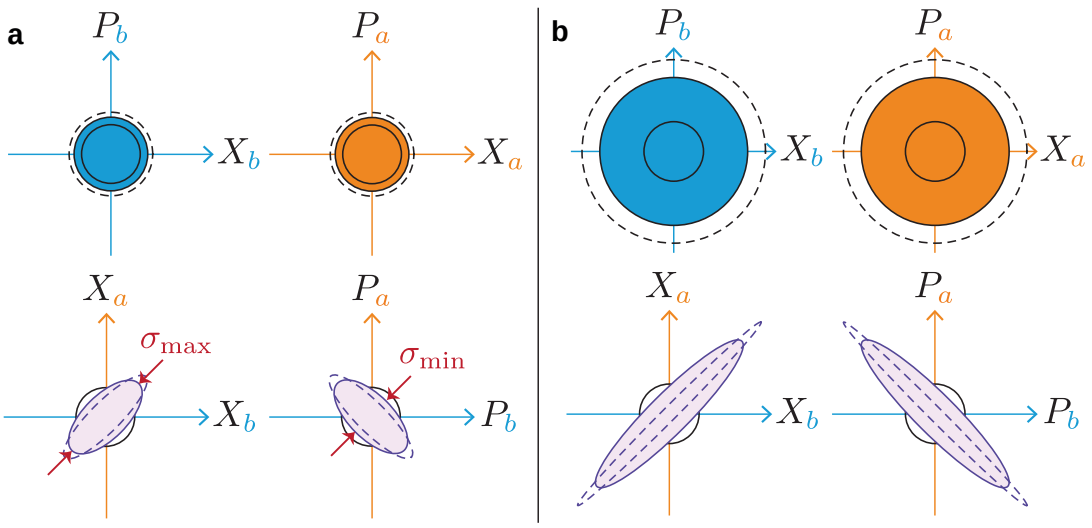

Figure 52: Reconstruction of the Wigner distribution at the input of the witness assuming symmetric Gaussian states, the axes of the squeezed ellipses correspond to σ_{min} and σ_{max}. The dashed contours correspond to the state inferred at the output of the entangler and the black circle correspond to the vacuum state. **a.** for an entangler gain $\cosh^2 r_E = 1.8$ dB corresponding to purity of $\mathrm{tr}(\rho^2) = 70\%$ and entanglement strength $E_N = 0.60$ ebits. **b.** for an entangler gain $\cosh^2 r_E = 7.2$ dB corresponding to purity $\mathrm{tr}(\rho^2) = 19\% \pm 1\%$ and entanglement strength of $E_N = 0.80$ ebits.

distillation protocol, only local operations and classical communication (LOCC) are allowed. Importantly, a no-go theorem states that it is impossible to perform the purification of a Gaussian state based on gaussian operation only [114] such as homodyne detection. Hence entanglement distillation necessarily brings some non-gaussianity in the purified entangled state. A distillation protocols for Gaussian state has been implemented in optics in 2010 by Furusawa and Sasaki [36]. The experiment consisted in triggering on events corresponding to a single-photon subtraction for both modes. The post-selection scheme is based on weakly coupled photo-detectors on both modes using high transparency beam-splitters. Hence, when both photodetectors get a click, the non-deterministic photon-subtraction operation occurred triggering the successful distillation event, the resulting state is purified and its entanglement is concentrated.

In the context of the superconducting circuit, the distillation protocols could be realized using qubits in a circuit QED architecture for implementing the non-gaussian operations. Such a scheme would enable to perform efficient distillation protocols based on non-Gaussian operation such as parity measurement or photon resolved counting.

7.5 NOISE CALIBRATION

In this experiment, one of the main experimental challenges has been to be able to guarantee the conversion from the spectral density $S_{out}[\omega_a]$ measured at room temperature into the variance of fluctuations $\mathrm{Var}(a_{out})$ at the output of the circuit expressed in photons.

Indeed, the spectral noise density measured by a spectrum analyzer at room temperature corresponds to the output noise $Var(a_{out})$ which is linearly amplified by the low-noise amplifying detection setup with a gain G_{LNA} and with extra noise S_{LNA}. Note that in practice, the added noise referred to the input of the chain is of the order of $S_{LNA}/G_{LNA} \approx 5$ K ≈ 20 photons. It is dominated by the added noise of the first amplifier of the chain which is a HEMT amplifier. Hence the measured spectral noise density reads

$$S_{out} = G_{\mathrm{LNA}}\hbar\omega_a Var(a_{out}) + S_{LNA}. \tag{172}$$

Therefore, one needs to calibrate precisely the gain of the amplifying setup G_{LNA} as well as sources of imperfection. This calibration is based on a thermal noise source whose emitted noise is entirely characterized by its temperature. These calibration measurements were performed in the same run as the entanglement measurement.

7.5.1 *Calibration setup*

The noise source consists in a 50 Ω load thermalized at temperature T_{ns} on a small copper plate(30 mm × 30 mm × 2 mm). In order to vary its temperature quickly enough and independently from the dilution refrigerator temperature, the copper plate is weakly thermally anchored to the mixing chamber stage through a thin stainless steel tubing 4 mm long and 2 mm^2 in cross-section. Its temperature T_{ns} can be finely tuned using a heater resistor and calibrated RuO_2 thermometer fixed to the copper plate. It can be varied from 90 mK to 900 mK within a few tens of minutes without any effect on the temperature T_{dil} of the mixing chamber to which the Josephson mixers are thermally anchored.

The noise emitted by the 50 Ω cryogenic load is sent to the input mode $a_{in,E}$ of the entangler through a microwave switch followed by a directional coupler as presented on the detailed setup in Fig. 53 . The microwave switch enables to choose between the "hot" position where it is fed by the thermal noise source at temperature T_{ns} and the "cold" position, where it is fed by a cold 50 Ω load thermalized at dilution refrigerator temperature T_{dil}. Note that reaching lower temperatures T_{ns} than 90 mK is possible but requires of the order of 50 hours for thermalization. Hence the use of a microwave switch to access almost instantaneously the base temperatures $T_{ns} = T_{dil}$.

Importantly, the microwave connection between the thermal load and the microwave switch is performed by a NbTi superconducting coaxial cable (displayed in red in Fig. 53). This cable ensures a very weak thermal link between the copper plate and the mixing chamber as well as very low microwave losses on a section where the temperature gradient can be important. It is essential to minimize the losses on the temperature gradient zone since it could lead to an uncontrolled emitted noise temperature.

7.5.2 *Pump leakage compensation circuit*

Instead of using a single split microwave source for pumping both mixers, it is more practical to use two synchronized sources (Fig. 53). The phase difference between the two pumps is then increased by slightly detuning one source with respect to the other.

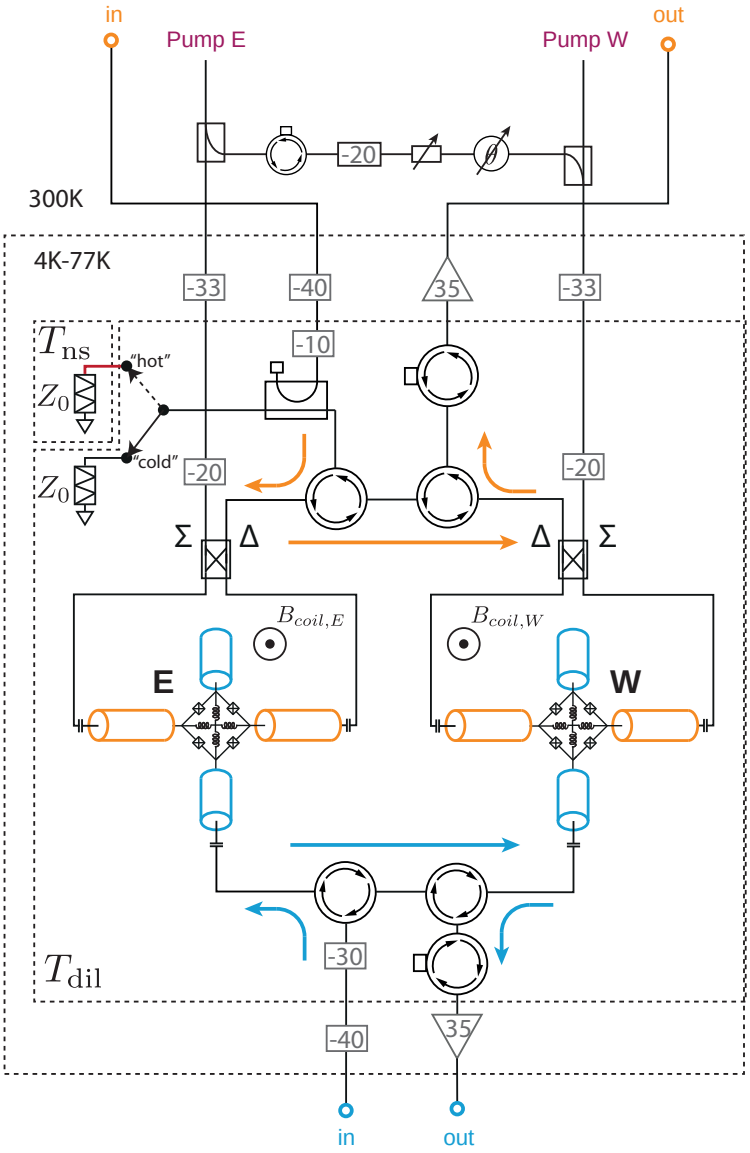

Figure 53: Detailed measurement and calibration setup. The noise source consists in a 50 Ω load thermalized at the tunable temperature T_{ns} on a small copper plate weakly thermally anchored to the mixing chamber stage. Its temperature can be varied quickly and independently of the temperature of the dilution refrigerator T_{dil}. The noise source is connected to $a_{in,E}$ the input of the entangler through a microwave switch enabling us to connect $a_{in,E}$ to the "cold" load strongly thermalized to dilution refrigerator at the temperature T_{dil}. The red wired connecting the hot load to the switch corresponds to the NbTi coaxial cable. The gray rectangles stand for microwave attenuators with attenuation in dB. The gray triangles are HEMT amplifiers. The two Josephson mixers (labeled E and W) are embedded in the same Cryoperm magnetic shield (see appendix C.1).

For the measurements presented in the main text, the detuning is $\delta\omega/2\pi = 0.3$ Hz. The phase difference is then given by $\phi = \delta\omega t$.

The frequency tunability of the mixers offer a way to remove any small contribution to the measured interferences coming from a direct beating between leaking pump signals. Such parasitic contributions appear, for instance, if the entangler pump signal leaks towards the witness pump port, and effective pump amplitude feeding the witness reads

$$\mathcal{A}_p(t) = \mathcal{A}_{p_W}[\sin(\omega_p t) + \epsilon \sin(\omega_p t + \delta\omega t + \theta)] \tag{173}$$

where $\omega_p = 14.390$ GHz is the witness pump frequency, θ is a fixed phase offset and $\epsilon \ll 1$ is the leakage fraction from the entangler pump to the witness pump. This translates into a modulating value of the squeezing parameter

$$r_W \propto 1 + \epsilon \cos(\delta\omega t + \theta). \tag{174}$$

Conveniently, by flux detuning the entangler to a working point where it does not present any non-linearity, all the observed modulation in the transmission comes from parasitic leaks. We could observe a tiny modulation corresponding to $\epsilon \sim 10^{-2}$. Reversing the roles of both mixers, we could determine that the leak from the witness pump towards the entangler was at least 2 orders of magnitude weaker.

In order to get rid of this leakage, we added a compensation circuit (see Fig. 53) at room temperature, consisting of a variable attenuator and a variable phase shifter. To get the best sensitivity, we tuned these variable components while operating the witness close to its parametric oscillation threshold (gain > 30 dB). Note that, without this compensation, the interference fringes shown in the main text would be slightly asymmetric due to the fact that $\theta \neq 0, \pi$ in the experiment.

7.5.3 *Modeling the imperfections of the circuit*

In what follows, we model all losses in the setup as losses in the wires and microwave components and thus we assume that the Josephson mixers are ideal, in the sense that the pure non-linear element do not add any spurious noise coming from uncontrolled channels. Actually, they degrade the efficiency, in the sense that spurious losses can pollute the modes of the mixers by coupling to a bath. But, all these imperfections can be modeled by beam splitters coupling the propagating modes to a thermal load at temperature of the dilution refrigerator T_{dil} (Fig. 54). For the same reasons, the mixer inefficiency cannot be discriminated from insertion losses before or in between the mixer.

The losses between the load noise source and the mixer port $a_{in,E}$ are modeled by a beam splitter with transmission γ (a fraction $1-\gamma$ of the power coming from the noise source reaches the entangler). Hence the equivalent setup is represented in Fig. 54.

As mentioned above the losses between the mixers are modeled by beam splitters with transmission α and β whose imbalance has been determined experimentally $(1-\beta)/(1-\alpha) = 0.945$ using classical fields (Fig. 49).

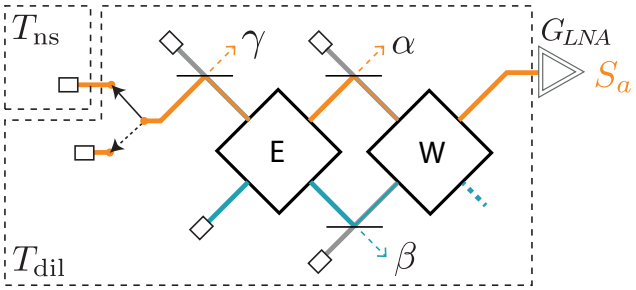

Figure 54: Equivalent setup, all losses and inefficiencies are modeled by beam-splitters coupling the propagating modes of interest to a bath at dilution refrigerator temperature T_{dil}.

7.5.4 *Calibration principle*

The noise emitted by a 50 Ω load corresponds to the black-body radiation emitted by a perfect absorber. The noise emitter is calibrated in the sense that it only depends on temperature T of the load and frequency of emission ω. Hence, the emitted spectral noise density reads [115]

$$S[\omega, T] = \frac{\hbar\omega}{2} \coth\left(\frac{\hbar\omega}{2kT}\right). \tag{175}$$

At high temperature $kT \gg \hbar\omega$, one recovers the Johnson-Nyquist noise $S[\omega, T] = kT$ which is linear with temperature. At low temperature $kT \ll \hbar\omega$, the noise density saturates down to vacuum noise $S[\omega, T] = \hbar\omega/2$.

The calibration consists in measuring the spectral noise density at room temperature while varying the temperature of the noise source T_{ns} and keeping the dilution refrigerator at its base temperature $T_{dil} = 45$ mK. The measurement is performed with three configurations: $S_{\rm off}$ when witness and entangler are turned off ($r_W = r_E = 0$), S_E when only the entangler is turned on ($r_W = 0$) and S_W when only the witness is turned on ($r_E = 0$).

In order to give simple expressions for these three noise powers, we introduce the attenuations $\bar{\alpha} = 1 - \alpha$, $\bar{\gamma} = 1 - \gamma$, and the noise spectra emitted at frequency ω_a is denoted $S_{{\rm dil},a} = \frac{\hbar\omega_a}{2} \coth\left(\hbar\omega_a / 2k_B T_{\rm dil}\right)$. The noise emitted by loads at a frequency ω_b is converted and measured at a frequency ω_a. Hence its spectral noise density is given by $S_{{\rm dil},b} = \frac{\hbar\omega_a}{2} \coth\left(\hbar\omega_b / 2k_B T_{\rm dil}\right)$. Note that due to frequency conversion, its magnitude is multiplied by a conversion factor ω_a/ω_b.

Finally, the noise spectra emitted by the noise source at frequency ω_a is $S_{\rm ns} = \frac{\hbar\omega_a}{2} \coth\left(\hbar\omega_a / 2k_B T_{\rm ns}\right)$ and the noise added by the low-noise amplifying chain (LNA) S_{LNA}.

With these notations, the spectral noise density measured at room temperature for the three configurations reads

$$\begin{aligned} S_{\text{off}} &= S_{\text{LNA}} + G_{\text{LNA}} \quad [\bar{\alpha}\bar{\gamma}S_{\text{ns}} + (1-\bar{\alpha}\bar{\gamma})S_{\text{dil},a}], \\ S_E &= S_{\text{LNA}} + G_{\text{LNA}} \quad [\bar{\alpha}\bar{\gamma}S_{\text{ns}}\cosh^2 r_E + \bar{\alpha}(1-\bar{\gamma})S_{\text{dil},a}\cosh^2 r_E \\ &\qquad\qquad +\bar{\alpha}S_{\text{dil},b}\sinh^2 r_E + (1-\bar{\alpha})S_{\text{dil},a}], \\ S_W &= S_{\text{LNA}} + G_{\text{LNA}} \quad [\bar{\alpha}\bar{\gamma}S_{\text{ns}}\cosh^2 r_W + (1-\bar{\alpha}\bar{\gamma})S_{\text{dil},a}\cosh^2 r_W \\ &\qquad\qquad +S_{\text{dil},b}\sinh^2 r_W]. \end{aligned} \tag{176}$$

This leads to

$$\frac{S_E - S_{\text{off}}}{\sinh^2 r_E} = G_{\text{LNA}}[\bar{\alpha}\bar{\gamma}S_{\text{ns}} + \bar{\alpha}(1-\bar{\gamma})S_{\text{dil},a} + \bar{\alpha}S_{\text{dil},b}], \tag{177}$$

$$\frac{S_W - S_{\text{off}}}{\sinh^2 r_W} = G_{\text{LNA}}[\bar{\alpha}\bar{\gamma}S_{\text{ns}} + (1-\bar{\alpha}\bar{\gamma})S_{\text{dil},a} + S_{\text{dil},b}]. \tag{178}$$

Three expressions can be derived in order to calibrate the setup from these two equations.

- When the switch feeds the cold load, $S_{\text{ns}} = S_{\text{dil},a}$ and for temperatures much smaller than a single photon $k_B T_{\text{dil}} \ll \hbar\omega_a < \hbar\omega_b$, we have $S_{\text{ns}} = S_{\text{dil},a} = S_{\text{dil},b} = \hbar\omega_a/2$ and from Eq. (178), we get

$$S_{\text{ns}} = S_{\text{dil},a} = \frac{1}{2} \Rightarrow \frac{S_W - S_{\text{off}}}{\hbar\omega_a \sinh^2 r_W} = G_{\text{LNA}}. \tag{179}$$

- In the same conditions,

$$S_{\text{ns}} = S_{\text{dil},a} = \frac{1}{2} \Rightarrow \frac{S_E - S_{\text{off}}}{\hbar\omega_a \sinh^2 r_E} = \bar{\alpha}G_{\text{LNA}}. \tag{180}$$

- The noise S_{ns} depends linearly on the load temperature T_{ns} in the high temperature limit as $S_{\text{ns}} \sim k_B T_{\text{ns}}$. Therefore, the slopes of the asymptotical behaviors of the above noise differences are

$$k_B T_{\text{ns}} \gg \hbar\omega_a \Rightarrow \frac{S_E - S_{\text{off}}}{k_B T_{\text{ns}} \sinh^2 r_E} = \frac{S_W - S_{\text{off}}}{k_B T_{\text{ns}} \sinh^2 r_W} = \bar{\alpha}\bar{\gamma}G_{\text{LNA}}. \tag{181}$$

Therefore, by varying the temperature T_{ns} of the noise source from the vacuum fluctuation regime up to the thermal fluctuation regime, one gets access to the gain of the chain as well as all the sources of imperfection.

7.5.5 *Experimental calibration of gain and imperfection*

The noise power was measured according to the procedure in the table above by first ramping up (filled circles in Fig. 55) and down (open circles) T_{ns} between 10 values between 90 mK and 900 mK while keeping T_{dil} to its base value, 45 mK. Each step uses a feedback temperature control with less than few mK variations. This whole

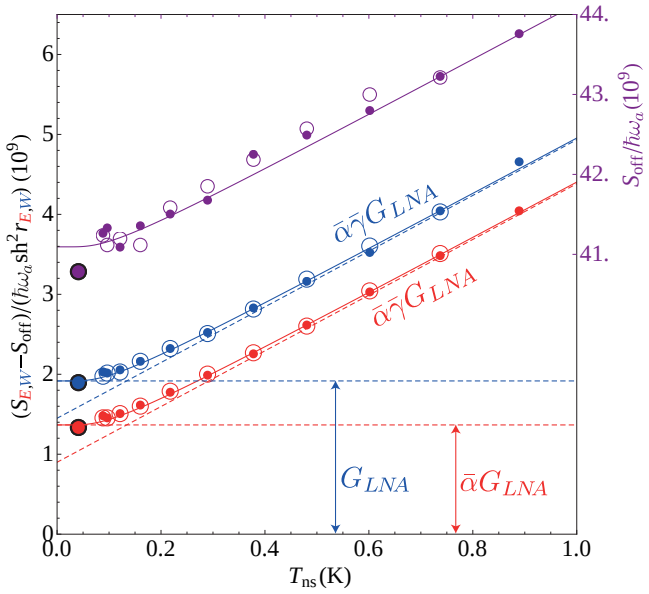

Figure 55: **Red dots**: difference between measured spectral densities S_E and S_{off} normalized by $\hbar\omega_a \sinh^2 r_E$ as a function of noise source temperature T_{ns}. These values are averaged over 6 entangler gains from 3 to 100. Filled circles correspond to the measurements made with increasing temperature from dot to dot. Empty circles correspond to decreasing temperatures. **Blue dots**: same measurements for the witness averaged over 3 witness gains from 10 to 100. **Purple dots**: level of noise S_{off} when both mixers are not pumped. Note that the scale is not divided by $\sinh^2 r$. **Dashed lines**: The slope of both red and blue curves at large temperature and the offset of these curves lead to independent determination of the three free parameters to calibrate. **Lines**: best fit of the data using Eqs. (177,178) with $\alpha = 0.33 \pm 0.05$, $\gamma = 0.28 \pm 0.11$ and $G_{\text{LNA}} = 92.8 \pm 0.04$dB.

step requires about 5 hours, mainly to ensure good thermalization. The fact that up and down ramping measurement collapse is a good indication of thermalization. It is important to note that the noise measured for the nine values of the gains G_E and G_A from 3 to 100 coincide once normalized (Fig. 55).

At the end of this first step, we then switch to the cold load connected to T_{dil} and immediately perform the measurement of Fig. 50 and 49.

From the measured noise powers as a function of $T_{\rm ns}$ and base temperature $T_{dil} = 45$ mK, leading to $S_{{\rm dil},a} = \hbar\omega_a/2$, the three relations above determine the gain $G_{\rm LNA} = 92.8 \pm 0.04$dB and the loss factors $\alpha = 0.33 \pm 0.05$ and $\gamma = 0.28 \pm 0.11$ (Fig. 55). Note that the cross-over between zero point fluctuations and Johnson-Nyquist regimes occurs at the expected value of $T_{\rm ns}$ indicating that the cold load reaches the vacuum state.

Hence, the calibrated noise fluctuation at the output of the circuit can be given in photons unit.

$$\boxed{{\rm Var}(a_{out,W}) = \frac{S_{on} - S_{\rm off}}{G_{\rm LNA}\hbar\omega_a} + \frac{1}{2}.} \tag{182}$$

where S_{on} is the measured spectral density at the frequency ω_a, and S_{off} the same measurement when the mixers are tuned off.

Conjugated with the fits of Fig. 49 in the main text, we get $\beta = 0.36 \pm 0.05$. In this experiment, the system efficiency for the coupling of the entangler to the noise source is thus $\bar{\gamma} = 72\% \pm 11\%$. Importantly, this measurement is an independent calibration of the efficiency of the Josephson mixer $\eta = 72\% \pm 11\%$. This measurement have already been presented in section 5.6.2 for that purpose.

Finally, we stress again that this gain calibration procedure has been performed right before the entanglement demonstration experiment in order to avoid drift of the experimental parameters.

7.5.6 *Noise measurement procedure*

To reduce drifts and uncertainties during the measurement, we used the following automatized procedure. The final a channel output is split, and sent to both a 4-port Vector Network Analyzer (VNA) and a Power Spectrum Analyzer (PSA). The b output is sent to the VNA also. We can precisely compensate for drifts in the gain of both the entangler and witness (or equivalently, the value of r_W and r_E), thanks to a feedback scheme on the value of each pump power. For each couple of chosen gains G_E for the entangler and G_W for the witness (set by the pump powers P_E and P_W), the following sequential procedure is performed in a couple of minutes only.

operation	entangler	witness	comments
measure transmission reference	Off	Off	VNA
measure noise power S_{off}	Off	Off	PSA, RBW : 510 kHz
feedback on P_E to reach G_E	On	Off	VNA, precision:±0.05 dB
measure noise power S_E	On	Off	PSA, RBW : 510 kHz
feedback on P_W to reach G_W	Off	On	VNA, precision:±0.05 dB
measure noise power S_W	Off	On	PSA, RBW : 510 kHz
measure transmission: $r_{a\to a}$	On	On	VNA
measure transmission: $t_{a\to b}$	On	On	VNA
measure noise power $S_{on}(\Delta\varphi)$	On	On	PSA, RBW : 510 kHz

7.5.7 *Experimental calibration of the vacuum fluctuation level*

The quantitative agreement between the experimental measurement and expected behavior demonstrates that the input is in the quantum regime when connected to the "cold" load. However, to check that extra thermal noise is not brought into the experiment through loss ports, we have varied the temperature of the whole dilution refrigerator T_{dil}. By doing so, we observe extra thermal fluctuations brought through the loss ports controlled by the dilution refrigerator temperature.

Hence, we repeat the noise power measurements for several dilution refrigerator temperatures (100 mK, 180 mK, 230 mK and 260 mK) waiting 5 hours between each step to ensure thermalization.

It is possible to explain quantitatively the variation of thermal noise power as a function of T_{ns} for each temperature T_{dil} with Eqs. (177) and (178) with fixed $\alpha = 0.33$ and $\gamma = 0.28$ (as shown in Fig. 56), however we need to adjust the gain G_{LNA}. Indeed, 5 to 10 hours separate each measurement at a given temperature T_{dil}, due to slow thermalization of the whole setup. Hence, it is likely that variations of the gain G_{LNA} within a fraction of a decibel are entirely due to drifts of the following amplifiers.

The agreement between measurement and theoretical expectations for all temperatures and gains G_E, G_A (Fig. 56) is then consistent with vacuum state at the input of the mixers at the lowest temperatures reported in the main text. Note that this agreement is all the more impressive that we are sensitive to the fact that $S_{\text{dil},a}$ and $S_{\text{dil},b}$ do not depend identically on temperature due to their frequency difference.

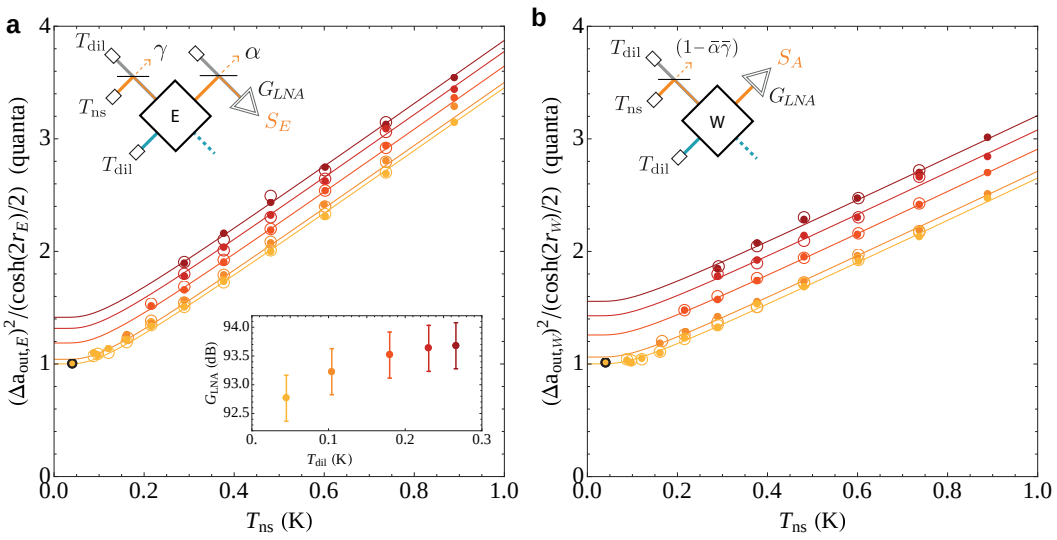

Figure 56: **a.** Dots: Normalized variance of the output field, averaged over all gains G_E and G_W, obtained using Eq. (182) with the measured values of $S_E - S_{\rm off}$ and the fitted gain $G_{\rm LNA}$ as a function of temperature $T_{\rm ns}$ for various values of $T_{\rm dil} = 45$ mK, 100 mK, 180 mK, 230 mK and 260 mK (represented by colors from yellow to red). Circles: same data for decreasing temperatures $T_{\rm ns}$ from one point to the next. Lines: theory using Eq. (177). **inset** Dots and error bars represent the result of the following fitting procedure. For each temperature $T_{\rm dil}$, the noise measurements as a function of $T_{\rm ns}$, for $G_W = 10$ or $G_E = 10$, are compared to Eqs. (177,178) as in Fig. 55. The losses are fixed for all temperatures to the previously found values $\alpha = 0.33$ and $\gamma = 0.28$ and the gain $G_{\rm LNA}$ is fitted for each value of $T_{\rm dil}$ (single value explaining all probed values of $T_{\rm ns}$ for both mixers). **b.** Same as previously with the witness on and the entangler off. Lines use Eq. (178).

7.6 CONCLUSION

In this part, we have shown how the Josephson mixer can generate and distribute entangled microwave radiations on separated transmission lines and different frequencies by spontaneous parametric down-conversion. Using two Josephson mixers, we have provided the first demonstration of entanglement between spatially separated propagating fields in the microwave domain. Furthermore, this non-classical interferometric configuration shows that this entanglement can be used in actual quantum information protocols. Therefore, a new variety of entangled states, the so-called EPR states, which are encoded on continuous variables, is now available in this frequency range.

The main results in this part are the following

- First demonstration of EPR state entanglement at microwave frequencies.
- Derivation of the Josephson mixer as an entanglement generator and witness.

The main unpublished results in this part are the following

- First experimental realization of an SU(1,1) interferometer in section 7.1.3
- In Ref. [105], we had only proven that the Josephson mixer is an entanglement witness for symmetric Gaussian states. Here, we extend the proof to any input state Eq. (159)
- Equivalence between the Josephson mixer witness and the original EPR witness Eq. (161)
- Demonstration of the usable quantity of entanglement in a lossy circuit in contrast with inferred entanglement at the output of the entanglement generator in section 7.4.3
- Signature of frequency conversion in a non-degenerate parametric amplifier as seen in the dependence of noise power on temperature as seen in $S_{\mathrm{dil,b}}$ in section 7.5.4

Part IV

ENTANGLEMENT STORAGE

In the past decades, a broad range of fundamental discoveries have been made in the field of quantum information science, from quantum computation algorithms that place public-key cryptography at risk [116] to quantum key distribution protocols that provides unconditional cryptographic security [117] . This union of quantum mechanics and information science has allowed great advances in the understanding of the quantum world and in the ability to control individual quantum systems coherently. Unique ways in which quantum systems process and distribute information have been identified, and powerful new perspectives for understanding the complexity and subtleties of quantum dynamical phenomena have emerged.

Microwave signals have been demonstrated to couple efficiently to various atomic or mesoscopic systems in the microwave domain such as Rydberg atoms [118], spin ensembles [119] or mechanical resonators [120]. Once coupled to various quantum systems, microwave fields could realize quantum networks [4], in which entangled information is processed by quantum nodes and distributed through photonic channels.

Each node of the network should generate and distribute microwave entangled fields while controlling their emission and reception in time [121, 122]. We have seen in the previous part that superconducting circuits are able to generate entanglement (part iii). On the other hand, quantum memories provide control in time as demonstrated in emerging implementations in the microwave domain using spin ensembles, superconducting circuits or mechanical resonators. In this section, we present a promising device for the storage and manipulation of microwave radiation based on the Josephson mixer. Our device offers the advantage of having a large storage efficiency and the ability to generate entanglement shared between a memory and a propagating mode of a transmission line.

8

QUANTUM MEMORY FOR MICROWAVE LIGHT

A quantum memory for light is a key element for the realization of future quantum information networks

A memory should be able to store and retrieve a quantum state of light on demand, without corrupting the information it carries. Such a device requires two key ingredients that seem antagonist at first. On one hand, a highly coherent storage medium with a vast enough Hilbert space for the quantum information to be mapped in and out. On the other hand the ability to address the storage medium on demand, efficiently and quickly compared to the coherence time of the memory. Note that unlike a classical memory, the retrieval of the quantum information is corrupting the content of the memory. Various implementations of such quantum memories exist in the optical domain [123, 124, 125, 126, 127, 128]. Recently in the microwave domain, a few quantum memories for continuous variables state of light have been realized based on various storage medium as well as various coupling method. Let us briefly review the various strategies explored in the microwave domain.

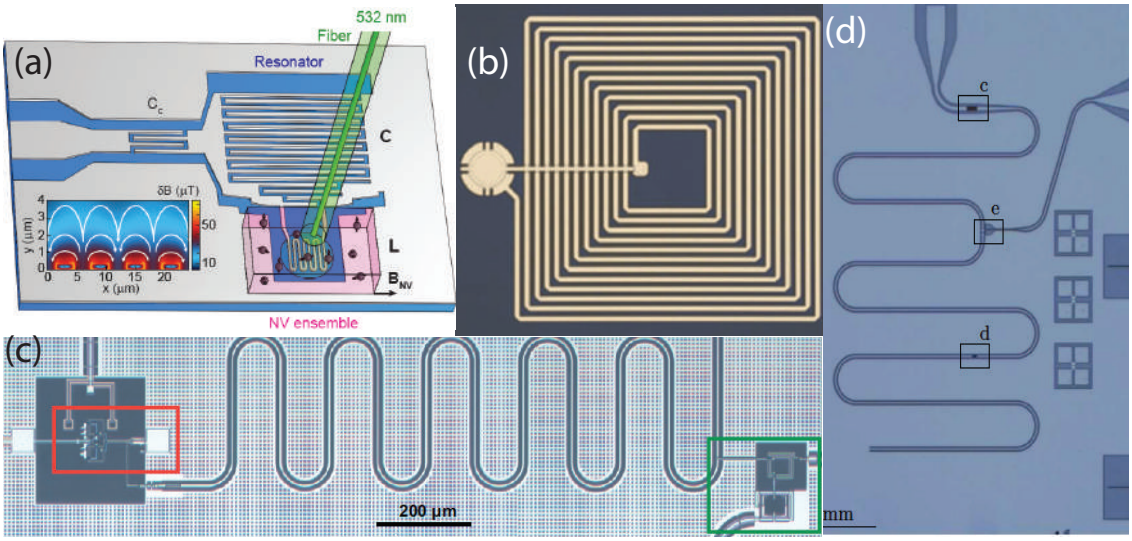

Figure 57: (a) Schematic of the setup of the Saclay group where NV centers that are embedded in a diamond crystal are coupled to a lumped element microwave resonator. [31](b) Microscope picture from the Boulder group of a mechanical resonator made of a membrane forming one electrode of the capacitance of a lumped element LC oscillator [129]. (c) Picture from the Santa Barbara group of a device made of a CPW memory resonator whose coupling to the transmission line is implemented by a SQUID shorted to the ground (green box). Note that a phase qubit is embedded in the resonator (red box) [130]. (d) Picture from the Chalmers group, a CPW memory resonator is addressed across a frequency tunable CPW resonator [34].

One strategy consists in coupling spin ensembles to a microwave resonator. The spin ensemble is constituted of nitrogen vacancy (NV) colored centers in diamond. The NV has an electron spin $S = 1$ which resonates at 2.88 GHz at zero magnetic field as well as a nuclear spin. These confined systems are naturally well decoupled from their environment such that they can reach in principle long coherence times up to a second.

However, this inherent decoupling is also a drawback since it is very challenging to address them individually with microwaves. However, the collective excitation of an ensemble of N spins enhances the coupling by a factor $\sqrt{N}$. The strong coupling to a superconducting circuit can therefore be reached with a large ensemble of spins. Remarkably, the collective excitation in the regime of low excitation are described by Dicke spin states which behave as a coherent states. Therefore, an arbitrary quantum state of the microwave field can be mapped onto the spin ensemble.

The Saclay group [29] and the Atsugi group [30] have both demonstrated the mapping of a qubit state on such a spin ensemble in 2011. The coupling between a superconducting circuit and a spin ensemble was time-controlled using the frequency tunability of their superconducting circuit. The coupling is turned on by bringing them on resonance and off otherwise.

One important limitation of these experiments is the spread of frequencies of individual spins due to their different local magnetic environment. Such an inhomogeneous broadening limits the storage time to few hundreds of nanosecond timescale in these experiements.

When the microwave field is mapped on the spin ensemble, the associated Dicke state decays quickly into dark[1] modes of the spin ensemble due to the dephasing of individual spins. Hopefully, most of dephasing is reversible. The initial bright[2] state can indeed be retrieved at a later time using refocusing technics similar to spin echo as demonstrated recently in the experiment performed in the Saclay group [31].

Remarkably, this apparent limitation can even be turned into an advantage. Such a deterministic dephasing and refocusing can be exploited in order to realize a multimode memory [31, 131, 132]. Indeed, when the quantum information has leaked out to dark modes, another state can be mapped on the bright mode of the spin ensemble and so on. The operation can be repeated as long as the dephasing stays reversible. In the end, the refocusing is applied and the quantum states are retrieved one after the other such that the last in is the first out.

However, due to uncontrolled fluctuations of the magnetic field associated to impurities such as the carbon 13 nuclear spin in diamond, a fraction of the dephasing is non-reversible and cannot be refocused. Hence the collective excitations are also far more sensitive to decoherence than for a single spin, limiting the lifetime to a few tens of microseconds.

1 dark refers to states which are not coupled to the microwave cavity
2 bright refers to states coupled to the microwave cavity

The possibility to cool a mechanical resonator down to its ground state [133, 134] has paved the way toward the implementation of quantum memories based on mechanical modes.

Indeed, mechanical resonators combine high quality factors with low resonance frequency. Hence, coherence time of the order of a fraction of a second can be approached.

Beautiful experiments are carried out by the Boulder group [133]. One of the two capacitive plates of a microwave LC oscillator made of a thin superconducting membrane is suspended at few tens of nanometers above the opposite plate. One drum mode of the membrane vibrates at a dozen of MHz, its position modulates the capacitance of the microwave LC oscillator. Remarkably, such a parametric coupling between mechanics and microwaves can be described in a formally similar manner as Josephson Ring Modulator as mentioned in part iii. When the system is excited with a pump tone at the difference between microwave and the mechanical frequencies (red sideband), phonons of the mechanical modes are up-converted into photons of the microwave mode and vice versa.

First, phonon-photon conversion enables them to cool the mechanical mode into its ground state. Second, it allows the transfer and storage of a microwave quantum state into a mechanical quantum state [129].

Moreover, when the system is excited at the sum of microwave and mechanical frequencies (blue sideband), two-mode squeezing of photon mode and phonon mode has been performed, leading to an EPR entanglement between microwaves and the mechanical mode when cooled in its ground state [32].

The mechanical storage of a highly non-classical state such as a Schrödinger cat state would lead to a coherent superposition between two positions of an ensemble of atoms, although at typical distance much shorter than interatomic distances (few fm). However, in the optical domain, optically trapped microspheres cooled to their ground state could lead to quantum superpositions of the order of their micrometer size. Such a macroscopic superposition could lead to a promising test of the decoherence induced by quantum gravity [135].

Furthermore, mechanical memories offer a promising way of efficiently transducing microwaves to optics. Such a quantum transducer is highly desirable for the implementation of a large scale quantum network. Indeed, the position degree of freedom of the resonator can be efficiently coupled to both a microwave and an optical cavity as demonstrated by the Boulder group [136]. When such a transducer will be available in the quantum regime, various quantum states of the microwave field would be efficiently generated with a cavity QED architecture. They could be then transfered and stored in a mechanical resonator and then be up-converted to optical frequency and propagate on much greater distances than in the microwave domain paving the way to earth scale quantum networks.

Another very promising strategy for the implementation of a quantum transducer is explored in the Tokyo group [137]. Their system is based on the collective magnetic excitation (magnon) in yttrium iron garnet (YIG), a high quality factor ferromagnetic insulator. On one hand, magnons can strongly couple to the microwave mode of a cavity

via resonant magnetic interaction. On the other hand, magnons can modulate the polarization of light at optical frequencies via Faraday effect using the same principle as optical isolators.

8.3 MICROWAVE CAVITIES

Another strategy consists in making an all-microwave quantum memory based on the confinement of the microwave field in a high-quality factor superconducting cavity as a storage medium. In the current implementations, the tunable coupling is based on a circuit of Josephson junctions.

Such a memory is attractive given that superconducting resonators have shown exceptional coherence properties with quality factors beyond 10^{10}. Indeed, in Paris group (LKB) experiments in the context of cavity QED with Rydberg atoms use superconducting cavities made of Niobium-coated parabolic mirrors in a Fabry-Perot configuration that reach single-photon lifetimes of 130 ms for a resonance frequency at 50 GHz [47]. Furthermore, in the Yale group, closed cylindrical aluminum cavities [138] reached a lifetime of 10 ms for a resonance frequency at 11 GHz.

In 2D geometry, single photon lifetimes between 10 and 50 μs have been achieved in thin film resonators with careful surface preparation and geometrical optimization with lumped element [139] and coplanar waveguide resonator [43]. It is important to note that these figures are given in the single photon regime, where quality factors can be lower than at higher occupation due to the presence of parasitic two-level systems [140].

Few groups have recently implemented such a cavity based quantum memory. First, the Santa Barbara group has realized in 2013 a coplanar waveguide resonator whose coupling rate depends on a flux tunable inductor [33, 130]. Therefore, the tunable coupling consists in shorting the central conductor of a coplanar waveguide resonator with a SQUID, a loop of two Josephson junctions. The inductance of the SQUID is tuned with a magnetic flux bias so that the resonator can be ground shorted or partially open with tens of MHz coupling (Fig 58a).

The Chalmers group has also recently implemented a quantum memory. It consists in a coplanar waveguide resonator which is coupled to a transmission line through a frequency tunable resonator. The tunable resonator consists in a coplanar waveguide resonator in which a SQUID is embedded. The coupling resonator frequency is tuned be the magnetic flux threading a SQUID (Fig 58b). Therefore, the coupling is turned on by bringing the tunable resonator on resonance with the memory cavity and off otherwise [34]. Finally, both implementations rely on fast flux lines to tune SQUIDs. Note that there is a proposal for implementing such a tunable coupling between superconducting resonator based on a superconducting qubit [141].

We are following a similar strategy in Paris based on the Josephson mixer. Two experiments have been carried out. A preliminary one involves a 2D microstrip resonator acting as a memory cavity (Fig. 60). A more elaborated one involves a 3D superconducting cavity to benefit from their long cavity lifetime. As opposed to other existing implementations, the coupling mechanism is based on the genuine non-linearity of the Josephson junction. Instead of using the tunable character of a SQUID inductance,

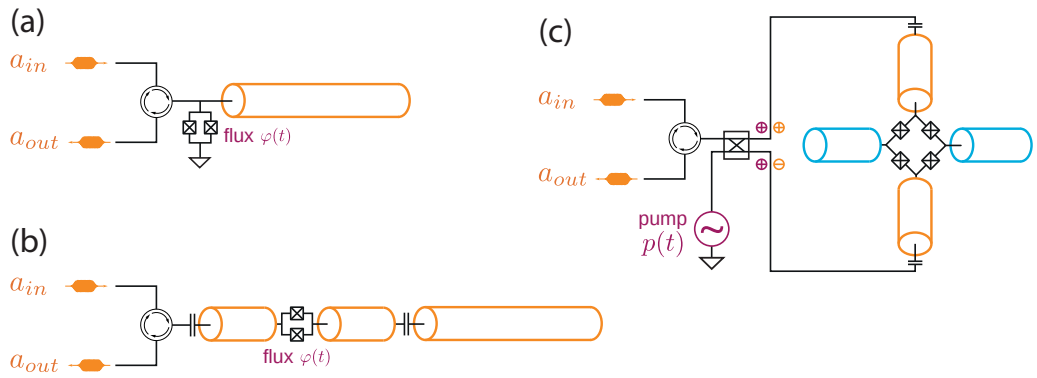

Figure 58: Schematic of the three different implementation of quantum memories based on superconducting resonators. (a) Grounded tunable inductors [33, 130]. (b) Tunable resonator [34]. (c) Frequency conversion.

we exploit the parametric frequency conversion which implements an effective beam-splitter whose transparency depends on amplitude and frequency of a pump tone (Fig 58c). Therefore, our microwave memory is controlled by microwaves.

8.3.1 *Parametric conversion as a tunable coupling*

As previously demonstrated by Abdo and coworkers [142] at Yale, the Josephson Ring Modulator can implement lossless frequency conversion between its two modes. The conversion rate is controlled by the pump amplitude and the conversion frequency is controlled by the pump frequency.

Our idea has been to use this effect to realize a microwave switch between a memory cavity and a transmission line.

As presented on Fig. 59, the two modes of the Josephson mixer consist in

- a high quality factor memory mode labeled m and its resonance frequency ω_m.
- a buffer mode labeled a which is strongly coupled to a transmission line in the vicinity of its resonant frequency ω_a.

The JRM bridges the two modes. It provides a dissipation-less non-linearity and enables us to convert of the microwave field between modes a and m conditionally to the presence of a microwave pump p (Fig. 59). The frequency of the pump is set at the difference of their frequency $\omega_p = \omega_a - \omega_m$.

In the rotating frame, the three-wave mixing Hamiltonian reads

$$H_{3\mathrm{WM}} = \hbar\chi(pe^{-i\omega_p t} + p^* e^{i\omega_p t})(ae^{-i\omega_a t} + a^\dagger e^{i\omega_a t})(me^{-i\omega_m t} + m^\dagger e^{i\omega_m t}) \tag{183}$$

The rotating wave approximation (RWA) consists in eliminating the fast-rotating terms considering that $\omega_p = \omega_a - \omega_m$ which leads to

$$H_{3\mathrm{WM}} = \hbar\chi(pa^\dagger m + p^* a m^\dagger) \tag{184}$$

Therefore, the three-wave mixing Hamiltonian becomes a beam-splitter hamiltonian with an implicit frequency conversion. In other words, the Josephson mixer implements

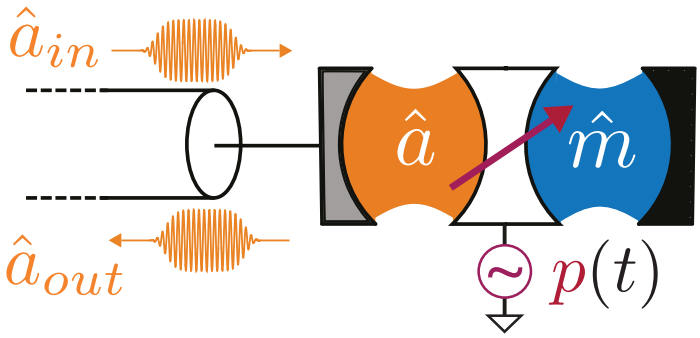

Figure 59: Schematic of the quantum memory based on high-quality factor cavity. The pump amplitude $p(t)$ enables us to tune the coupling between the buffer mode a and the memory mode m. The buffer mode a is strongly coupled to the propagating modes a_{in} and a_{out}.

a noiseless frequency mixer. The conversion rate $\chi|p|$ between modes a and b can be varied in time to switch the coupling on and off. The a mode being strongly coupled to the propagating fields a_{in} and a_{out}, one can capture an itinerant wave-packet from the input mode a_{in} into the memory and retrieve it at a later time in the output mode a_{out}.

8.3.2 *Microwave storage in a microstrip resonator*

A proof-of-principle experiment has been realized using the device used in part iii (Fig. 60c). It is a Josephson Mixer similar to $JM-C$ described in part i.

In order to isolate the memory mode from its transmission line, the m mode of the mixer has been physically disconnected from its coupling pad by removing wire bonds from the chip. Therefore, the memory mode m is a $\lambda/2$ microstrip mode which resonates at $\omega_m/2\pi = 8.81$ GHz.

The buffer mode a is a $\lambda/2$ microstrip mode which resonates around $\omega_a/2\pi = 5.57$ GHz. Note that, for the proof-of-principle experiment, the quality factor of the memory cavity has not been optimized.

8.3.3 *Microwave storage in a 3D superconducting cavity*

A more elaborated experiment has then been carried out where the memory cavity consists in a 3D superconducting cavity made of aluminum (Fig. 61). The memory mode is the TE110 mode of the cavity resonating at $\omega_m/2\pi = 7.78$ GHz. It is capacitively coupled to the JRM through microstrip antennas plunging into the cavity field through holes. Note that the capacitive coupling is performed symmetrically with respect to the Josephson ring in order to preserve the symmetry of the three-wave mixing modes. The JRM bridges the antennas, strongly coupled to the memory mode, to the $\lambda/2$ microstrip buffer mode, strongly coupled to the propagating modes of a transmission line though gap capacitors.

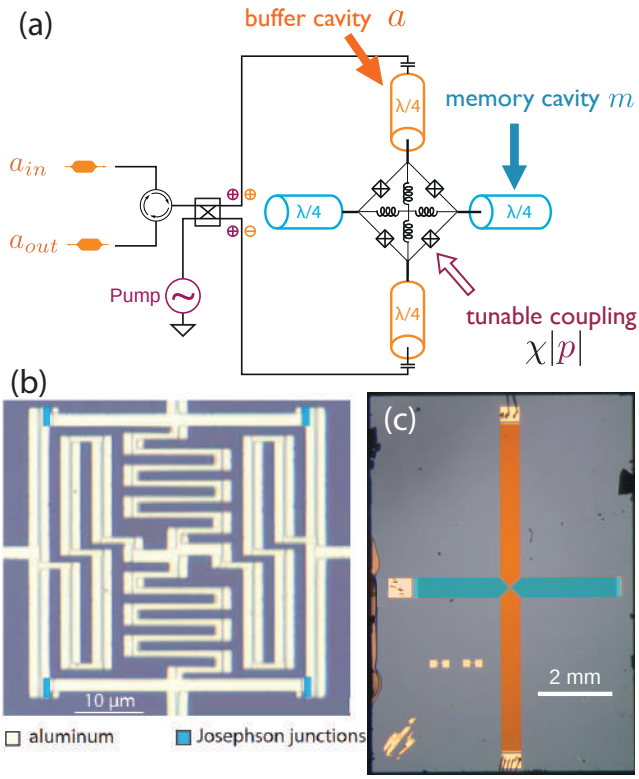

Figure 60: (a) Schematic of the preliminary experiment. This experiment has been performed with the same sample used for the entanglement experiment. One of the microstrip mode (previously labelled b) has been disconnected from the transmission line, it is now the memory mode $\hat{m}$ parametrically coupled to a low-Q buffer mode $\hat{a}$, thus to input/output propagating modes $\hat{a}_{in}$ and $\hat{a}_{out}$ through a 180 degree hybrid coupler. (b) Optical microscope image of the Josephson ring. The meanders in the center of the ring implement the four linear inductances. The stripes on the meanders are due to the fabrication process based on shadow evaporation. (c) Optical image of the microstrip $\lambda/2$ resonators, colored in blue for the memory and in orange for the buffer. The Josephson ring sits at the intersection of the resonators.

To design such a device, a quantitative modeling of the conversion was needed. Quantum Langevin equation formalism introduced in section A.6 provides an ideal theoretical framework. It has enabled us to extract rigorously the effective coupling between the memory mode and propagating modes as a function of physical parameters coming into play in the conversion process.

8.4 Dynamics of the Josephson mixer as a memory

8.4.1 *Quantum Langevin equation*

The quantum Langevin equation offers a convenient framework to study the interplay between the memory mode m, the buffer mode a and the propagating mode a_{in} and a_{out} as a function of the pump amplitude p.

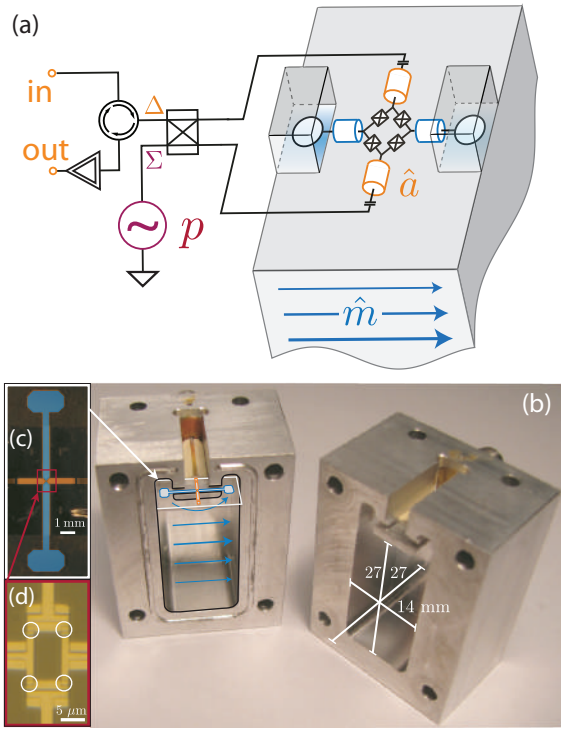

Figure 61: (a) Schematic of the experimental setup. A high-Q memory mode $\hat{m}$ is parametrically coupled to a low-Q buffer mode $\hat{a}$, hence to input/output propagating modes $\hat{a}_{in}$ and $\hat{a}_{out}$, depending on the pump amplitude p. (b) The on-chip circuit couples to a 3D superconducting cavity via antennas. The blue arrows represent the polarization of the fundamental mode TE110 in the cavity. The Josephson ring and buffer resonator are on-chip. The differential mode (Δ) couples with the buffer mode while the common mode (Σ) is used for addressing the pump. (c) Picture of the aluminum circuit fabricated on a c-plane sapphire substrate. The antennas (blue) and the buffer microstrip resonator (orange) are highlighted in false color. (d) Optical microscope image of the Josephson ring at the crossing between antennas and buffer resonator. The Josephson junctions are circled in white.

The Quantum Langevin equation gives the evolution of electromagnetic modes coupled to propagating modes.

$$\begin{cases} \frac{\partial a}{\partial t} &= \frac{i}{\hbar}[H,a] - \frac{\kappa_a}{2}a + \sqrt{\kappa_a}a_{in} \\ \frac{\partial m}{\partial t} &= \frac{i}{\hbar}[H,m] - \frac{\kappa_m}{2}m + \sqrt{\kappa_m}m_{in} \end{cases} \tag{185}$$

In the conversion mode, the system Hamiltonian in the rotating wave approximation ($\omega_p = \omega_a - \omega_m$) reads

$$H = \hbar\omega_a^{\text{res}} a^\dagger a + \hbar\omega_m^{\text{res}} m^\dagger m + \hbar\chi(p\, a^\dagger m + p^* a m^\dagger) \tag{186}$$

The interaction Hamiltonian couples linearly the two Langevin equation

$$\begin{cases} \frac{\partial a}{\partial t} &= -i\omega_a^{\text{res}} a - i\chi p m - \frac{\kappa_a}{2}a + \sqrt{\kappa_a}a_{in} \\ \frac{\partial m}{\partial t} &= -i\omega_m^{\text{res}} m - i\chi p^* a - \frac{\kappa_m}{2}m + \sqrt{\kappa_m}m_{in} \end{cases} \tag{187}$$

Here, as in the experiment we will discuss, we consider only a constant pump amplitude. Note that the following expressions need to be modified in case of a varying pump amplitude.

One can write the Langevin equation in the frequency domain knowing that $p(t) = p_0 e^{-i\omega_p t}$ considering that $\omega_p = \omega_a^{\rm res} - \omega_m^{\rm res}$

$$\left\{\begin{array}{rcl} 0 &=& i(\omega_a - \omega_a^{\rm res} + i\frac{\kappa_a}{2})a[\omega_a] - i\chi p_0 m[\omega_m] + \sqrt{\kappa_a}a_{in}[\omega_a] \\ 0 &=& i(\omega_m - \omega_m^{\rm res} + i\frac{\kappa_m}{2})m[\omega_m] - i\chi p_0^* a[\omega_a] + \sqrt{\kappa_m}m_{in}[\omega_m] \end{array}\right. \tag{188}$$

From this equation, we can derive the quantum scattering relation between the input mode a_{in} and m_{in} and the cavity modes m and a,

$$\begin{array}{rcl} m[\omega_m] &=& \dfrac{i(\chi p_0)^*\sqrt{\kappa_a}}{(\omega_m - \omega_m^{\rm res} + i\kappa_m/2)(\omega_a - \omega_a^{\rm res} + i\kappa_a/2) - |\chi p_0|^2} a_{in}[\omega_a] \\ && + \dfrac{i\sqrt{\kappa_m}(\omega_a - \omega_a^{\rm res} + i\kappa_a/2)}{(\omega_m - \omega_m^{\rm res} + i\kappa_m/2)(\omega_a - \omega_a^{\rm res} + i\kappa_a/2) - |\chi p_0|^2} m_{in}[\omega_m], \end{array} \tag{189}$$

$$\begin{array}{rcl} a[\omega_a] &=& \dfrac{i\sqrt{\kappa_a}(\omega_m - \omega_m^{\rm res} + i\kappa_m/2)}{(\omega_m - \omega_m^{\rm res} + i\kappa_m/2)(\omega_a - \omega_a^{\rm res} + i\kappa_a/2) - |\chi p_0|^2} a_{in}[\omega_a] \\ && + \dfrac{i(\chi p_0)^*\sqrt{\kappa_a}}{(\omega_m - \omega_m^{\rm res} + i\kappa_m/2)(\omega_a - \omega_a^{\rm res} + i\kappa_a/2) - |\chi p_0|^2} m_{in}[\omega_m]. \end{array} \tag{190}$$

We now define $\Delta = \omega_a - \omega_a^{\rm res} = \omega_m - \omega_m^{\rm res}$ and we can eliminate the buffer mode a from these equations using the input/output relation $\sqrt{\kappa_a}a = a_{in} + a_{out}$.

8.4.2 *Amplitude scattering coefficient*

The losses of mode m can be modeled as propagating modes $m_{in/out}$ evolving on an uncontrolled port then $\langle m_{in}[\omega_m]\rangle = 0$. Thus, the scattering coefficients read

$$\begin{array}{rcl} \langle m[\omega_m]\rangle &=& \dfrac{i\chi p_0^*\sqrt{\kappa_a}}{(\Delta + i\kappa_m/2)(\Delta + i\kappa_a/2) - |\chi p_0|^2}\langle a_{in}[\omega_a]\rangle, \\ \langle m[\omega_m]\rangle &=& \dfrac{-i\chi p_0^*\sqrt{\kappa_a}}{(\Delta + i\kappa_m/2)(\Delta - i\kappa_a/2) - |\chi p_0|^2}\langle a_{out}[\omega_a]\rangle, \\ \langle a_{out}[\omega_a]\rangle &=& -\dfrac{(\Delta + i\kappa_m/2)(\Delta - i\kappa_a/2) - |\chi p_0|^2}{(\Delta + i\kappa_m/2)(\Delta + i\kappa_a/2) - |\chi p_0|^2}\langle a_{in}[\omega_a]\rangle. \end{array} \tag{191}$$

We can rewrite these equations such that the denominators are put under a factorized form.

$$\begin{array}{rcl} \langle m[\omega_m]\rangle &=& \dfrac{-4\chi p_0^*\sqrt{\kappa_a}}{(\gamma_i^a - 2i\Delta)(\gamma_i^m - 2i\Delta)}\langle a_{in}[\omega_a]\rangle, \\ \langle m[\omega_m]\rangle &=& \dfrac{-4\chi p_0^*\sqrt{\kappa_a}}{(\gamma_o^a + 2i\Delta)(\gamma_o^m + 2i\Delta)}\langle a_{out}[\omega_a]\rangle, \\ \langle a_{out}[\omega_a]\rangle &=& -\dfrac{(\gamma_o^a + 2i\Delta)(\gamma_o^m + 2i\Delta)}{(\gamma_i^a - 2i\Delta)(\gamma_i^m - 2i\Delta)}\langle a_{in}[\omega_a]\rangle. \end{array} \tag{192}$$

Therefore, poles of the scattering coefficient are given by $\pm i\gamma_{i/o}^{a/m}/2$. The i/o labeling depends on whether the scattering coefficient couples $\langle m\rangle$ to $\langle a_{in}\rangle$ or $\langle a_{out}\rangle$. The a/m

labeling refers to the zero pump limit, $\gamma^a_{i/o} \to \kappa_a$ and $\gamma^m_{i/o} \to \pm\kappa_m$. This labeling will become clear when the temporal evolution of the fields will be considered.

Actually, the dynamical coupling rates between the propagating modes a_{in} and a_{out} and the memory mode m, which occur through the buffer, is defined as (recall that $\kappa_m < \kappa_a$)

$$\gamma^m_i = \frac{\kappa_a + \kappa_m}{2} - \sqrt{\left(\frac{\kappa_a - \kappa_m}{2}\right)^2 - 4|\chi p_0|^2} \tag{193}$$

and

$$\gamma^m_o = \frac{\kappa_a - \kappa_m}{2} - \sqrt{\left(\frac{\kappa_a + \kappa_m}{2}\right)^2 - 4|\chi p_0|^2}. \tag{194}$$

Similarly, the dynamical coupling rates between the propagating modes a_{in} and a_{out} and the buffer mode a are defined as

$$\gamma^a_i = \frac{\kappa_a + \kappa_m}{2} + \sqrt{\left(\frac{\kappa_a - \kappa_m}{2}\right)^2 - 4|\chi p_0|^2} \tag{195}$$

and

$$\gamma^a_o = \frac{\kappa_a - \kappa_m}{2} + \sqrt{\left(\frac{\kappa_a + \kappa_m}{2}\right)^2 - 4|\chi p_0|^2}. \tag{196}$$

8.5 DYNAMICAL COUPLING RATES

In the limit of a long-lived memory $\kappa_a \gg \kappa_m$, we can define the input/output coupling rate to the memory

$$\boxed{\gamma^m_{io} = \frac{\kappa_a}{2}\left[1 - \sqrt{1 - 16\frac{|\chi p_0|^2}{\kappa_a^2}}\right]} \tag{197}$$

such that[3]

$$\begin{aligned} \gamma^m_i &\approx \gamma^m_{io} + \kappa_m, \\ \gamma^m_o &\approx \gamma^m_{io} - \kappa_m. \end{aligned} \tag{198}$$

Besides, the input/output coupling rate to the buffer can be defined

$$\gamma^a_{io} = \frac{\kappa_a}{2}\left[1 + \sqrt{1 - 16\frac{|\chi p_0|^2}{\kappa_a^2}}\right] \tag{199}$$

such that

$$\boxed{\gamma^a_{io} = \kappa_a - \gamma^m_{io} \approx \gamma^a_i \approx \gamma^a_o}. \tag{200}$$

3 Eq. (198) is clearly valid for low pump amplitudes $4|\chi p_0| \ll \kappa_a$. In fact, it remains valid for all pump amplitudes in the sense that $\pm\kappa_m$ becomes inaccurate only for pump power such that $\gamma^m_{io} \gg \kappa_m$.

8.5.1 *Limits on the coupling rates*

We can decompose the two limits on the coupling rates

- For weak pump tone the coupling increases linearly with pump power

$$\gamma_{io}^{m}(|\chi p_0| \ll \kappa_a) = \frac{4|\chi p_0|^2}{\kappa_a}. \tag{201}$$

- For stronger pump tone $|\chi p_0| > \kappa_a/4$, the system enters in the strong regime limit where the coupling rate χp_0 exceeds the buffer exit rate $\kappa_a/2$, thus the two modes hybridize. The dynamical coupling rate becomes complex.

  Its real part defines the effective coupling rate. It saturates to half the buffer escape rate

$$\gamma_{io}^{m}(|\chi p_0| > \kappa_a/4) = \frac{\kappa_a}{2}. \tag{202}$$

  Its imaginary part corresponds to the dispersive shift of resonance frequencies,

$$\delta\omega_{\pm}^{m}(|\chi p_0| > \kappa_a/4) = \mathrm{Im}(\gamma_{io}^{a/m}/2) = \pm\sqrt{|\chi p_0|^2 - \left(\frac{\kappa_a}{4}\right)^2}. \tag{203}$$

  To put it simply, the conversion rate between modes at frequency ω_a and ω_m becomes large enough so that, effectively, these two modes hybridize. The new resonant modes are combinations of the buffer and memory modes, despite the frequency detuning between them. The strong coupling induces a splitting between the new resonant modes, whose magnitude scales with the pump amplitude.

8.5.2 *Effect of the antennas*

The 3D cavity is capacitively coupled to the Jopsephson Ring Modulator through antennas. This capacitive coupling κ_c placed in series with the conversion coupling $|\chi p_0|$, leads to an effective conversion rate between m and a given by

$$|\chi p_0|^2 \leftarrow \frac{1}{\dfrac{1}{(\kappa_c/2)^2} + \dfrac{1}{|\chi p_0|^2}}. \tag{204}$$

Hence, the effective coupling rate reads

$$\boxed{\gamma_{io}^{m} = \frac{\kappa_a}{2}\left(1 - \sqrt{1 - \frac{4}{\kappa_a^2\left(\dfrac{1}{\kappa_c^2} + \dfrac{1}{4|\chi p_0|^2}\right)}}\right)}. \tag{205}$$

When the conversion rate is small compared to this capacitive coupling, the dynamical coupling is not modified

$$\gamma_{io}^{m}(|\chi p| \ll \kappa_c) = \frac{4|\chi p_0|^2}{\kappa_a}. \tag{206}$$

However when the conversion rate overcomes the capacitive coupling, we observe a saturation of the dynamical coupling rate due to the antennas. It is given by

$$\gamma_{io}(|\chi p_0| \gg \kappa_c) = \frac{\kappa_a}{2}\left(1 - \sqrt{1 - \left(\frac{2\kappa_c}{\kappa_a}\right)^2}\right). \tag{207}$$

8.6 DETERMINATION OF THE COUPLING TO THE ANTENNAS

The antenna coupling has been designed and tested with dedicated samples. These samples consisted of capacitive pads directly connected to the input connectors as shown in Fig. 62. At room temperature, the 3D cavity was probed in reflection (Fig. 62b) in a similar way that one would probe in reflection a two port $\lambda/2$ resonator as the buffer resonator for instance (Fig. 62a). The measured reflection coefficient as a function of the frequency has enabled us to extract the direct coupling rate κ_c between the 50 Ω microstrip line and the 3D cavity. Various shapes and sizes of capacitive pads have been tested. We have selected the capacitive pads providing a capacitive coupling rate of $\boxed{\kappa_c = 3 \text{ MHz}}$. It corresponds to the geometry represented in Fig. 62b and detailed in Fig. 63c.

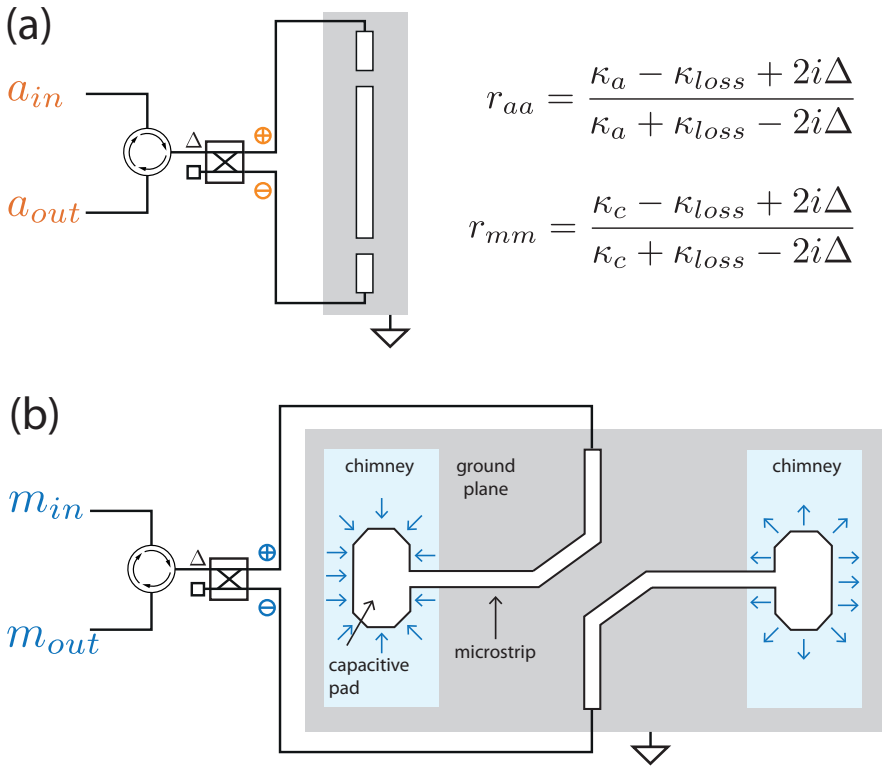

Figure 62: Capacitive couplings calibration (a) Setup for the reflection measurement of two ports $\lambda/2$ microstrip resonator. (b) Setup for the reflection measurement of the 3D memory cavity for testing the capacitive pads of the antenna.

The main requirement on a quantum memory is the ability to write and read much faster than the memory lifetime κ_m^{-1}. Longer lifetime can be reached using 3D superconducting cavity as a storage medium. Note that the memory lifetime does not come into play in the dynamical coupling rate.

The dynamical coupling rate of the cavity γ_{io}^m defines the speed at which quantum information is processed by the device.

Ultimately, the dynamical bandwidth is limited by half the buffer coupling rate $\kappa_a/2$. This limit is reached in the strong coupling regime. In practice, two ingredients come into play in the design of the Josephson mixer.

- The participation ratios of the ring ξ_a and ξ_m in modes a and m.
- The quality factor of the buffer Q_a which temporarily confines the microwave field to enhance its conversions. The ability to reach the strong coupling regime results from the interplay between these two ingredients. In this regime, the dynamic coupling rate reaches its saturation value $\kappa_a/2$.

  Therefore, the conversion rate between the memory and the buffer must satisfy

  $$\chi|p_0| > \frac{\kappa_a}{4}. \tag{208}$$

  However, the maximum pump amplitude is bounded due to the finite non-linearity of the junction. In other words, the current provided by the pump flowing in the junctions must stay far below the critical current. This bound has been estimated in section 3.1.5 to (we use an unshunted JRM here)

  $$\chi|p_{\max}| \sim \frac{1}{8}\sqrt{\xi_a\xi_m\omega_a\omega_m}. \tag{209}$$

  In the limit of $\omega_a \sim \omega_m$, the constraint to reach the strong coupling regime reads

  $$\boxed{\frac{\sqrt{\xi_a\xi_b\omega_a\omega_m}}{\kappa_a} \sim Q_a\sqrt{\xi_a\xi_m} > 2}. \tag{210}$$

  Schematically, the useful non-linearity can be characterized by the factor $\sqrt{\xi_a\xi_m}Q_a$. It is diluted by the geometric mean of the participation ratios $\sqrt{\xi_a\xi_m}$, but enhanced by the quality factor of the buffer Q_a. The resulting factor must be larger than one in order to sustain the strong coupling regime and convert the microwave field from a to m every $\kappa_a/4$.

  Note that if this limit is not achieved, the memory can work perfectly but at a lower pace than $\kappa_a/2$. In this case, it is valuable to lower the coupling rate of the buffer in order to increase the strength of the conversion. As a consequence, the optimal trade-off corresponds to the case when the threshold of the strong coupling regime is just reached.

  $$Q_a\sqrt{\xi_a\xi_m} \sim 2. \tag{211}$$

  In that case, the dynamical bandwidth is about to be limited by buffer coupling rate but the non-linearity of the JRM is optimally exploited.

9

IMPLEMENTATION OF A SUPERCONDUCTING QUANTUM MEMORY

We now apply the considerations derived in the previous chapter to design a memory based on the Josephson mixer. After detailing how the particular device we designed emerged, we proceed to demonstrating the capture, storage and retrieval of microwave signals.

9.1 DESIGN OF THE MEMORY

9.1.1 *Required specifications*

In order to maximize the number of read/write operations during the memory lifetime, one needs to increase by design the ratio γ_{io}/κ_m. According to the previous section, this optimization has to be made in the following manner.

- One needs to minimize κ_m by using low loss superconducting resonators. The best ones so far are 3D cavities. In the experiment, we use the fundamental mode (TE110) of a 3D cavity made out of 99.99% pure aluminum resonating at 7.8 GHz.
- The coupling rate κ_c between the 3D mode and the differential mode of the Josephson Ring Modulator needs to be as large as possible (ideally $2\kappa_c > \kappa_a$) in order not to limit the memory input/output rate γ_{io}. In practice, we use two identical antennas (Fig. 63) connected to the ring that are aligned with the electric field of the TE110 mode of the 3D cavity. It is possible to increase at will the coupling κ_c by decreasing the distance between the antenna tips and the cavity walls. However, as this gap decreases, it becomes more and more difficult to ensure the following constraint. In the experiment, we chose to leave a gap of 750 μm (Fig. 63) so that the total area of the tip contributes to the coupling and leads to $\kappa_c \approx 2\pi \times$ 3 MHz.
- The 3D mode must be well isolated from the common mode of the Josephson Ring Modulator to prevent deteriorating the lifetime κ_m^{-1}. Since this coupling is also proportional to κ_c, one needs to suppress it by symmetry. In our design, we ensure that the whole device is as symmetric as possible around the ring. In particular, both antennas need to couple identically to the field.
- The coupling rate κ_a needs to be as large as possible to increase γ_{io}. However, this must be done while allowing the device to reach the strong coupling regime (Eq. (210)) so that $2\kappa_a < \omega_a\sqrt{\xi_a\xi_m}$. We have chosen $\kappa_a = 2\pi \times$ 8 MHz in the experiment for $\omega_a \approx 2\pi \times 9$ GHz.

– Finally, it is useful to get the largest possible participation ratios ξ_a and ξ_m in order to push the bound of the above constraint. According to Eq (36), these ratios can be increased with larger Josephson junction inductances L_J, hence smaller critical current I_0. Note that this strategy can lower the maximal amplitude of the signal to store as described in section 5.5. Yet, since the memory needs to process far less energy than a quantum limited amplifier, it is not a critical parameter. This increase of the participation ratios also comes at the price of increasing the shift of the resonance frequencies due to the variations in pump power described in Eq. (55). In the experiment, we have chosen $I_0 = 1\ \mu$A.

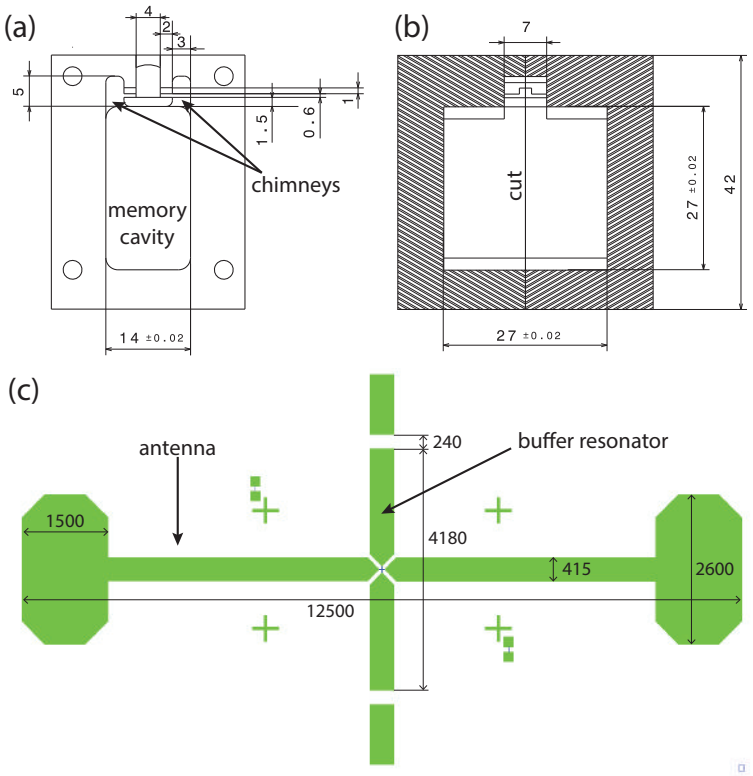

Figure 63: (a) One half of the cavity is shown from the front side (lengths in mm). (b) A section of the two halves of the cavity put together is shown from the side (lengths in mm). The cut is represented as a vertical, thick black line in the center. (c) Drawing of the device used in e-beam lithography (lengths in microns). The two symmetric antennas ending within the chimneys by oval shaped pads are oriented horizontally.

9.1.2 *Impact of the 3D geometry on the Josephson mixer design*

Using a 3D mode as one of the two resonators of the Josephson Mixer brought up several issues.

First, by choosing a superconducting 3D cavity, it becomes an issue to flux bias the ring using an external coil, since the Meissner effect forbids the field to enter the cavity. For this reason, we have placed the ring outside of the cavity.

Since the cavity TE110 mode needs to address a differential mode of the ring (mode Y in Fig. 9), two symmetric antennas start from the ring and enter each in a chimney sticking out of the cavity. The two chimneys are aligned in the direction of the electric field for the TE110 mode so that the antennas couple to it evanescently (Fig. 64). There is just enough room between the chimneys to put a superconducting coil made of a NbTi/Cu wire wrapped around a copper screw that sits right above the ring.

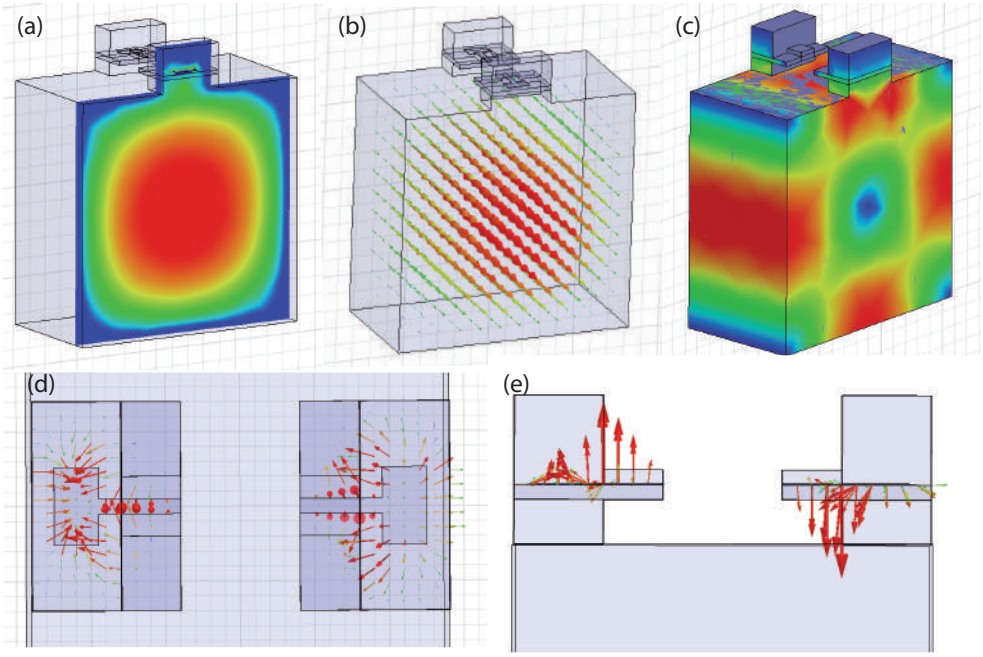

Figure 64: Simulations of the fundamental mode at 7.8 GHz, well separated from the second mode at 13 GHz. (a) Amplitude of the electric field along a section of the cavity crossing the pads of the antenna of the TE110 mode (blue is zero and red is maximal). (b) Vectorial view of the TE110 mode. (c) Current intensity along the surface of the cavity. (d) (e) Coupling of the TE110 mode to the capacitive pads, electric field at the surface of the substrate.

Second, it is not clear how to insert the chip on which the Josephson Ring Modulator is fabricated inside of these chimneys. We have decided to cut the cavity in two identical parts in the middle of the chimneys, ensuring that no current line is interrupted (see Fig. 64). In practice, the chimneys have an open slit (0.6 mm $\times$ 7 mm in section and 8 mm long) on their edge so that the sapphire chip enters them.

Third, in order to maximize the buffer coupling rate κ_a, it was decided to keep a microstrip geometry for this mode. The microstrip resonator and its feedlines are located in the gap between the two chimneys (Fig. 61). A ground plane in aluminum is evaporated on the back of the sapphire chip in all areas out of the chimneys and the width of the strip is designed to ensure a 50 Ω characteristic impedance.

Finally, the antennas have various resonant modes themselves. The first two modes are a $\lambda/2$ mode which resonates around 4 GHz and a $3\lambda/2$ mode which resonates around 11 GHz. These frequencies are also flux tunable due to the non zero participation ratio of the ring to these modes. The antenna has been designed such that it does not resonate with the 3D cavity mode at 7.8 GHz. It is possible to quantify the extra memory loss due to the presence of the antennas. By analogy with the Purcell effect, and considering the dispersive coupling between the antenna and memory modes, the loss rate can be estimated as $\kappa_{2D}(\kappa_c/\Delta)^2 < 2\pi \times 10$ Hz, where $\Delta/2\pi > 2$ GHz is the frequency detuning and $\kappa_{2D}/2\pi < 1$ MHz the internal loss of the antennas. The corresponding loss rate is thus compatible with memory lifetimes of more than a ms.

9.2 Experimental characterization of the 3D memory device

9.2.1 *Tunability and participation ratios*

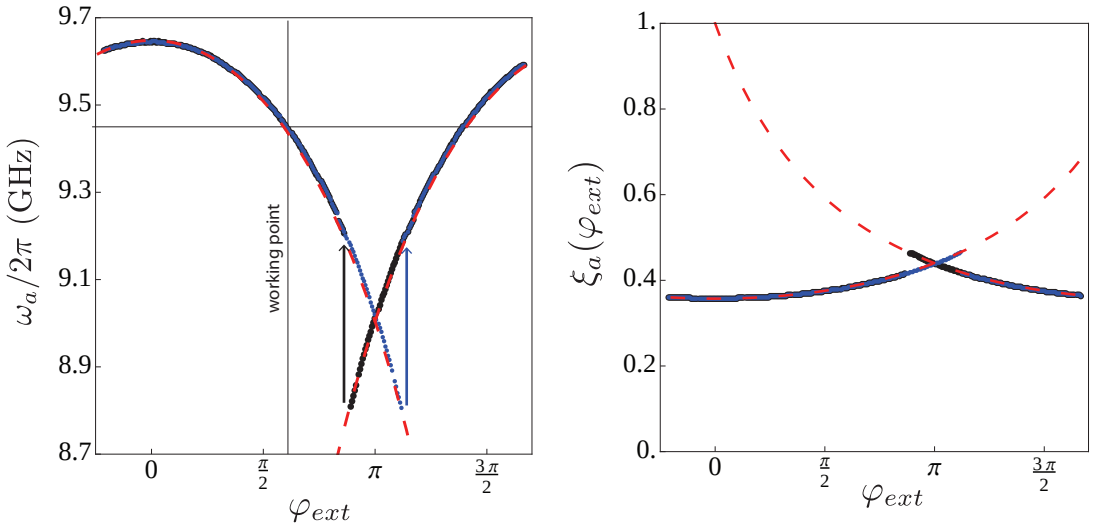

Figure 65: Left panel: resonance frequency of the buffer mode ω_a as a function of the reduced flux through the ring φ_{ext}. The blue dots are measured with increasing field while the black dots are measured with decreasing field. Red dashed lines show fits of the expected resonance frequency using Eq. (212) with $\xi_a^0(\varphi_{ext}) = \xi_a(\varphi_{ext} = 0) = 0.35$ and $\omega_0/2\pi = 12.03$ GHz.

Owing to the tunability of the Josephson Ring inductance, it is possible to change *in situ* the buffer and cavity modes using the external magnetic flux threading the loop. The measured resonance frequency of the buffer resonator is presented on figure 65 as a function of the flux. The frequency spans more than 800 MHz in the range $\omega_a/2\pi = 8.8$ GHz $- 9.6$ GHz. Note that the frequency tunability is larger than in similar devices used for amplification [27, 143], where participation ratios are smaller in order to preserve enough dynamical range. This flux dependence

can be used to determine critical parameters of the device. Indeed, using Eqs.(12) and (36), we get

$$\omega_a(\varphi_{ext}) = \frac{1}{\sqrt{(L_{res} + L_J(\varphi_{ext}))C_{res}}} = \frac{\omega_a^0}{\sqrt{1 + \frac{\xi_a^0}{1-\xi_a^0}\frac{1}{\cos\varphi_{ext}/4}}}. \tag{212}$$

The measurement is well reproduced for a zero-flux participation ratio $\xi_a^0 = \xi_a(\varphi_{ext} = 0) = 0.35$ and a bare resonance frequency $\omega_0/2\pi = 12.03$ GHz (Fig. 65). From these values, the critical current of junctions can be inferred to $I_0 = 1.1\ \mu A$. Similarly, the inferred participation ratio is shown in Fig. 65(b) as a function of magnetic flux.

In contrast to the buffer mode, the 3D cavity resonance frequency is only tunable over 200 kHz (not shown here). This is due to the non galvanic and evanescent coupling of the Josephson ring to the cavity mode through the chimneys. The participation ratio of the ring in the 3D mode can be estimated from the tunability ranges

$$\xi_m \sim \frac{200\text{ kHz}}{800\text{ MHz}}\xi_a \sim 10^{-4}. \tag{213}$$

The constraint (210) enabling to reach the strong coupling regime is therefore well verified despite a very low participation ratio on the cavity side

$$Q_a\sqrt{\xi_a\xi_m} = 1300 \times \sqrt{0.35 \times 10^{-4}} \simeq 8 > 2. \tag{214}$$

In particular, this design manages to almost reach the coupling strength of the fully 2D microstrip device (Fig. 60) for which $\xi_a \sim 0.1$, $\xi_m \sim 0.05$ and $Q_a \sim 200$ leading to

$$Q_a\sqrt{\xi_a\xi_m} = 200 \times \sqrt{0.1 \times 0.05} \simeq 14 > 2. \tag{215}$$

9.2.2 *Stability of the device in flux*

Since there are no shunting inductances in the Josephson ring as for sample $JM - A$ discussed in section i, the JRM becomes metastable for flux bias departing from $\varphi_{ext} = \pi$ and can jump to another super-current configuration by accepting an extra flux quantum into the ring. This metastability presents a hysteric behavior, ramping the flux up and down the jump from one configuration to another happens at a different flux bias as presented figure 65.

Phase-slips occur much earlier than for $JM - A$ as the flux is swept (Fig. 22). It might be due to larger participation ratios and higher frequencies, but it is not in quantitative agreement with tunneling across the potential barrier which should occur around $\varphi_{ext} \sim 1.4\pi$ as inferred from Eq. (15). One hypothesis would be that in case of a slight asymmetry between junctions, the phase slip can occur earlier. However, we repeatedly observed this behavior in the 3D devices, which indicates that this is not the main explanation.

For this sample, it is safe to work at flux point away from half flux quantum $\varphi_{ext} = \pi$ that was supposed to be stable. In the present experiment, all measurements are performed at $\varphi_{ext} \approx 0.6\pi$.

Note that around $\varphi_{ext} \approx 0.8\pi$, we observe an anti-crossing in the resonance frequency with a frequency lifting of about 5 MHz. It is certainly due to the coupling of the memory to a two level system (TLS) trapped in the oxide of one of the junctions [140]. We have observed the frequency of the TLS changing from one cooldown to another, which is consistent with defects of the junction oxide. Note that the coupling to TLS is more easily resolved with the larger quality factors used in the memory compared to previous parts in which a large bandwidth was needed.

9.2.3 *Reflection measurements*

Before demonstrating how this device behaves as a quantum memory, it is useful to characterize its dynamical response in the Fourier domain. This can be done by measuring the reflection coefficient on the buffer mode as a function of frequency and pump power for continuous waves using a vector network analyzer (VNA). Two sets of experimental results are presented in this section, the first one is realized with the preliminary 2D microstrip memory (Fig. 60) and the second one with the 3D superconducting memory (Fig. 61).

Using Eq. (192), one can rewrite the reflection coefficient as a function of the coupling rate to the memory γ_{io}^m

$$r_{aa} = \frac{\langle a_{out}[\omega_a]\rangle}{\langle a_{in}[\omega_a]\rangle} = -\frac{(\kappa_a - \gamma_{io}^m + 2i\Delta)(\gamma_{io}^m - \kappa_m + 2i\Delta)}{(\kappa_a - \gamma_{io}^m - 2i\Delta)(\gamma_{io}^m + \kappa_m - 2i\Delta)}. \tag{216}$$

Note that the reflection coefficient corresponds to two reflections in series. The first one corresponds to the reflection on the buffer resonator with a coupling rate $\kappa_a - \gamma_{io}^m$ without loss[1]. The second reflection corresponds to a reflection on the memory at a rate γ_{io}^m with a memory loss rate κ_m. The role of γ_{io}^m as the read/write rate of the memory hence becomes clear.

The reflection coefficient r_{aa} is shown on the figures 66 for the 2D microstrip memory and 67 for the 3D cavity memory. One can identify the following regimes of power in these curves.

- No coupling for $|\chi p_0| = 0$.
  The frequency conversion between the cavities is turned off as $\gamma_{io}^m = 0$. The usual behavior of single resonators measured in reflection are observed: a 2π phase shift develops as the frequency crosses the resonance. The almost constant reflection magnitude can be used to calibrate the measurement

1 Actual losses of the buffer resonator are not included in the model because they are small compared to the buffer exit rate κ_a.

lines. In polar representation, it corresponds to a single loop around zero with a radius close to one as shown on Fig. 66(a) and Fig. 67(a).

– Under-coupled for $0 < |\chi p_0| < \sqrt{\kappa_a \kappa_m / 4}$ corresponding to a coupling rate $0 < \gamma_{io}^m < \kappa_m$.
The frequency conversion becomes effective but slower than the memory loss rate. Indeed, schematically, a small part of input microwave field is transferred from the buffer to the memory, where it is dissipated before being released back in the buffer. This regime corresponds to the over-damped regime of a single resonator. An extra loop appears in the quadrature phase space. This loop translates into a slope change in the phase shift and the appearance of a dip in the reflected amplitude as shown on Fig. 66(b) and Fig. 67(b).

– Critical regime for $|\chi p_0| = \sqrt{\kappa_a \kappa_m / 4}$.
The coupling rate γ_{io}^m is equal to the memory loss rate κ_m at resonance so that the reflection goes to zero. At this point, a continuous wave incoming on a is entirely converted into the memory mode and entirely exits through the losses. This leads to a sharp extinction of the reflection amplitude as shown on Fig. 66(c) and Fig. 67(c).

– Over-coupled regime for $\sqrt{\kappa_a \kappa_m / 4} < |\chi p_0| < \kappa_a / 4$ corresponding to a coupling rate $\kappa_m < \gamma_{io}^m < \dfrac{\kappa_a}{2}$.
The conversion rate overcomes memory losses such that a part of the field is retrieved in the transmission line. A 4π phase shift develops in reflection, 2π coming from the buffer and 2π from the memory as shown on Fig. 67(d).

– Strong coupling regime $\kappa_a / 4 < |\chi p|$ corresponds to the saturation of the coupling rate $\gamma_{io}^m = \dfrac{\kappa_a}{2}$.
When the conversion rate $|\chi p_0|$ exceeds the buffer exit rate, the two modes hybridize and the coupling rate is now limited by the buffer exit rate. Hence, the 4π resonance splits into two 2π resonances of width $\kappa_a / 2$, resulting from the bonding and anti-bonding of the buffer and memory modes as shown on Fig. 66(d). Note that the strong coupling regime cannot be fully reached by the 3D cavity design since the coupling rate κ_c to the antennas limits the maximum conversion rate between the buffer and the memory as mentioned in 8.5.2.

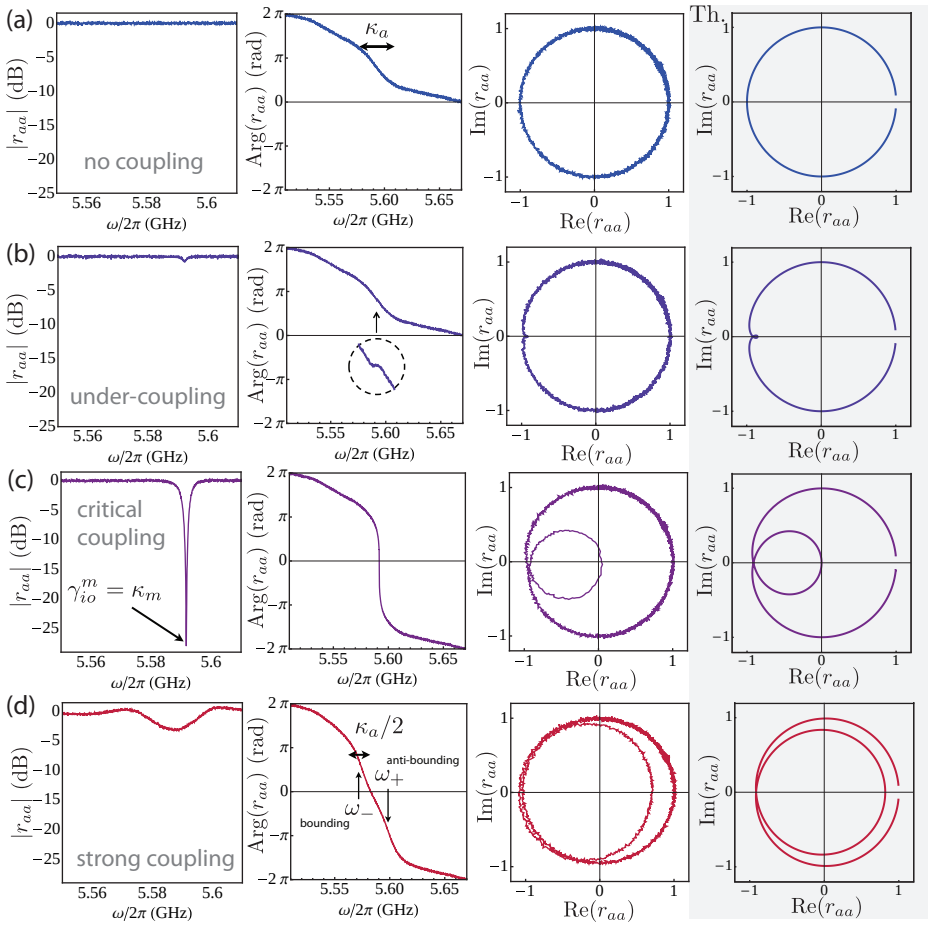

Figure 66: **2D design** - Reflection coefficient r_{aa} as a function of frequency for various values of the pump power. *First column* Measured amplitude. *Second column* Measured phase. *Third column* Measured reflection coefficient in polar coordinates. *Fourth column* Theory, reflection coefficient in polar coordinates expected from Eq. (216). **(a)** No coupling ($C = 4|\chi p|^2/\kappa_a\kappa_m = 0$). **(b)** Under-coupling regime ($C = 0.079$). **(c)** Critical coupling ($C = 1$). **(d)** Strong coupling regime ($C = 11.7$), full hybridization as described in (203).

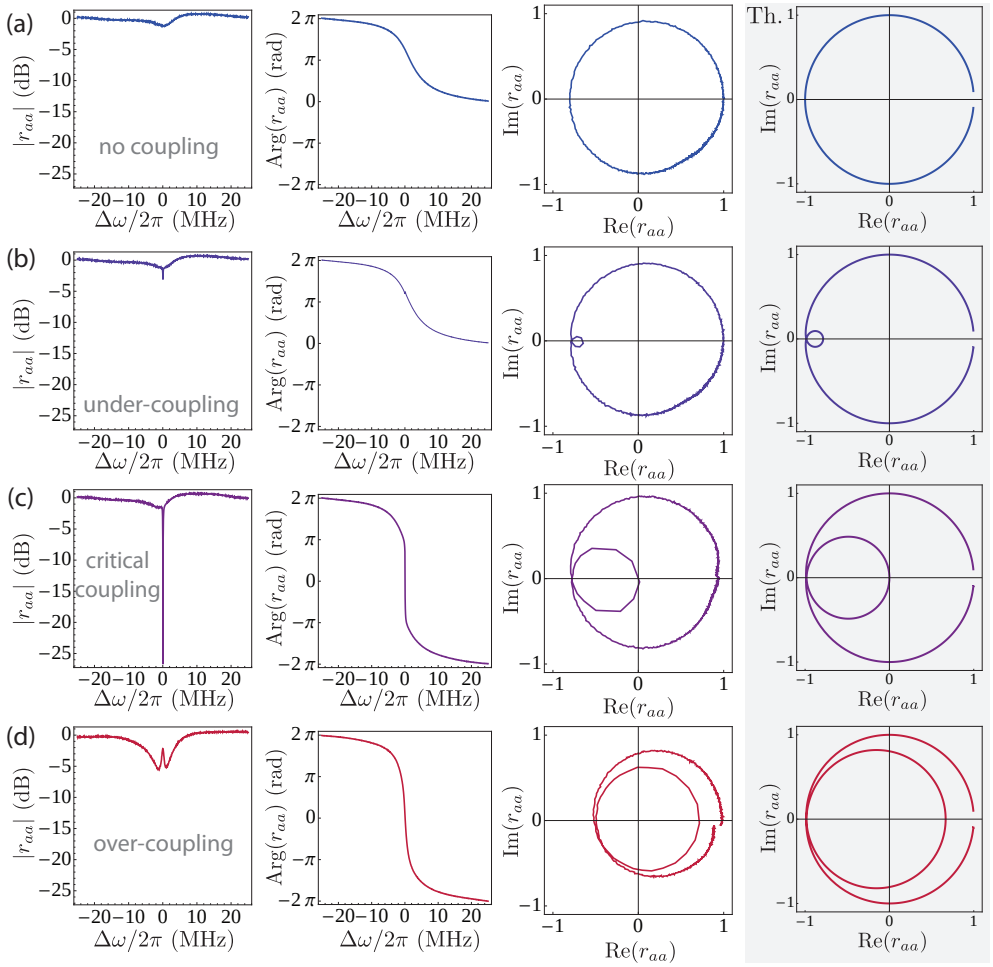

Figure 67: **3D design** - Reflection coefficient r_{aa} as a function of the frequency difference from the resonant frequency for various values of the pump power. *First column* Measured amplitude. *Second column* Measured phase. *Third column* Measured reflection coefficient in polar coordinates. *Fourth column* Theory, reflection coefficient in polar coordinates expected from Eq. (216). **(a)** No coupling ($C = 4|\chi p|^2/\kappa_a\kappa_m = 0$). **(b)** Under-coupling regime ($C = 0.12$). **(c)** Critical coupling ($C = 1$). **(d)** Over-coupling regime ($C = 5.1$).

9.2.4 *Kerr effect*

The pump amplitude will be varied in time to turn the memory on and off. It is therefore important to know by how much the pump power affects the resonance frequency of the buffer and memory modes. This can be addressed using the expressions for the Kerr effects associated with the JRM in section 3.1.6.

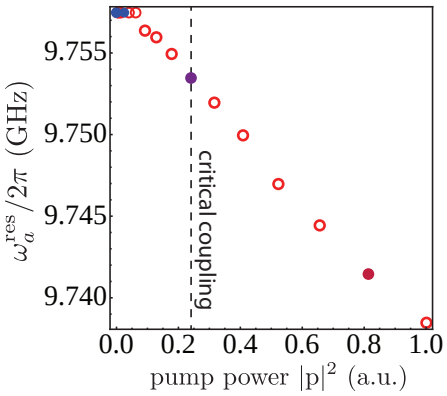

Figure 68: Measured buffer resonance frequency as a function of pump power $|p|^2$ in arbitrary unit. The filled circles correspond to the trace shown in Fig. 67 and the open circles corresponds to data not shown here.

Importantly, the cross-Kerr effect involving the pump are dominant here. Indeed, we are probing the resonators at low photon number (~ 100), thus the self-Kerr terms $(a^\dagger a)^2$ and $(m^\dagger m)^2$ as well as the cross-Kerr term $a^\dagger a m^\dagger m$ are negligible compared to the cross-Kerr involving the pump that is strongly driven. The correction to the resonance frequencies of mode a at rest is given by (see 3.1.6)

$$\begin{aligned} K_{ap}|p|^2 &= \frac{1}{16L_J^0}\cos\frac{\varphi}{4}Z_a\xi_a^2|\varphi_p|^2 \\ &= \frac{1}{16}\omega_a\xi_a|\varphi_p|^2. \end{aligned} \tag{217}$$

As derived in the previous section, the strong coupling regime is reached for

$$\chi|p| = \frac{\varphi_p}{4}\tan\frac{\varphi_{ext}}{4}\sqrt{\xi_a\xi_m\omega_a\omega_m} \sim \frac{\kappa_a}{2\sqrt{2}}. \tag{218}$$

Therefore, the frequency shift of the buffer mode induced by the pump in the strong coupling regime reads

$$K_{ap}|p|^2 \sim \frac{1}{(8\tan\frac{\varphi}{4})^2}\frac{\kappa_a^2}{2\xi_m\omega_m} \sim \frac{2\kappa_a}{\xi_m Q_a} \approx 2\pi\times 10\text{ MHz}. \tag{219}$$

Similarly, the frequency shift induced by the pump on the memory mode m can be estimated to

$$K_{mp}|p|^2 \sim \frac{\kappa_m}{2\xi_a Q_m} < 2\pi\times 1\text{ kHz}. \tag{220}$$

Similarly to what is observed in the experiment, the Kerr frequency shift is negligible on the memory cavity.

We can use the same expressions for the microstrip 2D design, and get

$$K_{ap}|p|^2 \sim \frac{\kappa_a}{2\xi_m Q_a} \approx \frac{2\pi \times 28 \text{ MHz}}{2 \times 0.1 \times 200} \approx 2\pi \times 1 \text{ MHz}. \tag{221}$$

The estimated value of the Kerr frequency shift is in agreement with the one measured on the buffer mode a and presented in 68. We observe a linear dependence with pump power and a shift of 20 MHz for the largest pump powers in the strong coupling regime.

9.2.5 *Estimation of the memory lifetime*

For small coupling rate $\gamma_{io}^m < \kappa_m$ in the under-coupled regime, the losses in the memory cavity become the dominant exit rate. The spectral width of the memory cavity that is measured across the buffer gives directly the memory loss rate κ_m. Indeed, for a detuning Δ much smaller than κ_a, the reflection coefficient reads

$$r_{aa} \approx -\frac{\gamma_{io}^m - \kappa_m + 2i\Delta}{\gamma_{io}^m + \kappa_m - 2i\Delta}. \tag{222}$$

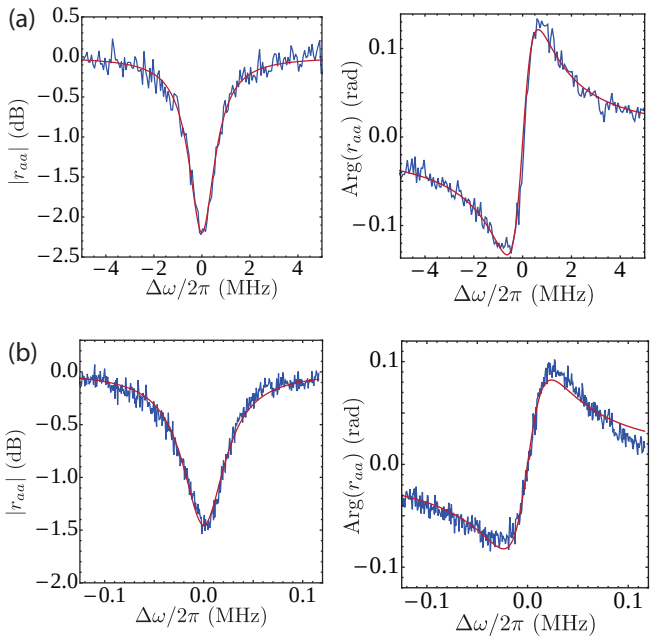

Figure 69: Amplitude and phase of the reflection coefficient r_{aa} as a function of frequency in the under coupled regime (low pump power). Zoom on data sets from Fig. 66(b) and Fig. 67(b). **(a)** For the 2D design the best fit using Eq. (222) corresponds to a coupling rate $\gamma_{io}^m = 2\pi \times 0.16$ MHz and a memory loss rate $\kappa_m = 2\pi \times 1.3$ MHz. **(b)** For the 3D design, $\gamma_{io}^m = 2\pi \times 4$ kHz and $\kappa_m = 2\pi \times 48$ kHz.

For the 2D design, whose measured reflection is shown in Fig. 69a, we get a loss rate $\kappa_m/2\pi = 1.3$ MHz. Therefore, the quality factor of the microstrip resonator

is $Q_m = \omega_m/\kappa_m \approx 7000$. From the loss rate we can estimate the memory lifetime $\tau_m = 1/\kappa_m = 120$ ns. The performance of the microstrip resonators is likely limited by strong radiation losses, which should be limited in the 3D cavity.

For the 3D design, the measured and predicted reflection coefficients are plotted on Fig. 69b. Note that the frequency scale is zoomed in by more than an order of magnitude compared to the 2D curves in Fig. 69a. We extract a loss rate $\kappa_m/2\pi = 48$ kHz leading to a quality factor of 160 000 and an estimated memory lifetime of $\tau_m = 1/\kappa_m = 3.3$ μs. This lifetime constitutes almost a 30-fold improvement compared to the 2D architecture. However, it is quite far from the record quality factors in fully closed cavities. As we will show later, these estimations are confirmed by time-controlled experiments of capture and storage.

9.2.6 *Estimation of the coupling rate*

In the limit of small coupling rate $\gamma_{io}^m \ll \kappa_a/2$, one can also extract the coupling rate from reflection measurements and using Eq. (222). The resulting coupling rate as a function of pump power is shown in Fig. 70. As expected from Eq. (206) the coupling rate is linear with pump power in the limit of small coupling.

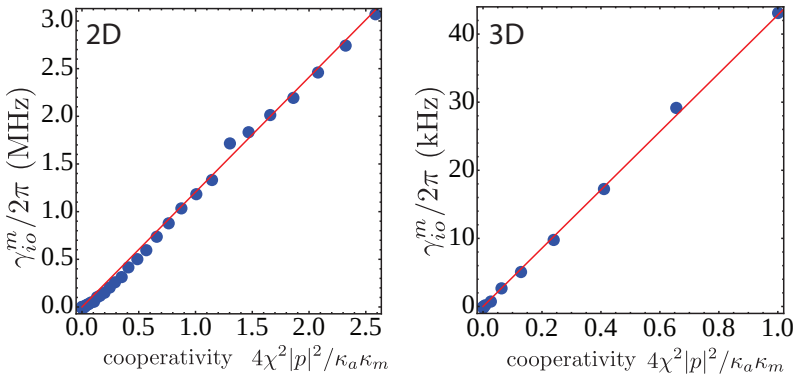

Figure 70: Dots: Read/write rate γ_{io}^m of the memory extracted from reflection measurements and represented as a function of the cooperativity $C = 4|\chi p|^2/\kappa_a\kappa_m$. Line: linear fit of the dots. The left panel corresponds to the 2D memory and the right one to the 3D memory.

9.3 DEMONSTRATION OF THE CATCH AND RELEASE OF A MICROWAVE PULSE

9.3.1 *Time-controlled storage and retrieval*

In a practical quantum network architecture, the quantum memory of each node must be able to store, process and exchange a quantum field in a time-controlled way. The temporal shape of the transmitted fields plays a crucial role in the efficiency of each node. Indeed, the temporal envelope of the field released by the sender memory must be adjusted to be efficiently captured by the receiver memory. For a finite memory bandwidth, the optimal temporal shape is symmetric by time reversal [121].

In principle in our device, it is possible to generate and capture time symmetric pulses by properly adjusting the pump amplitude in time. However, due to the Kerr effect discussed in section 9.2.4, finding the optimal pump temporal shape is a difficult problem. In what follows, we thus focus on the dual approach in which the temporal shape of an incoming coherent state is optimized so that it is most efficiently captured by a square pump pulse.

Let us first consider a sequence in which the memory records an incoming pulse before time 0 and then keep it stored. The corresponding pump amplitude remains constant at $t < 0$ and zero for $t > 0$, so that the input/output rate is given by $\gamma_{io}(t) = \gamma_0\theta(-t)$ where θ is the Heaviside function. The incoming pulse, sent before time 0 propagates on the transmission line towards the memory while the pump is on so that $\langle a_{in}(t)\rangle = f_{in}(t)\theta(-t)$. What is the temporal shape of this wave packet that maximizes the efficiency of its capture by the memory?

Here, by efficient, we mean that the memory keeps as much of the incoming energy as possible without releasing it. This corresponds to requesting that $\langle a_{out}(t)\rangle = 0$ at all times when the pump amplitude ensures that $\gamma_{io}(t) = \gamma_0\theta(-t)$. Given that the incoming pulse stops at time 0, this condition is met for $t > 0$ as long as the buffer mode a stays empty, which leads to

$$\begin{cases} \langle a_{out}(t)\rangle = 0 & \text{for } t < 0 \\ \langle a(t=0)\rangle = 0. \end{cases} \tag{223}$$

This criterion depends on negative times only so that its solutions $\langle a_{in}(t)\rangle = f_{in}(t)\theta(-t)$ can be found by considering a constant coupling $\gamma_{io}(t) = \gamma_0$ even at positive times.

9.3.1.1 *Absorption without reflection*

Let us first note that the poles of the Fourier transform of $\langle a_{in}(t)\rangle$ are all in the upper-half plane of the complex plane since it is non-zero only for $t < 0$. Moreover, the first line of Eq. (223) imposes that $\langle a_{out}(t)\rangle$ must be zero for $t < 0$,

thus the poles of its Fourier transform must all be in the lower-half plane of the complex plane.

This stringent condition can be satisfied since the reflection coefficient relating a_{out} to a_{in} input and output has poles and zeros that are perfectly fit for transforming poles of the upper-half plane into poles of the lower-half plane. Indeed, for large coupling rates $\gamma_{io}^m \gg \kappa_m$, the reflection coefficient reads

$$\langle a_{out}[\omega_a]\rangle = -\frac{(\kappa_a - \gamma_{io}^m + 2i\Delta)(\gamma_{io}^m + 2i\Delta)}{(\kappa_a - \gamma_{io}^m - 2i\Delta)(\gamma_{io}^m - 2i\Delta)}\langle a_{in}[\omega_a]\rangle. \tag{224}$$

By choosing the poles of the input signal $\langle a_{in}[\omega_a]\rangle$ to coincide with the zeros of the scattering coefficient, one gets an output field $\langle a_{out}[\omega_a]\rangle$ with poles in the lower half-plane only as requested.

Therefore, the optimal input signal is of the form

$$\langle a_{in}[\omega_a]\rangle = \frac{\alpha}{\gamma_{io}^m + 2i\Delta} + \frac{\beta}{\kappa_a - \gamma_{io}^m + 2i\Delta} \tag{225}$$

and leads to an output signal equal to

$$\begin{aligned} \langle a_{out}[\omega_a]\rangle \quad = \quad & -\alpha\frac{\kappa_a - \gamma_{io}^m + 2i\Delta}{(\kappa_a - \gamma_{io}^m - 2i\Delta)(\gamma_{io}^m - 2i\Delta)} && (226)\\ & -\beta\frac{\gamma_{io}^m + 2i\Delta}{(\kappa_a - \gamma_{io}^m - 2i\Delta)(\gamma_{io}^m + \kappa_m - 2i\Delta)}. && (227) \end{aligned}$$

In the time domain, the input field corresponds to an increasing exponential of the form

$$\langle a_{in}(t)\rangle = \alpha\theta(-t)e^{\frac{\gamma_{io}^m}{2}t} + \beta\theta(-t)e^{\frac{\kappa_a - \gamma_{io}^m}{2}t}. \tag{228}$$

Qualitatively, the first term is mostly absorbed by the memory at a rate γ_{io}^m and the second term is mostly absorbed by the buffer at the $\gamma_{io}^b = \kappa_a - \gamma_{io}^m$. Up to now, we have not considered the second line in Eq. (223), which ensures that a complete transfer to the memory has been performed. One must then find the right balance between α and β to verify $\langle a(t=0)\rangle = 0$.

9.3.1.2 *Complete transfer*

For a complete transfer, one must be sure that no fields remain in the buffer at $t = 0$ when the coupling is turned off. This constraint imposes that

$$\langle a(t=0)\rangle = \int_{-\infty}^{+\infty}\langle a[\omega_a]\rangle \mathrm{d}\omega_a = 0, \tag{229}$$

leading to

$$\kappa^{-1/2}\int_{-\infty}^{+\infty}\langle a_{in}[\omega_a]\rangle + \langle a_{out}[\omega_a]\rangle \mathrm{d}\omega_a = 0. \tag{230}$$

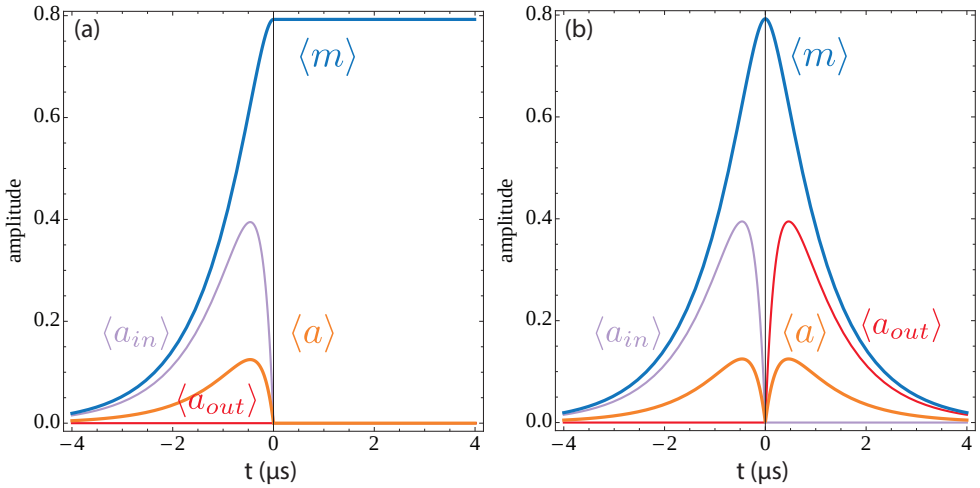

Figure 71: (a) Expected time dependence of the various mode amplitudes for the optimal temporal shape of the input field $\langle a_{in}\rangle$ and a pump amplitude turned off at time 0 so that $\gamma_{io}^m = \theta(-t) \times 2\ \mu\text{s}^{-1}$. Here, we assume $\kappa_a = 10\ \mu\text{s}^{-1}$ and $\kappa_m = 0$. (b) Same curves when the pump is kept on so that $\gamma_{io}^m = 2\ \mu\text{s}^{-1}$.

This condition is met when $\alpha = -\beta$. Hence the optimally absorbed input fields read

$$\langle a_{in}[\omega_a]\rangle \propto \frac{1}{\kappa_a/2 - \gamma_{io}^m}\left(\frac{1}{\gamma_{io}^m + 2i\Delta} - \frac{1}{\kappa_a - \gamma_{io}^m + 2i\Delta}\right) \tag{231}$$

$$\propto \frac{1}{(\gamma_{io}^m - \kappa_m + 2i\Delta)(\kappa_a - \gamma_{io}^m + 2i\Delta)} \tag{232}$$

and leads to an output field

$$\langle a_{out}[\omega_a]\rangle \propto \frac{-1}{\kappa_a/2 - \gamma_{io}^m}\left(\frac{1}{\gamma_{io}^m - 2i\Delta} - \frac{1}{\kappa_a - \gamma_{io}^m - 2i\Delta}\right) \tag{233}$$

$$\propto \frac{-1}{(\gamma_{io}^m - \kappa_m - 2i\Delta)(\kappa_a - \gamma_{io}^m - 2i\Delta)}. \tag{234}$$

We can now give the expressions of the optimally catched input signal in the time domain (see Fig. 71)

$$\boxed{\langle a_{in}(t)\rangle \propto \theta(-t)(e^{\frac{\gamma_{io}^m}{2}t} - e^{\frac{\kappa_a - \gamma_{io}^m}{2}t})}. \tag{235}$$

The first term ensures absorption without reflection, while the second term permits the complete transfer of the absorbed pulse from the buffer to the memory cavity. It is worth to note that the optimally captured signal is simply the time-reverse of a signal retrieved from an initially occupied memory. This retrieved signal can be observed experimentally on a_{out} by preparing the memory in a coherent state with the pump off, and then turning it on (or on Fig. 71b at $t > 0$).

With this signal shape at the input, no signal is reflected and $\langle a_{out}(t)\rangle = 0$ if the pump is turned off at time 0, and the field is stored in the memory mode m (see Fig. 71a). However, if the pump remains on at all times, the output field is given by (see Fig. 71b)

$$\boxed{\langle a_{out}(t)\rangle \propto \theta(t)(e^{-\frac{\gamma_{io}^m}{2}t} - e^{-\frac{\kappa_a - \gamma_{io}^m}{2}t})}. \tag{236}$$

Finally, in the special case of the strong coupling regime for which $\gamma_{io}^m = \kappa_a/2$, the above expression breaks down and the optimal signals are given by

$$\langle a_{in}(t)\rangle \propto \theta(-t)te^{\kappa_a t/2}, \tag{237}$$

$$\langle a_{out}(t)\rangle \propto \theta(t)te^{-\kappa_a t/2}. \tag{238}$$

9.3.2 *Catch and release of coherent pulses*

In this section, we demonstrate that the memory based on the JRM can store and release on demand a coherent pulse with the shape described above. The magnetic flux through the ring is chosen so that the buffer cavity frequency is $\omega_a/2\pi = 9.4356$ GHz, while the 3D cavity frequency is $\omega_m/2\pi = 7.8166$ GHz. The pump tone is thus applied at the difference frequency $\omega_p/2\pi = 1.649$ GHz.

The pulse sequence used for this experiment is shown in Fig. 73a. A constant pump amplitude is first applied on the device while the input signal described in Eq. (235) enters the memory at time $t < 0$. The input/output rate at this amplitude is $\gamma_{io}^m = 9\ \mu s^{-1}$. The pump is then quickly turned off at time 0 such that the input coherent state should be captured by the memory. Note that the field at the input is in a coherent state with about 10 photons on average.

At a later time τ, the pump is turned on again with the same amplitude in order to retrieve the content of the memory on the transmission line. After amplification by a low-noise amplifying setup, the output is down-converted to 40 MHz using a mixer and averaged 6×10^4 times using an oscilloscope.

It is possible to directly measure the input signal that is sent to the device by turning off the pump at all times. In this case, the measured average amplitude $\langle a_{out}(t)\rangle$ (top trace in Fig. 73b) is a direct reproduction of the undistorted input signal.

In the following measurements (traces below the top one in Fig. 73b) the pump is turned on before time 0 during memory writing and after time τ during memory readout as described above. As can be seen in Fig. 73b, almost no output signal is measured before time 0 as expected for the optimal pulse shape used at the input. Quantitatively, only 5% of the incoming pulse energy is reflected back before time 0.

When the pump is turned back on after a delay τ from 0 μs to 8 μs, the device releases the captured state back in the transmission line as can be seen in Fig. 73b.

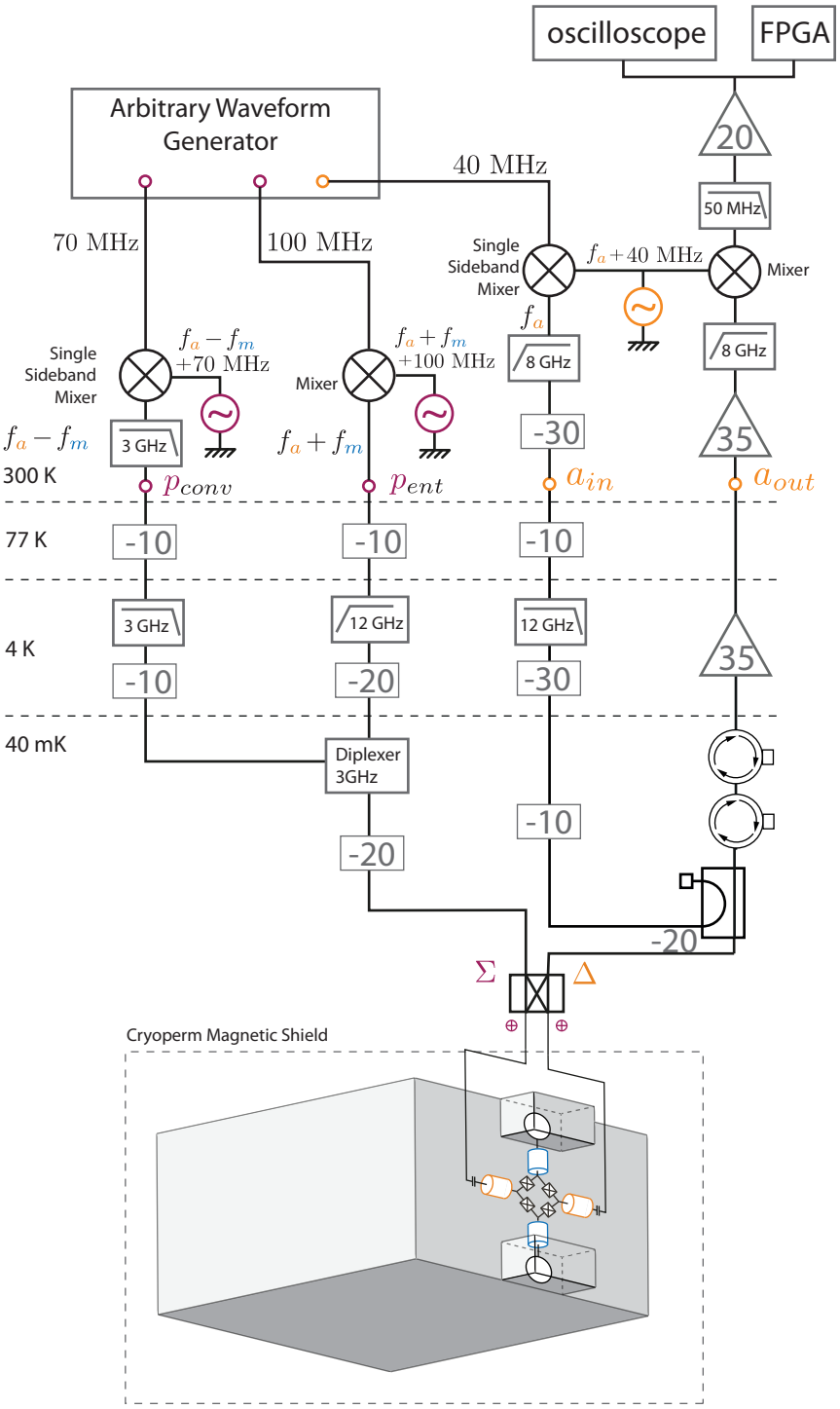

Figure 72: Scheme of the measurement setup. Boxes represent attenuators and triangle amplifiers whose gain is indicated in dB. The pulse sequences are generated by an arbitrary waveform generator whose output is upconverted using mixers. The output signal is downconverted to 40 MHz before being measured by an oscilloscope or an ADC coupled to an FPGA board.

Note that the temporal shape of the released pulse is indeed the time reverse of the optimal pulse we used.

Due to the finite lifetime of the cavity, the retrieved field is more and more damped as the storage time increases. The efficiency of the memory is defined as the ratio between the energy of the incoming wavepacket and the energy of the retrieved wavepacket. Interestingly, it can be estimated by the oscillating voltage measured with the oscilloscope alone (Fig. 73b). The total energy of the incoming wave packet scales as $\int_{-T}^{0} |\langle V_{out}^{\text{off}}(t)\rangle|^2 \mathrm{d}t$, which is measured when the pump is turned off. Here, T is an arbitrary temporal cutoff given by a few γ_{io}^{-1} ($T = 1$ μs for the 3D memory and $T = 200$ ns for the 2D memory). Moreover, the total energy of the outgoing wavepacket scales as $\int_{\tau}^{\tau+T} |\langle V_{out}^{\text{on}}(t)\rangle|^2 \mathrm{d}t$, with τ the release time of the memory. More precisely, if one does not want to overestimate the efficiency by incorrectly counting the noise of the measurement output as useful energy, it is good to subtract the background noise, so that the efficiency reads

$$\eta = \frac{\int_{\tau}^{\tau+T} |\langle V_{out}^{\text{on}}(t)\rangle|^2 - |\langle V_{out}^{\text{off}}(t)\rangle|^2 \mathrm{d}t}{\int_{-T}^{0} |\langle V_{out}^{\text{off}}(t)\rangle|^2 \mathrm{d}t} \tag{239}$$

The measured efficiency is shown in Fig. 73c as a function of the storage time τ. It endures an exponential decay as a function of delay time $\eta(\tau) = \eta_0 e^{-\tau/\tau_m}$, where $\tau_m = 3.3$ μs (107 ns for the 2D memory) is in quantitative agreement with the one found from the spectral measurements in Fig. 69.

Note that it is not possible to distinguish the effects of energy damping and dephasing from that measurement alone since we are only measuring the average of the field amplitude. However, measurements presented in the next section (Fig. 82) demonstrate that dephasing is negligible.

9.3.3 *Efficiency*

From figure 74c, one can estimate the limit efficiency of the memory to be $\eta_0 = 80\%$. It is similar to the 81% efficiency of the mechanical memory [129] and much greater than the efficiency achieved in the spin-ensembles. In a recent work at Santa Barbara [33], the efficiency of a memory based on a superconducting microwave cavity has been well optimized up to 97.4% [33], which is required for fault-tolerant deterministic quantum protocols.

Indeed, the efficiency of our device can be improved by optimizing again the temporal shape of the input field and the pump. To reach better efficiency, one needs to take into account the deformation of the waveform during propagation as well as higher order non-linearities such as the Kerr-effect that bring slight deviations from the optimal waveform. An effective way to maximize the efficiency would be to use a linear optimization algorithm starting from the theoretical optimal waveform such that simplex or genetic algorithms.

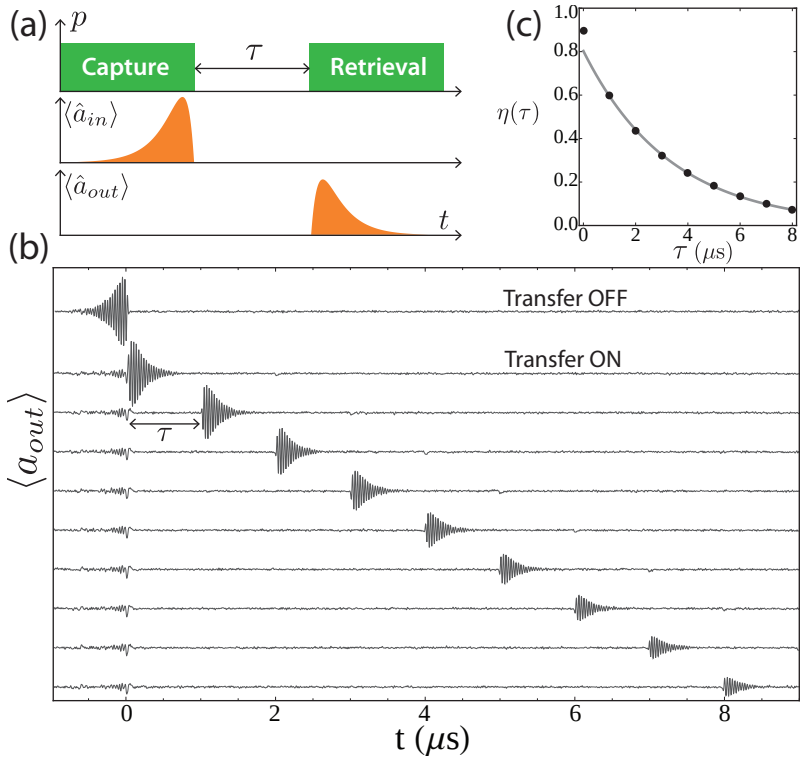

Figure 73: **3D memory device (a)** Capture, store and release protocol. Pulse sequences for the pump field p (green) at the difference frequency $\omega_p = \omega_a - \omega_m$, the input field $\langle a_{in} \rangle$ and the resulting output field $\langle a_{out} \rangle$ (orange). The temporal shape of the input field is chosen in order to optimize the capture efficiency. **(b)** Time traces of the amplitude of the output field down converted to 40 MHz and averaged 6×10^4 times. The top trace is measured without pump and reveals the optimized input signal. The following traces correspond to the sequence of (a) with increasing delay τ between capture and retrieval from 0 μs to 8 μs. **(c)** Dots: retrieval efficiency η as function of delay τ. η is defined as the ratio of the retrieved energy normalized to the input energy. Plain line: exponential decay $\eta_0 e^{-\tau/\tau_m}$ characterizing the memory lifetime. Best fit obtained for $\eta_0 = 80\%$ and $\tau_m = 3.3$ μs.

9.3.4 *Lifetime*

The measured lifetime is smaller than what is typically achieved with superconducing resonators where bare 3D cavity have been demonstrated to reach 10 ms [138] in the context of circuit QED. This clearly leaves room for improvement in the future for our device.

The origin of this rather short lifetime is currently under investigation, but there are evidences that the holes that separate the 3D cavity from the antennas bring spurious losses due to surface roughness. It might be possible to improve the lifetime by at least an order of magnitude by making slight modifications in the current design and fabrication techniques.

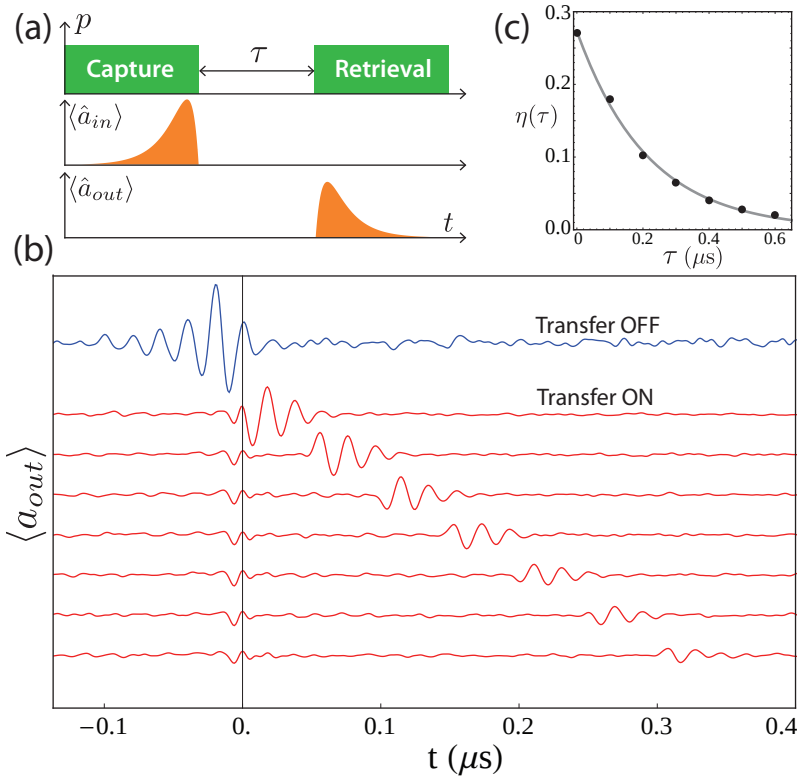

Figure 74: **2D memory device (a)** Capture, store and release protocol. Pulse sequences for the pump field p (green) at the difference frequency $\omega_p = \omega_a - \omega_m = 2\pi \times 3.27$ GHz with $\omega_a = 2\pi \times 5.54$ GHz and $\omega_m = 2\pi \times 8.81$ GHz, the input field $\langle a_{in} \rangle$ and the resulting output field $\langle a_{out} \rangle$ (orange). The temporal shape of the input field is chosen in order to optimize the capture efficiency. **(b)** Time traces of the amplitude of the output field down converted to 40 MHz and averaged 3×10^4 times. The top trace is measured without pump and reveals the optimized input signal. The following traces correspond to the sequence of (a) with increasing delay τ between capture and retrieval from 0 ns to 300 μns. **(c)** Dots: retrieval efficiency η as function of delay τ. η is defined as the ratio of the retrieved energy normalized to the input energy. Plain line: exponential decay $\eta_0 e^{-\tau/\tau_m}$ characterizing the memory lifetime. Best fit obtained for $\eta_0 = 27\%$ and $\tau_m = 107$ ns.

We note that the superconducting memory of the Santa Barbara group was demonstrated to reach comparable lifetimes of 3 μs even if it is claimed in the letter that 45 μs can be reached [33].

The mechanical memory achieved lifetimes of 28 ms thanks to the high quality factor and very low frequency (10 MHz) of the mechanical mode. As a result the main drawback is that, for such low frequencies, spurious thermal fluctuations quickly degrade the coherence properties of the field. Hence, the effective coherence lifetime is estimated to be 90 μs [129]. The spin-ensemble memory have typical coherence lifetime of a few tens of μs [132]. Therefore, it good to acknowledge that state of the art microwave memories have not yet overcome few tens of microseconds of storage time, similarly to the decoherence of superconducting qubits.

group	Paris	Paris	UCSB	Chalmers	Boulder	Saclay
reference	unpublished	[144]	[33]	[34]	[129]	[31]
storage medium	microstrip cavity	3D cavity	CPW cavity	CPW cavity	mechanical membrane	spin ensemble
coupling type	frequency conversion	frequency conversion	tunable inductor	tunable resonator	frequency conversion	tunable resonator
lifetime	107 ns	3.3 μs	3 μs	18μs	90 μs	$\sim$ 10 μs
access time	35 ns	110 ns	50 ns	14 ns	$\sim$ 20 μs	$\sim$ 30 ns
# operations	3	30	60	1300	$\sim$ 5	$\sim$ 300
efficiency	27 %	80 %	97.4 %		80 %	2×10^{-4}
repetition time	0	0	0	0	$\sim$ 10 ms	$\sim$ 5 s
entanglement generator	yes	yes	no	no	yes	no

Table 2: Summary of performance of quantum memories for microwave radiations. Note that Santa Barbara group is claiming lifetime of 45 μs lifetime is claimed with similar cavities but it is still not demonstrated.

9.3.5 *Number of operations within a lifetime*

A useful memory needs to be able to write and read several pulses during its storage time. The read/write time is given by the inverse of the coupling rate $\tau_{io} = 1/\gamma_{io}^m = 110$ ns (same order of magnitude to the Santa Barbara group with 50 ns). The number of operations is quantified by the product $\gamma_{io}^m \tau_m = 30$ (60 for Santa Barbara). To put this number in perspective, this figure of merit is the main drawback of the mechanical memory for which access times are very long with typical values of 20 μs leading to about 5 operations only within a lifetime currently.

All the measurements presented until now deal with coherent states of microwave radiation, and are thus in the classical regime. It is possible to show that the phase of the coherent states is well preserved and demonstrate that the memory should work in the quantum regime, but we will see in the next section that one can go a step beyond and entangle the memory with a propagating mode.

10

ENTANGLEMENT OF THE MEMORY WITH A PROPAGATING FIELD

Promisingly, the device cannot only be used as a memory but also as an entanglement generator. In a second experiment, we demonstrate the generation of an EPR state distributed between the propagating mode a_{out} and the memory mode m. This feature gets the role of the Josephson mixer closer to the node of a quantum network based on continuous variables in which entanglement is shared over the network.

Up to now, we have presented the circuit mostly as a quantum memory such as the one in Ref. [33, 34]. In fact, using the versatility of the Josephson mixer, we can also generate a pair of entangled states (similarly to what was done in chapter 6) shared between the memory and a propagating mode of the transmission line.

When a pump tone is applied at the sum frequency $\omega_p = \omega_a + \omega_m$ with both modes initially in the vacuum, an EPR pair is generated through spontaneous parametric down-conversion and distributed between the buffer and memory modes. The buffer being strongly coupled to the transmission line, the entangled field continuously leaks out in the propagating mode a_{out}. As a result the memory mode at frequency ω_m gets entangled with a mode of the transmission line at frequency ω_a.

At a later time, the content of the memory mode m can be released in the conversion regime by applying a pump tone at $\omega_p = |\omega_a - \omega_m|$ as described in the last section.

This device, which is both able to generate continuous variable entanglement and to store it efficiently, offers new perspectives in the context of quantum networks [122, 121] for the realization of quantum protocols involving various hybrid quantum system interfaced in the microwave domain.

In this experiment, the entanglement generation consists in a sequential time-controlled protocol. Therefore, the witnessing method introduced in part 6 cannot be used in this context.

Indeed, the entanglement witness consisted in recombining two continuously generated entangled mode on a second Josephson mixer. By measuring a drop of the fluctuation at the output of the witness below what is classically allowed for separable state, we were able to conclude that the input state where exhibiting quantum correlation beyond what is classically allowed.

Here, such a witness could have been set up, however it would have been much more challenging due to the sequential nature of the protocol. The setup would have consisted in a second quantum node based on the Josephson mixer as a

witnessing node operated in a sequential way. The witnessing protocol would then consist in two steps.

First, the entangled propagating mode generated by the entangling node must be captured efficiently by the witnessing node. Thus, a pump pulse is applied at the sum frequency on the entangling node while a pump at the difference frequency is applied on the witnessing node with the right temporal shape. Second, the entangling node must release the other part of the pair from its memory into the transmission line while the witnessing node must recombine this entangled propagating mode with the content of its memory in amplification regime. Thus, a pump pulse is applied at the difference frequency on the entangling node with the right temporal shape while a pump at the sum frequency is applied on the witnessing node.

Finally, by measuring the resulting fluctuations at the output of the witnessing node, one would measure a drop of the fluctuations below the classical limit if the state is entangled.

Remarkably, note that each step is the time reversed of the other. The first step consists in entangling the two nodes and the second step to disentangling them. This strategy is an elegant way to demonstrate entanglement but it is much more challenging experimentally. We have therefore used a more direct approach.

10.1 Experimental demonstration of entanglement distribution

The entanglement demonstration presented in this work consists in a brute-force noise correlation measurement based on a fast acquisition card in the same spirit as the experiments carried out in Zurich [8, 145], Munich [28] and Boulder [32].

The goal is to perform a full tomography of the two-mode (memory and propagating mode) quantum state in order to infer its covariance matrix and extract its entanglement strength. The strategy consists in recording the distribution of the measurement outcomes of all four quadratures of the two-mode state at room temperature on a large number of realizations. Then, using an ON-OFF subtraction technique, one can extract the tiny signal corresponding to the quantum microwave field out of the noise added by the amplifying setup and reconstruct its covariance matrix.

10.1.1 *Field Programmable Gate Array (FPGA)*

The noise correlation measurement has been performed using a Field Programmable Gate Array (FPGA) board able to process and sort the microwave signal with a high repetition rate. Such a high repetition rate is compulsory since we did not use a quantum limited amplifier. Hence, a large uncorrelated noise hides the signal. In order to discriminate the tiny microwave field drowned in the noise,

one need to acquire a well resolved distribution within a short time in order to avoid phase and gain drifts.

We programmed an Innovative Integration X6-RX board ourselves using a block-diagram language from Xilinx based on the Matlab Simulink software. The block-diagram is then compiled into VHDL before being flashed into the FPGA.

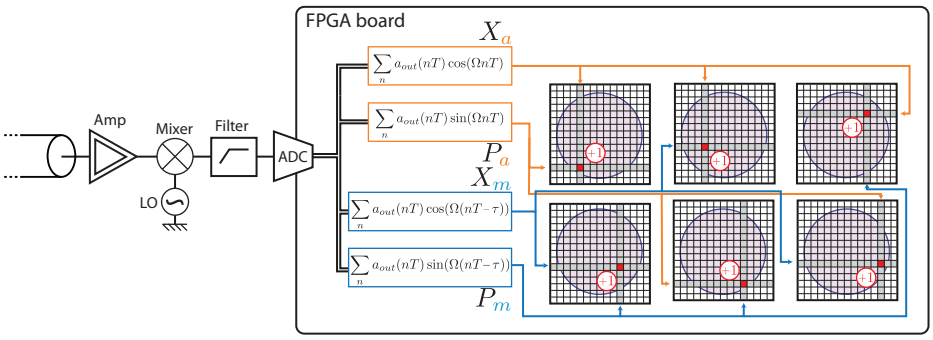

Figure 75: Schematic of the room-temperature analogue signal processing followed by the FPGA digital processing. The FPGA board updates 6 histograms in real time representing projections of the Husumi Q function of the two-mode state on 6 possible quadrature phase spaces.

The microwave signal at the output of the amplification setup is first analogically down-converted, filtered and reamplified. Then, it is digitized at a rate of 160 MS.s^{-1} by the ADC of the FPGA board.

The board is programmed for multiplying the resulting traces by four different preloaded sequences run in parallel. It enables to perform a digital IQ demodulation with temporal envelopes that match the temporal modes of the buffer and memory after the storage time delay τ. The demodulated trace is then summed over the whole sequence leading to the measurement outcomes X_a, P_a, X_m and P_m. At the end of each sequence, the measurement outcomes are sorted and incremented into the 6 correlation histograms. The histograms are 128×128 array with a depth of 10 bits per address. At the end of the whole measurement, the histogram are uploaded into a computer through a PCI express port.

10.1.2 *Measured quadrature histograms*

The pulse sequence used in the experiment starts by a square pump pulse at $\omega_p = \omega_a + \omega_m = 17.28$ GHz during 500 ns that generates an EPR state (Fig. 76a). While one part of the pair is stored in the memory mode m, the other part propagates in the transmission line, is amplified by a low-noise amplifying detection setup and recorded using the FPGA board. After a delay $\tau = 200$ ns, a square pulse is applied on the pump field at $\omega_p = \omega_a - \omega_m$ with an amplitude such that the output rate is $\gamma_{io}^m = 2\pi \times 1.5$ MHz as in the capture and retrieval measurement presented Fig. 73 and lasting for 500 ns. This pulse releases the memory state into a new propagating mode at frequency ω_a, which is then amplified and

measured using the heterodyne detection setup. At the end of a sequence, one realization of the four mode quadratures X_a, P_a and X_m, P_m have been measured. The measurement outcomes are incremented in 6 histograms corresponding to all combinations of quadratures. The pulse sequence is repeated 4×10^7 times with a repetition rate of 10 μs. The protocol is performed with the entangling pump turned on and off every minute to avoid pump phase and gain drifts. The whole measurement took approximately 10 minutes. Finally, the normalized distribution of the measurement outcomes at the output of the amplification setup are obtained and shown on Fig. 76 for the entangling pump turned on (b), turned off (c) and subtraction of the two previous normalized distributions (d).

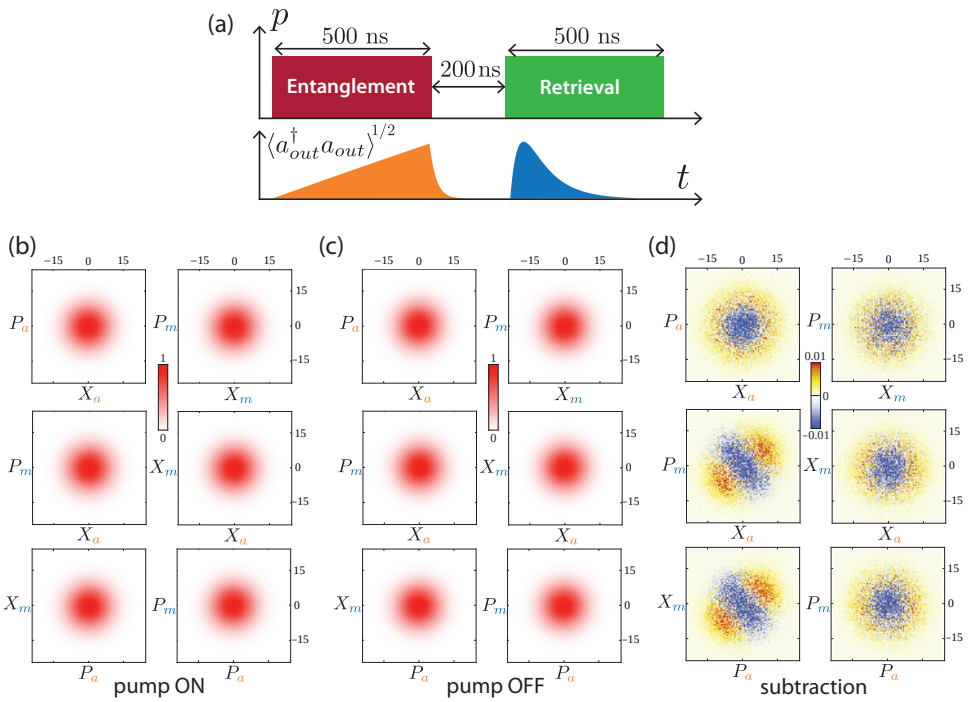

Figure 76: Entanglement between memory and propagating mode. **(a)** Scheme of the pulse sequence. Top: pump amplitude p is shown in red for $\omega_p = \omega_a + \omega_m$ and in green for $\omega_p = \omega_a - \omega_m$. Bottom: temporal shape of output noise amplitude. **(b)** distribution of the measurement outcomes at the output of the amplification setup for the entangling pump turned on, **(c)** turned off and **(c)** subtraction of the distributions. The axes are calibrated in $\sqrt{\#\text{photon}}$.

It is important to realize that, despite the detuning between memory mode and buffer mode frequencies, the two parts of the EPR pair are collected in two different time bins of the field a_{out} at the same frequency and using same amplification setup. Thus, the scale for the mode a and m are the same and one needs to calibrate one amplification setup only.

The subtracted histograms do not represent an actual probability distribution as they contain negative parts. However, they give a hint of the nature of the correlations between quadratures of different modes. The positive and negative parts in the subtracted distribution naturally arise from the subtraction of two

normalized gaussian distributions where the first one has a higher variance than the second as sketch on Fig. 77. Hence, in the single-mode histograms along (X_a, P_a) and along (X_m, P_m), a phase-independent increase in the fluctuations is observed. This corresponds to the thermal state produced in a mode by tracing out the EPR state on the other mode.

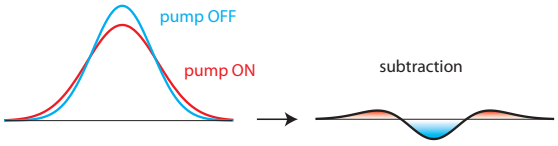

Figure 77: Subtraction of two normalized gaussian distributions

In contrast, the histograms along the quadratures of two different modes (X_a,P_m) and (P_a,X_m) exhibit a large anisotropy along the bisector (diagonal) indicating correlations between memory and propagating modes. For instance, the measurement outcomes X_a and P_m are likely to have the same sign when the entanglement pump is on. These correlations need to be characterized quantitatively in order to demonstrate whether or not they are non-classical.

10.1.3 *Inferring memory mode properties from the measurement*

It is useful to introduce some notations for describing the modes that are actually measured in the experiment. The quadratures of two modes are measured in this experiment. First, the one emitted on a_{out} by the device during the entanglement pulse, which is amplified into a mode A_{out} that is measured by the FPGA board. Then after a time τ, the one, also emitted on a_{out}, during the memory release pulse, which is amplified into a mode M_{out}.

Using results of section 6.4 to describe what happens during the entanglement step, one can express the first outgoing mode $a_{out,1}$ as a function of the modes at the input of the memory during the entanglement pulse,

$$a_{out,1} \quad = S^{\dagger} a_{in} S \quad = \cosh(r) a_{in,1} + e^{i\varphi_P} \sinh(r) m^{\dagger}_{in,1}, \tag{240}$$

where φ_P is the phase of the pump and $G = \cosh^2 r$ is the power direct gain of the Josephson mixer, when it is used as a parametric amplifier. The vacuum state at the inputs is then converted into a two-mode squeezed vacuum state $|Sq\rangle = S\,|0\rangle_{a_{out,1}}\,|0\rangle_m = \cosh(r)^{-1} \sum \tanh(r)^n\,|n\rangle_a\,|n\rangle_m$.

The output signal $a_{out,1}$ is then amplified by a low noise amplifying setup with a gain G_{amp}. The uncorrelated noise added by the amplifying setup is modeled by a bosonic operator h_{in} whose effective temperature is mainly determined by

the noise temperature of the cold HEMT amplifier (see Fig. 72). In the end, the actually measured amplitude reads

$$\begin{aligned} A_{out} &= \sqrt{G_{amp}}a_{out,1} + \sqrt{G_{amp}-1}h^{\dagger}_{1,in} \\ &= \sqrt{G_{amp}}(\cosh(r)a_{in,1} + e^{i\varphi_P}\sinh(r)m^{\dagger}_{in,1}) + \sqrt{G_{amp}-1}h^{\dagger}_{1,in}. \end{aligned} \tag{241}$$

The expresion of M_{out} can be derived similarly by considering extra losses coming from the imperfect efficiency η of the memory storage. The memory mode is converted into a propagating mode on a_{out}, but at a later time τ compared to the previously measured field. Let us denote it as $a_{out,2}$. The losses of the device can be modeled by the contribution of an extra mode $m_{in,2}$, which is uncorrelated with any other mode so that we get

$$\begin{aligned} a_{out,2} &= \sqrt{\eta}S^{\dagger}m_{in,1}S + \sqrt{1-\eta}m_{in,2} \\ &= \sqrt{\eta}[\cosh(r)m_{in,1} + e^{-i\varphi_P}\sinh(r)a^{\dagger}_{in}] + \sqrt{1-\eta}m_{in,2} \end{aligned} \tag{242}$$

and

$$\begin{aligned} M_{out} &= \sqrt{G_{amp}}a_{out,2} + \sqrt{G_{amp}-1}h^{\dagger}_{2,in} \\ &= \sqrt{G_{amp}}(\sqrt{\eta}[\cosh(r)m_{in,1} + e^{-i\varphi_P}\sinh(r)a^{\dagger}_{in,1}] + \sqrt{1-\eta}m_{in,2}) \\ &\quad + \sqrt{G_{amp}-1}h^{\dagger}_{2,in}. \end{aligned} \tag{243}$$

With these definitions, one can now model the measured quadrature histograms (Fig. 76b,c) as marginals of the Husumi Q-function of (A_{out}, M_{out}) [146]. The moments of the Q-function, hence of the measured histograms, are simply the normally ordered moments of the field operators.

$$\langle A^{p_a}_{out}M^{p_m}_{out}A^{\dagger q_a}_{out}M^{\dagger q_m}_{out}\rangle = \int_{\mathbf{C}^2}\alpha^{p_a}\mu^{p_m}(\alpha^*)^{q_a}(\mu^*)^{q_m}Q(\alpha,\mu)\mathrm{d}^2\alpha\mathrm{d}^2\mu. \tag{244}$$

Using this equality, it becomes possible to determine the covariance matrix of the fields A_{out} and M_{out} and to infer from there the covariance matrix of the fields $a_{out,1}$ and m, which can witness entanglement between them.

10.2 CALIBRATION OF THE MEASURED AMPLITUDES

In order to demonstrate entanglement, it is necessary to calibrate the quadrature measurements. The essential assumption in the calibration is that input fields are in vacuum at thermal equilibrium given that the cryostat temperature is 45 mK $\ll \hbar\omega/k_b \approx 0.4$ K. This implies that $\langle\Delta a^2_{in}\rangle = \langle\Delta m^2_{in}\rangle = 1/2$. Note that in this device, m_{in} is a virtual port modeling the 3D cavity losses. This

assumption is strongly backed up by experiments in circuit QED with similar cavities performed in our group (see the end of section II.A in the supplementary material of Ref. [64]).

The principle of the calibration was introduced by the Zurich group during the first observation of two-mode squeezing at microwave frequency [8]. It relies on the fact that zero point fluctuations feed the input of an amplifier. By measuring the total noise power at the end of the detection setup as a function of the gain of the amplifier, one can estimate the total amplitude gain of the setup, from the amplifier input to the measurement apparatus. The extra noise added by the measurement setup is considered constant and does not alter the calibration.

The Josephson mixer that implements a quantum memory can also be seen as a phase-preserving amplifier, meaning that the output fluctuations are $\langle \Delta a_{out,1}^2 \rangle = \cosh^2(r)\langle \Delta a_{in,1}^2 \rangle + \sinh^2(r)\langle \Delta m_{in,1}^2 \rangle = \cosh(2r)/2$ where $\cosh(r)$ is the amplitude gain. This happens when the pump frequency is $\omega_p = \omega_a + \omega_m$. We can then use the above technique to infer the memory and propagating mode quadrature amplitudes for a given measurement outcome recorded by the FPGA. In this section, we first present a way to calibrate the gain of the quantum memory acting as an amplifier, then we present the method we used to reconstruct the covariance matrix of the fields at the output of the quantum node.

10.2.1 *Measurement of the amplitude gain*

In the experiment, entanglement is generated between the memory and a propagating mode by sending a square pump pulse at frequency $\omega_p = \omega_a + \omega_m$ with an initially empty memory. If instead the memory is initially occupied by a coherent state, the same pulse will result in parametric amplification of that coherent state. Since, the pump is not continuous, we have developed a protocol to perform an accurate measurement of this pulsed amplitude gain.

First, as in Fig. 73, we capture an incoming coherent state in the quantum memory by sending a pulse with average power P_{in} at the level of the waveform generator (see Fig. 72). Then we turn on the entanglement pulse by applying a pump at the sum frequency $\omega_p = \omega_a + \omega_m$. It provides a direct amplitude gain $\sqrt{G} = \cosh(r)$ on the memory mode m and a cross amplitude gain $\sqrt{G-1} = \sinh(r)$ from the memory mode m to the transmission line mode a_{out}. Finally we retrieve the amplified captured state in the transmission line by turning on the pump tone at $\omega_p = \omega_a - \omega_m$ again.

We can repeat this procedure without the entanglement pulse, thus without amplitude gain: $\sqrt{G} = \cosh(0) = 1$. The ON/OFF ratio of the squared integrated amplitude of the retrieved pulse (Fig. 78) directly provides a value for the gain $G = \cosh^2(r)$. Importantly, this protocol enables to determine the gain independently of the losses due to the inefficiency of the device, since they are the damping of the cavity is the same for ON and OFF amplifier regimes.

As shown in Figure 78, we repeat this measurement for an increasing incoming wave packet energy. The amplification process is linear on this energy scale, and it is important to check that the device in not saturated. The ratio of the slopes gives a gain $G = \cosh^2(r) = 2.29$ for the Josephson mixer, in this pulsed amplifier regime.

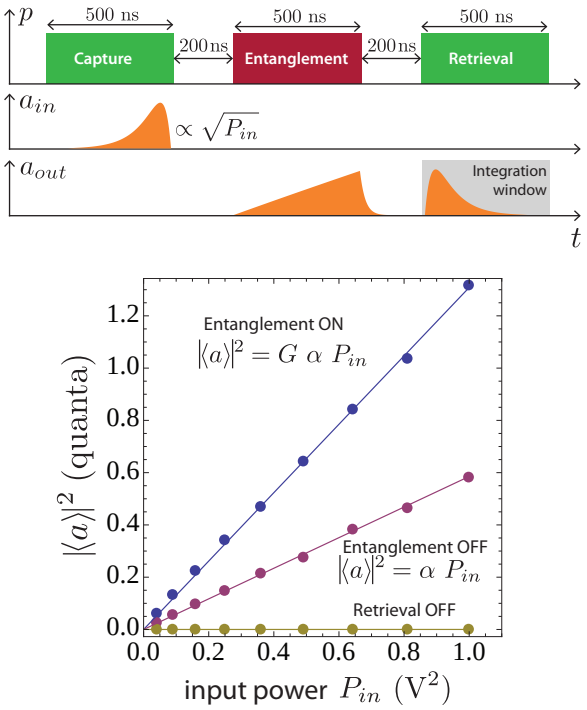

Figure 78: Amplitude gain measurement protocol. The upper panel presents the timing of the pulsed measurement. The lower panel presents the measured squared amplitude of the retrieved field as a function of the power of the source that generates the captured wave (square of the modulation amplitude expressed at the level of the waveform generator of Fig. 72). The squared amplitude gain is given by the ratio between the blue (ON) and purple (OFF) slopes.

10.2.2 *Determination of the gain of the detection setup*

It is now possible to use the measured noise power of the zero point fluctuations to infer the total gain G_{amp} of the measurement setup. In that purpose, one must find a way to subtract the uncorrelated noise from the amplifying setup

h_{in}. Assuming that the modes $a_{in,1}$ and $m_{in,1}$ are in the vacuum state at rest, Eq. (241) leads to

$$\begin{aligned}\langle A^{\mathrm{r}}_{out} A^{r\dagger}_{out}\rangle &= G_{amp}\langle a_{out,1}a^{\dagger}_{out,1}\rangle_{|Sq\rangle} + (G_{amp}-1)\langle h^{\dagger}_{in,1}h_{in,1}\rangle_{thermal} \\ &= G_{amp}(\cosh^2(r)\langle a_{in,1}a^{\dagger}_{in,1}\rangle_{|0\rangle} + \sinh^2(r)\langle m^{\dagger}_{in,1}m_{in,1}\rangle_{|0\rangle}) \\ &\quad +(G_{amp}-1)\langle h^{\dagger}_{in,1}h_{in,1}\rangle_{thermal} \\ &= G_{amp}\cosh^2(r) + (G_{amp}-1)\langle h^{\dagger}_{in,1}h_{in,1}\rangle_{thermal}.\end{aligned} \tag{245}$$

By subtracting the variances of A_{out} when the pump is turned on (r>0) or off (r=0), one gets

$$\langle A^{\mathrm{on}}_{out}A^{on\dagger}_{out}\rangle - \langle A^{\mathrm{off}}_{out}A^{\mathrm{off}\dagger}_{out}\rangle = G_{amp}(\cosh^2(r)-1). \tag{246}$$

Using the calibration $\cosh^2(r) = 2.29$ above and the Q function in phase space A_{out} given by the measured histogram in Fig. 76d, the gain is found to be

$$\boxed{G_{amp} = \frac{1}{\cosh^2(r)-1}\int \mathrm{d}^2\alpha\ |\alpha|^2(Q^{\mathrm{on}}(\alpha) - Q^{\mathrm{off}}(\alpha))}. \tag{247}$$

10.3 CHARACTERIZATION OF THE ENTANGLED STATE

10.3.1 *Reconstruction of the covariance matrix*

The states that are produced by the memory are Gaussian states. In particular the EPR state is Gaussian with zero mean (see Eq. (137)). As such, it is fully characterized [70] by its covariance matrix $\mathcal{V}$, whose elements are given by the symmetrically ordered second moments in their quadratures $\mathcal{V}_{ij} = 2\langle\xi_i\xi_j + \xi_j\xi_i\rangle$ as shown in Eq. (141). These elements are also the second order moments of the Wigner distribution [146] $\mathcal{V}_{ij} = 4\int_{\mathbf{C}^4}\xi_i\xi_j W(\boldsymbol{\xi})\mathrm{d}\boldsymbol{\xi}$. Since the measured histograms are not Wigner distributions but Husumi Q functions, it is convenient to introduce the Q-covariance matrix (or normally ordered covariance matrix), whose elements are $(\mathcal{V}_Q)_{ij} = 4\int_{\mathbf{C}^4}\xi_i\xi_j Q(\boldsymbol{\xi})\mathrm{d}\boldsymbol{\xi} = \mathcal{V}_{ij} + \delta_{ij}$.

The experiment leads to a direct measurement of $\mathcal{V}_Q$ for the modes A_{out} and M_{out}. We will now see how to relate it to the covariance matrix $\mathcal{V}$ for the modes $a_{out,1}$ and $a_{out,2}$. For the sake of clarity in the following expressions, we identify $a \equiv a_{out,1}$ (since $a_{out,1}$ corresponds to what was directly produced on mode a) and $m \equiv a_{out,2}$ (since $a_{out,2}$ comes from what was stored in the memory). Besides, without loss of generality, we assume that the mean value of the field operators are zero $\langle a\rangle = \langle m\rangle = 0$, which is experimentally verified.

The measured histograms give an access to the Q-covariance matrix $\mathcal{V}_Q^{Meas,\mathrm{on}}$ and $\mathcal{V}_Q^{Meas,\mathrm{off}}$. If we assume that the modes $h_{in,1}$ and $h_{in,2}$, which model the noise added by the detection setup, are in a thermal state without correlations, one gets from the first equalities in Eqs. (241) and (243) that

$$\mathcal{V}_Q^{Meas,\mathrm{on}} = G_{amp}(\mathcal{V} + \mathbb{I}_4) + (G_{amp}-1)\mathcal{V}^{\mathrm{thermal}}. \tag{248}$$

where

$$\mathcal{V}^{\text{thermal}} = 2 \begin{pmatrix} \langle h^\dagger_{in,1} h_{in,1} \rangle & 0 & 0 & 0 \\ 0 & \langle h^\dagger_{in,1} h_{in,1} \rangle & 0 & 0 \\ 0 & 0 & \langle h^\dagger_{in,2} h_{in,2} \rangle & 0 \\ 0 & 0 & 0 & \langle h^\dagger_{in,2} h_{in,2} \rangle \end{pmatrix}_{\text{thermal}} . \quad (249)$$

This expression can also be used when the entanglement pulse is turned off, in which case $\mathcal{V} = \mathbb{1}_4$, so that

$$\mathcal{V}_Q^{Meas,\text{off}} = 2G_{amp}\mathbb{I}_4 + (G_{amp} - 1)\mathcal{V}^{\text{thermal}}. \quad (250)$$

Finally, the added noise contribution can indeed be removed and one gets a way to extract the covariance matrix $\mathcal{V}$ between the memory mode and the propagating mode from Fig. 76d since

$$\boxed{\mathcal{V} = \frac{1}{G_{amp}}(\mathcal{V}_Q^{Meas,\text{on}} - \mathcal{V}_Q^{Meas,\text{off}}) + \mathbb{I}_4}. \quad (251)$$

10.3.2 *Measured covariance matrix*

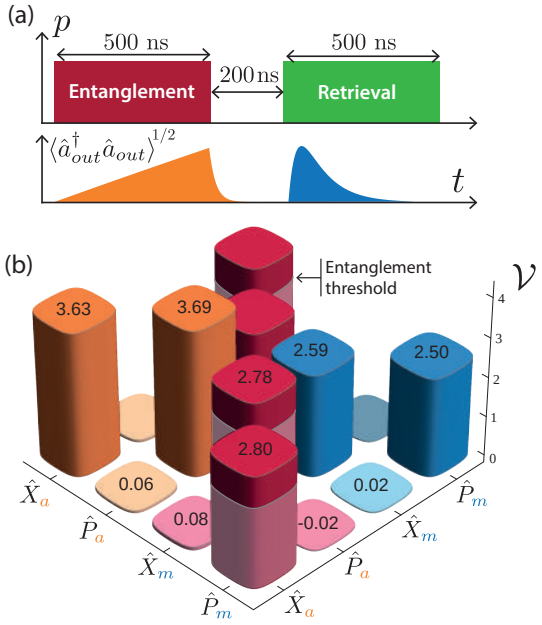

Figure 79: Entanglement between memory and propagating mode. **(a)** Scheme of the pulse sequence. Top: pump amplitude p is shown in red for $\omega_p = \omega_a + \omega_m$ and in green for $\omega_p = \omega_a - \omega_m$. Bottom: output noise amplitude in time. **(b)** Measured two-mode covariance matrix. The convention used is such that the vacuum state corresponds to the unity matrix. The 2×2 block- diagonal matrices in orange and blue represent the single mode a and m covariance matrices. The off-diagonal matrices in red represent the correlations between modes. Correlations go beyond the classically allowed greyed regions which demonstrates entanglement.

It is meaningful to decompose $\mathcal{V}$ in four 2×2 block matrices.

$$\mathcal{V} = \begin{pmatrix} \boldsymbol{\alpha} & \boldsymbol{\chi} \\ \boldsymbol{\chi}^T & \boldsymbol{\mu} \end{pmatrix}. \tag{252}$$

The diagonal blocks $\boldsymbol{\alpha}$ and $\boldsymbol{\mu}$ are the single-mode covariance matrices for a and m respectively. Since each mode of the EPR pair is in a thermal state once the other part of the pair has been dismissed (traced out) as shown in Eq. (134), there is no correlation between the quadratures X and P of a single mode (a or m) and the variances ΔX^2 and ΔP^2 are almost equal. For mode a, by definition of the calibration process, one gets $\mathcal{V}_{11} \approx \mathcal{V}_{22} \approx \cosh(2r)/4 = 3.66$ (Fig. 79b). The memory mode is less occupied because of losses at a rate τ_m^{-1} during the entanglement pulse and the waiting time $\tau = 200$ ns so that $\mathcal{V}_{33} \approx \mathcal{V}_{44} \approx 2.55$, which is indeed close to $\mathcal{V}_{11} e^{-(\tau_{\text{entang}}+\tau)/\tau_m} \approx 2.9$. Conversely, the off-diagonal blocks $\boldsymbol{\chi}$ correspond to the correlations between modes. These should be zero for a thermal state. In each experiment, the phase of the pump field was optimized to put all the weight of the correlations in the two terms $\mathcal{V}_{14} \approx \mathcal{V}_{23} \approx 2.79$.

10.3.3 *Reconstruction of the Wigner distribution*

Assuming that the state is Gaussian, one can reconstruct its Wigner function from its covariance matrix by computing the eigenvalues and the eigenvectors of the 2×2 covariance submatrices. The eigenvectors gives the orientation of the ellipse axes and the square root of the eigenvalues gives the major and minor radii. As shown in Fig. 80, the single mode Wigner contour corresponds to a thermal state. In contrast, X_m equal to P_a (and X_a equal to P_m) to a better precision than level of vacuum fluctuations, which is a sign of entanglement between the two modes a and m. Note that the fact that the correlations are maximal between (X_a, P_b) and (P_a, X_b) and not (X_a, X_b) and $(P_a, -P_b)$ is only determined by the phase reference used during the experiment.

10.3.4 *Evidence of entanglement*

10.3.4.1 *Qualitative proof of entanglement*

As demonstrated previously in Eq. (336), two modes are entangled if their covariance matrix verifies the following inequality

$$(\sqrt{|\det \boldsymbol{\alpha}|} - 1)(\sqrt{|\det \boldsymbol{\mu}|} - 1) > |\det \boldsymbol{\chi}|. \tag{253}$$

Note that this inseparability inequality is a sufficient criterion for any two-mode state, gaussian or not. As shown in Fig. 79, the measured off-diagonal elements indeed overcome this threshold, demonstrating the entanglement between the memory mode m and the propagating mode $a_{out,1}$.

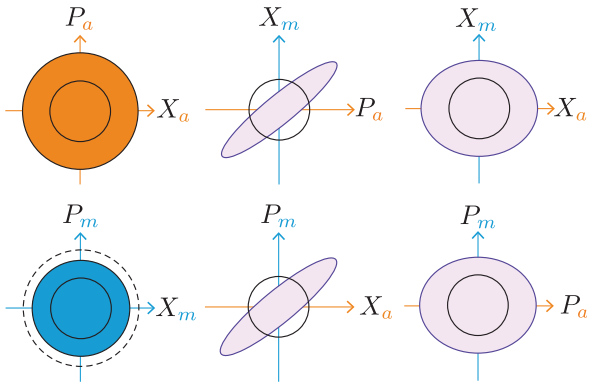

Figure 80: Reconstructed contours of the Wigner distributions. The dashed line in the (X_m, P_m) phase space allows to compare the memory thermal state with the size of the contour in the (X_a, P_a). The thick circles in the center of each plot represent the Wigner contour of the vacuum states.

10.3.4.2 *Quantifying entanglement*

Similarly to what was done with propagating modes in section 6, one can quantify the amount of entanglement between the two modes by the logarithmic negativity E_N. It corresponds to an upper bound for distillable entanglement that is computable for Gaussian state using from the covariance matrix with Eq. (337). Here, the memory and the propagating modes share $E_N = 1.36$ entangled bits (e-bits).

Now that we have demonstrated the ability of the device to generate and preserve entanglement between the memory and a transmission line, let us investigate how long can the entanglement be preserved.

10.3.5 *Lifetime of the entangled state*

The measurement can be repeated for various storage times τ. For each measurement, the covariance matrices and the contour of the Wigner distributions are reconstructed (Fig. 81). As expected, the temperature of the memory mode decays with storage time due to the finite memory lifetime. Moreover the extent of the incursion of the Wigner contour below the vacuum fluctuation level (black circle) decreases with time, meaning that the entanglement strength also decreases with time.

More quantitatively, the amplitude $\sqrt{|\det \boldsymbol{\mu}|}$ of the memory mode fluctuations decreases exponentially with τ (Fig. 82b) as expected from the experiment with coherent states. This leads to a relaxation time for the memory of $T_1 = 2.3 \pm 0.1$ μs in agreement with the memory lifetime τ_m measured using coherent states in the same cool down of the device[1]. The small variations in the noise of the

1 This is not the same lifetime as in Fig. 73. Both measurements were done on the same device, but were separated by a thermal cycle of the dilution refrigerator during which the lifetime had decreased

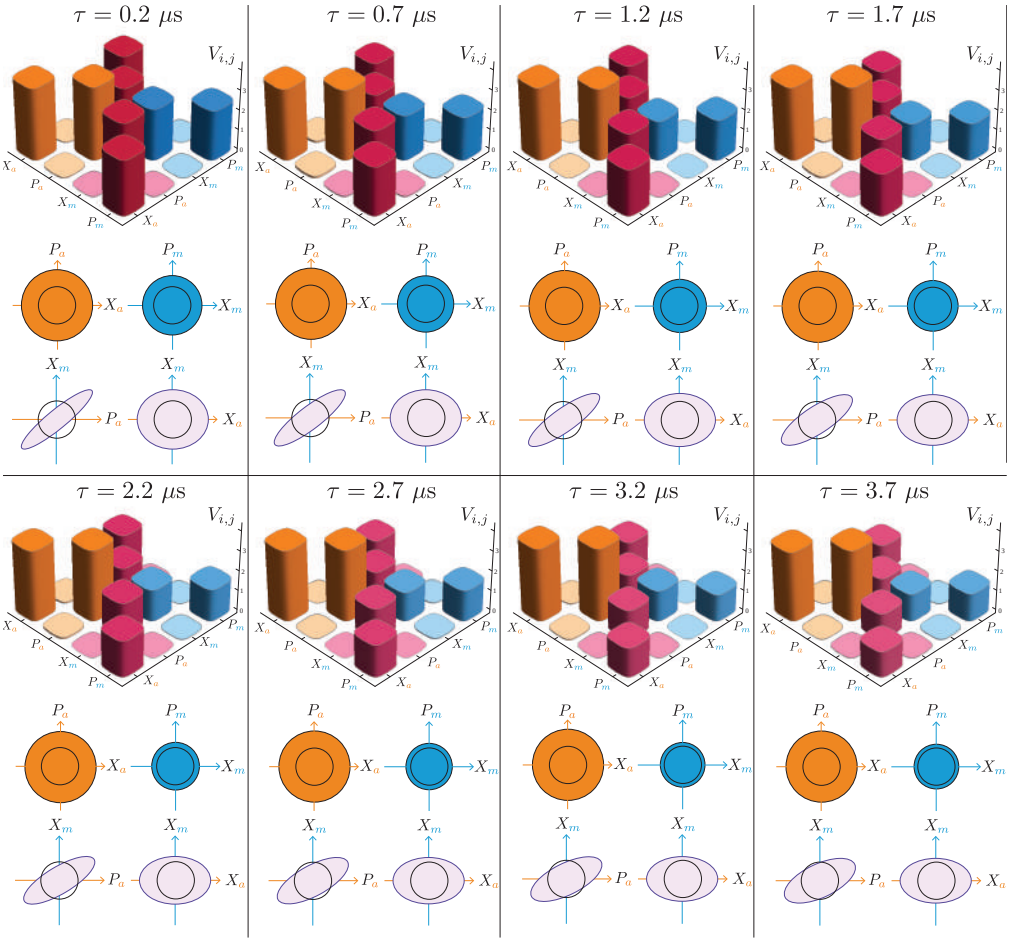

Figure 81: Reconstructed covariance matrices and contours of the Wigner distribution as a function of the storage time τ.

propagating mode $\sqrt{|\det\boldsymbol{\alpha}|}$ with τ give a sense of the measurement uncertainty (Fig. 82b) since this covariance terms should be constant of τ. Interestingly, the two-mode correlations also decay exponentially (Fig. 82c). The corresponding characteristic time is the decoherence time $T_2 = 4.5 \pm 0.1\ \mu$s of the memory.

Importantly, the fact that $T_2 \approx 2T_1$ demonstrates that energy relaxation dominates all decoherence mechanisms during the storage of a quantum state. The logarithmic negativity also decreases with τ as shown in Fig. 82d.

from 3.3 μs to 2.3 μs. We do not understand the origin of this decrease. Note that the lifetime varies as a function of magnetic flux in the Josephson ring in an indeterminate manner.

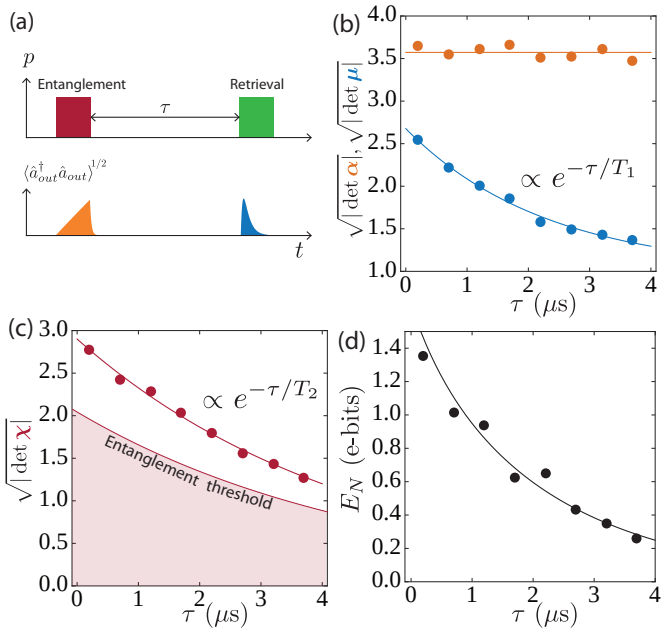

Figure 82: Covariance matrix and entanglement as a function of the storage time τ. (a) Pulse sequence with tunable storage time τ. (b) Dots: diagonal terms of the covariance matrix $\mathcal{V}$ giving the energy of each mode. Lines: average value (for α) and exponential fit (for β). The decay rate of the terms in β gives the energy relaxation time $T_1 = 2.3 \pm 0.1$ μs. (c) Dots: Off-diagonal amplitudes in $\mathcal{V}$ representing the coherence between memory and propagating modes. Line: exponential fit, whose rate sets the decoherence time $T_2 = 4.5 \pm 0.1$ μs. Correlations above the entanglement threshold ($E_N = 0$) demonstrate entanglement between memory and propagating modes. (d) Dots: Logarithmic negativity E_N measuring the entanglement between modes. Line:

10.4 CONCLUSION

In conclusion, we have realized quantum node based on a hybrid 2D/3D superconducting circuit. The efficient capture, storage and retrieval of a coherent state was demonstrated. Moreover, the device permits the generation and storage of entangled states distributed between the node and photonics channels. The versatility of the device paves the way for complex quantum communication protocols in the microwave domain such as continuous variable quantum teleportation as detailed below. Besides, it provides a useful resource for 3D cavities where the on-demand extraction of a field quantum state was needed. This could be used to implement readout and feedback in cavity networks or even quantum computation with the memory field itself [147, 37]. Finally, superconducting qubits can easily be embedded in this device, which could lead to protected quantum memories [4] and even protected quantum computing with microwave fields [147, 37].

The main results of this part are the following.

- Description of a quantum memory based on a high internal quality factor 3D superconducting cavity dynamically coupled by a Josephson mixer both able to store and generate entanglement.
- Successful implementation of state-of-the-art device with a time-bandwidth product of 30 and 80% efficiency.
- Demonstration of distribution of entanglement between the memory and propagating microwave radiations.
- First step toward quantum network based on hybrid quantum information processing connecting continuous variables and quantum bits.

The main unpublished results of this part are the following.

- Demonstration of the behavior of the preliminary version of the quantum memory that was based on a microstrip 2D resonator instead of a 3D cavity in Fig. 60 and 74.
- Derivation of the input/output coupling rate (197).
- Characterization of the quantum memory using reflectometry measurements 9.2.3.
- Measurement of the input/output coupling rates in Fig. 70.
- Review of the performances of the various kinds of quantum memories for microwaves in Table 2.

10.5 PERSPECTIVES

In order to illustrate the potential applications of our device, we describe here a basic quantum network made of two quantum nodes. Here we describe the teleportation protocol inspired by the review of Braunstein and Van Loock [70].

The simplest formalism to describe continuous-variable quantum teleportation is based on the Heisenberg representation [70]. Alice intends to teleport the state in her memory mode $m_A(t_s)$ at starting time t_s into the memory of Bob $m_B(t_f)$ at final time t_f. The teleportation protocol is schematically represented on Fig. 83 and detailed here.

- EPR state generation by Bob

  First, Bob applies a pump tone at the sum frequency $\omega_p = \omega_a + \omega_m$ in order to generate an EPR state shared between the transmission line and the memory at time t_1,

$$\begin{aligned} a_{out,B}(t_1) &= \cosh r_B a_{in,B}(t_s) + \sinh r_B m_B^\dagger(t_s) \\ m_B^\dagger(t_1) &= \cosh r_B m_B^\dagger(t_s) + \sinh r_B a_{in,B}(t_s) \end{aligned} . \tag{254}$$

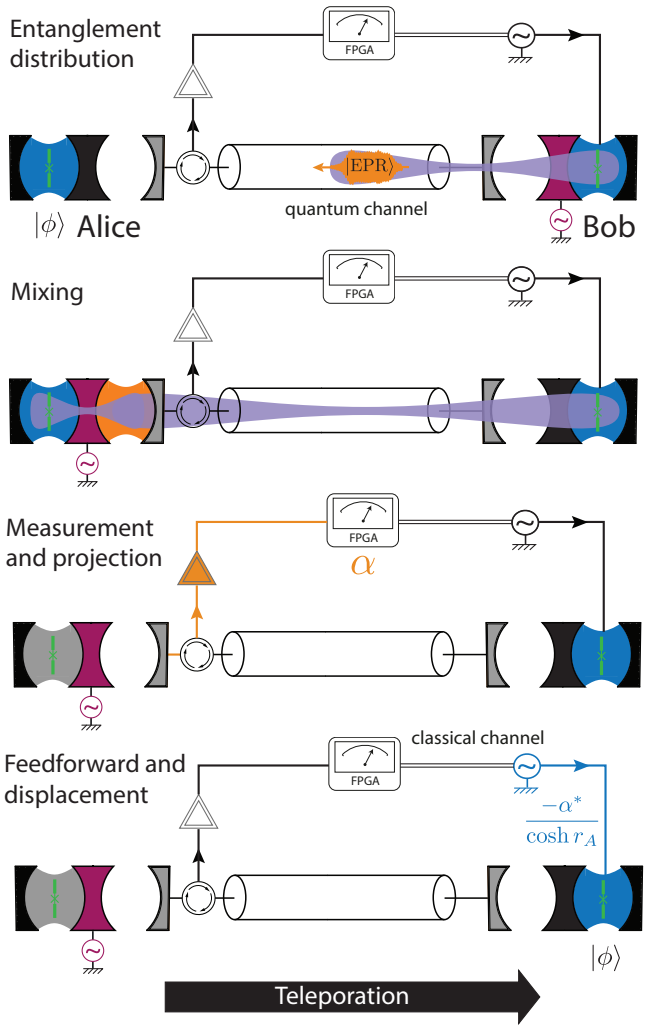

Figure 83: Continuous-variable quantum teleportation protocol

– Entanglement distribution to Alice

  Then, the propagating mode is sent to Alice. By matching the modes, the input mode of Alice at time t_2 reads

$$a_{in,A}(t_2) = a_{out,B}(t_1). \tag{255}$$

– Mixing of the EPR state and the state to teleport by Alice

  Alice then applies a pump tone at the sum frequency $\omega_p = \omega_a + \omega_m$ in order to mix and amplify the mode entangled with Bob's memory and the mode to teleport (note that the phase of the pump is different than for Bob).

$$\begin{aligned} a_{out,A}(t_3) &= \cosh r_A a_{out,B}(t_1) - \sinh r_A m_A^\dagger(t_s), \\ m_A^\dagger(t_3) &= \cosh r_A m_A^\dagger(t_s) - \sinh r_A a_{out,B}(t_1). \end{aligned} \tag{256}$$

  Note that this step has corrupted the content of Alice's memory.

It is convenient to rewrite Eq. (256) under the form

$$m_B^\dagger(t_1) = \frac{\sinh r_A}{\cosh r_A} m_A^\dagger(t_s) - (a_{out,B}(t_1) - m_B^\dagger(t_1)) + \frac{a_{out,A}(t_3)}{\cosh r_A}. \quad (257)$$

By noticing that $(a_{out,B}(t_1), m_B(t_1))$ are in an EPR state, we can write

$$m_B(t_1) = \underbrace{\tanh r_A m_A(t_s)}_{\text{to teleport}} - \underbrace{e^{-r_B}(a_{in,B}^\dagger(t_s) - m_B(t_s))}_{\text{EPR correlated}} + \underbrace{\frac{a_{out,A}^\dagger(t_3)}{\cosh r_A}}_{\text{to be measured}}. \quad (258)$$

– Measurement and projection of the output of Alice

The output of the Alice device must be amplified and read out at room temperature. The measurement outcome associated with the operator $a_{out,A}(t_3)$ is α.

– Feedforward and state teleportation to Bob

The measurement outcome is sent through a classical channel to Bob. Finally, Bob displaces the content of its memory by the measurement outcome complex conjugate once divided by the amplitude gain of the amplification performed by Alice such that, for large r_A and r_B,

$$\begin{aligned} m_B(t_f) &= m_B(t_1) - \frac{\alpha^*}{\cosh r_A} \\ &\approx m_A(t_s) - \underbrace{e^{-r_B}(a_{in,B}^\dagger(t_s) - m_B(t_s))}_{\to 0} + \underbrace{\frac{a_{out,A}^\dagger(t_3) - \alpha^*}{\cosh r_A}}_{\to 0}. \end{aligned} \quad (259)$$

The state has been successfully teleported with a perfect fidelity for large gain $r_a, r_B \gg 1$. However, every defect inducing decoherence will decrease the fidelity of the protocol [72]. Note also that, owing to the amplification performed by Alice, the overall fidelity is less sensitive to the measurement uncertainty due to the factor $1/\cosh r_A$.

Part V

APPENDIX

A

QUANTUM CIRCUITS

In this first appendix, I will introduce the theoretical tools needed in the following parts. In particular, a definition of the propagating quantum fields and their relation to resonant fields using the quantum Langevin equation are given. This derivation follows the lectures of Michel Devoret at the College de France [148] as well as the appendix of the reviews on quantum circuits [149, 63].

A.1 CIRCUIT QUANTIZATION

Fabry-Perot resonators used in Cavity QED, lumped-element LC resonators and planar resonators used in cavity QED can all be modeled as harmonic oscillators. When isolated, all these physical systems behave as photon boxes preserving quantum coherence of the electromagnetic mode.

The electromagnetic Lagrangian is defined by

$$\mathcal{L} = \int\int\int_V \frac{\epsilon_0}{2} E^2 - \frac{1}{2\mu_0} B^2 d^3x. \tag{260}$$

The case of the lumped LC oscillator is enlightening. The electromagnetic energy oscillates between electrostatic energy located in the capacitor C associated to the charges Q accumulated on the plates and magnetic energy associated to the magnetic flux Φ in the inductive coil L (Fig.84).

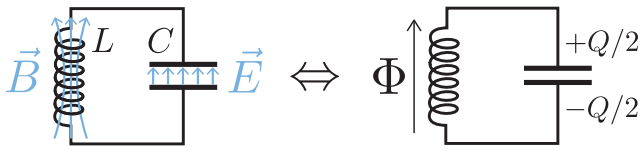

Figure 84: LC circuit

The Lagrangian as a function of the charge Q and flux Φ can be reduced to

$$\mathcal{L} = \frac{Q^2}{2C} - \frac{\Phi^2}{2L}. \tag{261}$$

In this circuit, the Kirchhoff's laws set the kinetic relations between the flux Φ and the charge Q

$$\Phi = -L\dot{Q}, \qquad\qquad Q = C\dot{\Phi}. \tag{262}$$

Hence, the charge Q and flux Φ are the canonical conjugated variables of a system verifying the following relations

$$\frac{\partial \mathcal{L}}{\partial \dot{Q}} = -L\dot{Q} = \Phi, \qquad \frac{\partial \mathcal{L}}{\partial \dot{\Phi}} = C\dot{\Phi} = Q. \tag{263}$$

In the canonical quantization, the flux coordinate Φ and its conjugate momentum Q can be promoted into quantum operators obeying the commutation relation

$$\boxed{[\Phi, Q] = i\hbar}. \tag{264}$$

Then, the Hamiltonian of the quantized circuit reads

$$H = \dot{\Phi}Q - \mathcal{L} = \frac{Q^2}{2C} + \frac{\Phi^2}{2L}. \tag{265}$$

Similarly to the standard procedure for the quantization of a mechanical harmonic oscillator, one can express the conjugated variables Q and Φ as a function of the creation and annihilation operators a and $a^\dagger$ satisfying the commutation relation $[a, a^\dagger] = 1$

$$\Phi = \sqrt{\frac{\hbar Z}{2}}(a + a^\dagger), \qquad Q = -i\sqrt{\frac{\hbar}{2Z}}(a - a^\dagger). \tag{266}$$

where $Z = \sqrt{L/C}$ is the characteristic impedance of the electromagnetic mode. Also, for the sake of simplicity, we have dropped the hat notation from quantum operators.

Finally, we can put the Hamiltonian in the following form

$$\boxed{H = \hbar\omega_r(a^\dagger a + 1/2)} \tag{267}$$

where $\omega_r = 1/\sqrt{LC}$ is the natural resonance frequency[1] of the LC oscillator.

The stationary states of the Hamiltonian are the Fock states $|n\rangle$. They represent states for which the number of quanta n in the electromagnetic mode is well defined. We have $a^\dagger a|n\rangle = n|n\rangle$, where $a^\dagger a$ is the number operator.

A.2 DISSIPATION AND INPUT/OUPTUT FORMALISM

In general, electromagnetic circuits always suffer from dissipation. The problem is that linear dissipative elements, such as resistors, cannot be modeled using a closed quantum system since resistors evolve irreversibly. Following the idea of Caldeira-Leggett, the dissipation can actually be modeled by coupling the isolated system to a large ensemble of non-dissipative modes i.e. a large ensemble of LC-oscillators. The simplest modeling consists in coupling the isolated system to a semi-infinite transmission-line which indeed contains an infinity of propagating modes.

1 For the sake of simplicity, we use the word frequency for ω_r and $\omega_r/2\pi$. The first is expressed in rad.s^{-1} and the second in Hz

A.2.1 *The transmission line*

A transmission line can be modeled as a succession of N infinitesimal lumped LC circuits (see Fig.85). The inductance $\ell\delta x$ represents the infinitesimal inductance of a length δx of the central conductor and the capacitance $c\delta x$ represents the infinitesimal capacitance from the central conductor to the shielding ground on a length δx. This transmission line itself is non-dissipative since all of its constitutive elements are reactances (i.e. imaginary impedances). Remarkably, the number of modes handled by this circuit is equal to the number of LC lumped elements. Thus, a semi-infinite line constitutes an infinite bath of mode and effectively acts as a dissipative impedance viewed from one side of the line as highlighted by Nyquist in 1928 [115].

A.2.2 *Impedance of a semi-infinite transmission line*

A simple recursive reasoning enables us to calculate the impedance of a semi-infinite transmission line and incorporate a dissipative environment in the model. The impedance Z_{n+1} of a line containing $n+1$ infinitesimal lumped elements (see Fig.85) can be expressed as a function of the impedance Z_n

$$Z_{n+1} = \left[\left(Z_n + \frac{j(\ell\delta x)\omega}{2}\right) \parallel \frac{1}{j(c\delta x)\omega}\right] + \frac{j(\ell\delta x)\omega}{2}. \tag{268}$$

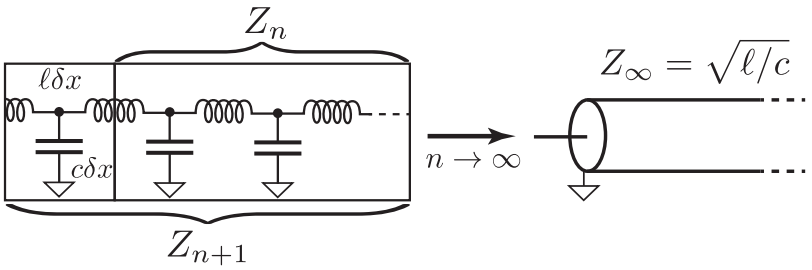

Figure 85: Impedance of a transmission line

If we consider the line to be semi-infinite, we see that impedance converges towards a fix point Z_∞ of this recursive equation. In other words, adding one extra element doesn't change anymore the overall impedance, leading to the equation

$$Z_\infty = (Z_\infty + \frac{j(\ell\delta x)\omega}{2}) \parallel (\frac{1}{j(c\delta x)\omega}) + \frac{j(\ell\delta x)\omega}{2}. \tag{269}$$

Hence the semi-infinite transmission line impedance Z_∞ reads

$$\boxed{Z_\infty = \sqrt{\frac{\ell}{c}}\sqrt{1 - \frac{\omega^2\ell c\delta x^2}{4}} \underset{\delta x\to 0}{\longrightarrow} \sqrt{\frac{\ell}{c}}}. \tag{270}$$

For a continuous line, one may take $\delta x \to 0$ so that the cut-off frequency for propagation $\omega_c = 2/(\delta x\sqrt{\ell c})$ disappears. Remarkably, the impedance Z_∞ turns dissipative (real) whereas the system is only constituted of non-dissipative elements. The apparent dissipative behavior is due to the ability of the line to send the input energy towards infinity. The bath generated by the line dilutes the input energy in the continuum of propagating modes.

A.2.3 *Propagating modes in the transmission line*

In this section, I will show how a bath of propagating modes can be quantized in the same way as harmonic oscillator modes. This approach provides solid grounds for the physics I have probed experimentally. In order to model propagating mode

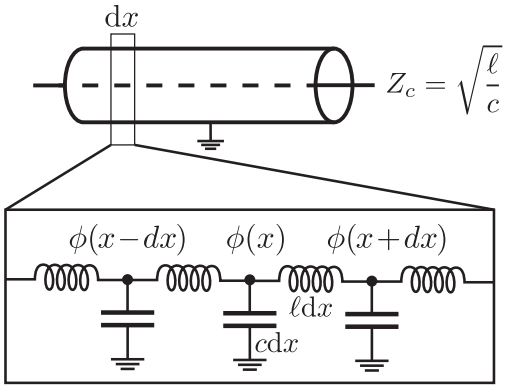

Figure 86: The infinite transmission line

on a transmission line, it is convenient to introduce the local flux variable $\phi(x,t)$ associated to the voltage $V(x,t)$ across the line at the position x defined as (see Fig.86)

$$\phi(x,t) = \int_{-\infty}^{t} V(x,\tau)\mathrm{d}\tau. \tag{271}$$

The voltage drop across the capacitance in each segment is $V(x,t) = \partial_t\phi(x,t)$. The current flowing across the inductance in each segment is set by the constitutive relation $I(x,t) = \dfrac{\partial_x\phi(x,t)\mathrm{d}x}{\ell\mathrm{d}x} = \dfrac{\partial_x\phi(x,t)}{\ell}$.
Thus, the Lagrangian of the semi-infinite line is given by

$$\mathcal{L} = \int_{-\infty}^{+\infty} \mathrm{d}x\ \frac{c}{2}(\partial_t\phi)^2 - \frac{1}{2\ell}(\partial_x\phi)^2. \tag{272}$$

The momentum conjugated to the flux $\phi(x,t)$ is defined as the charge density

$$q(x,t) \equiv \frac{\delta\mathcal{L}}{\delta\partial_t\phi} = c\partial_t\phi = cV(x,t). \tag{273}$$

Thus, the Hamiltonian reads

$$\mathcal{H} = q\partial_t\phi - \mathcal{L} = \int_{-\infty}^{+\infty} \mathrm{d}x \; \frac{q^2}{2c} + \frac{1}{2\ell}(\partial_x\phi)^2. \tag{274}$$

The variables dynamics is described by the Euler-Lagrange equation leading to the wave equations

$$\begin{aligned} \partial_t^2\phi - v^2\partial_x^2\phi &= 0, \\ \partial_t^2 q - v^2\partial_x^2 q &= 0, \end{aligned} \tag{275}$$

where $v = 1/\sqrt{\ell c}$ is the propagation velocity.

We can now introduce the wave amplitude propagating right or left which put on the same footing ϕ and q

$$A^{\rightleftharpoons}(x,t) \equiv \frac{1}{2\sqrt{Z_c}}V(x,t) \pm \frac{\sqrt{Z_c}}{2}I(x,t) = \frac{\sqrt{v}}{2\sqrt{c}}q(x,t) \pm \frac{\sqrt{v}}{2\sqrt{\ell}}\partial_x\phi(x,t). \tag{276}$$

The wave equation is reduced into two decoupled equations for the left-moving amplitudes and the right-moving amplitudes

$$\partial_t A^{\rightleftharpoons} \pm v\partial_x A^{\rightleftharpoons} = 0. \tag{277}$$

These decoupled equations mean that the propagating amplitudes $A^{\rightleftharpoons}$ depend only on the combination of time and position $\tau^{\pm} = t \pm x/v$. Thus, for the propagating amplitudes the space and time degrees of freedom are locked through

$$\begin{aligned} A^{\rightarrow}(x,t) &= A^{\rightarrow}(x=0, t-x/v) = A^{\rightarrow}(x-vt, t=0) \equiv A^{\rightarrow}(\tau^-), \\ A^{\leftarrow}(x,t) &= A^{\leftarrow}(x=0, t+x/v) = A^{\leftarrow}(x+vt, t=0) \equiv A^{\leftarrow}(\tau^+). \end{aligned} \tag{278}$$

A.3 PROPAGATING MODE QUANTIZATION

In the canonical quantization, the flux $\phi(x,t)$ and its conjugate momentum $q(x,t)$ on the same node (see Eq.273) can be promoted to quantum operators obeying the commutation relation

$$\boxed{[\phi(x_1,t), q(x_2,t)] = i\hbar\delta(x_1 - x_2)}. \tag{279}$$

Moreover, given that $[\partial_x\phi(x,t), q(x',t)] = \partial_x[\phi(x,t), q(x',t)] = i\hbar\partial_x\delta(x-x')$. Then, the propagating amplitudes operators verify the commutation relations

$$\boxed{\begin{aligned} [A^{\rightarrow}(\tau), A^{\rightarrow}(\tau')] &= i\frac{\hbar}{2}\partial_{\tau-\tau'}\delta(\tau-\tau'), \\ [A^{\leftarrow}(\tau), A^{\leftarrow}(\tau')] &= i\frac{\hbar}{2}\partial_{\tau-\tau'}\delta(\tau-\tau'), \\ [A^{\leftarrow}(\tau), A^{\rightarrow}(\tau')] &= 0. \end{aligned}} \tag{280}$$

As expected, the left and right moving amplitudes are independent.

The Hamiltonian, expressed as a function of the propagating amplitudes, reads

$$\mathcal{H} = \int_{-\infty}^{+\infty} \mathrm{d}\tau \; A^{\leftarrow}(\tau)^2 + A^{\rightarrow}(\tau)^2. \tag{281}$$

Note that the amplitude operators are real valued (hermitian) at this stage

$$(A^{\rightleftharpoons}(\tau))^\dagger = A^{\rightleftharpoons}(\tau). \tag{282}$$

In order to recover the analogue of the non-hermitian creation and annihilation operators for the propagating fields, we must move to the Fourier space. We can now define the Fourier transform of the propagating amplitude operators

$$A^{\rightleftharpoons}[\omega] = \int_{-\infty}^{+\infty} \mathrm{d}\tau \; e^{i\omega\tau} \; A^{\rightleftharpoons}(\tau). \tag{283}$$

In the spectral domain, the amplitude operators are now non-hermitian

$$(A^{\rightleftharpoons}[\omega])^\dagger = A^{\rightleftharpoons}[-\omega]. \tag{284}$$

The commutation relation becomes

$$[A^{\rightleftharpoons}[\omega], A^{\rightleftharpoons}[\omega']^\dagger] = \frac{\hbar\omega}{2}\delta(\omega - \omega'). \tag{285}$$

Using the Parseval relation, we can express the Hamiltonian in the spectral domain

$$\mathcal{H} = \int_{-\infty}^{+\infty} \mathrm{d}\omega \; A^{\rightarrow}[\omega]^\dagger A^{\rightarrow}[\omega] + A^{\leftarrow}[\omega]^\dagger A^{\leftarrow}[\omega]. \tag{286}$$

The Hamiltonian as a function of positive frequency only reads

$$\mathcal{H} = \int_{0}^{+\infty} \mathrm{d}\omega \left\{A^{\rightarrow}[\omega]^\dagger, A^{\rightarrow}[\omega]\right\} + \left\{A^{\leftarrow}[\omega]^\dagger, A^{\leftarrow}[\omega]\right\}, \tag{287}$$

where $\{.,.\}$ stands for the anti-commutator.
We can identify the amplitude operators with the quantum field operators defined by

$$a^{\rightleftharpoons}[\omega] \equiv \frac{A^{\rightleftharpoons}[\omega]}{\sqrt{\hbar|\omega|/2}}. \tag{288}$$

The field operators are non-hermitian

$$(a^{\rightleftharpoons}[\omega])^\dagger = a^{\rightleftharpoons}[-\omega]. \tag{289}$$

and obey the following commutation relations

$$\boxed{\begin{array}{rcl} \left[a^{\rightleftharpoons}[\omega], a^{\rightleftharpoons}[\omega']^\dagger\right] & = & \mathrm{sign}[\omega]\delta(\omega - \omega'), \\ \left[a^{\rightarrow}[\omega], a^{\leftarrow}[\omega']^\dagger\right] & = & 0. \end{array}} \tag{290}$$

Expressed as a function of the field operators, the Hamiltonian looks very much like that of a collection of harmonic oscillator

$$\mathcal{H} = \int_0^{+\infty} \mathrm{d}\omega \; \frac{\hbar\omega}{2} \left\{ a^{\rightarrow}[\omega]^\dagger, a^{\rightarrow}[\omega] \right\} + \frac{\hbar\omega}{2} \left\{ a^{\leftarrow}[\omega]^\dagger, a^{\leftarrow}[\omega] \right\}. \tag{291}$$

We now give the link back to observable quantity in time

The observable quantities in the time domain can be expressed as a function of these quantum field operators

$$\begin{aligned} V(x,t) &= \sqrt{\frac{\hbar Z}{2}} \int_{-\infty}^{+\infty} \frac{\mathrm{d}\omega}{2\pi} \sqrt{|\omega|} (e^{-i\omega(t-x/v)} a^{\rightarrow}[\omega] + e^{-i\omega(t+x/v)} a^{\leftarrow}[\omega]), \\ I(x,t) &= \sqrt{\frac{\hbar}{2Z}} \int_{-\infty}^{+\infty} \frac{\mathrm{d}\omega}{2\pi} \sqrt{|\omega|} (e^{-i\omega(t-x/v)} a^{\rightarrow}[\omega] - e^{-i\omega(t+x/v)} a^{\leftarrow}[\omega]), \end{aligned} \tag{292}$$

$$\begin{aligned} q(x,t) &= \sqrt{\frac{\hbar c}{2v}} \int_{-\infty}^{+\infty} \frac{\mathrm{d}\omega}{2\pi} \sqrt{|\omega|} (e^{-i\omega(t-x/v)} a^{\rightarrow}[\omega] + e^{-i\omega(t+x/v)} a^{\leftarrow}[\omega]), \\ \phi(x,t) &= i\sqrt{\frac{\hbar \ell v}{2}} \int_{-\infty}^{+\infty} \frac{\mathrm{d}\omega}{2\pi} \frac{\sqrt{|\omega|}}{\omega} (e^{-i\omega(t-x/v)} a^{\rightarrow}[\omega] + e^{-i\omega(t+x/v)} a^{\leftarrow}[\omega]). \end{aligned} \tag{293}$$

A.4 DEFINING THE QUANTUM FIELD OPERATOR IN THE TIME DOMAIN

The definition of the creation and anhilition field operators faces an issue in the time domain. Indeed, in the spectral domain, positive frequencies correspond to the absorption of a quanta $a[|\omega|]$ whereas negative frequencies correspond to emission of a quanta $a[-|\omega|] = a^\dagger[|\omega|]$. Such a distinction arise from the commutation relation $[a^{\rightleftharpoons}[|\omega|], a^{\rightleftharpoons}[|\omega'|]^\dagger] = \delta(\omega - \omega')$ which is spectrally oriented.

However, in the time domain, the contributions of the positive and negative frequencies are gathered up, ending such a distinction which lead to an Hermitian operator. I will show that the frequency decoupling is naturally performed in the context of the rotating wave approximation (RWA). This approximation consists in restricting the probing of a resonant system to the vicinity of its resonance frequency Ω. In this rotating frame, the terms oscillating faster than a cut-off bandwidth $\Delta\omega$ can be neglected.

Within this framework, the time-domain definition of the quantum field operator prevents the coupling of positive and negative frequencies

$$\boxed{a^{\rightleftharpoons}(\tau) = \int_{\Omega - \frac{\Delta\omega}{2}}^{\Omega + \frac{\Delta\omega}{2}} \frac{\mathrm{d}\omega}{2\pi} \; e^{-i\omega\tau} a^{\rightleftharpoons}[\omega] \equiv \int_{(+)} \frac{\mathrm{d}\omega}{2\pi} \; e^{-i\omega\tau} a^{\rightleftharpoons}[\omega]}. \tag{294}$$

The rotating frequency Ω must be much higher than the bandwidth $\Delta\omega$ in which the system is probed. It means that the waves rotating out of this bandwidth and

in particular the counter-rotating waves oscillating at 2Ω are filtered out. Note also that this criterion corresponds also to a Markovian approximation which suppose that the quantum noise remains white within the probing bandwidth $\Delta\omega$. The spectral texture of the noise is neglected.

Moreover, the frequency span $\Delta\omega$ must be much larger than the characteristic bandwidth γ corresponding to the dynamics of the probed system in order to resolve its time evolution. Thus, the rotating wave approximation holds for the hierarchy $\Omega \gg \Delta\omega \gg \gamma$.

Note that this hierarchy corresponds also to heterodyne detection scheme where $\Delta\omega$ corresponds to the intermediate frequency at which the energy spectrum is transposed, filtered and digitized. In this case $1/\Delta\omega$ is set by the finite time resolution.

The conjugated operators correspond to creation operators

$$a^{\rightleftharpoons}(\tau)^\dagger = \int_{\Omega-\frac{\Delta\omega}{2}}^{\Omega+\frac{\Delta\omega}{2}} \frac{\mathrm{d}\omega}{2\pi}\, e^{i\omega\tau} a^{\rightleftharpoons}[\omega]^\dagger. \tag{295}$$

Note that the creation operator is then defined like the annihilation operator but on an integration interval in the negative frequencies.

$$\boxed{a^{\rightleftharpoons}(\tau)^\dagger = \int_{-\Omega-\frac{\Delta\omega}{2}}^{-\Omega+\frac{\Delta\omega}{2}} \frac{\mathrm{d}\omega}{2\pi}\, e^{-i\omega\tau} a^{\rightleftharpoons}[\omega] \equiv \int_{(-)} \frac{\mathrm{d}\omega}{2\pi}\, e^{-i\omega\tau} a^{\rightleftharpoons}[\omega]}. \tag{296}$$

Let's determine the commutation relations with these operators

$$\begin{aligned} [a^{\rightleftharpoons}(\tau), a^{\rightleftharpoons}(\tau')^\dagger] &= \frac{\Delta\omega}{\pi}\mathrm{sinc}(\Delta\omega(\tau-\tau'))e^{-i\Omega(\tau-\tau')} \\ &\equiv \delta_{\frac{1}{\Delta\omega}}(\tau-\tau') \end{aligned}. \tag{297}$$

$\delta_{\frac{1}{\Delta\omega}}(\tau)$ goes towards $\delta(\tau)$ when the finite time resolution is much finer than the characteristic time of the system evolution $1/\Delta\omega \ll 1/\gamma$. Thus, the canonical commutation relation is satisfied in the context of the RWA.

$$\boxed{[a^{\rightleftharpoons}(\tau), a^{\rightleftharpoons}(\tau')^\dagger] = \delta(\tau-\tau')}. \tag{298}$$

We can now express the physical observable as a function of the field operator in time in the vicinity of the central frequency Ω

$$\boxed{A^{\rightleftharpoons}(\tau) = \sqrt{\frac{\hbar\Omega}{2}}(a^{\rightleftharpoons}(\tau) + a^{\rightleftharpoons}(\tau)^\dagger)}, \tag{299}$$

$$\begin{aligned} q^{\rightleftharpoons}(\tau) &= \frac{1}{v}\sqrt{\frac{\hbar\Omega}{2Z}}(a^{\rightleftharpoons}(\tau) + a^{\rightleftharpoons}(\tau)^\dagger), \\ \phi^{\rightleftharpoons}(\tau) &= i\sqrt{\frac{\hbar Z}{2\Omega}}(a^{\rightleftharpoons}(\tau) - a^{\rightleftharpoons}(\tau)^\dagger). \end{aligned} \tag{300}$$

We have shown that it is possible to recover the commutation relation for propagating modes both in the time and frequency domain.

$$[a^{\rightleftharpoons}(\tau), a^{\rightleftharpoons}(\tau')^\dagger] = \delta(\tau - \tau') \quad \text{and} \quad [a^{\rightleftharpoons}[\omega], a^{\rightleftharpoons}[\omega']^\dagger] = \text{sign}(\omega)\delta(\omega - \omega'). \quad (301)$$

Interestingly, these basis choices are two extreme ways to tile the frequency-time plane, either an infinitesimal time tiling or an infinitesimal frequency tiling. There are intermediate ways to tile the time-frequency plane with a discrete wavelet basis. Such a time-frequency tiling requires primitive cells of area $\boxed{\Delta\omega \times \Delta\tau = 2\pi}$ to preserve the time-energy Heisenberg uncertainty.

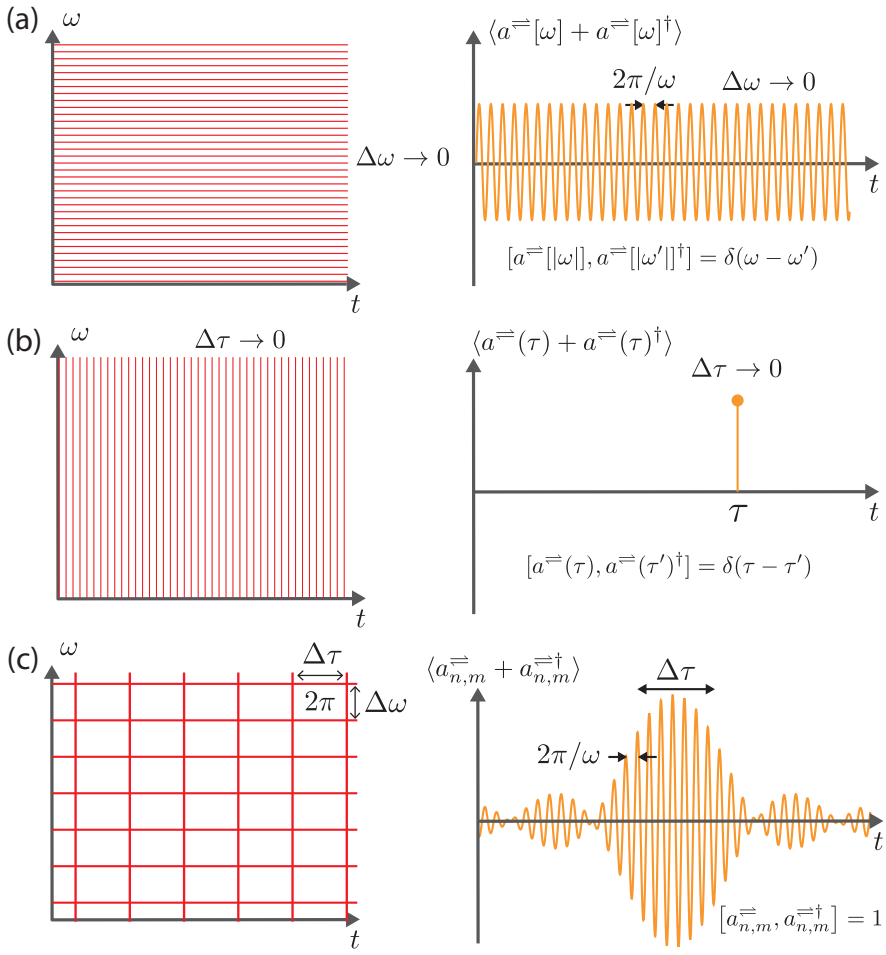

Figure 87: Tiling of the frequency-time plane and the corresponding averaged propagating operators. (a) Spectral domain, frequency is well defined. (b) Temporal domain, time is well defined. Note that the creation and anhilition operators are well defined in the limit of the RWA only. (c) Wavelet basis, the Shannon wavelet is defined around a frequency and a time bin such that $\Delta\omega \times \Delta\tau = 2\pi$.

One example is the Shannon wavelet basis $\{\Psi_{n,p}\}$, which defines a time-frequency tiling with rectangular cells centered around $(n\Delta\omega, p\Delta\tau)$ where n and p are integers.

It is defined in the frequency domain as gate function centered on $n\Delta\omega$ with a width $\Delta\omega$ and a carrier oscillating at $p\Delta\tau$

$$\Psi_{n,p}[\omega] = \frac{e^{-i\omega p\Delta\tau}}{\sqrt{\Delta\omega}}\theta[-(\omega-(n+1/2)\Delta\omega)]\theta[\omega-(n-1/2)\Delta\omega], \tag{302}$$

in the time domain the wavelet corresponds to a cardinal sinus function centered on $p\Delta\tau$ with a width $\Delta\tau$ and a carrier oscillating at $n\Delta\omega$

$$\Psi_{n,p}(t) = \sqrt{\Delta\omega}e^{in\Delta\omega t}\mathrm{sinc}[\pi(t-p\Delta\tau)/\Delta\tau]. \tag{303}$$

Crucially, the basis is orthonormal both in time and frequency

$$\int_{-\infty}^{+\infty}\Psi^*_{n,p}[\omega]\Psi_{m,q}[\omega]\mathrm{d}\omega = \int_{-\infty}^{+\infty}\Psi^*_{n,p}(t)\Psi_{m,q}(t)\mathrm{d}t = \delta_{n,m}\delta_{p,q}. \tag{304}$$

The creation and anhilition operators decomposed on the wavelet basis are defined by their time-frequency cell coordinates (n,p) given by

$$a^{\rightleftharpoons}_{n,p} = \int_{-\infty}^{+\infty}\Psi_{n,p}[\omega]a^{\rightleftharpoons}[\omega]\mathrm{d}\omega = \frac{1}{\sqrt{\Delta\omega}}\int_{\Delta\omega(n-1/2)}^{\Delta\omega(n+1/2)}e^{-i\omega p\Delta\tau}a^{\rightleftharpoons}[\omega]\mathrm{d}\omega. \tag{305}$$

Remarkably, the commutation relations are preserved in the wavelet basis and are equal to unity due to the tiling condition $\Delta\omega\times\Delta\tau = 2\pi$,

$$\boxed{\left[a^{\rightleftharpoons}_{n,p}, a^{\rightleftharpoons\dagger}_{m,q}\right] = \mathrm{sign}(n)\delta_{n,m}\delta_{p,q}}. \tag{306}$$

The creation and annihilation operators $a^{\rightleftharpoons}_{n,p}$ defined in the wavelet basis correspond to proper propagating harmonic oscillator for which the quantum of energy $\hbar(n\Delta\omega)$ is well-defined. Note that various choices of wavelet bases exist, but some bases take better advantage of spectral and temporal specificities. The most appropriate basis is matched with the response of sources or detectors in time or frequency.

Note that in the following part of the thesis, I will often implicitly use the commutation relation in the wavelet bases equal to unity instead of the standard delta commutation relations of Eq.301. In particular, it makes sense to use the wavelet bases when the propagating fields have been integrated during a measurement. Thus, the specific bases is defined by the integration bandwidth RBW of the spectrum analyzer as in Part. iii, or by time-integration window as in Part. iv.

A.6 QUANTUM LANGEVIN EQUATION

The driving or the readout of a LC oscillator requires a coupling to the environment. The oscillator is exposed to energy leakage but also to incoming vacuum or thermal fluctuations as required by the fluctuation-dissipation theorem. This can be modeled using the quantum Langevin equation.

The Langevin equation has been introduced for classical mechanics in 1908 as a phenomenological description of the Brownian motion. It consists in introducing a friction term and a noise term in the fundamental relation of dynamics. It has enabled to formalize the link between fluctuation and dissipation that was previously described by Einstein in 1905 in the same context.

In the context of electrical circuits, the link between fluctuation and dissipation has been highlighted by Nyquist [115]. He has demonstrated that a dissipative environment can be modeled as a resistance associated with a noise source emitting Johnson-Nyquist thermal noise.

As mentioned in sectionA.2.2, the quantum description of dissipation can be modeled by the coupling of the system of interest to a continuum of non-dissipative modes such as a transmission line. This model gives a natural support for dissipation and noise and then driving and readout. This description is analogous to both Nyquist model and Langevin approach and can be extended to the quantum regime.

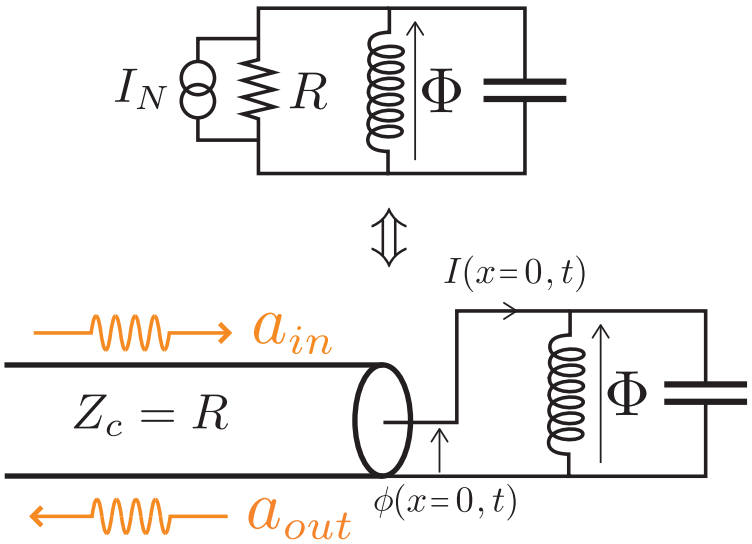

Figure 88: Nyquist model and its transmission line equivalent

I will show that the coupling between propagating modes and a localized one can be described through the quantum Langevin equation. Indeed, we are now in position to deal with a quantum LC oscillator coupled to a semi-infinite line of characteristic impedance $Z_c = R$ extending from $x = 0$ to $x = \infty$. In that half-line, the left and right-moving propagating waves are no longer independent since they are coupled by the boundary. We are now calling $A_{in}(t)$ and $A_{out}(t)$ the wave amplitude $A^{\rightarrow}(x = 0, t)$ and $A^{\leftarrow}(x = 0, t)$ at the boundary.

The evolution of the LC oscillator annihilation operator a coupled to the bath of propagating modes can be determined in the Heisenberg picture by

$$i\hbar\partial_t a = [a, H] = [a, H_{sys}] + [a, H_{int}] + [a, H_{bath}]. \tag{307}$$

$H_{sys} = \hbar\omega_a(a^\dagger a + 1/2)$ is the Hamilonian of the LC oscillator. H_{bath} is the Hamiltonian of the continuum of modes in the transmission line. These bath modes are formally separated from the LC mode leading to $[a, H_{bath}] = 0$.

The interaction Hamiltonian can be derived from the work performed by an external current source with an impedance R delivering a current $I(x = 0)$ over the potential $V = \partial_t\Phi$ across the LC oscillator.

$$H_{int} = -\Phi.I(x = 0) = -\Phi.\frac{A_{in}(t) - A_{out}(t)}{\sqrt{R}}. \tag{308}$$

In the context of the rotating wave approximation in the vicinity of the resonance frequency ω_a, we can express the amplitude operators as a function of the propagating quantum field operators using Eq.266 and Eq.299

$$H_{int} = -\sqrt{\frac{\hbar Z_a}{2}}(a + a^\dagger)\sqrt{\frac{\hbar\omega_a}{2R}}(a_{in} - a_{out} + a_{in}^\dagger - a_{out}^\dagger). \tag{309}$$

Moreover, in the RWA, the fast oscillating terms are removed from the Hamiltonian

$$H_{int} = -\frac{\hbar}{2}\sqrt{\gamma_a}(a^\dagger(a_{in} - a_{out}) + a(a_{in}^\dagger - a_{out}^\dagger)) \tag{310}$$

where we have introduced the coupling rate

$$\gamma_a = \omega_a\frac{Z_a}{R}. \tag{311}$$

The Heisenberg equation of the annihilation operator a is thus

$$\partial_t a = \frac{1}{i\hbar}[a, H_{sys}] + i\frac{\sqrt{\gamma_a}}{2}(a_{in} - a_{out}). \tag{312}$$

Moreover, the flux across the LC oscillator is equal to the flux across the transmission line $\Phi = \phi(x = 0)$. According to Eq.266 and 300, this leads to

$$\sqrt{\frac{\hbar Z_a}{2}}(a + a^\dagger) = i\sqrt{\frac{\hbar R}{2\omega_a}}(a_{in} + a_{out} - a_{in}^\dagger - a_{out}^\dagger). \tag{313}$$

Separating the contribution of oscillating and counter-oscillating operators in the RWA, we get the input/output relation

$$\sqrt{\gamma_a}a = i(a_{in} + a_{out}). \tag{314}$$

For sake of simplicity and without loss of generality, we will use a different phase reference for a_{in} and a_{out} in the following parts. Namely

$$\begin{cases} a_{in} & \leftarrow & a_{in}e^{i\pi/2}, \\ a_{out} & \leftarrow & a_{out}e^{i\pi/2}. \end{cases} \tag{315}$$

Leading to

$$\boxed{\sqrt{\gamma_a}a = a_{in} + a_{out}}. \tag{316}$$

The quantum Langevin equation can be expressed as a function of the input field operator

$$\boxed{\partial_t a = \frac{1}{i\hbar}[a, H_{sys}] - \frac{\gamma_a}{2}a + \sqrt{\gamma_a}a_{in}}. \tag{317}$$

or as a function of the output field operator

$$\partial_t a = \frac{1}{i\hbar}[a, H_{sys}] + \frac{\gamma_a}{2}a + \sqrt{\gamma_a}a_{out}. \tag{318}$$

The quantum Langevin equation makes it possible to describe in the same framework both the damping of a quantum oscillator at a rate γ_a in a bath of oscillators as well as the unavoidable quantum fluctuations brought at the same rate γ_a. Furthermore, the equation applies for any system and only requires the input impedance to be specified. Therefore, it constitutes the ideal framework to describe our quantum circuits interacting with propagating modes.

B

POSITIVE PARTIAL TRANSPOSE CRITERION AND NEGATIVITY

B.1 POSITIVE PARTIAL TRANSPOSE CRITERION AND NEGATIVITY

A bipartite non-entangled state ρ_{ab} can always be described by a statistical mixture of separable pure states $\rho_{a,i} \otimes \rho_{b,i}$

$$\rho_{ab} = \sum_i p_i \rho_{a,i} \otimes \rho_{b,i}, \tag{319}$$

otherwise, it is inseparable. Note that if the set of pure density matrix $\{\rho_{a(b),i}\}$ are not orthogonal projectors then discord appears [82].

A powerful criterion to decide separability of a density matrix is positivity of the partial transpose (PPT). Indeed, for a separable state ρ_{ab}, its partial transposition over b, $\rho_{ab}^{T_b}$ yields to another well-defined density. In particular, its eigenvalues $\{p_i\}$ are all positives. Indeed

$$\rho_{ab}^{T_b} = \sum_i p_i \rho_{a,i} \otimes (\rho_{b,i})^T = \sum_i p_i \rho_{a,i} \otimes \rho_{b,i}^* \tag{320}$$

where $(\rho_{b,i})^T = \rho_{b,i}^*$ is a legitimate density matrix.

The PPT criterion is necessary for separable states. If $\rho_{ab}^{T_b}$ gets a single negative eigen-value then the partially transpose state is unphysical, hence ρ_{ab} is unseparable or entangled.

The negativity N is a proper measure of entanglement[150] based on the PPT criterion. It is defined as the sum of the negative eigenvalues of the partially transpose state, $N = \left|\sum_{p_i<0} p_i\right|$.

One advantage of the negativity is that it can be computed for any density matrix. Indeed, it is related to the trace norm of $\rho_{ab}^{T_b}$ where the trace norm of an hermitian operator A is given $||A|| = \mathrm{Tr}(\sqrt{A^\dagger A}) = \sum_i |\alpha_i|$ where the α_i are the eigenvalues of A. Indeed

$$||\rho_{ab}^{T_b}|| = \sum_i |p_i| = \left|\sum_i p_i\right| + 2\left|\sum_{p_i<0} p_i\right| = 1 + 2N. \tag{321}$$

The negativity is given by

$$N = \frac{||\rho_{ab}^{T_b}|| - 1}{2}. \tag{322}$$

A more operational measure of entanglement based on the PPT criterion is the logarithmic negativity[150].

$$\boxed{E_N = \log ||\rho_{ab}^{T_b}||}. \tag{323}$$

It constitutes an upper bound on distillable entanglement[150]. In other words, it corresponds to the maximal number of entanglement bit (equivalent Bell pairs) that Alice and Bob can extract from the state using only Local Operation and Classical Communication (LOCC). It is measured in entangled bits (ebits). Note that for pure states, logarithmic negativity coincides with entanglement measure based on the mutual information described above.

B.1.1 *Covariance matrices and Symplectic transformations*

The dominant decoherence mechanism in our experimement is the energy loss in microwave cables. It can be modeled as beam splitter interactions with modes of the environment in the vacuum state. This interaction preserves the Gaussian character of the incoming state. Although this state is now partially mixed, it can still be described entirely by its covariance matrix[70]. Note that this Gaussian hypothesis is not required to decide of inseparable character of a density matrix from the covariance matrix but it is needed in order to quantify it using the PPT criterion[70].

For Gaussian states, the operations on density matrices are equivalent to operations on covariance matrices [151, 152]. Indeed, a unitary operators U acting on a density matrices ρ can be mapped onto a symplectic operators S acting onto a covariance matrices V. The symplectic operators preserve the commutation relations encoded in Ω given by $\Omega_{ij} = [\xi_i, \xi_j]$ with $\xi = (x_1, p_1, x_2, p_2)$. Hence, this can be expressed as

$$\rho \to U^\dagger \rho U \Leftrightarrow V \to S^T V S \tag{324}$$

where

$$U^\dagger U = \mathbb{I} \Leftrightarrow S^T \Omega S = \Omega \quad \text{with} \quad \Omega = \begin{pmatrix} 0 & 1 & 0 & 0 \\ -1 & 0 & 0 & 0 \\ 0 & 0 & 0 & 1 \\ 0 & 0 & -1 & 0 \end{pmatrix}. \tag{325}$$

Symplectic operations are operations which conserve the total amount of information in phase space since they are associated with a unitary operation. The purity of a Gaussian state being defined by $\mathrm{Tr}(\rho^2) = \det(V)^{-1/2}$, symplectic operations preserve covariance matrix determinant.

Note that the scattering matrix associated to the two-ode squeezing is the symplectic transformation associated with the two-mode squeezing operator.

B.1.2 *PPT criterion from the covariance matrix*

Finally, the positiveness criterion of the density matrix can be translated to covariance matrix by

$$\rho \geq 0 \Rightarrow V + i\Omega \geq 0 \Leftrightarrow \mathbb{I} + i\Omega \geq 0. \tag{326}$$

Note that if the vacuum $\mathbb{I}$ is saturating the bound, all pure state are saturating the bound since $V = S^T \mathbb{I} S$. Moreover, this relation is equivalent to Heiseinberg incertitude principle[151, 153]. By applying Ω on the left of the matrix inequality, this leads to a criterion on the so-called symplectic spectrum of V

$$\rho \geq 0 \Rightarrow \text{spect}(|i\Omega V|) \geq 1. \tag{327}$$

We get all the tools in order to translate the PPT criterion in term of a Gaussian state and its covariance matrix V.

Indeed, the partial transpose operation amounts to a partial time reversal transformation for the state. For Gaussian state, it corresponds to a sign change in the momentum variable of the transpose part such as $p_2 \to -p_2$. Thus, the partially transpose on the covariance matrix $\tilde{V}$ corresponds to flipping the sign of the off-diagonal matrix element associated with p_2[153].

The separability criterion stands on legitimacy of the partially transpose covariance matrix $\tilde{V}$ of the state. A state ρ is entangled if the symplectic spectrum of its partially transpose covariance matrix $|i\Omega\tilde{V}|$ gets a eigen-value ν_- strictly lower than 1. It corresponds to the contraposition of Eq.(327).

$$\tilde{\nu}_- < 1 \Rightarrow \rho^{T_b} \text{non-positive} \Rightarrow ||\rho_{ab}^{T_b}|| > 1 \Rightarrow \text{AB entangled}. \tag{328}$$

This criterion is very general, in particular it doesn't of the Gaussian character of the state. However for Gaussian state, it possible to go one step further by quantifying the strength of the entanglement.

B.1.3 *Measure of entanglement for a bipartite gaussian state*

For gaussian states, we have $||\rho^{T_b}|| = \tilde{\nu}_-^{-1}$. Consequenclty, the symplectic eigenvalues of $\tilde{V}$ is a direct measure of the entanglement

$$E_N = -\log \tilde{\nu}_-. \tag{329}$$

Physically, it is meaningful to decompose the covariance matrix of a two-mode gaussian mixed state in four 2×2 block matrices where the diagonal blocks $\boldsymbol{\alpha}$ and $\boldsymbol{\beta}$ are the single-mode covariance matrices for a and b respectively. Conversely, the off-diagonal blocks $\boldsymbol{\gamma}$ correspond to the correlations between the modes.

The covariance matrix can always be put in the standard form using local Gaussian (symplectic) operations $S_a S_b$[153].

$$\boldsymbol{V} = \begin{pmatrix} \boldsymbol{\alpha} & \boldsymbol{\gamma} \\ \boldsymbol{\gamma}^T & \boldsymbol{\beta} \end{pmatrix} \Leftrightarrow S_a S_b \boldsymbol{V} S_b^T S_a^T = \begin{pmatrix} a & 0 & c_+ & 0 \\ 0 & a & 0 & c_- \\ c_+ & 0 & b & 0 \\ 0 & c_- & 0 & b \end{pmatrix}. \tag{330}$$

Note that the determinant of the block-matrix are preserved under these local symplectic transformation $\det(\boldsymbol{\alpha}) = a^2$, $\det(\boldsymbol{\beta}) = b^2$, $\det(\boldsymbol{\gamma}) = c_+ c_-$ and $\det \boldsymbol{V} = (ab - c_+^2)(ab - c_-^2)$.

The partially transpose on the covariance matrix $\tilde{V}$ leads to flipping the sign of $\det(\boldsymbol{\gamma}) \to -\det(\boldsymbol{\gamma})$. The Partially

$$\tilde{\boldsymbol{V}} = \begin{pmatrix} a & 0 & c_+ & 0 \\ 0 & a & 0 & -c_- \\ c_+ & 0 & b & 0 \\ 0 & -c_- & 0 & b \end{pmatrix} \Rightarrow \boldsymbol{\Omega}.\tilde{\boldsymbol{V}} = \begin{pmatrix} 0 & a & 0 & -c_- \\ -a & 0 & -c_+ & 0 \\ 0 & -c_- & 0 & b \\ -c_+ & 0 & -b & 0 \end{pmatrix}. \tag{331}$$

Then one can compute the two symplectic eigen-values for a bipartite Gaussian state [153].

$$\tilde{\nu}_\pm = \frac{1}{\sqrt{2}} \sqrt{\Delta \pm \sqrt{\Delta^2 - 4 \det(V)}} \tag{332}$$

where $\Delta = \det \alpha + \det \beta - 2 \det \gamma$

Leading to

$$E_N = -\frac{1}{2} \log \left(\frac{\Delta - \sqrt{\Delta^2 - 4 \det(V)}}{2} \right). \tag{333}$$

The inseparability criterion is equivalent to a inequality relation between the determinants in the covariance matrix.

$$E_N > 0 \Leftrightarrow \det \alpha + \det \beta - 2 \det \gamma - \det V > 1. \tag{334}$$

B.1.4 *PPT criterion for a general two-mode squeezed vacuum state*

In the general case the covariance-matrix of a two mode squeezed state which underwent decoherence is given by

$$\boldsymbol{V} = \begin{pmatrix} \boldsymbol{\alpha} & \boldsymbol{\gamma} \\ \boldsymbol{\gamma}^T & \boldsymbol{\beta} \end{pmatrix} = \begin{pmatrix} a & 0 & c\cos\theta & c\sin\theta \\ 0 & a & c\sin\theta & -c\cos\theta \\ c\cos\theta & c\sin\theta & b & 0 \\ c\sin\theta & -c\cos\theta & 0 & b \end{pmatrix}. \tag{335}$$

In this case, the inseparability criterion from (334) can be simplified as

$$E_N > 0 \Leftrightarrow (a-1)(b-1) < c^2 < (a+1)(b+1). \tag{336}$$

The lower bound separate separable state from entangled state and the upper bound separate the entangled states from an unphysical states which do not satisfy the uncertainty principle.

Finally the logarithmic negativity is given by

$$E_N = -\log\left(\frac{a+b-\sqrt{(a-b)^2+4c^2}}{2}\right). \tag{337}$$

C

EXPERIMENTAL TECHNIQUES

C.1 LOW NOISE MEASURMENT

The experiments described in this thesis have been performed in a *Cryoconcept* dry dilution refrigerator with a base temperature of $\sim$ 40 mK. The wiring of the refrigerator is a substantial task. The goal is to achieve low enough heat power not to heat up the base plate of the cryostat while bringing down all microwave signals required for the experiment. An example of detailed wiring scheme is presented in Fig. 89. RF cables for input signals are strongly attenuated and filtered to progressively thermalize the electromagnetic field down to the base temperature. Note that the attenuators are well thermally anchored at each stage. Furthermore, cupronickel coaxial cables are used on the way down to minimize the heat exchange between the stages. At base temperature, mostly copper coaxial cables are used to minimize the losses between the cryogenic microwave components. Note that all normal metal cable assemblies were bought with mounted connectors. Superconducting Niobium/Titanium (NbTi) coaxial cables are used for output signals between the base temperature and the HEMT amplifiers at 4K in order to minimize the losses as well as the heat exchange between the stages.

We also need DC lines in order to current bias the coil which provides the magnetic flux threading the loop. These DC lines are twisted to avoid flux noise and are strongly filtered using a homemade Ecosorb filter that absorbs AC signals up to infrared frequencies. Below 4K, this twisted pair is made of NbTi/Cu (in a copper matrix) to avoid Joule dissipation and above 4K in manganin to minimize heat exchange between the stages of the cyrostat.

One advantage of dry cryogenic systems over traditional wet refrigerator is the large space available at base temperature. Fig.91 and Fig.90 show pictures of the refridgerator before closing.

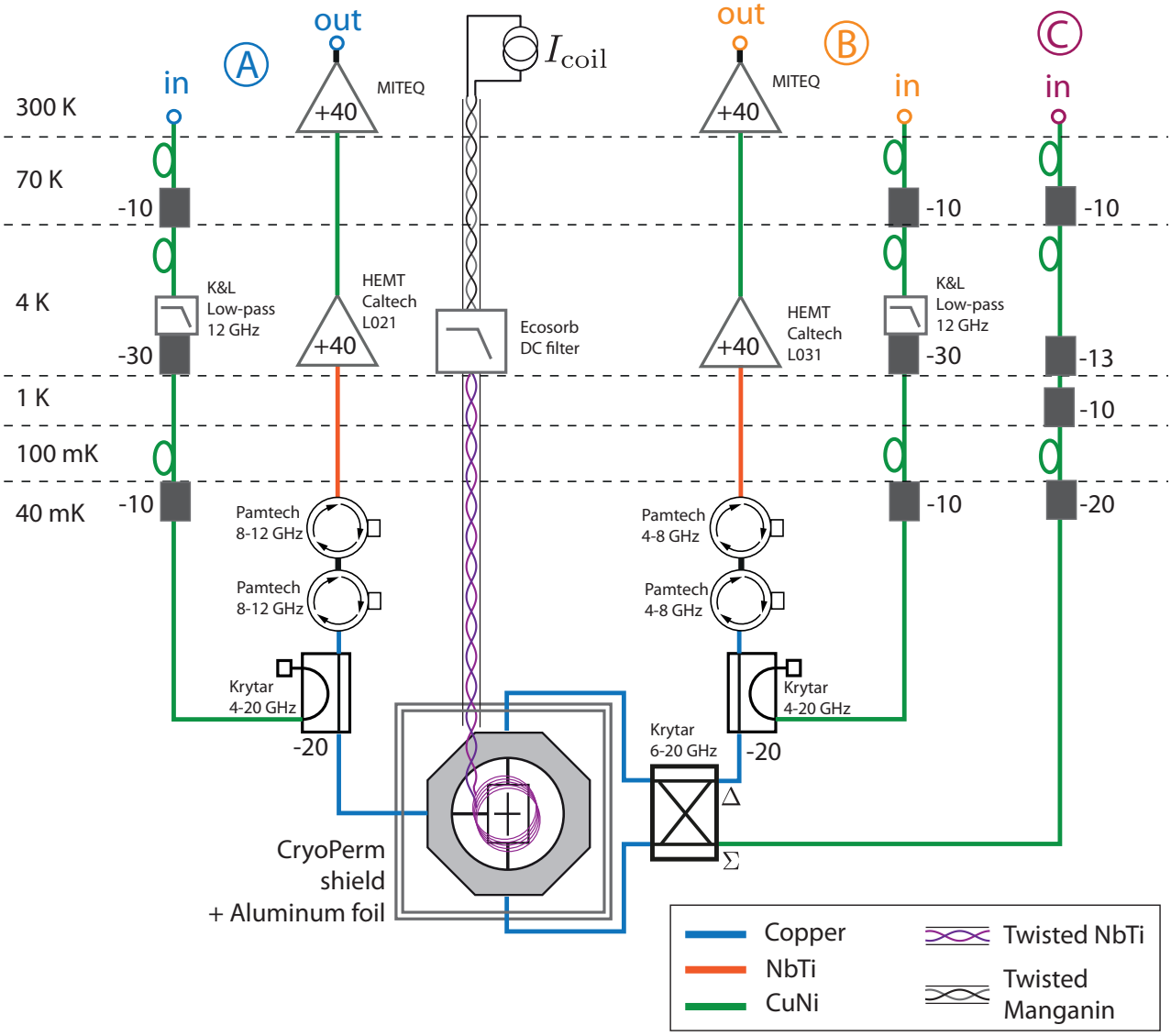

Figure 89: Wiring scheme used in a typical experiment (here the one of part i).

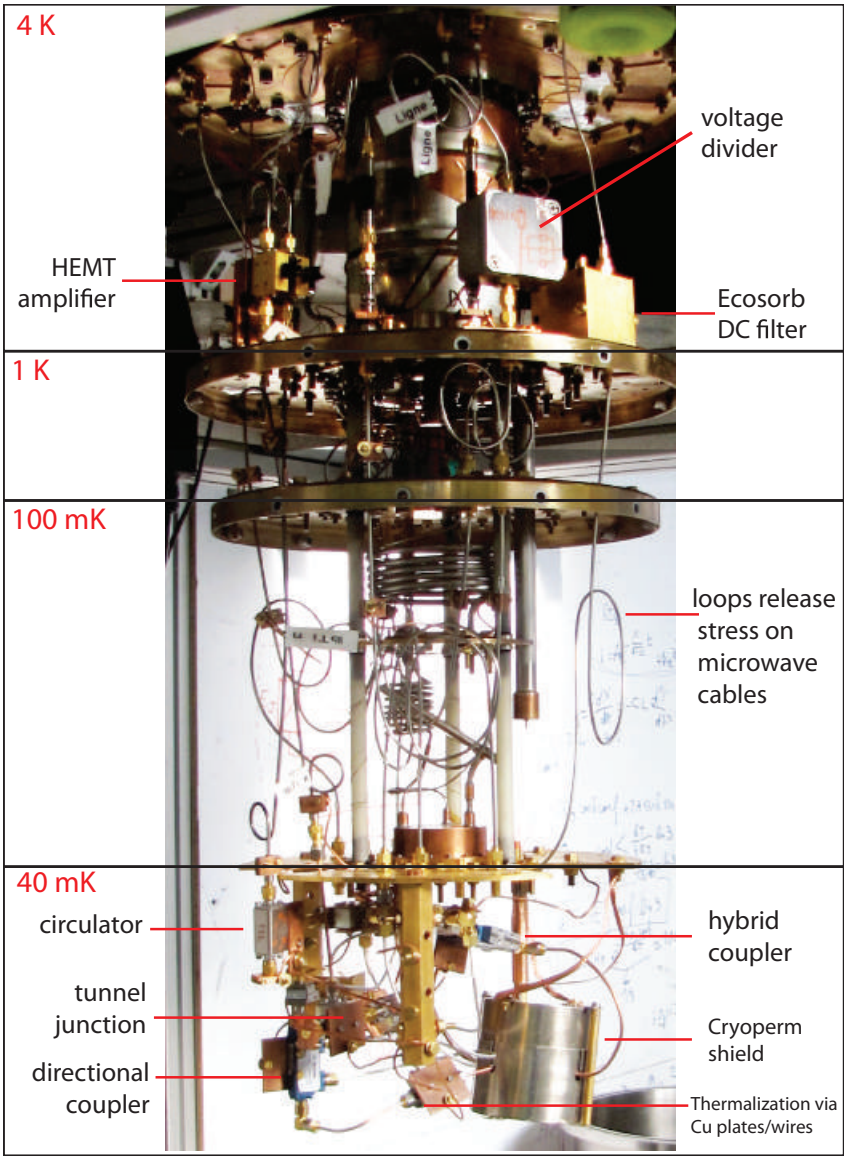

Figure 90: Picture of the Cryoconcept dilution refrigerator for experiments described in part i.

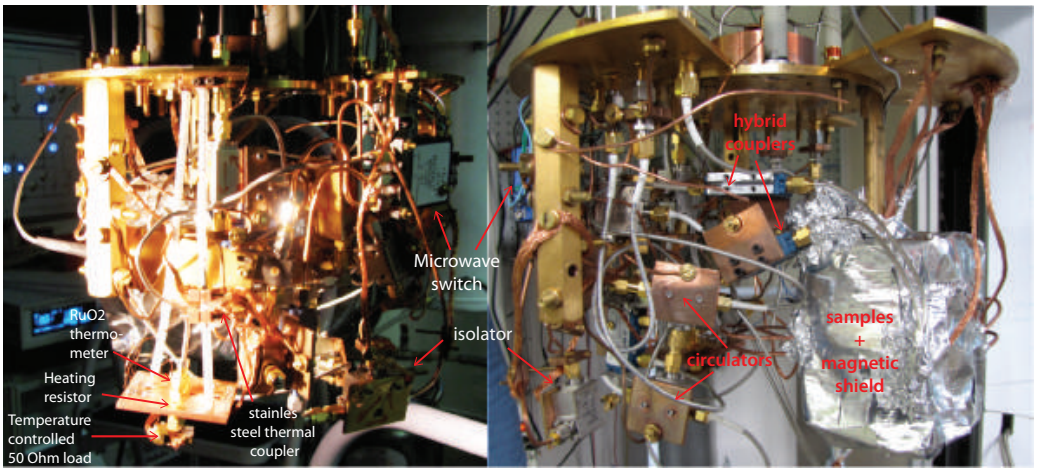

Figure 91: Two pictures of the base temperature stage of our dilution refrigerator for the entanglement demonstration described in chapter 7. On the left, we can see the calibration setup based on a tunable thermal noise source. On the right, we can see the samples in the cryoperm shield covered with aluminum foils, as well as the microwave cables and components across which the EPR states propagate during the experiment, see Fig. 48.

The sample holder must be designed with great care in order to maximize the quantum efficiency of our devices. Indeed, it must provide a way to extract and input signals to/from the device without disturbing its microwave properties. In particular, its resonance modes must be high frequency enough not to interfere with the microwave processing of the sample. It must also prevent external radiation to couple to the device, hence it is a light-tight box.

Josephson mixer samples were mounted into an octogonal copper sample holder using silver paste. The advantage of silver paste is that it provides good thermal and electrical conductivity for the gold ground plane evaporated at the bottom of the substrate. A Josephson mixer sample mounted onto sample is shown in Fig.92.

The sample holder forms a cylindrical cavity with approximate dimensions 18 mm diameter and 4.3 mm height. Anritsu K102F microwave connectors go through the side of the sample holder. These connectors are specified for cryogenic environment and ensures a low loss connection between microstrip and standard SMA cables. A key element of the connector is the glass bead which provides a soft transition between the SMA connector on one side and the microstrip soldered to a sliding contact on the other side. The printed circuit board (PCB) consists in 50 Ω microstrip transmission lines on TMM10i substrate. It is designed such that no spurious resonant modes appear near the superconducting mode frequencies. The lowest box mode for this geometry is around 12 GHz, as can be seen from the transmission measurement performed at room temperature on an empty sample holder in Fig. 92. The transmission between two ports is less than 1dB when a through line on PCB is wire bonded in place of the chip.

A magnetic coil is placed at the back of the sample holder behind 3 mm of copper so that the botton of the coil is at 3.5 mm from the JRM. The winding of the coil consists in 5000 turns of NbTi superconducting wire around the axis. The field produced in the Josephson Ring is about 0.06 ± 0.02 T/A.

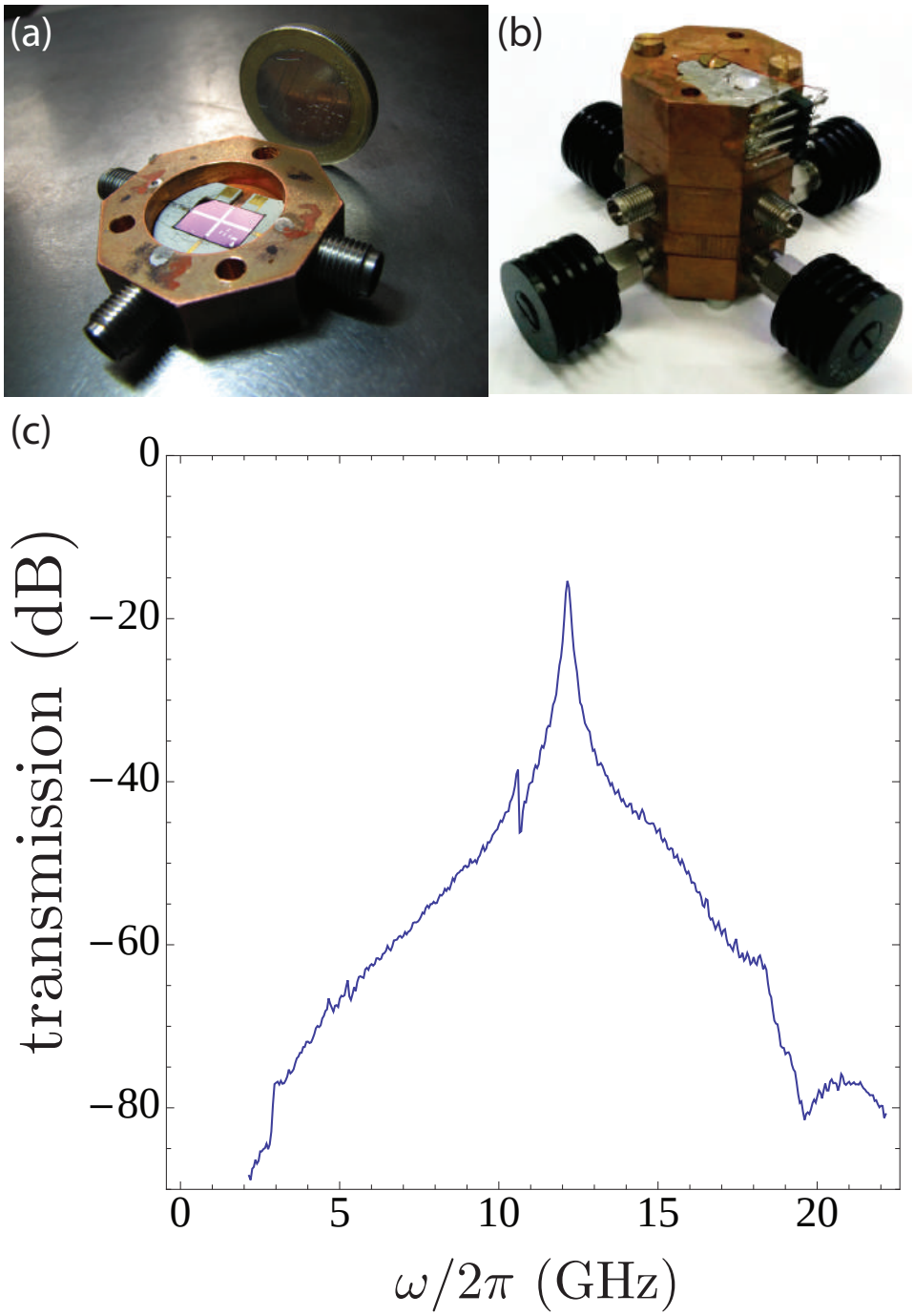

Figure 92: (a) Josephson mixer samples mounted into the octagonal copper sample holder "octobox". (b) Two sample holders back-to-back with their respective coil used for the entanglement experiment. (c) transmission measurement performed at room temperature on an empty sample holder.

C.3 TRANSLATION BETWEEN THE NOTATIONS OF THIS WORK AND PREVIOUS ONES

Sample in this work	Sample in the notebook
JM-A	JPC07
JM-B	JPC12
JM-C	JPC14
JM-D	JPC15
Entangler	JPC17a
Witness	JPC17b
Low-impedance amplifier	JDC05
$2D$ memory	JPC17a→QMPC1
$3D$ memory	QMPC11-15

C.4 NANOFABRICATION PROCESSES FOR JOSEPHSON MIXER

All samples are fabricated in a single step by electron-beam lithography at Ecole Normale Superieure and a single step evaporation in Paris 7. We use the Dolan bridge technique [40] to fabricate the Josephson junction. The recipe for the nano fabrication is the following

C.4.1 *Substrate cleaning*

- rough cleaning in Acetone with clean-room cotton bud
- 2 min ultrasound in Acetone
- rince with Isopropanol (IPA)
- N_2 blow dry
- O_2 plasma, 30 min with plasma cleaner or 10 min with reactive ion etching (RIE)

C.4.2 *Spin coating*

We use a trilayer MAA/MAA/PMMA resist to get a 1.2 μm-high mask. It enables us to make larger junctions.

- bake at 185°C for 2 min on a hot plate
- 3 drops of MAA EL10
- spinning at 4000 rpm for 60 s (accelaration 4000 rpm/s)
- bake at 185°C for 4 min (Sapphire) or 3 min (Si) on a hot plate

- wait for 1 min
- 3 drops of MAA EL10
- spinning at 4000 rpm for 60 s (accelaration 4000 rpm/s)
- bake at 185°C for 4 min (Sapphire) or 3 min (Si) on a hot plate
- wait for 1 min
- 2 drops of PMMA
- spinning at 4000 rpm for 60 s (accelaration 4000 rpm/s)
- bake at 185°C for 4 min (Sapphire) or 3 min (Si) on a hot plate

C.4.3 *Aluminum deposition on sapphire chip for e-beam writing*

In the case of Sapphire substrates, a thin layer of aluminum is deposited on top of the resist to evacuate charges during e-beam lithography and avoid charge offset. The aluminum is evaporated with a Joule evaporator.

- wait for 30 min until vacuum $< 10^{-5}$ mBar
- evaporate $10 - 15$ nm aluminum at a rate of 0.5 nm/s

C.4.4 *e-beam lithography*

E-beam lithography is performed on a Raith e-beam writer. The whole pattern is done in a single step-lithography.

- JRM : 7.5 μm aperture with 283 μC/cm^2 ($\times$1.2 for sapphire) with a current of $\sim$ 25 pA
- resonators : 120 μm aperture with 283 μC/cm^2 ($\times$1.2 for sapphire)with a current of $\sim$ 5 nA

C.4.5 *Development*

Note that for sapphire the thin layer of aluminum must be removed before development.

- (Sapphire) aluminum removal $\sim$ 30 s in KOH ($\sim$ 5 KOH pastilles in 100 ml in DI water). Check visually that the Al layer is etched successfully.
- (Sapphire) $\sim$ 30 s in water and N_2 blow dry
- 35 s in MIBK:IPA solution (1:3)
- 20 s in IPA
- N_2 blow dry

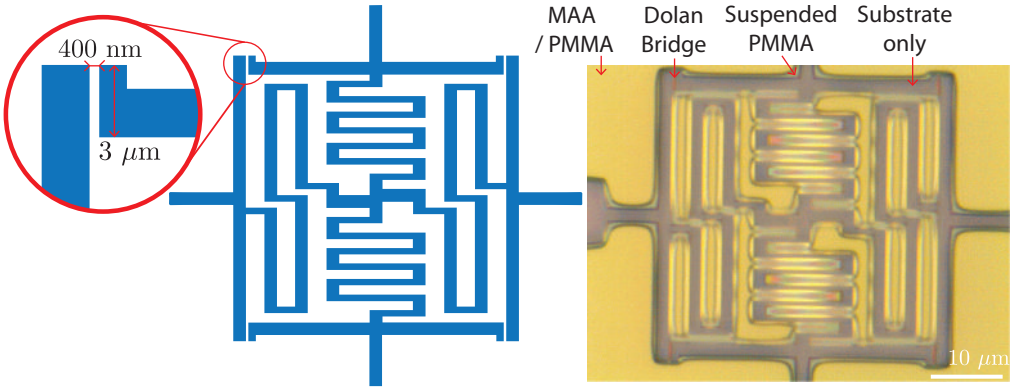

Figure 93: Optical microscope picture of the resist mask of a JRM after development (JM-C). The Dolan Bridge are created using back-scattering of electron near the pattern.

C.4.6 *Aluminum deposition*

High purity aluminum is deposited using the Plassys e-beam evaporator of the Paris 7 clean-room.

- purge ArO_2 oxidation line
- 45 min pumping before reaching 3×10^{-6} mBar
- 5 s of ion milling at $-35°$ (500V, -100V, 50mA, 12sccn ArO_2)
- 5 s of ion milling at $+35°$ (500V, -100V, 50mA, 12sccn ArO_2)
- evaporation of the first Al layer: 100 nm at 1 nm/s and $-35°$
- oxydation 7 min at 20 mBar of ArO_2 atmosphere.
- evaporation of the second Al layer: 130 nm at 1 nm/s and $+35°$
- capping oxydation 5 min at 40 mBar of ArO_2 atmosphere.

C.4.7 *Lift-off*

- 10-15 min in acetone in 55°C-water bath.
- rinse with acetone
- 2 s ultrasound in acetone (to remove small pieces of aluminum in the grid)
- rinse with IPA
- N_2 blow dry

C.5 GRIDS IN THE MICROSTRIP RESONATORS

To prevent from spurious vortices in the large aluminum strips forming the $\lambda/2$ resonator, associated flux noise and quasiparticles , the strips were designed with

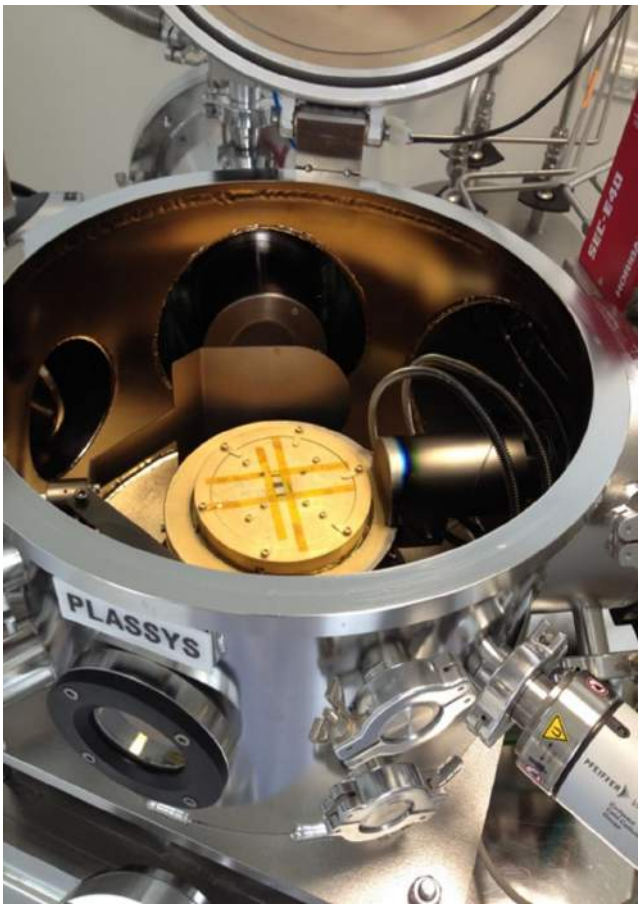

Figure 94: Sapphire chip ready for evaporation.

holes, thus forming a grid. The grid intends to localize the vortices in the holes all over the aluminum strip. Note that the unit cell being far smaller than the wavelength, it does not affect the microwave characteristics of the microstrip resonator.

C.6 ROOM TEMPERATURE RESISTANCE OF JOSEPHSON JUNCTIONS

The critical current I_0 is related to the resistance of the junction in normal state R_n by the Ambegaokar-Baratoff relation.

$$I_0 R_n = \frac{\pi \Delta}{2e} \tag{338}$$

with e the electron charge and Δ the superconductor gap, for aluminum $\Delta \approx 180\ \mu$eV. Therefore, we can directly test the critical current of the junctions by measuring the resistance at room temperature. However, a systematic discrepancy of the value of the resistance has been observed between room temperature and low temperature, it is of the order of $R_n^{300\mathrm{K}} \approx 1.2 R_n^{4\mathrm{K}}$.

Note that this test is not directly possible for shunted JRM since junctions get DC shorted by the meanders.

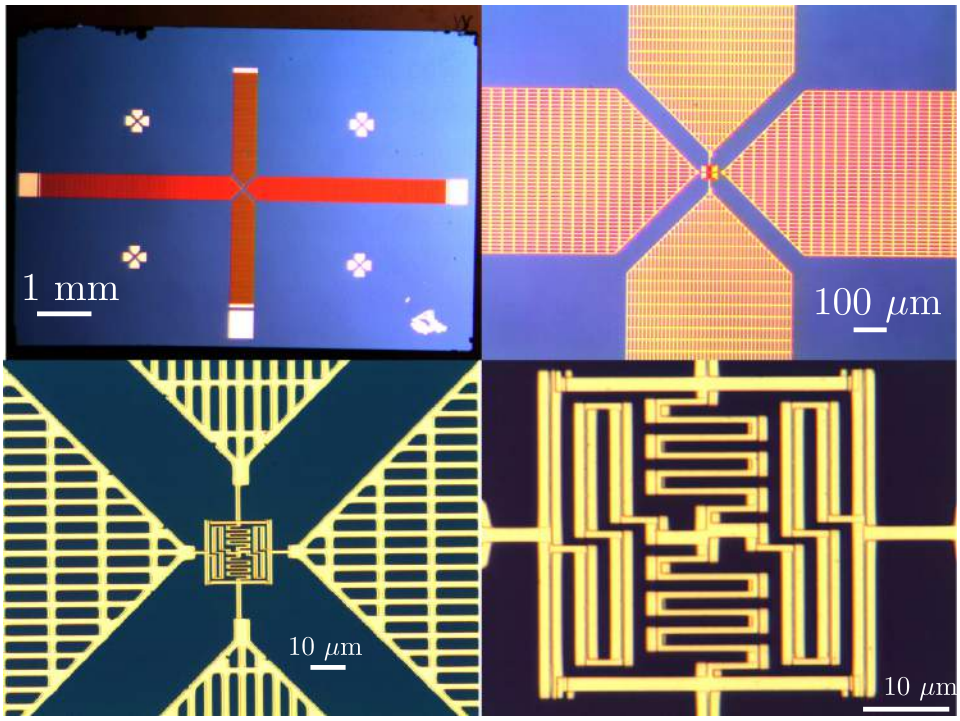

Figure 95: Optical microscope picture of the sample after lift-off

C.7 AMPLIFYING CHAIN

Let us consider an amplifying chain constituted of n amplifiers in series. Each amplifier has a gain G_i and adds to the signal a noise N_i referred to its input. Therefore, the gain of the amplifying chain is $G_{tot} = G_1 \times G_2 \times ... \times G_n$ and the noise at the output is given by

$$N_{output} = (G_1 G_2 ... G_n) N_1 + (G_2 G_3 ... G_n) N_2 + (G_3 G_4 ... G_n) N_3 + ... \quad (339)$$

Thus the noise of the amplifying chain referred to its input is

$$N_{tot} = \frac{N_{output}}{G_{tot}} = N_1 + \frac{N_2}{G_1} + \frac{N_3}{G_1 G_2} + ... \quad (340)$$

The efficiency of a phase-preserving amplifier is given by $\eta_i = \dfrac{2}{2N_i + 1}$ where the added noise N_i is expressed in photons. Hence, the efficiency of an amplifying chain is given by

$$\boxed{\eta_{tot}^{-1} = \eta_1^{-1} + \frac{\eta_2^{-1}}{G_1} + \frac{\eta_3^{-1}}{G_1 G_2} + ...} \quad (341)$$

Therefore, if the first amplifier has a large enough gain such that $G_1 \eta_2 \gg \eta_1$, then the first amplifier efficiency dominates the efficiency of the chain $\eta_{tot} \approx \eta_1$.

This explains why the first amplifier is of particular importance in an amplifier chain.

For instance, the specification of the HEMT amplifier by Caltech gives a noise temperature $T_{HEMT} = 5$ K leading to an added noise $N_{HEMT} = 13$ photons at 5 GHz. In practice by taking into account the insertion loss before the HEMT, we have $N_{HEMT} \sim 20$ photons, leading to a quantum efficiency of $\eta_{HEMT} \sim 5\%$. If one adds a quantum limited amplifier before the HEMT with a gain of 20 dB, the efficiency of the quantum limited amplifier dominates the efficiency of the chain since $G_{JM}\eta_{HEMT} = 5 \gg \eta_{JM} = 1$, leading to $\eta_{tot} \approx \eta_{JM} \sim 1$.

Part VI

BIBLIOGRAPHY

BIBLIOGRAPHY

[1] J. Raimond and S. Haroche, "Exploring the Quantum," *Oxford University Press, USA.*, vol. 82, no. 1, p. 86, 2006. (Cited on pages 1 and 93.)

[2] R. J. Schoelkopf and S. M. Girvin, "Wiring up quantum systems.," *Nature*, vol. 451, pp. 664–9, Feb. 2008. (Cited on page 1.)

[3] Z.-L. Xiang, S. Ashhab, J. You, and F. Nori, "Hybrid quantum circuits: Superconducting circuits interacting with other quantum systems," *Reviews of Modern Physics*, vol. 85, pp. 623–653, Apr. 2013. (Cited on pages 1 and 53.)

[4] M. H. Devoret and R. J. Schoelkopf, "Superconducting Circuits for Quantum Information: An Outlook," *Science*, vol. 339, pp. 1169–1174, Mar. 2013. (Cited on pages 1, 53, 133, and 184.)

[5] S. Deléglise, I. Dotsenko, C. Sayrin, J. Bernu, M. Brune, J.-M. Raimond, and S. Haroche, "Reconstruction of non-classical cavity field states with snapshots of their decoherence.," *Nature*, vol. 455, pp. 510–4, Sept. 2008. (Cited on page 1.)

[6] M. Hofheinz, H. Wang, M. Ansmann, R. C. Bialczak, E. Lucero, M. Neeley, A. D. O'Connell, D. Sank, J. Wenner, J. M. Martinis, and A. N. Cleland, "Synthesizing arbitrary quantum states in a superconducting resonator.," *Nature*, vol. 459, pp. 546–9, May 2009. (Cited on page 1.)

[7] F. Mallet, M. Castellanos-Beltran, H. Ku, S. Glancy, E. Knill, K. Irwin, G. Hilton, L. Vale, and K. Lehnert, "Quantum State Tomography of an Itinerant Squeezed Microwave Field," *Physical Review Letters*, vol. 106, pp. 1–4, June 2011. (Cited on pages 1 and 108.)

[8] C. Eichler, D. Bozyigit, C. Lang, M. Baur, L. Steffen, J. Fink, S. Filipp, and A. Wallraff, "Observation of Two-Mode Squeezing in the Microwave Frequency Domain," *Physical Review Letters*, vol. 107, pp. 1–5, Sept. 2011. (Cited on pages 1, 4, 6, 57, 58, 60, 108, 172, and 177.)

[9] C. Eichler, D. Bozyigit, C. Lang, L. Steffen, J. Fink, and A. Wallraff, "Experimental State Tomography of Itinerant Single Microwave Photons," *Physical Review Letters*, vol. 106, pp. 3–6, June 2011. (Cited on page 1.)

[10] G. Kirchmair, B. Vlastakis, Z. Leghtas, S. E. Nigg, H. Paik, E. Ginossar, M. Mirrahimi, L. Frunzio, S. M. Girvin, and R. J. Schoelkopf, "Observation of quantum state collapse and revival due to the single-photon Kerr effect," *Nature*, vol. 495, pp. 205–209, Mar. 2013. (Cited on page 1.)

[11] B. Vlastakis, G. Kirchmair, Z. Leghtas, S. E. Nigg, L. Frunzio, S. M. Girvin, M. Mirrahimi, M. H. Devoret, and R. J. Schoelkopf, "Deterministically encoding quantum information using 100-photon Schrödinger cat states.," *Science (New York, N.Y.)*, vol. 342, pp. 607–10, Nov. 2013. (Cited on page 1.)

[12] N. Bergeal, F. Schackert, M. Metcalfe, R. Vijay, V. E. Manucharyan, L. Frunzio, D. E. Prober, R. J. Schoelkopf, S. M. Girvin, and M. H. Devoret, "Phase-preserving amplification near the quantum limit with a Josephson ring modulator," *Nature*, vol. 465, pp. 64–68, May 2010. (Cited on pages 1, 3, 4, 16, 38, and 63.)

[13] N. Bergeal, R. Vijay, V. E. Manucharyan, I. Siddiqi, R. J. Schoelkopf, S. M. Girvin, and M. H. Devoret, "Analog information processing at the quantum limit with a Josephson ring modulator," *Nature Physics*, vol. 6, pp. 296–302, Feb. 2010. (Cited on pages 1, 3, 4, 16, and 63.)

[14] A. Einstein, B. Podolsky, and N. Rosen, "Can Quantum-Mechanical Description of Physical Reality Be Considered Complete' ?," *Physical Review*, pp. 2–5, 1935. (Cited on pages 2 and 97.)

[15] B. Yurke, L. Corruccini, P. Kaminsky, L. Rupp, A. Smith, A. Silver, R. Simon, and E. Whittaker, "Observation of parametric amplification and deamplification in a josephson parametric amplifier," *Physical Review A*, vol. 39, no. 5, p. 2519, 1989. (Cited on pages 4 and 57.)

[16] B. Yurke, P. Kaminsky, R. Miller, E. Whittaker, A. Smith, A. Silver, and R. Simon, "Observation of 4.2-K equilibrium-noise squeezing via a Josephson-parametric amplifier," *Physical Review Letters*, vol. 60, no. 9, pp. 764–767, 1988. (Cited on pages 4 and 107.)

[17] R. Movshovich, B. Yurke, P. Kaminsky, A. Smith, A. Silver, R. Simon, and M. Schneider, "Observation of Zero-Point Noise Squeezing via a Josephson-Parametric amplifier," *Physical Review Letters*, vol. 65, no. 12, pp. 1419–1422, 1990. (Cited on pages 4 and 107.)

[18] I. Siddiqi, R. Vijay, F. Pierre, C. M. Wilson, M. Metcalfe, C. Rigetti, L. Frunzio, and M. H. Devoret, "RF-Driven Josephson Bifurcation Amplifier for Quantum Measurement," *Physical Review Letters*, vol. 93, p. 207002, Nov. 2004. (Cited on pages 4 and 57.)

[19] M. A. Castellanos-Beltran, K. D. Irwin, G. C. Hilton, L. R. Vale, and K. W. Lehnert, "Amplification and squeezing of quantum noise with a tunable Josephson metamaterial," *Nature Physics*, vol. 4, pp. 929–931, Oct. 2008. (Cited on pages 4, 60, and 108.)

[20] T. Yamamoto, K. Inomata, M. Watanabe, K. Matsuba, T. Miyazaki, W. D. Oliver, Y. Nakamura, and J. S. Tsai, "Flux-driven Josephson parametric amplifier," *Applied Physics Letters*, vol. 93, no. 4, p. 042510, 2008. (Cited on pages 4 and 58.)

[21] R. Vijay, M. H. Devoret, and I. Siddiqi, "Invited review article: The Josephson bifurcation amplifier.," *The Review of scientific instruments*, vol. 80, p. 111101, Nov. 2009. (Cited on pages 4 and 60.)

[22] C. M. Wilson, G. Johansson, a. Pourkabirian, M. Simoen, J. R. Johansson, T. Duty, F. Nori, and P. Delsing, "Observation of the dynamical Casimir effect in a superconducting circuit.," *Nature*, vol. 479, pp. 376–9, Nov. 2011. (Cited on pages 4, 6, 58, 60, and 108.)

[23] M. Hatridge, R. Vijay, D. H. Slichter, J. Clarke, and I. Siddiqi, "Dispersive magnetometry with a quantum limited SQUID parametric amplifier," *Physical Review B*, vol. 83, p. 134501, Apr. 2011. (Cited on pages 4, 57, and 60.)

[24] J. Mutus, T. White, E. Jeffrey, D. Sank, R. Barends, J. Bochmann, Y. Chen, Z. Chen, B. Chiaro, A. Dunsworth, J. Kelly, A. Megrant, C. Neill, P. OMalley, P. Roushan, A. Vainsencher, W. J., I. Siddiqi, R. Vijay, A. Cleland, and J. M. Martinis, "Design and characterization of a lumped element single-ended superconducting microwave parametric amplifier with on-chip flux bias line," *Applied Physics Letters*, pp. 2–6, 2013. (Cited on pages 4, 57, 58, and 60.)

[25] B. Ho Eom, P. K. Day, H. G. LeDuc, and J. Zmuidzinas, "A wideband, low-noise superconducting amplifier with high dynamic range," *Nature Physics*, vol. 8, pp. 623–627, July 2012. (Cited on pages 4 and 60.)

[26] C. Caves, "Quantum limits on noise in linear amplifier," *Physical Review D*, vol. 26, no. 8, p. 1817, 1982. (Cited on pages 5 and 54.)

[27] N. Bergeal, F. Schackert, L. Frunzio, and M. H. Devoret, "Two-Mode Correlation of Microwave Quantum Noise Generated by Parametric Down-Conversion," *Physical Review Letters*, vol. 108, p. 123902, Mar. 2012. (Cited on pages 6 and 152.)

[28] E. P. Menzel, R. Di Candia, F. Deppe, P. Eder, L. Zhong, M. Ihmig, M. Haeberlein, A. Baust, E. Hoffmann, D. Ballester, K. Inomata, T. Yamamoto, Y. Nakamura, E. Solano, A. Marx, and R. Gross, "Path Entanglement of Continuous-Variable Quantum Microwaves," *Physical Review Letters*, vol. 109, p. 250502, Dec. 2012. (Cited on pages 6, 108, 109, and 172.)

[29] Y. Kubo, C. Grezes, A. Dewes, T. Umeda, J. Isoya, H. Sumiya, N. Morishita, H. Abe, S. Onoda, T. Ohshima, V. Jacques, A. Dréau, J.-F. Roch, I. Diniz, A. Auffeves, D. Vion, D. Esteve, and P. Bertet, "Hybrid Quantum Circuit with a Superconducting Qubit Coupled to a Spin Ensemble," *Physical Review Letters*, vol. 107, p. 220501, Nov. 2011. (Cited on pages 8 and 136.)

[30] X. Zhu, S. Saito, A. Kemp, K. Kakuyanagi, S.-i. Karimoto, H. Nakano, W. J. Munro, Y. Tokura, M. S. Everitt, K. Nemoto, M. Kasu, N. Mizuochi,

and K. Semba, "Coherent coupling of a superconducting flux qubit to an electron spin ensemble in diamond.," *Nature*, vol. 478, pp. 221–4, Oct. 2011. (Cited on pages 8 and 136.)

[31] C. Grezes, B. Julsgaard, Y. Kubo, M. Stern, T. Umeda, J. Isoya, H. Sumiya, H. Abe, S. Onoda, T. Ohshima, V. Jacques, J. Esteve, D. Vion, D. Esteve, K. Mø lmer, and P. Bertet, "Multimode Storage and Retrieval of Microwave Fields in a Spin Ensemble," *Physical Review X*, vol. 4, p. 021049, June 2014. (Cited on pages 8, 135, 136, and 169.)

[32] T. a. Palomaki, J. D. Teufel, R. W. Simmonds, and K. W. Lehnert, "Entangling mechanical motion with microwave fields.," *Science (New York, N.Y.)*, vol. 342, pp. 710–3, Nov. 2013. (Cited on pages 8, 63, 137, and 172.)

[33] J. Wenner, Y. Yin, Y. Chen, R. Barends, B. Chiaro, E. Jeffrey, J. Kelly, A. Megrant, J. Y. Mutus, C. Neill, P. J. J. OMalley, P. Roushan, D. Sank, A. Vainsencher, T. C. White, A. N. Korotkov, A. N. Cleland, and J. M. Martinis, "Catching Time-Reversed Microwave Coherent State Photons with 99.4% Absorption Efficiency," *Physical Review Letters*, vol. 112, p. 210501, May 2014. (Cited on pages 8, 138, 139, 166, 168, 169, and 171.)

[34] M. Pierre, I.-M. Svensson, S. Raman Sathyamoorthy, G. Johansson, and P. Delsing, "Storage and on-demand release of microwaves using superconducting resonators with tunable coupling," *Applied Physics Letters*, vol. 104, p. 232604, June 2014. (Cited on pages 8, 135, 138, 139, 169, and 171.)

[35] N. Lee, H. Benichi, Y. Takeno, S. Takeda, J. Webb, E. Huntington, and A. Furusawa, "Teleportation of nonclassical wave packets of light.," *Science (New York, N.Y.)*, vol. 332, pp. 330–3, Apr. 2011. (Cited on page 11.)

[36] H. Takahashi, J. Neergaard-Nielsen, M. Takeuchi, M. Takeoka, K. Hayasaka, A. Furusawa, and M. Sasaki, "Entanglement distillation from Gaussian input states," *Nature Photonics*, vol. 4, no. February, pp. 2–5, 2010. (Cited on pages 11, 90, 109, and 119.)

[37] Z. Leghtas, G. Kirchmair, B. Vlastakis, R. J. Schoelkopf, M. H. Devoret, and M. Mirrahimi, "Hardware-Efficient Autonomous Quantum Memory Protection," *Physical Review Letters*, vol. 111, p. 120501, Sept. 2013. (Cited on pages 11 and 184.)

[38] D. McNamee, "Hey, what's that sound : Ring modulators," *The Guardian*, no. Monday 9 November 2009. (Cited on page 15.)

[39] N. Roch, E. Flurin, F. Nguyen, P. Morfin, P. Campagne-Ibarcq, M. H. Devoret, and B. Huard, "Widely Tunable, Nondegenerate Three-Wave Mixing Microwave Device Operating near the Quantum Limit," *Physical Review Letters*, vol. 108, pp. 1–5, Apr. 2012. (Cited on pages 17, 24, 50, and 84.)

[40] G. Dolan, "Offset masks for lift-off photoprocessing," *Applied Physics Letters*, vol. 31, no. 5, pp. 337–339, 1977. (Cited on pages 35 and 217.)

[41] F. Schackert, "A practical quantum-limited parametric amplifier based on the Josephson ring modulator," *Thesis, Yale university*, 2013. (Cited on page 36.)

[42] B. Abdo, F. Schackert, M. Hatridge, C. Rigetti, and M. Devoret, "Josephson amplifier for qubit readout," *Applied Physics Letters*, vol. 99, no. 16, p. 162506, 2011. (Cited on pages 37 and 84.)

[43] A. Megrant, C. Neill, R. Barends, B. Chiaro, Y. Chen, L. Feigl, J. Kelly, E. Lucero, M. Mariantoni, P. J. J. O Malley, D. Sank, A. Vainsencher, J. Wenner, T. C. White, Y. Yin, J. Zhao, C. J. Palmstroom, J. M. Martinis, and A. N. Cleland, "Planar superconducting resonators with internal quality factors above one million," *Applied Physics Letters*, vol. 100, no. 11, p. 113510, 2012. (Cited on pages 38 and 138.)

[44] J.-D. Pillet, E. Flurin, F. Mallet, and B. Huard, "A compact design for the Josephson mixer: The lumped element circuit," *Applied Physics Letters*, vol. 106, p. 222603, June 2015. (Cited on pages 38 and 79.)

[45] D. M Pozar, "Microwave Engineering," *Wiley*, 1998. (Cited on page 40.)

[46] W. H. Zurek, "Decoherence, einselection, and the quantum origins of the classical," *Reviews of Modern Physics*, vol. 75, pp. 715–775, May 2003. (Cited on page 53.)

[47] S. Gleyzes, S. Kuhr, C. Guerlin, J. Bernu, S. Deléglise, U. Busk Hoff, M. Brune, J.-M. Raimond, and S. Haroche, "Quantum jumps of light recording the birth and death of a photon in a cavity.," *Nature*, vol. 446, pp. 297–300, Mar. 2007. (Cited on pages 53 and 138.)

[48] P. Campagne-Ibarcq, E. Flurin, N. Roch, D. Darson, P. Morfin, M. Mirrahimi, M. H. Devoret, F. Mallet, and B. Huard, "Persistent Control of a Superconducting Qubit by Stroboscopic Measurement Feedback," *Physical Review X*, vol. 3, p. 021008, May 2013. (Cited on pages 53, 69, 76, 78, 84, and 85.)

[49] H. Haus and J. Mullen, "Quantum Noise in Linear Amplifiers," *Physical Review*, vol. 128, no. 5, 1962. (Cited on page 54.)

[50] W. K. Wootters and W. H. Zurek, "A single quantum cannot be cloned," 1982. (Cited on page 54.)

[51] G. Y. Xiang, T. C. Ralph, A. P. Lund, N. Walk, and G. J. Pryde, "Heralded noiseless linear amplification and distillation of entanglement," *Nature Photonics*, vol. 4, pp. 316–319, Mar. 2010. (Cited on page 56.)

[52] M. Hatridge, S. Shankar, M. Mirrahimi, F. Schackert, K. Geerlings, T. Brecht, K. M. Sliwa, B. Abdo, L. Frunzio, S. M. Girvin, R. J. Schoelkopf, and M. H. Devoret, "Quantum back-action of an individual variable-strength measurement.," *Science (New York, N.Y.)*, vol. 339, pp. 178–81, Jan. 2013. (Cited on page 56.)

[53] K. W. Murch, S. J. Weber, C. Macklin, and I. Siddiqi, "Observing single quantum trajectories of a superconducting quantum bit," *Nature*, vol. 502, pp. 211–214, Oct. 2013. (Cited on page 56.)

[54] A. Kamal, A. Marblestone, and M. Devoret, "Signal-to-pump back action and self-oscillation in double-pump Josephson parametric amplifier," *Physical Review B*, vol. 79, p. 184301, May 2009. (Cited on page 57.)

[55] M. A. Castellanos-Beltran and K. W. Lehnert, "Widely tunable parametric amplifier based on a superconducting quantum interference device array resonator," *Applied Physics Letters*, vol. 91, no. 8, p. 083509, 2007. (Cited on page 57.)

[56] X. Zhou, V. Schmitt, P. Bertet, D. Vion, W. Wustmann, V. Shumeiko, and D. Esteve, "High-gain weakly nonlinear flux-modulated Josephson parametric amplifier using a SQUID array," *Physical Review B*, vol. 89, p. 214517, June 2014. (Cited on pages 58 and 60.)

[57] O. Yaakobi, L. Friedland, C. Macklin, and I. Siddiqi, "Parametric amplification in Josephson junction embedded transmission lines," *Physical Review B*, vol. 87, p. 144301, Apr. 2013. (Cited on page 60.)

[58] C. Macklin, D. Slichter, O. Yaakobi, L. Friedland, V. Bolkhovsky, D. Braje, G. Fitch, W. Oliver, and I. Siddiqi, "Josephson traveling-wave parametric amplifier for superconducting qubit readout," *Bulletin of the American Physical Society*, vol. Volume 59, Mar. 2014. (Cited on page 61.)

[59] F. Massel, T. T. Heikkilä, J.-M. Pirkkalainen, S. U. Cho, H. Saloniemi, P. J. Hakonen, and M. a. Sillanpää, "Microwave amplification with nanomechanical resonators.," *Nature*, vol. 480, pp. 351–4, Dec. 2011. (Cited on page 63.)

[60] R. Schoelkopf, P. Burke, A. Kozhevnikov, D. Prober, and M. Rooks, "Frequency Dependence of Shot Noise in a Diffusive Mesoscopic Conductor," *Physical Review Letters*, vol. 78, pp. 3370–3373, Apr. 1997. (Cited on page 73.)

[61] L. Spietz, K. Irwin, M. Lee, and J. Aumentado, "Noise performance of lumped element direct current superconducting quantum interference device amplifiers in the 4-8 GHz range," *Applied Physics Letters*, vol. 97, no. 14, p. 142502, 2010. (Cited on page 76.)

[62] F. R. Ong, M. Boissonneault, F. Mallet, A. Palacios-Laloy, A. Dewes, A. C. Doherty, A. Blais, P. Bertet, D. Vion, and D. Esteve, "Circuit QED with a Nonlinear Resonator: ac-Stark Shift and Dephasing," *Physical Review Letters*, vol. 106, p. 167002, Apr. 2011. (Cited on page 77.)

[63] B. Abdo, A. Kamal, and M. Devoret, "Nondegenerate three-wave mixing with the Josephson ring modulator," *Physical Review B*, vol. 87, p. 014508, Jan. 2013. (Cited on pages 84 and 191.)

[64] P. Campagne-Ibarcq, L. Bretheau, E. Flurin, A. Auffèves, F. Mallet, and B. Huard, "Observing Interferences between Past and Future Quantum States in Resonance Fluorescence," *Physical Review Letters*, vol. 112, p. 180402, May 2014. (Cited on pages 85 and 177.)

[65] E. Schrödinger, "Discussion of probability relations between separated systems," *Mathematical Proceedings of the Cambridge Philosophical Society*, vol. 31, p. 555, Oct. 1935. (Cited on page 89.)

[66] W. Zurek, "Environment-Assisted Invariance, Entanglement, and Probabilities in Quantum Physics," *Physical Review Letters*, vol. 90, p. 120404, Mar. 2003. (Cited on page 89.)

[67] G. Chiribella, G. M. D Ariano, and P. Perinotti, "Informational derivation of quantum theory," *Physical Review A*, vol. 84, pp. 1–39, July 2011. (Cited on pages 89 and 90.)

[68] G. Chiribella and P. Perinotti, "Quantum Theory, Namely the Pure and Reversible Theory of Information," *Entropy*, vol. 14, no. 14, p. 1877, 2012. (Cited on page 90.)

[69] N. Linden, S. Popescu, A. Short, and A. Winter, "Quantum mechanical evolution towards thermal equilibrium," *Physical Review E*, vol. 79, p. 061103, June 2009. (Cited on page 90.)

[70] S. Braunstein and P. V. Loock, "Quantum information with continuous variables," *Reviews of Modern Physics*, vol. 77, no. April, p. 513, 2005. (Cited on pages 90, 93, 117, 118, 179, 185, and 206.)

[71] A. Furusawa, J. Sorensen, S. Braunstein, C. Fuchs, H. Kimble, and E. S. Polzik, "Unconditional quantum teleportation," *Science*, vol. 282, pp. 706–709, Oct. 1998. (Cited on pages 90, 107, and 108.)

[72] F. Grosshans and P. Grangier, "Quantum cloning and teleportation criteria for continuous quantum variables," *Physical Review A*, vol. 64, p. 010301, June 2001. (Cited on pages 90 and 187.)

[73] F. Grosshans and P. Grangier, "Continuous Variable Quantum Cryptography Using Coherent States," *Physical Review Letters*, vol. 88, p. 057902, Jan. 2002. (Cited on page 90.)

[74] N. Menicucci, P. van Loock, M. Gu, C. Weedbrook, T. Ralph, and M. Nielsen, "Universal Quantum Computation with Continuous-Variable Cluster States," *Physical Review Letters*, vol. 97, p. 110501, Sept. 2006. (Cited on page 90.)

[75] M. Yukawa, R. Ukai, P. van Loock, and A. Furusawa, "Experimental generation of four-mode continuous-variable cluster states," *Physical Review A*, vol. 78, p. 012301, July 2008. (Cited on page 90.)

[76] C. Weedbrook, S. Pirandola, R. García-Patrón, N. J. Cerf, T. C. Ralph, J. H. Shapiro, and S. Lloyd, "Gaussian quantum information," *Reviews of Modern Physics*, vol. 84, pp. 621–669, May 2012. (Cited on page 90.)

[77] P. Jouguet, S. Kunz-Jacques, A. Leverrier, P. Grangier, and E. Diamanti, "Experimental demonstration of long-distance continuous-variable quantum key distribution," *Nature Photonics*, vol. 7, pp. 378–381, Apr. 2013. (Cited on page 90.)

[78] M. Collett, "Exact density-matrix calculations for simple open systems," *Physical Review A*, vol. 38, no. 5, pp. 2233–2247, 1988. (Cited on page 91.)

[79] G. Adesso and F. Illuminati, "Strong Monogamy of Bipartite and Genuine Multipartite Entanglement: The Gaussian Case," *Physical Review Letters*, vol. 99, p. 150501, Oct. 2007. (Cited on page 97.)

[80] H. Ollivier and W. Zurek, "Quantum discord: a measure of the quantumness of correlations," *Physical Review Letters*, vol. 88, pp. 15–18, Dec. 2001. (Cited on pages 97 and 98.)

[81] L. Henderson and V. Vedral, "Classical, quantum and total correlations," *Journal of physics A*, vol. 34, 2001. (Cited on page 98.)

[82] K. Modi, A. Brodutch, H. Cable, T. Paterek, and V. Vedral, "The classical-quantum boundary for correlations: Discord and related measures," *Reviews of Modern Physics*, vol. 84, pp. 1655–1707, Nov. 2012. (Cited on pages 98, 99, and 205.)

[83] C. Weedbrook and S. Pirandola, "Discord Empowered Quantum Illumination," *arXiv preprint*, no. 1312.3332, 2013. (Cited on page 99.)

[84] A. Ferraro, L. Aolita, D. Cavalcanti, F. M. Cucchietti, and A. Acín, "Almost all quantum states have nonclassical correlations," *Physical Review A*, vol. 81, p. 052318, May 2010. (Cited on page 99.)

[85] W. Wan, Y. Chong, L. Ge, H. Noh, A. D. Stone, and H. Cao, "Time-reversed lasing and interferometric control of absorption.," *Science (New York, N.Y.)*, vol. 331, pp. 889–92, Feb. 2011. (Cited on page 100.)

[86] F. Schackert, A. Roy, M. Hatridge, M. H. Devoret, and A. D. Stone, "Three-Wave Mixing with Three Incoming Waves: Signal-Idler Coherent Attenuation and Gain Enhancement in a Parametric Amplifier," *Physical Review Letters*, vol. 111, p. 073903, Aug. 2013. (Cited on pages 101 and 113.)

[87] L. Duan, G. Giedke, J. Cirac, and P. Zoller, "Inseparability criterion for continuous variable systems," *Physical review letters*, vol. 84, pp. 2722–5, Mar. 2000. (Cited on page 103.)

[88] J. Bell, "On the Einstein Podolsky Rosen paradox," *Physics*, vol. 1, no. 3, pp. 195–200, 1964. (Cited on page 104.)

[89] J. Clauser, M. Horne, A. Shimony, and R. Holt, "Proposed experiment to test local hidden-variable theories," *Physical Review Letters*, vol. 23, no. 15, pp. 880–884, 1969. (Cited on page 104.)

[90] A. Aspect, J. Dalibard, and G. Roger, "Experimental Test of Bell's Inequalities Using Time-Varying Analyzers," *Physical Review Letters*, vol. 49, no. 25, p. 1804, 1982. (Cited on page 104.)

[91] A. Aspect, P. Grangier, and G. Roger, "Experimental Realization of Einstein-Podolsky-Rosen-Bohm Gedankenexperiment: A New Violation of Bell's Inequalities," *Physical Review Letters*, vol. 49, no. 2, pp. 91–94, 1982. (Cited on page 104.)

[92] T. Scheidl, R. Ursin, J. Kofler, S. Ramelow, X.-S. Ma, T. Herbst, L. Ratschbacher, A. Fedrizzi, N. K. Langford, T. Jennewein, and A. Zeilinger, "Violation of local realism with freedom of choice.," *Proceedings of the National Academy of Sciences of the United States of America*, vol. 107, pp. 19708–13, Nov. 2010. (Cited on page 104.)

[93] M. Giustina, A. Mech, S. Ramelow, B. Wittmann, J. Kofler, J. Beyer, A. Lita, B. Calkins, T. Gerrits, S. W. Nam, R. Ursin, and A. Zeilinger, "Bell violation using entangled photons without the fair-sampling assumption.," *Nature*, vol. 497, pp. 227–30, Apr. 2013. (Cited on page 104.)

[94] G. Weihs, T. Jennewein, C. Simon, H. Weinfurter, and A. Zeilinger, "Violation of Bell's inequality under strict Einstein locality conditions," *Physical Review Letters*, vol. 81, no. 23, p. 5039, 1998. (Cited on page 104.)

[95] M. Ansmann, H. Wang, R. C. Bialczak, M. Hofheinz, E. Lucero, M. Neeley, A. D. O'Connell, D. Sank, M. Weides, J. Wenner, A. N. Cleland, and J. M. Martinis, "Violation of Bell's inequality in Josephson phase qubits.," *Nature*, vol. 461, pp. 504–6, Sept. 2009. (Cited on page 104.)

[96] B. Hensen, H. Bernien, A. Dréau, A. Reiserer, N. Kalb, M. Blok, J. Ruitenberg, R. Vermeulen, R. Schouten, C. Abellán, *et al.*, "Experimental loophole-free violation of a bell inequality using entangled electron spins separated by 1.3 km," *arXiv preprint arXiv:1508.05949*, 2015. (Cited on page 104.)

[97] Z. Ou, S. Pereira, H. Kimble, and K. Peng, "Realization of the Einstein-Podolsky-Rosen Paradox for Continuous variables," *Physical Review Letters*, vol. 68, no. 25, pp. 3663–3666, 1992. (Cited on pages 107 and 108.)

[98] C. Silberhorn, P. K. Lam, O. Weiß, F. König, N. Korolkova, and G. Leuchs, "Generation of Continuous Variable Einstein-Podolsky-Rosen Entanglement via the Kerr Nonlinearity in an Optical Fiber," *Physical Review Letters*, vol. 86, pp. 4267–4270, May 2001. (Cited on pages 107 and 108.)

[99] T. C. Zhang, K. W. Goh, C. W. Chou, P. Lodahl, and H. J. Kimble, "Quantum teleportation of light beams," *Physical Review A*, vol. 67, p. 033802, Mar. 2003. (Cited on page 107.)

[100] W. P. Bowen, N. Treps, B. C. Buchler, R. Schnabel, T. C. Ralph, H.-A. Bachor, T. Symul, and P. K. Lam, "Experimental investigation of continuous-variable quantum teleportation," *Physical Review A*, vol. 67, p. 032302, Mar. 2003. (Cited on page 107.)

[101] X. Li, Q. Pan, J. Jing, J. Zhang, C. Xie, and K. Peng, "Quantum Dense Coding Exploiting a Bright Einstein-Podolsky-Rosen Beam," *Physical Review Letters*, vol. 88, p. 047904, Jan. 2002. (Cited on page 107.)

[102] W. P. Bowen, N. Treps, R. Schnabel, and P. K. Lam, "Experimental Demonstration of Continuous Variable Polarization Entanglement," *Physical Review Letters*, vol. 89, p. 253601, Dec. 2002. (Cited on page 107.)

[103] A. Wallraff, D. I. Schuster, A. Blais, L. Frunzio, R.-S. Huang, J. Majer, S. Kumar, S. M. Girvin, and R. J. Schoelkopf, "Strong coupling of a single photon to a superconducting qubit using circuit quantum electrodynamics.," *Nature*, vol. 431, no. 7005, pp. 162–167, 2004. (Cited on page 107.)

[104] J. D. Teufel, T. Donner, M. A. Castellanos-Beltran, J. W. Harlow, and K. W. Lehnert, "Nanomechanical motion measured with precision beyond the standard quantum limit," *Nature Nanotechnology*, vol. 4, no. November, p. 5, 2009. (Cited on page 107.)

[105] E. Flurin, N. Roch, F. Mallet, M. Devoret, and B. Huard, "Generating entangled microwave radiation over two transmission lines," *Physical Review Letters*, vol. 109, pp. 1–5, Oct. 2012. (Cited on pages 108, 117, and 129.)

[106] B. Yurke, S. L. McCall, and J. R. Klauder, "SU(2) and SU(1,1) interferometers," *Physical Review A*, vol. 33, no. 6, pp. 4033–4054, 1986. (Cited on pages 109 and 113.)

[107] V. Giovannetti, S. Lloyd, and L. Maccone, "Quantum-enhanced measurements: beating the standard quantum limit.," *Science (New York, N.Y.)*, vol. 306, pp. 1330–6, Nov. 2004. (Cited on pages 109 and 110.)

[108] J. Kong, F. Hudelist, Z. Y. Ou, and W. Zhang, "Cancellation of Internal Quantum Noise of an Amplifier by Quantum Correlation," *Physical Review Letters*, vol. 111, p. 033608, July 2013. (Cited on page 109.)

[109] G. Adesso, "Gaussian Interferometric Power," *Physical Review A*, vol. 90, no. 022321, 2014. (Cited on page 109.)

[110] R. Schnabel, N. Mavalvala, D. E. McClelland, and P. K. Lam, "Quantum metrology for gravitational wave astronomy.," *Nature communications*, vol. 1, p. 121, Jan. 2010. (Cited on page 110.)

[111] L. collaboration, "Enhanced sensitivity of the LIGO gravitational wave detector by using squeezed states of light," *Nature Photonics*, vol. 7, pp. 613–619, July 2013. (Cited on page 111.)

[112] I. Ruo Berchera, I. P. Degiovanni, S. Olivares, and M. Genovese, "Quantum Light in Coupled Interferometers for Quantum Gravity Tests," *Physical Review Letters*, vol. 110, p. 213601, May 2013. (Cited on page 111.)

[113] C. J. Hogan, "Interferometers as probes of Planckian quantum geometry," *Physical Review D*, vol. 85, p. 064007, Mar. 2012. (Cited on page 111.)

[114] J. Eisert, S. Scheel, and M. B. Plenio, "Distilling Gaussian States with Gaussian Operations is Impossible," *Physical Review Letters*, vol. 89, p. 137903, Sept. 2002. (Cited on page 119.)

[115] H. Nyquist, "Thermal agitation of electric charge in conductors," *Physical Review*, vol. 32, no. 1, pp. 110–113, 1928. (Cited on pages 123, 193, and 201.)

[116] P. Shor, "Polynomial-time algorithms for prime factorization and discrete logarithms on a quantum computer," *SIAM journal on computing*, vol. 26, no. 5, pp. 1484–1509, 1997. (Cited on page 133.)

[117] H. Bennett Ch and G. Brassard, "Quantum cryptography: public key distribution and coin tossing int," in *Conf. on Computers, Systems and Signal Processing (Bangalore, India, Dec. 1984)*, pp. 175–9, 1984. (Cited on page 133.)

[118] P. Goy, J. Raimond, M. Gross, and S. Haroche, "Observation of Cavity-Enhanced Single-Atom Spontaneous Emission," *Physical Review Letters*, vol. 50, pp. 1903–1906, 1983. (Cited on page 133.)

[119] Y. Kubo, F. R. Ong, P. Bertet, D. Vion, V. Jacques, D. Zheng, A. Dréau, J.-F. Roch, A. Auffeves, F. Jelezko, J. Wrachtrup, M. F. Barthe, P. Bergonzo, and D. Esteve, "Strong Coupling of a Spin Ensemble to a Superconducting Resonator," *Physical Review Letters*, vol. 105, p. 140502, Sept. 2010. (Cited on page 133.)

[120] C. A. Regal, J. D. Teufel, and K. W. Lehnert, "Measuring nanomechanical motion with a microwave cavity interferometer," *Nature Physics*, vol. 4, pp. 555–560, May 2008. (Cited on page 133.)

[121] J. Cirac, P. Zoller, H. Kimble, and H. Mabuchi, "Quantum State Transfer and Entanglement Distribution among Distant Nodes in a Quantum Network," *Physical Review Letters*, vol. 78, pp. 3221–3224, Apr. 1997. (Cited on pages 133, 161, and 171.)

[122] H. J. Kimble, "The quantum internet.," *Nature*, vol. 453, pp. 1023–30, June 2008. (Cited on pages 133 and 171.)

[123] A. I. Lvovsky, B. C. Sanders, and W. Tittel, "Optical quantum memory," *Nature Photonics*, vol. 3, pp. 706–714, Dec. 2009. (Cited on page 135.)

[124] K. S. Choi, H. Deng, J. Laurat, and H. J. Kimble, "Mapping photonic entanglement into and out of a quantum memory.," *Nature*, vol. 452, pp. 67–71, Mar. 2008. (Cited on page 135.)

[125] K. Jensen, W. Wasilewski, H. Krauter, T. Fernholz, B. M. Nielsen, M. Owari, M. B. Plenio, A. Serafini, M. M. Wolf, and E. S. Polzik, "Quantum memory for entangled continuous-variable states," *Nature Physics*, vol. 7, pp. 13–16, Nov. 2010. (Cited on page 135.)

[126] M. P. Hedges, J. J. Longdell, Y. Li, and M. J. Sellars, "Efficient quantum memory for light.," *Nature*, vol. 465, pp. 1052–6, June 2010. (Cited on page 135.)

[127] E. Bimbard, R. Boddeda, N. Vitrant, A. Grankin, V. Parigi, J. Stanojevic, A. Ourjoumtsev, and P. Grangier, "Homodyne Tomography of a Single Photon Retrieved on Demand from a Cavity-Enhanced Cold Atom Memory," *Physical Review Letters*, vol. 112, p. 033601, Jan. 2014. (Cited on page 135.)

[128] A. Nicolas, L. Veissier, L. Giner, E. Giacobino, D. Maxein, and J. Laurat, "A quantum memory for orbital angular momentum photonic qubits," *Nature Photonics*, vol. 8, pp. 1–5, Aug. 2014. (Cited on page 135.)

[129] T. A. Palomaki, J. W. Harlow, J. D. Teufel, R. W. Simmonds, and K. W. Lehnert, "Coherent state transfer between itinerant microwave fields and a mechanical oscillator," *Nature*, vol. 495, pp. 210–214, Mar. 2013. (Cited on pages 135, 137, 166, 168, and 169.)

[130] Y. Yin, Y. Chen, D. Sank, P. J. J. O Malley, T. C. White, R. Barends, J. Kelly, E. Lucero, M. Mariantoni, A. Megrant, C. Neill, A. Vainsencher, J. Wenner, A. N. Korotkov, A. N. Cleland, and J. M. Martinis, "Catch and Release of Microwave Photon States," *Physical Review Letters*, vol. 110, p. 107001, Mar. 2013. (Cited on pages 135, 138, and 139.)

[131] H. Wu, R. E. George, J. H. Wesenberg, K. Mø lmer, D. I. Schuster, R. J. Schoelkopf, K. M. Itoh, A. Ardavan, J. J. L. Morton, and G. A. D. Briggs, "Storage of Multiple Coherent Microwave Excitations in an Electron Spin Ensemble," *Physical Review Letters*, vol. 105, p. 140503, Sept. 2010. (Cited on page 136.)

[132] B. Julsgaard, C. Grezes, P. Bertet, and K. Mø lmer, "Quantum Memory for Microwave Photons in an Inhomogeneously Broadened Spin Ensemble," *Physical Review Letters*, vol. 110, p. 250503, June 2013. (Cited on pages 136 and 168.)

[133] J. D. Teufel, T. Donner, D. Li, J. W. Harlow, M. S. Allman, K. Cicak, a. J. Sirois, J. D. Whittaker, K. W. Lehnert, and R. W. Simmonds, "Sideband cooling of micromechanical motion to the quantum ground state.," *Nature*, vol. 475, pp. 359–63, July 2011. (Cited on page 137.)

[134] A. D. O'Connell, M. Hofheinz, M. Ansmann, R. C. Bialczak, M. Lenander, E. Lucero, M. Neeley, D. Sank, H. Wang, M. Weides, J. Wenner, J. M. Martinis, and A. N. Cleland, "Quantum ground state and single-phonon control of a mechanical resonator.," *Nature*, vol. 464, pp. 697–703, Apr. 2010. (Cited on page 137.)

[135] T. Li, S. Kheifets, and M. G. Raizen, "Millikelvin cooling of an optically trapped microsphere in vacuum," *Nature Physics*, vol. 7, no. March, p. 18, 2011. (Cited on page 137.)

[136] R. Andrews, R. Peterson, and T. Purdy, "Bidirectional and efficient conversion between microwave and optical light," *Nature Physics*, vol. 10, no. April, pp. 321–326, 2014. (Cited on page 137.)

[137] Y. Tabuchi, S. Ishino, T. Ishikawa, R. Yamazaki, K. Usami, and Y. Nakamura, "Hybridizing ferromagnetic magnons and microwave photons in the quantum limit," *Physical review letters*, vol. 113, no. 8, p. 083603, 2014. (Cited on page 137.)

[138] M. Reagor, H. Paik, G. Catelani, L. Sun, C. Axline, E. Holland, I. M. Pop, N. A. Masluk, T. Brecht, L. Frunzio, M. H. Devoret, L. Glazman, and R. J. Schoelkopf, "Reaching 10 ms single photon lifetimes for superconducting aluminum cavities," *Applied Physics Letters*, vol. 102, no. 19, p. 192604, 2013. (Cited on pages 138 and 167.)

[139] K. Geerlings, S. Shankar, E. Edwards, L. Frunzio, R. J. Schoelkopf, and M. H. Devoret, "Improving the quality factor of microwave compact resonators by optimizing their geometrical parameters," *Applied Physics Letters*, vol. 100, no. 19, p. 192601, 2012. (Cited on page 138.)

[140] J. M. Sage, V. Bolkhovsky, W. D. Oliver, B. Turek, and P. B. Welander, "Study of loss in superconducting coplanar waveguide resonators," *Journal of Applied Physics*, vol. 109, no. 6, p. 063915, 2011. (Cited on pages 138 and 154.)

[141] A. Baust, E. Hoffmann, M. Haeberlein, M. Schwarz, P. Eder, J. Goetz, F. Wulschner, E. Xie, L. Zhong, F. Quijandría, *et al.*, "Tunable and switchable coupling between two superconducting resonators," *Physical Review B*, vol. 91, no. 1, p. 014515, 2015. (Cited on page 138.)

[142] B. Abdo, K. Sliwa, F. Schackert, N. Bergeal, M. Hatridge, L. Frunzio, A. D. Stone, and M. Devoret, "Full Coherent Frequency Conversion between Two Propagating Microwave Modes," *Physical Review Letters*, vol. 110, p. 173902, Apr. 2013. (Cited on page 139.)

[143] B. Abdo, K. Sliwa, L. Frunzio, and M. Devoret, "Directional Amplification with a Josephson Circuit," *Physical Review X*, vol. 3, p. 031001, July 2013. (Cited on page 152.)

[144] E. Flurin, N. Roch, J.-D. Pillet, F. Mallet, and B. Huard, "Superconducting quantum node for entanglement and storage of microwave radiation," *Physical review letters*, vol. 114, no. 9, p. 090503, 2015. (Cited on page 169.)

[145] C. Eichler, D. Bozyigit, and A. Wallraff, "Characterizing quantum microwave radiation and its entanglement with superconducting qubits using linear detectors," *Physical Review A*, vol. 86, pp. 1–13, Sept. 2012. (Cited on page 172.)

[146] C. M. Caves, J. Combes, Z. Jiang, and S. Pandey, "Quantum limits on phase-preserving linear amplifiers," *Physical Review A*, vol. 86, p. 063802, Dec. 2012. (Cited on pages 176 and 179.)

[147] M. Mirrahimi, Z. Leghtas, V. V. Albert, S. Touzard, R. J. Schoelkopf, L. Jiang, and M. H. Devoret, "Dynamically protected cat-qubits: a new paradigm for universal quantum computation," *New Journal of Physics*, vol. 16, p. 045014, Apr. 2014. (Cited on page 184.)

[148] M. Devoret, "Circuits et signaux quantiques, Lecture II : Modes of a circuit and propagation of signals," *Lectures at the College de France (physinfo.fr)*, 2008. (Cited on page 191.)

[149] A. Clerk, M. Devoret, S. Girvin, F. Marquardt, and R. Schoelkopf, "Introduction to quantum noise, measurement, and amplification," *Reviews of Modern Physics*, vol. 82, no. 2, p. 1155, 2010. (Cited on page 191.)

[150] G. Vidal and R. Werner, "Computable measure of entanglement," *Physical Review A*, vol. 65, p. 032314, Feb. 2002. (Cited on pages 205 and 206.)

[151] R. Simon, N. Mukunda, and B. Dutta, "Quantum-noise matrix for multimode systems: U(n) invariance, squeezing, and normal forms," *Physical Review A*, vol. 49, no. 3, pp. 1567–1583, 1994. (Cited on pages 206 and 207.)

[152] R. Simon, E. Sudarshan, and N. Mukunda, "Gaussian-Wigner distributions in quantum mechanics and optics," *Physical Review A*, 1987. (Cited on page 206.)

[153] G. Adesso and F. Illuminati, "Gaussian measures of entanglement versus negativities: Ordering of two-mode Gaussian states," *Physical Review A*, vol. 72, p. 032334, Sept. 2005. (Cited on pages 207 and 208.)